

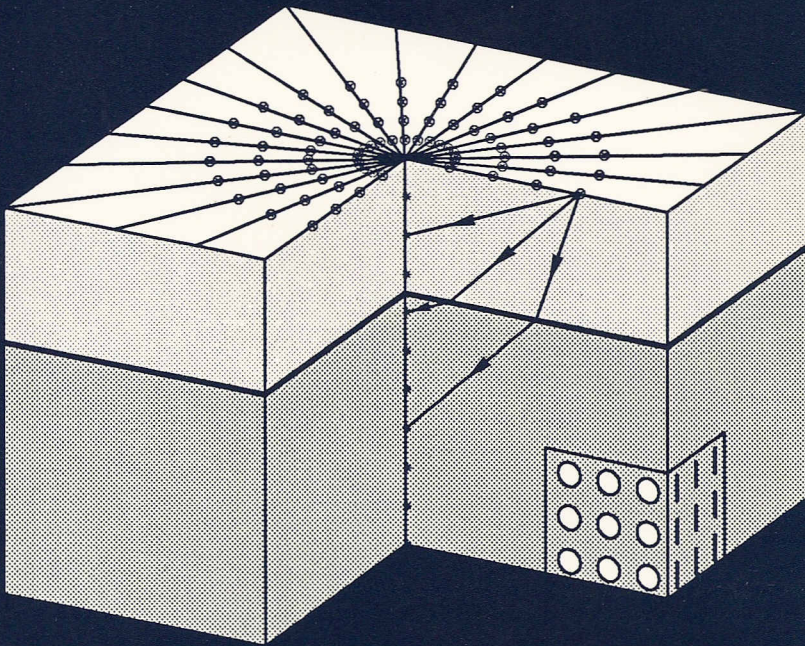
GEOLOGICA ULTRAIECTINA

Mededelingen van het
Instituut voor Aardwetenschappen der
Rijksuniversiteit te Utrecht

No. 54

CRACK-INDUCED ANISOTROPY

AND ITS EFFECT ON
VERTICAL SEISMIC PROFILING



JAN DOUMA

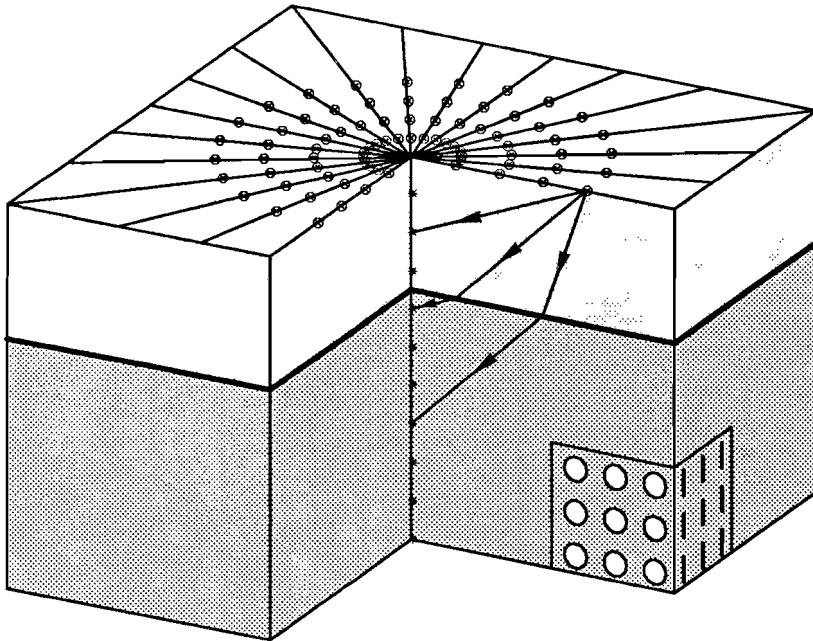
GEOLOGICA ULTRAIECTINA

Mededelingen van het
Instituut voor Aardwetenschappen der
Rijksuniversiteit te Utrecht

No. 54

CRACK-INDUCED ANISOTROPY

AND ITS EFFECT ON
VERTICAL SEISMIC PROFILING



JAN DOUMA

CIP-DATA KONINKLIJKE BIBLIOTHEEK, DEN HAAG

Douma, Jan

Crack-induced anisotropy and its effect on vertical seismic profiling / Jan Douma. - [Utrecht : Institute for Earth Sciences, University Utrecht]. -

Ill., fig., tab. - (Geologica Ultraiectina ; no. 54)

Thesis Utrecht. - With ref.

ISBN 90-71577-07-4

SISO 562 UDC 550.3(043.3)

Subject heading: geophysics.

**CRACK-INDUCED ANISOTROPY
AND ITS EFFECT ON
VERTICAL SEISMIC PROFILING**

**DE ANISOTROPIE TEN GEVOLGE VAN CRACKS
EN HAAR EFFECT OP
VERTICAL SEISMIC PROFILING**

(met een samenvatting in het Nederlands)

PROEFSCHRIFT

**TER VERKRIJGING VAN DE GRAAD VAN DOCTOR AAN
DE RIJKSUNIVERSITEIT TE UTRECHT OP GEZAG VAN
DE RECTOR MAGNIFICUS PROF. DR. J.A. VAN GINKEL
VOLGENS BESLUIT VAN HET COLLEGE VAN DEKANEN
IN HET OPENBAAR TE VERDEDIGEN OP WOENSDAG
7 DECEMBER 1988 DES NAMIDDAGS TE 12.45 UUR**

DOOR

JAN DOUMA

GEBOREN OP 17 DECEMBER 1961 TE HARKEMA

PROMOTOR: PROF. DR. K. HELBIG

Aan mijn ouders

'Science is fun!'

Theme of the National Science Week (U.S.A.)

*The research described in this
thesis was carried out at the:*

*Department of Exploration Geophysics,
Institute for Earth Sciences,
University of Utrecht,
Budapestlaan 4, P.O. Box 80.021,
3508 TA Utrecht,
The Netherlands.*

Contents

Contents

Chapter 1

| | |
|--------------------|----|
| Introduction | 11 |
| References | 14 |

Chapter 2

| | |
|---|----|
| The effect of the aspect ratio on crack-induced anisotropy | 17 |
| 2.1 Introduction | 18 |
| 2.2 Flat crack models | 19 |
| 2.3 Ellipsoidal inclusion models | 20 |
| 2.4 Wave propagation in cracked media | 21 |
| 2.5 Numerical results and discussion | 24 |
| 2.5.1 Comparison of elastic constants | 24 |
| 2.5.2 Comparison of the group velocities | 25 |
| 2.5.3 Normalized difference between group velocities | 28 |
| 2.5.4 The influence of the effective density on the group velocity | 30 |
| 2.5.5 Anisotropy analysis using the parameters δ , ϵ , and γ | 33 |
| 2.6 Conclusions | 34 |
| 2.7 References | 35 |

Chapter 3

| | |
|--|----|
| Elastic wave propagation in media with parallel fractures and aligned cracks | 37 |
| 3.1 Introduction | 38 |
| 3.2 Elastic moduli of stratified media | 39 |
| 3.3 General model for long thin parallel fractures | 43 |
| 3.4 Joints and microcracks | 51 |
| 3.5 Non-flat ellipsoidal inclusions | 54 |
| 3.6 Discussion and conclusions | 57 |
| 3.7 References | 58 |

Chapter 4

| | |
|--|----|
| The representability of cracked media by periodically layered media | 61 |
| 4.1 Introduction | 62 |
| 4.2 Stability constraints of a transversely isotropic medium | 63 |
| 4.3 Stability constraints of periodically layered media | 65 |
| 4.4 The representability of cracked media by RSSIL-media | 67 |
| 4.5 Cracked media represented in the h, k, τ, l parameter space | 72 |
| 4.6 Results | 73 |

Contents

| | | |
|------------------|--|-----|
| 4.7 | Conclusions | 81 |
| 4.8 | Appendix A | 82 |
| 4.9 | Appendix B | 84 |
| 4.10 | Appendix C | 85 |
| 4.11 | References | 86 |
| <i>Chapter 5</i> | | |
| | Shear-wave splitting in isotropic media | 89 |
| 5.1 | Introduction | 90 |
| 5.2 | Theory | 92 |
| 5.2.1 | Decomposition into SH- and SV-waves | 93 |
| 5.2.2 | Transmission coefficients | 94 |
| 5.2.3 | Complex transmission coefficients | 97 |
| 5.2.4 | The polarization of the transmitted S-wave | 100 |
| 5.3 | Example: interface between sandstone and halite | 101 |
| 5.4 | Conclusions | 106 |
| 5.5 | References | 106 |
| <i>Chapter 6</i> | | |
| | The effect of a changing aspect ratio of aligned cracks on shear-wave VSPs | 107 |
| 6.1 | Introduction | 108 |
| 6.2 | The influence of the aspect ratio on crack-induced anisotropy | 109 |
| 6.3 | The model | 111 |
| 6.3.1 | The anisotropic medium | 111 |
| 6.3.2 | The VSP geometry | 113 |
| 6.4 | The modelling | 113 |
| 6.5 | Conclusions | 118 |
| 6.6 | References | 119 |
| <i>Chapter 7</i> | | |
| | VSP travelt ime inversion for transversely isotropic media | 121 |
| 7.1 | Introduction | 122 |
| 7.2 | Theory | 123 |
| 7.2.1 | Review of elastic wave propagation in anisotropic media | 123 |
| 7.2.2 | Forward modelling schemes in anisotropic media | 126 |
| 7.2.3 | Isotropic travelt ime inversion of VSP data | 127 |
| 7.2.4 | Transversely isotropic travelt ime inversion of VSP data | 127 |
| 7.3 | The VSP geometry | 132 |
| 7.4 | The transversely isotropic structures | 134 |
| 7.5 | Results | 136 |

Contents

| | |
|--|-----|
| 7.5.1 Isotropic travelttime inversion | 136 |
| 7.5.2 Transversely isotropic travelttime inversion | 141 |
| 7.6 Conclusions | 149 |
| 7.7 Appendix | 150 |
| 7.8 References | 157 |
| <i>Chapter 8</i> | |
| Summary and Conclusions | 161 |
| <i>Samenvatting (Summary in Dutch)</i> | |
| <i>Acknowledgements</i> | 163 |
| <i>Curriculum Vitae</i> | 166 |
| | 167 |

Chapter 1

INTRODUCTION

Seismic waves travelling through the Earth have given much information about the Earth's interior. Dependent as they are on the volume density and the elastic constants of the medium they pass, seismic waves are one of the most important tools a geophysicist can use in determining the distribution of these physical parameters through the Earth. Using this tool seismologists have been able to visualize even the deepest parts of the Earth, while exploration geophysicists have been able to describe many complicated geological structures, such as hydrocarbon reservoirs, in the Earth's upper part.

In the interpretation of seismic data it is often assumed that the medium being studied is isotropic with respect to elastic wave propagation. Even if the medium is actually anisotropic, i.e. the velocities and displacements of the waves depend on the direction of wave propagation, the assumption of isotropy may often be used if only P-wave data (which are only slightly affected by anisotropy) are considered (Krey and Helbig, 1956). Because in most seismic studies carried out until recently only P-waves were used anisotropy could often be ignored.

In the last few years, however, a considerable increase in the use of shear waves, which are much more affected by anisotropy than P-waves, can be noted. Consequently, there is a growing amount of seismic data showing the effects of anisotropy (Crampin, 1987). If these data would still be interpreted using the assumption of isotropy one might end up with erroneous results. Only if the anisotropy is properly taken into account the correct interpretations are obtained. Moreover, information about the cause of anisotropy, which is often an internal structure of the rocks, such as aligned inclusions or fine layering, with dimensions much smaller than the seismic wavelengths used, might be obtained then. Considering the many anisotropy observations being reported in seismic data, nowadays, much effort should be paid to study all characteristics and applications of anisotropy. With this in mind the research as described in this thesis, which is aimed at a better understanding of the anisotropy caused by aligned inclusions, has been carried out.

In the last decade much attention (in particular by Crampin and co-authors) has been paid to the anisotropy shown by media containing distributions of stress-aligned (normal to

the minimum compressional stress) circular cracks (e.g. Crampin, 1978, 1981, 1984, 1985, 1987). Although there are other causes of seismic anisotropy, such as aligned crystals, sequences of thin layers, etc. (Crampin, Chesnokov and Hipkin, 1984) many anisotropy observations only seem explicable by assuming distributions of stress-aligned cracks. Because crack-induced anisotropy has been identified in many types of rocks (e.g. igneous, metamorphic, and sedimentary rocks) stress-aligned cracks are assumed to pervade most rocks in the Earth's crust. These fluid-filled cracks (which have dimensions ranging from a few tens of micrometres in igneous and metamorphic rocks to a few millimetres in sedimentary rocks) are strongly affected by stress changes: not only their direction might be changed, but their shape, number or the fluid inside the cracks might be changed as well (Crampin, 1987). Therefore, studying variations of crack-induced anisotropy in terms of changes of the crack configuration might become an important technique to monitor the stress field. Such a technique would have important applications in both seismology (earthquake prediction) and exploration geophysics (monitoring the internal structure of hydrocarbon reservoirs).

Such studies can of course only be carried out if the characteristics of the anisotropy shown by media containing aligned inclusions are understood. For this reason several crack models have been derived in the past. One of the most 'popular' models that has often been used to explain observed anisotropy is Hudson's (1980, 1981) crack model. This model is based on the scattering of elastic waves by the cracks. A major assumption in this and most other crack models is the small aspect ratio α of the inclusions. (If a rotationally symmetrical ellipsoidal inclusion, having two equal semi-axes with length a and one semi-axis with length b , is considered (Fig. 1.1) the aspect ratio α is defined as $\alpha = b/a$). However, with the growing amount of evidence that the aspect ratio of the inclusions in the Earth is not necessarily small (Crampin, McGonigle and Ando, 1986b) and that it probably is the most important crack parameter being affected by stress changes (Peacock, Crampin, Fletcher and Booth, 1988) a model that can describe the anisotropy due to inclusions with large aspect ratios is needed. One of the models that can deal with large aspect ratios is Nishizawa's (1982) model. Unlike Hudson's model (which is based on the scattering of elastic waves) Nishizawa's model is based on a static approach. (For unknown reasons many people working in the field of anisotropy have been unaware of Nishizawa's method, which is a refinement of a (better-known) method presented by Anderson, Minster and Cole (1974)). In this thesis the consequences of Nishizawa's model for wave propagation in cracked media are studied.

In chapter 2 of this thesis the characteristics of the anisotropy (i.e. transverse isotropy) as described by Nishizawa's (1982) model are shown. These results are shown for rotationally symmetrical ellipsoidal inclusions ranging from flat cracks ($\alpha \ll 1$) up to spherical inclusions ($\alpha = 1$). Moreover, the range of aspect ratios for which Nishizawa's (1982) model and Hudson's (1980,1981) model are similar is studied in this chapter. This range, which appears to include not only small aspect ratios, is indicative (assuming the validity of Nishizawa's method) of the range of cracks for which Hudson's model (despite its small-aspect-ratio assumption) can still be used. From this it can be concluded whether

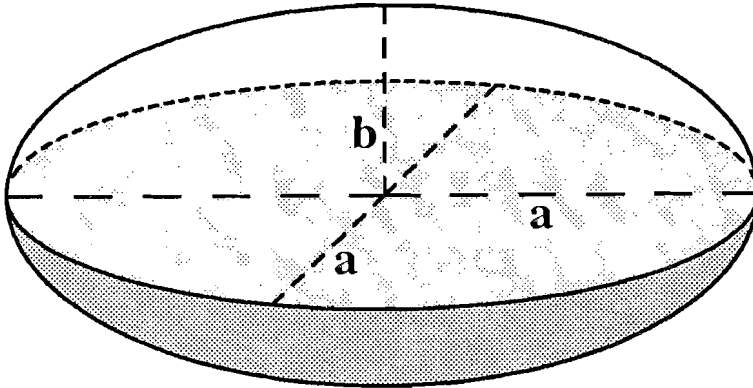


Fig. 1.1. Rotationally symmetrical ellipsoidal inclusion having two equal semi-axes with length a and one semi-axis with length b . The aspect ratio α of such an inclusion is defined as $\alpha = b/a$.

experiments (such as described by Crampin et al., 1986b) in which Hudson's model is used to model cracks with aspect ratios that violate Hudson's small-aspect-ratio-assumption should be revised or not.

In chapters 3 and 4 it is investigated whether the anisotropy effects shown by media containing aligned inclusions (as described by Nishizawa's and Hudson's model) can also be explained by media containing slip interfaces (simulating a fracture system composed of large, closely spaced, aligned joints) or by media containing sequences of thin isotropic layers. An eventual identity of the resultant anisotropy would imply that whenever such anisotropy is observed additional (e.g. geological) information is needed to obtain the actual cause of the anisotropy. Differences in the resultant anisotropy, however, would make it possible to derive methods to separate the cause of anisotropy. One of such methods, aimed at separating aligned cracks and sequences of thin isotropic layers as possible causes of anisotropy, is presented in chapter 4.

In anisotropic media there are three body waves with different velocities and with mutually orthogonal polarizations in every direction of phase propagation. In general none of these waves has a polarization parallel (longitudinal direction) or perpendicular (transverse direction) to the wave normal. For weak anisotropy, however, the polarization of the waves is close to these directions and, therefore, there are a quasi-longitudinal wave and two quasi-shear waves. Consequently, shear waves on entering an anisotropic medium generally split up into two quasi-shear waves: a fast and a slow one. This shear-wave splitting has often been used to interpret anisotropy observations. For cracked media the time delay between both quasi-shear waves and the polarization of the first-arriving quasi-shear wave have been used to derive estimates on the densities and directions of the aligned cracks, respectively (Crampin, Bush, Naville and Taylor, 1986a). Because the polarizations of shear waves recorded at the free surface may seriously be distorted by free-surface effects the preferred data acquisition method to study shear-wave splitting is three-

component Vertical Seismic Profiling (VSP). In VSP measurements where the receivers are located in the subsurface, shear waves do not suffer from disturbing free-surface effects.

The research described in chapter 5 shows that one should be cautious in interpreting shear-wave splitting, shown by VSP measurements, only in terms of anisotropy. It is described how even an isotropic medium containing steeply dipping interfaces may show shear-wave splitting in such measurements.

In the last two chapters of this thesis the effect of anisotropy on synthetic multi-offset VSP is studied. In chapter 6 it is investigated how multi-offset shear-wave VSPs carried out in media containing aligned inclusions change for a changing aspect ratio of the inclusions. Such research may have important applications because, as stated earlier, the aspect ratio is probably the crack parameter most likely to be modified by stress changes. If temporal anisotropy changes (such as reported by Peacock et al. (1988)) observed in repeated shear-wave VSPs can be interpreted in terms of a changing aspect ratio, temporal stress changes could be monitored. In chapter 6 synthetic VSP datasets are constructed and methods to recognize aspect ratio changes in these data are described.

At the end of this thesis (chapter 7) travelttime inversion methods are applied to synthetic multi-offset VSP travelttime data that were calculated (using anisotropic ray tracing) for a simple two-layered transversely isotropic model. First an inversion scheme based on isotropy is applied to these 'anisotropic' travelttimes. It is investigated how such an inversion scheme (with its wrong assumption) distorts the interface (separating the layers in our model) which it is inverting for. The results of this study describe the type of errors that may be expected when standard inversion schemes (based on the assumption of isotropy) are applied to VSP data obtained in anisotropic media without taking anisotropy into account. In the second part of chapter 7, however, inversion schemes are developed that do take anisotropy into account. They are aimed at determining both the elastic constants and the structures of transversely isotropic media.

REFERENCES

- Anderson, D.L., Minster, B. and Cole, D. 1974. The effect of oriented cracks on seismic velocities. *Journal of Geophysical Research* 79, 4011-4015.
- Crampin, S. 1978. Seismic wave propagation through a cracked solid: polarization as a possible dilatancy diagnostic. *Geophysical Journal of the Royal Astronomical Society* 53, 467-496.
- Crampin, S. 1981. A review of wave motion in anisotropic and cracked elastic-media. *Wave Motion* 3, 343-391.
- Crampin, S. 1984. Effective anisotropic elastic constants for wave propagation through cracked solids. *Geophysical Journal of the Royal Astronomical Society* 76, 135-145.
- Crampin, S. 1985. Evidence for aligned cracks in the Earth's crust. *First Break* 3, (3), 12-15.
- Crampin, S. 1987. Geological and industrial implications of extensive dilatancy anisotropy. *Nature* 328, 491-496.
- Crampin, S., Chesnokov, E.M. and Hipkin, R.G. 1984. Seismic anisotropy: the state of the art. *Geophysical Journal of the Royal Astronomical Society* 76, 1-16.

- Crampin, S., Bush, I., Naville, C. and Taylor, D.B. 1986a. Estimating the internal structure of reservoirs with shear-wave VSPs. *The Leading Edge* 5, No. 11, 35-39.
- Crampin, S., McGonigle, R. and Ando, M. 1986b. Extensive-dilatancy anisotropy beneath Mount Hood, Oregon and the effect of aspect ratio on seismic velocities through aligned cracks. *Journal of Geophysical Research* 91, 12703-12710.
- Hudson, J.A. 1980. Overall properties of a cracked solid. *Mathematical Proceedings of the Cambridge Philosophical Society* 88, 371-384.
- Hudson, J.A. 1981. Wave speeds and attenuation of elastic waves in material containing cracks. *Geophysical Journal of the Royal Astronomical Society* 64, 133-150.
- Krey, Th. and Helbig, K. 1956. A theorem concerning anisotropy of stratified media and its significance for reflection seismics. *Geophysical Prospecting* 4, 294-301.
- Nishizawa, O. 1982. Seismic velocity anisotropy in a medium containing oriented cracks-transversely isotropic case. *Journal of Physics of the Earth* 30, 331-347.
- Peacock, S., Crampin, S., Fletcher, J.B. and Booth, D.C. 1988. Shear-wave splitting in the Anza seismic gap, Southern California: temporal variations as possible precursors. *Journal of Geophysical Research* 93, 3339-3356.

Chapter 2

THE EFFECT OF THE ASPECT RATIO ON CRACK-INDUCED ANISOTROPY

ABSTRACT

Media containing aligned cracks show anisotropy with respect to elastic wave propagation. There are several models describing the wave propagation in cracked media, most of them only valid for cracks with small aspect ratios. One of these models (Hudson's model) is compared with a model valid for all aspect ratios (Nishizawa's model). The elastic constants and the group velocities are compared for both dry and liquid-filled inclusions with aspect ratios ranging from 0.0001 (flat cracks) up to 1 (spheres). The difference between both models is small for small aspect ratios but becomes larger for increasing aspect ratios. At a crack density of 0.05 both models give-within an error of 5%-the same results for aspect ratios up to 0.3. Therefore Hudson's model can be applied to a large range of cracked media even if the aspect ratio of the inclusions is not very small. The variation of the anisotropy as a function of the aspect ratio can be studied using Thomsen's dimensionless parameters δ , ϵ , and γ . They show how inclusions with large aspect ratios result in elliptical anisotropy.

This chapter has been published as:

Douma, J. 1988. The effect of the aspect ratio on crack-induced anisotropy. *Geophysical Prospecting* 36, 614-632.

2.1 INTRODUCTION

Anisotropy with respect to elastic wave propagation is becoming important in geophysical research nowadays. Seismic anisotropy was already studied more than 30 years ago (Postma, 1955; Helbig, 1956, 1958), but for a long time its effect was considered to be negligible. Helbig (1984) pointed out this was because most of the seismic data recorded were P-wave reflection data obtained for P-waves travelling at small angles against the vertical axis of the medium. In a transversely isotropic medium with a vertical axis of symmetry (e.g. caused by thin horizontal layering), such P-waves (and thus most of the reflection seismic surveys) would only be slightly affected (Krey and Helbig, 1956). This is the main reason why most seismic surveys could be carried out without taking the effect of anisotropy into account. However, for special acquisition geometries (like Vertical Seismic Profiling (V.S.P.)) where large angles of incidence may occur the effect of anisotropy still had to be taken into account (Uhrig and Van Melle, 1955).

During the last few years it has been realized that anisotropy can play an important role in seismic exploration. This is primarily due to the increasing use of shear waves, which are much more sensitive to anisotropy than P-waves (Crampin, Chesnokov and Hipkin, 1984). Without taking anisotropy into account it is often difficult to interpret shear-wave data (Alford, 1986). Secondly, it is due to the quantity of information that can be derived from shear waves showing anisotropy effects (Crampin (1985) claims that there is at least three times as much information in shear waves than in P-waves). Crampin shows in many papers how shear-wave splitting can be used to find the orientation and crack density of aligned circular cracks. Because these cracks may exist in hydrocarbon reservoirs this information may be of great importance in evaluating these reservoirs (Crampin, 1987). Cracks are also assumed to play an important role in earthquake prediction (Crampin, Evans and Atkinson, 1984). It is believed that the geometry of cracks will change due to variations in the stress field just before an earthquake takes place. Consequently, the resulting anisotropy may also change. If temporal changes in this anisotropy could be observed, it might be possible to monitor the build up of stress preceding an earthquake.

Recently anisotropy effects have been observed in seismic data and have been attributed to aligned cracks, although many other possible causes of anisotropy (e.g. thin layering, aligned crystals, aligned grains, etc.) may exist (Crampin, 1987). This could only be justified after theoretical models describing the wave propagation in cracked media had been developed and the results compared with experimental data. It turned out that many of the anisotropy effects observed in the Earth's crust could be modelled by cracked media. In the comparison between modelled and real data, hodograms and velocity variation diagrams were used. From the best fit the parameters describing the cracks (e.g. crack density, aspect ratio, and the orientation of the cracks) were estimated (Crampin, McGonigle and Bamford, 1980; Crampin, McGonigle and Ando, 1986)

However, a number of problems has to be solved before an inversion for these parameters will have a high level of confidence. Some of these problems were pointed out

at the workshop on anisotropy held at the 49th E.A.E.G. Meeting in Belgrade, 1987. (The papers presented at this workshop will be published in a special issue of *Geophysical Transactions*, Eötvös Loránd Geophysical Institute of Hungary.) There are, for example, serious practical problems with respect to the construction of reliable hodograms from three-component V.S.P. measurements and problems as to whether the two shear waves travel along the same raypath (as assumed in many anisotropy analyses). Moreover, it is even possible to have polarization effects in isotropic media that might be misinterpreted as anisotropy effects (Douma and Helbig, 1987).

Apart from these problems which may complicate the estimation of the crack parameters from experimental data, the theory used to describe the wave propagation in cracked media is also critical. Different theories may result in different crack parameters describing the same data. Therefore, it is important to know the limitations of each theory. We here investigate a theory valid for all aspect ratios of the cracks and compare it with one often used to describe the wave propagation in cracked media, but only valid for small aspect ratios.

2.2 FLAT CRACK MODELS

Several theories have been developed to calculate the effective elastic constants of media containing aligned circular cracks. All assume that the dimensions of the cracks are small with respect to the seismic wavelengths used. The theories that have often been used in geophysics are due to Garbin and Knopoff (1973, 1975a, b), and Hudson (1980, 1981). They are all based on the scattering of waves at the cracks. These theories have been used (Crampin, 1978, 1984; Crampin et al., 1980, 1986) to analyse wave propagation in cracked media and to explain observed anisotropy. The basic assumptions of these theories are that the cracks are in dilute concentration and have small aspect ratios.

A theory that is valid for large concentrations of cracks has been proposed recently by Thomsen (1988) and is based on the work of Hoenig (1979), who calculated the elastic constants of a cracked medium using a self-consistent approach. In such an approach the interactions between the cracks are taken into account by estimating the behaviour of a single crack in the composite medium as that of a single crack in the equivalent homogeneous medium. Although Hoenig's model is not restricted by the assumption of a dilute concentration of the cracks, it does assume a small aspect ratio of the cracks, just like the other models mentioned. Therefore we call them 'flat crack models' (Thomsen (1988) has compared some of these models). In a review on rock physics Yale (1985) considers the assumption of small aspect ratios a serious drawback of these models which should not exist anymore in future models. Apparently, Yale (1985) was unaware of theories that do model large aspect ratios correctly.

2.3 ELLIPSOIDAL INCLUSION MODELS

Anderson, Minster and Cole (1974) and Nishizawa (1982) presented models that calculate the effective elastic constants of media containing aligned ellipsoidal inclusions. (Note that there are some misprints in Nishizawa's (1982) paper: to use the equations for \bar{G}_{ijkl} in the appendix of that paper Nishizawa's Eq. (9) should be divided by 8π , the term 4π in (10) should be omitted and note that $\bar{G}_{ijkl} = \bar{G}_{jikl} = \bar{G}_{ijlk}$.) A small size of the inclusions with respect to the wavelengths used is assumed. The ellipsoids have two equal semi-axes with length a , whereas the third axis (the axis of rotational symmetry) may have any length b . The ratio b/a is called the aspect ratio. Circular cracks are one limiting case of these ellipsoids for very small aspect ratios ($b/a \rightarrow 0$). Unlike the flat crack models, Anderson's and Nishizawa's models are valid for all values of the aspect ratio.

Because both models seem to be rather unknown we will shortly review them here. They are based on the results obtained by Eshelby (1957). Eshelby suggested a static approach to calculate the effective elastic constants of a medium containing aligned ellipsoidal inclusions. His approach is based on two hypothetical processes:

1. introducing the inclusions keeping the surface tractions constant, and
2. introducing the inclusions keeping the surface displacements constant.

From the change in elastic energy of the medium due to these processes the elastic constants can be found. To avoid interactions between the inclusions their concentration has to be dilute.

Anderson's model is based on Eshelby's second process of keeping the surface displacements constant. Nishizawa (1982) pointed out that Anderson would have obtained different results by using the first process. To avoid this discrepancy Nishizawa developed a numerical algorithm which can calculate the effective elastic constants even for large concentrations of ellipsoids. Considering a volume concentration of ellipsoids embedded in a homogeneous background material the effective elastic constants of the background material containing only a small portion of ellipsoids (in order to use Eshelby's equations which are only valid for dilute concentrations of ellipsoids) are calculated. Then a small portion of the remaining concentration of ellipsoids is added to the resultant anisotropic medium calculated in the first step and the effective constants are calculated again. This process is repeated until the effect of the total concentration of inclusions has been calculated.

We compare Nishizawa's method with Hudson's flat crack model (Hudson, 1980, 1981). Hudson's model, based on the scattering of elastic waves by the cracks, has been derived for first- (no mutual interactions between the cracks) and second-order (crack-crack interactions are accounted for) terms in the crack density. Throughout this paper first- and second-order terms have been included when Hudson's model is used. The purpose of a comparison between Nishizawa's and Hudson's model is to obtain the aspect ratios for

which both models result in the same anisotropy. This will indicate the range of aspect ratios for which Hudson's flat crack model is valid. The need to know this range becomes clear when velocity variations in cracked media are studied for different aspect ratios using Hudson's model, although it is realized that the results may be suspect for large aspect ratios (Crampin et al., 1986). When it is known for what range of aspect ratios Hudson's model is valid, it can be judged whether the results of these studies should be corrected or not.

Further, Nishizawa's model is carefully studied to gain a better understanding of the role the aspect ratio of the cracks plays in the resultant anisotropy of cracked media. Although Crampin (1987, Table 1) shows that there are many parameters influencing the anisotropy, the aspect ratio is probably one of the most important parameters (Crampin, 1987).

2.4 WAVE PROPAGATION IN CRACKED MEDIA

A medium containing aligned circular cracks or aligned ellipsoidal inclusions can be replaced by a homogeneous transversely isotropic medium. Transverse isotropy is a special case of anisotropy and is described by five independent elastic constants, whereas anisotropy in general is described by up to 21 independent constants. Media having an axis of rotational symmetry which may be oriented in any direction show transverse isotropy. If this axis is not vertical this type of anisotropy is sometimes called 'azimuthal anisotropy' (Crampin, 1986).

Once the effective elastic constants of such a medium are known (e.g. when they have been calculated with one of the theoretical models described earlier) the characteristics of wave propagation through this medium can be modelled. Many such studies have been carried out (Helbig, 1958; Keith and Crampin, 1977a, b, c, and Crampin, 1981). We will summarize their main features.

In anisotropic media there are three body waves in every direction of phase propagation with mutually orthogonal displacements. In general, none of the waves has a polarization parallel (longitudinal direction) or perpendicular (transverse direction) to the wave normal. For weak anisotropy, however, the polarization of the waves is close to these directions and, therefore, there are a quasi-longitudinal wave (qP-wave) and two quasi-transverse waves (qS₁- and qS₂-wave). In any symmetry plane of the medium the polarization of the qP-wave and one of the quasi-transverse waves (called qSP) are parallel to this plane whereas the other quasi-transverse wave (called qSR) is polarized perpendicular to the plane. qP-, qSP-, and qSR-waves are studied in this paper.

All three waves have different velocities which depend on the angle between the wave normal and the symmetry axis of the medium. Two velocities can be used to describe wave propagation in anisotropic media: the phase velocity normal to the wavefront and the group velocity - the velocity of energy propagation. The exact formulae relating these quantities

to the elastic constants can be found in the references mentioned above.

The exact formulae for transverse isotropy contain five independent elastic parameters. This number can be reduced to four by using dimensionless parameters. In recent studies (Thomsen, 1986) approximate formulae were derived for weak transverse isotropy containing only three dimensionless parameters. These formulae give the linearized phase velocities $v(\theta)$:

$$v_{qP}(\theta) \approx v_P \left[1 + \delta \sin^2\theta \cos^2\theta + \varepsilon \sin^4\theta \right] \quad (1a)$$

$$v_{qSP}(\theta) \approx v_S \left[1 + \frac{v_P^2}{v_S^2} (\varepsilon - \delta) \sin^2\theta \cos^2\theta \right] \quad (1b)$$

$$v_{qSR}(\theta) \approx v_S \left[1 + \gamma \sin^2\theta \right] \quad (1c)$$

where $v_P = (c_{33}/\rho_e)^{1/2}$ and $v_S = (c_{44}/\rho_e)^{1/2}$ are the velocities along the symmetry axis (assumed to be directed along the x_3 -axis), ρ_e is the density of the effective medium, θ the angle between the wave normal and the symmetry axis, and c_{33} and c_{44} are elements of the elastic tensor denoted compactly according to the Voigt nomenclature (see e.g. Thomsen (1986)).

The anisotropy parameters δ , ε , and γ are combinations of elastic constants:

$$\delta = \frac{(c_{13} + c_{44})^2 - (c_{33} - c_{44})^2}{2c_{33}(c_{33} - c_{44})} \quad (2a)$$

$$\varepsilon = \frac{c_{11} - c_{33}}{2c_{33}} \quad (2b)$$

$$\gamma = \frac{c_{66} - c_{44}}{2c_{44}} \quad (2c)$$

As stated by Thomsen (1986) there is no reason to use these linearized expressions for computational purposes but they are useful because their simplicity in form aids in the understanding of the effect of anisotropy. The parameters are all zero for isotropic media and their deviation from zero can be regarded as a degree of anisotropy. The parameters δ ,

ϵ , and γ are easy to derive and interpret.

Equations (1a)-(1c) show that the parameter ϵ represents the relative difference between the qP-phase velocities perpendicular and parallel to the axis of symmetry:

$$\epsilon \approx \frac{v_{qP}(\pi/2) - v_P}{v_P} \quad (3a)$$

γ represents this difference for the qSR-waves:

$$\gamma \approx \frac{v_{qSR}(\pi/2) - v_S}{v_S} \quad (3b)$$

Finally, the parameter δ is:

$$\delta \approx 4 \left[\frac{v_{qP}(\pi/4)}{v_{qP}(0)} - 1 \right] - \left[\frac{v_{qP}(\pi/2)}{v_{qP}(0)} - 1 \right] \quad (3c)$$

and can thus be obtained from measurements at $\theta = 0^\circ$, 45° , and 90° . Because the parameters δ , ϵ , and γ can easily be estimated from real data the modelling of observed weak anisotropy is simpler with (1a)-(1c) than with most of the other (exact) formulae for phase velocities which need estimates of the elastic constants.

As shown by Thomsen (1986) δ , ϵ , and γ are < 0.2 for weak-to-moderate anisotropy. Furthermore, as shown by (1a), δ dominates most anisotropy effects at small angles θ for qP-waves (unless $\epsilon \gg \delta$), whereas ϵ does this at θ close to $\pi/2$.

Finally, Thomsen states that elliptical anisotropy will be observed if δ equals ϵ . Rudzki (1911) showed that such a type of anisotropy implies ellipsoidal qP-wavefronts while the qSP-wavefronts become spherical. Berryman (1979) and Helbig (1979) showed that elliptical anisotropy can never be caused by thin-layered isotropic media. The significance of elliptical anisotropy in exploration geophysics has been discussed by Helbig (1983).

Because the parameters δ , ϵ , and γ are easily interpretable and give a comprehensive view on anisotropy we used them to model and study the variation of the anisotropy as a function of the aspect ratio.

2.5 NUMERICAL RESULTS AND DISCUSSION

In this section we compare Nishizawa's ellipsoid model with Hudson's flat crack model. Nishizawa's model is also studied in terms of the parameters δ , ε , and γ .

The comparison is carried out for dry and liquid-filled inclusions. Both types of inclusions are investigated because they have often been used to model experimental data (e.g. Crampin et al., 1986). The dry inclusions have Lamé constants $\lambda_1 = \mu_1 = 0$, whereas the liquid-filled inclusions have Lamé constants $\lambda_1 = 15$ kbar and $\mu_1 = 0$. The isotropic background material is the same as used by Crampin (1984), i.e. its density $\rho_b = 2.6$ g cm⁻³ and its Lamé constants are $\lambda_2 = 291.4$ kbar and $\mu_2 = 291.6$ kbar (corresponding to a P-wave velocity of 5.8 km s⁻¹ and a S-wave velocity of 3.349 km s⁻¹). Different crack densities e are studied. Two possible expressions for the crack density e are:

$$e = \frac{Na^3}{V} \quad (4)$$

or

$$e = \frac{3\phi}{4\pi\alpha} \quad (5)$$

where N is the number of cracks of radius a in a volume V , ϕ the total volume of the inclusions, and α their aspect ratio.

2.5.1 Comparison of elastic constants

First the resultant elastic constants calculated with Nishizawa's and Hudson's model are compared (a similar comparison between Nishizawa's model and a joint model was carried out by Schoenberg and Douma (1988)). We define their normalized 'Euclidean distance' D as the root mean square of the normalized differences between the five independent elastic constants calculated with Nishizawa's model ($c_{11}^N, c_{13}^N, c_{33}^N, c_{44}^N, c_{66}^N$) and Hudson's model ($c_{11}^C, c_{13}^C, c_{33}^C, c_{44}^C, c_{66}^C$). The normalization is carried out with the elastic constants of the background material ($c_{11}^b, c_{13}^b, c_{33}^b, c_{44}^b, c_{66}^b$):

$$D = \left[\frac{\left[\left(\frac{c_{11}^N - c_{11}^C}{c_{11}^b} \right)^2 + \left(\frac{c_{13}^N - c_{13}^C}{c_{13}^b} \right)^2 + \left(\frac{c_{33}^N - c_{33}^C}{c_{33}^b} \right)^2 + \left(\frac{c_{44}^N - c_{44}^C}{c_{44}^b} \right)^2 + \left(\frac{c_{66}^N - c_{66}^C}{c_{66}^b} \right)^2 \right]}{5} \right]^{\frac{1}{2}} \quad (6)$$

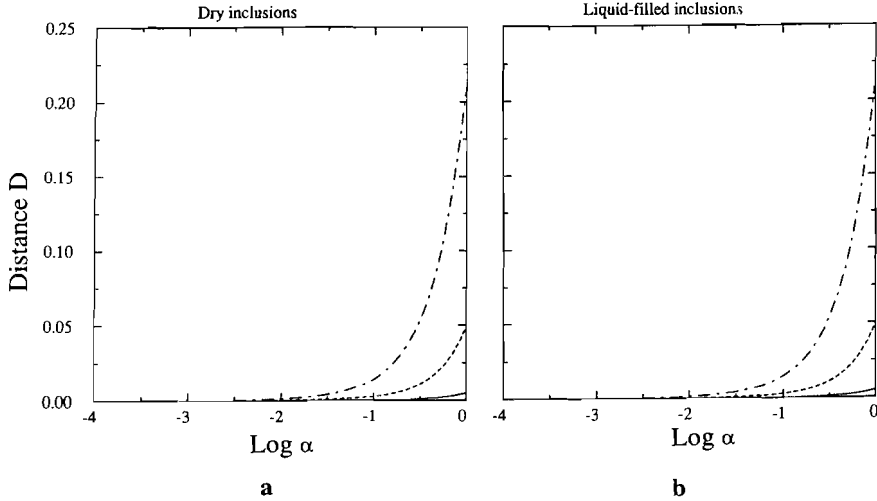


Fig. 2.1. Normalized distance D between Nishizawa's and Hudson's model as a function of the aspect ratio α of a) dry inclusions and b) liquid-filled inclusions embedded in an isotropic background medium. The results are shown for three crack densities $e = 0.001$ (—), $e = 0.01$ (---), and $e = 0.05$ (-.-).

In Fig. 2.1 the distance D is calculated for three crack densities $e = 0.001, 0.01,$ and 0.05 for aspect ratios ranging from $\alpha = 0.0001$ (almost flat cracks) up to $\alpha = 1$ (spheres). In Fig. 2.1a the result is shown for dry inclusions and in Fig. 2.1b for liquid-filled inclusions. Both figures show that the distance D is small for small aspect ratios but increases for increasing aspect ratio. Moreover, D increases for increasing crack density. If we consider $D = 0.05$ to be the upper limit for which Hudson's and Nishizawa's model give similar results, both Figs 2.1a and 2.1b show that this limit is reached at aspect ratios around $\alpha = 0.3$ for a crack density $e = 0.05$. It is clear from both figures that the distance is not sensitive to the type of inclusion. Thus, for a large range of aspect ratios both models give the same results. We will call this range of aspect ratios the 'crack range'. This crack range is large for small crack densities, but becomes smaller for increasing crack densities.

2.5.2 Comparison of the group velocities

Although the comparison of elastic constants shown in Figs 2.1a and 2.1b gives insight in the differences between Hudson's and Nishizawa's model, it is also instructive to compare the velocities resulting from both models. Modelled velocities (either phase- or group velocities) are often used to explain observed velocity variations in real data, and therefore, it is important to know how large the difference between the velocities calculated with both models is and at what angles this occurs. The velocity studied here is the group velocity, because this is the velocity of energy transport which is generally calculated from

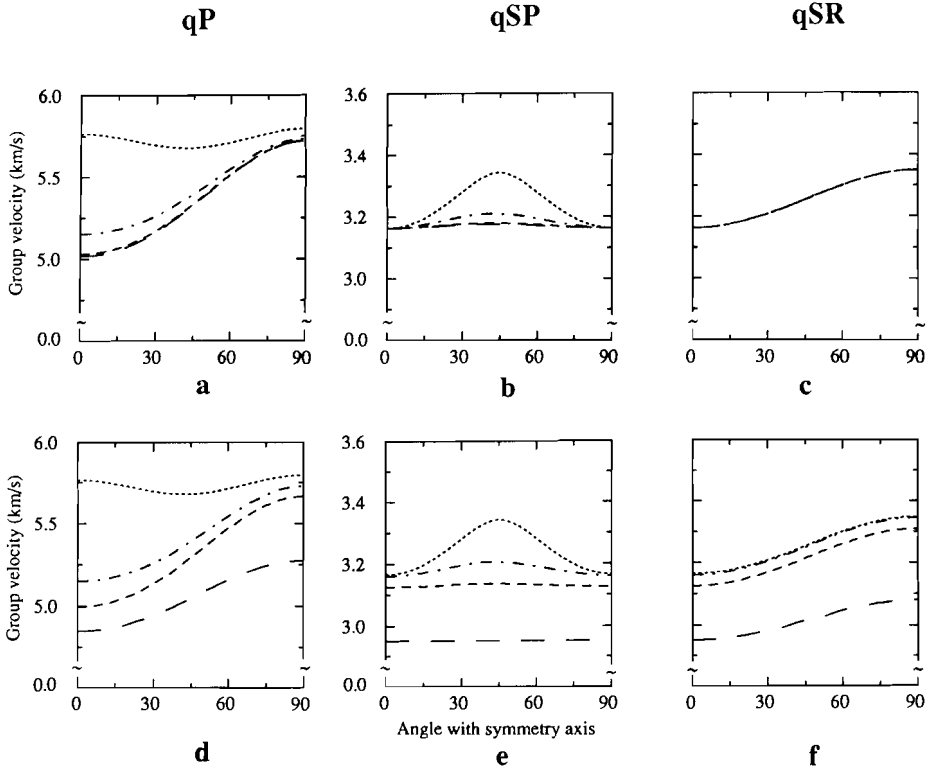


Fig. 2.2. The group velocity of the qP- (a, d), qSP- (b, e), and qSR-waves (c, f) travelling through an isotropic medium containing liquid-filled inclusions as a function of the angle (in degrees) between the ray direction and the symmetry axis of the effective medium. The upper figures (a, b, and c) are calculated with Hudson's model and lower ones (d, e, and f) with Nishizawa's model. Four aspect ratios of the inclusions are considered: $\alpha = 0.0001$ (\cdots), $\alpha = 0.01$ ($\cdots\cdots$), $\alpha = 0.1$ ($-\cdots-$), and $\alpha = 0.5$ ($-$). The crack density of the inclusions is $e = 0.05$

the arrival times of body waves.

To calculate the velocity not only the elastic constants of the effective medium need to be known but its density ρ_e as well. If the total porosity ϕ of the inclusions is small this density can very well be approximated by the density ρ_b of the background material (i.e. $\rho_e = \rho_b = 2.6 \text{ g cm}^{-3}$). However, for large porosities the density of the effective medium changes if the density of the inclusions is different from that of the background. Changes in the effective density should be taken into account in the calculation of the velocities. However, to study only the influence of the aspect ratio on the velocity we will first assume a constant effective density ($\rho_e = 2.6 \text{ g cm}^{-3}$).

Consider the liquid-filled inclusions embedded in the isotropic background medium. Let the crack density be $e = 0.05$. In the Figs 2.2a-c the resultant group velocities of the qP-, qSP-, and qSR-waves calculated with Hudson's model are shown, respectively, as a function of the angle against the symmetry axis. Figures 2.2d-f show the same for

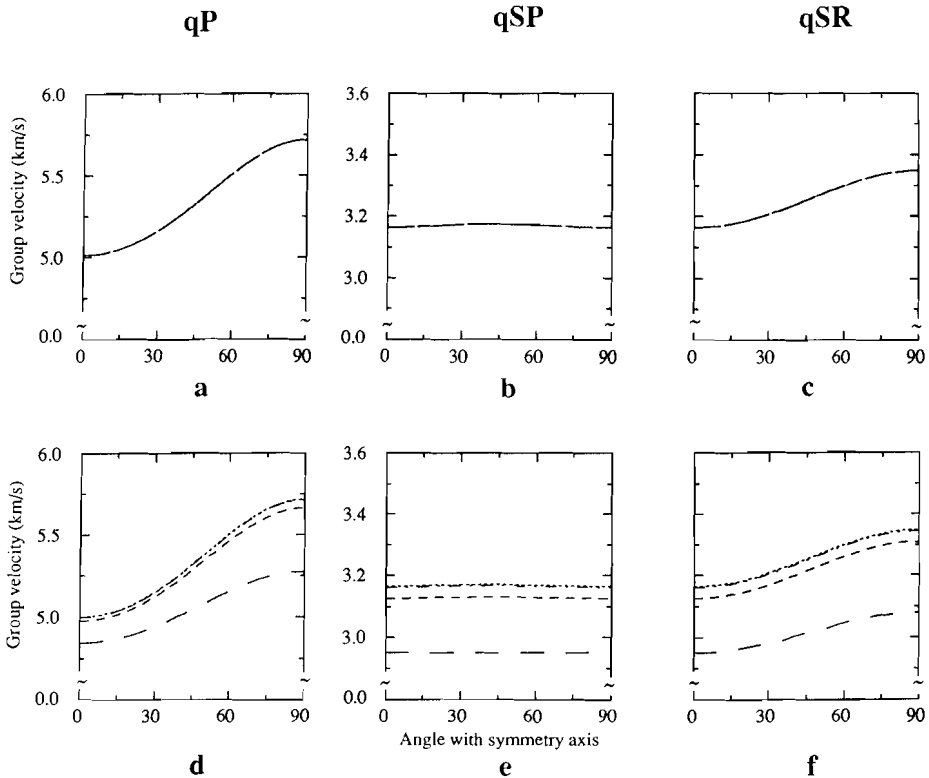


Fig. 2.3. As for Fig. 2.2, but for dry inclusions.

Nishizawa's model. In each figure the group velocity is calculated for four aspect ratios i.e. $\alpha = 0.0001, 0.01, 0.1,$ and 0.5 . Comparing the upper and lower figures it can be seen that both models give almost the same results for the small aspect ratios $\alpha = 0.0001$ and $\alpha = 0.01$. However, for the two larger aspect ratios $\alpha = 0.1$ and $\alpha = 0.5$, there is an increasing difference between the results of both models. In spite of this difference the variation of the group velocities as a function of the ray direction does not change much for increasing aspect ratios. This seems to confirm Crampin's assumption that the overall pattern of the velocity variations for large aspect ratios would be similar to that for small aspect ratios, although the exact values may be different (Crampin et al., 1986).

Figures 2.2d-f also show that an increasing aspect ratio tends to reduce the group velocity. Nishizawa's model shows that this is even true for the qSR-waves which do not show a dependence on the aspect ratio for Hudson's model.

The same calculations have been carried out for dry inclusions. The results are shown in Fig. 2.3, which confirms the conclusions drawn from Fig. 2.2: both models give almost the same results for small aspect ratios, whereas a difference between the results arises for large aspect ratios. Note, however, that for Hudson's model none of the waves (qP, qSP, and qSR) shows a dependence of the group velocity on the aspect ratio, whereas for

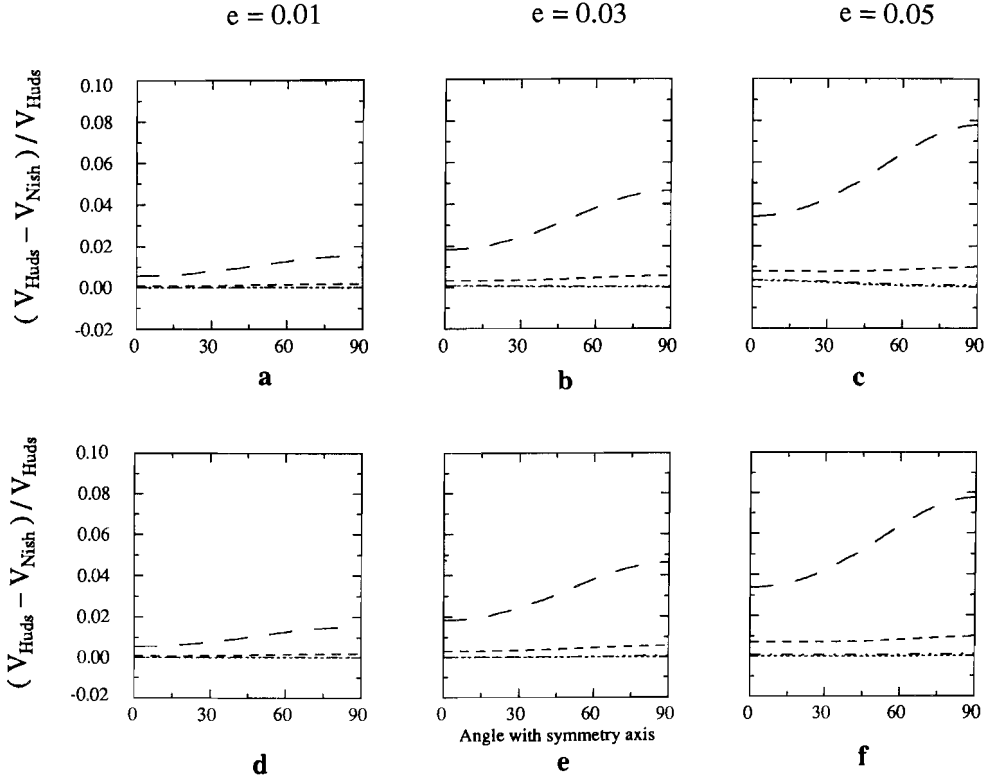


Fig. 2.4. Normalized difference between the qP-group velocities calculated with Hudson's and Nishizawa's model as a function of the ray direction. Three crack densities are studied: $e = 0.01$ (a and d), $e = 0.03$ (b and e), and $e = 0.05$ (c and f). Figures a, b, and c show the results for dry inclusions and figures d, e, and f for liquid-filled inclusions.

Nishizawa's model such a dependence exists for each of them.

The velocities of the media studied here are typical for basement forming material. Calculations carried out for sedimentary rocks (but not shown here) give the same similarities and differences between both models as observed in this section.

2.5.3 Normalized difference between group velocities

To study the exact values of the differences in group velocity between both models we calculated, for each wave (qP, qSP, and qSR), the normalized difference $D_{\text{NH}}(\theta)$ defined as:

$$D_{\text{NH}}(\theta) = \frac{v_{\text{Huds}}(\theta) - v_{\text{Nish}}(\theta)}{v_{\text{Huds}}(\theta)} \quad (7)$$

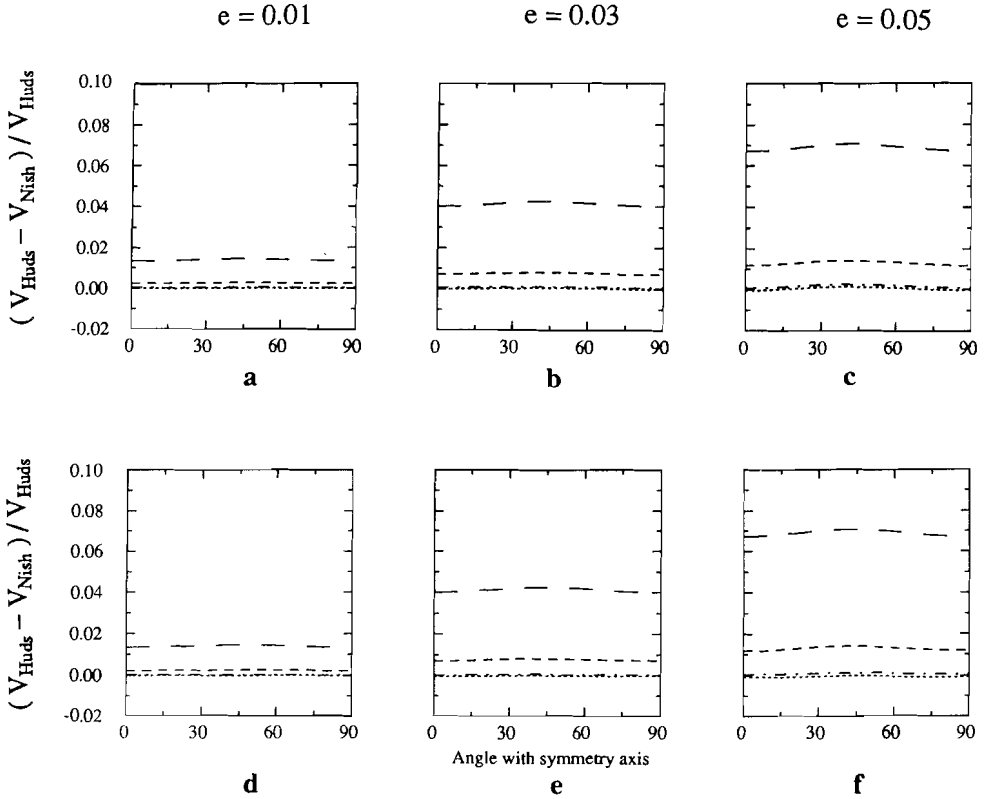


Fig. 2.5. As for Fig. 2.4, but for the qSP-group velocity.

where $v_{\text{Huds}}(\theta)$ and $v_{\text{Nish}}(\theta)$ denote the group velocities calculated with Hudson's and Nishizawa's model, respectively. This was done for three different crack densities $e = 0.01$, 0.03 , and 0.05 for both dry and liquid-filled inclusions. In Fig. 2.4 the results are shown for the qP-wave. The upper Figs 2.4a-c are calculated for the dry inclusions and the lower Figs 2.4d-f for the liquid-filled inclusions. Figures 2.4a-f show that there is hardly any difference between the results when either dry or liquid-filled inclusions are studied. They also show more quantitatively than Figs 2.2 and 2.3 that the difference between Hudson's and Nishizawa's model is almost zero for small aspect ratios but increases for larger aspect ratios. The differences also increase for increasing crack density and angle of incidence. In general, most of the differences are smaller than 0.05 indicating that for most of the crack parameters studied there is a good correspondence between the two models. Only for large aspect ratios α and large crack densities e (e.g. $\alpha = 0.5$ and $e = 0.05$) this correspondence starts to fail.

The same calculations have been carried out for qSP-(Fig. 2.5) and qSR-waves (Fig. 2.6). They all show the same characteristics as for the qP-waves (Fig. 2.4), except that qSP-waves always have a maximum difference at $\theta = 45^\circ$, whereas qP- and qSR-waves have such a maximum at $\theta = 90^\circ$.

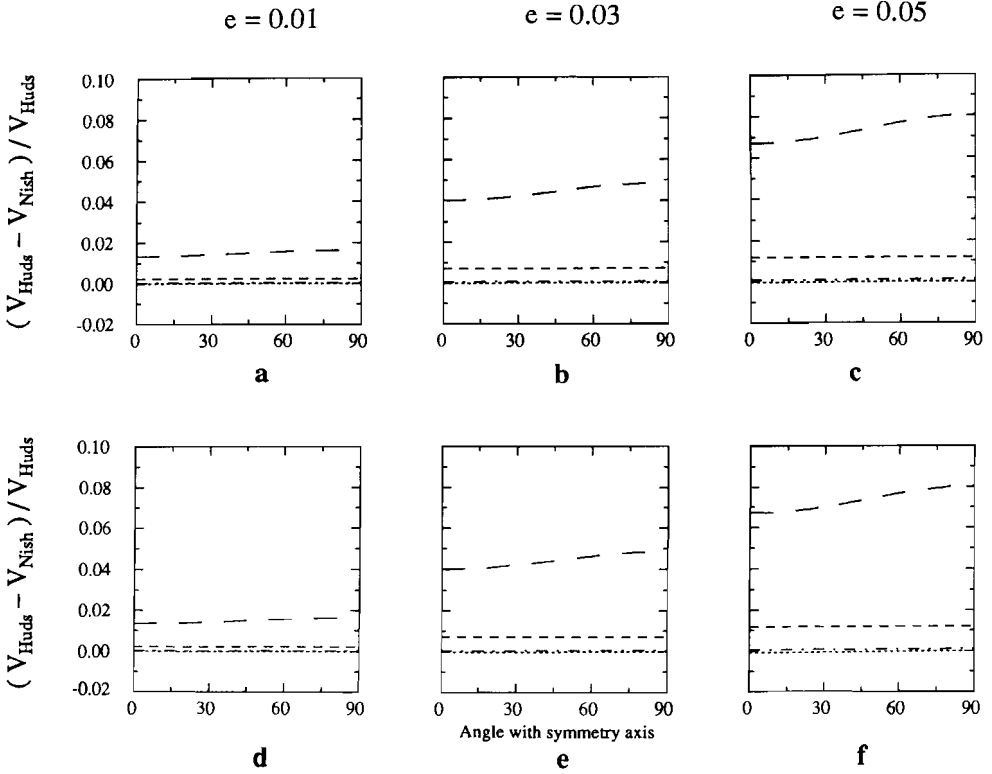


Fig. 2.6. As for Fig. 2.4, but for the qSR-group velocity.

2.5.4 The influence of the effective density on the group velocity

The results of Figs 2.4-2.6 are not influenced by a change in the density ρ_e of the effective medium, because the ratio $D_{NH}(\theta)$ does not depend on the density ρ_e . However, Figs 2.2 and 2.3 would be influenced by such a change. In these figures the density was assumed constant to isolate the effect of the aspect ratio on the group velocity. Therefore, the magnitudes of the velocities shown may be in error. The correct value of the effective density is

$$\rho_e = (1 - \phi) \rho_b + \phi \rho_i \quad (8)$$

where ρ_e , ρ_b , and ρ_i are the densities of the effective medium, background material, and the inclusion material, respectively, and ϕ is the volume concentration of the inclusions.

To study the effect of the density on the group velocities we calculated these velocities for our background medium containing liquid-filled and dry inclusions. The results are presented in Figs 2.7 and 2.8, respectively. Figures 2.7a-c and 2.8a-c show the group

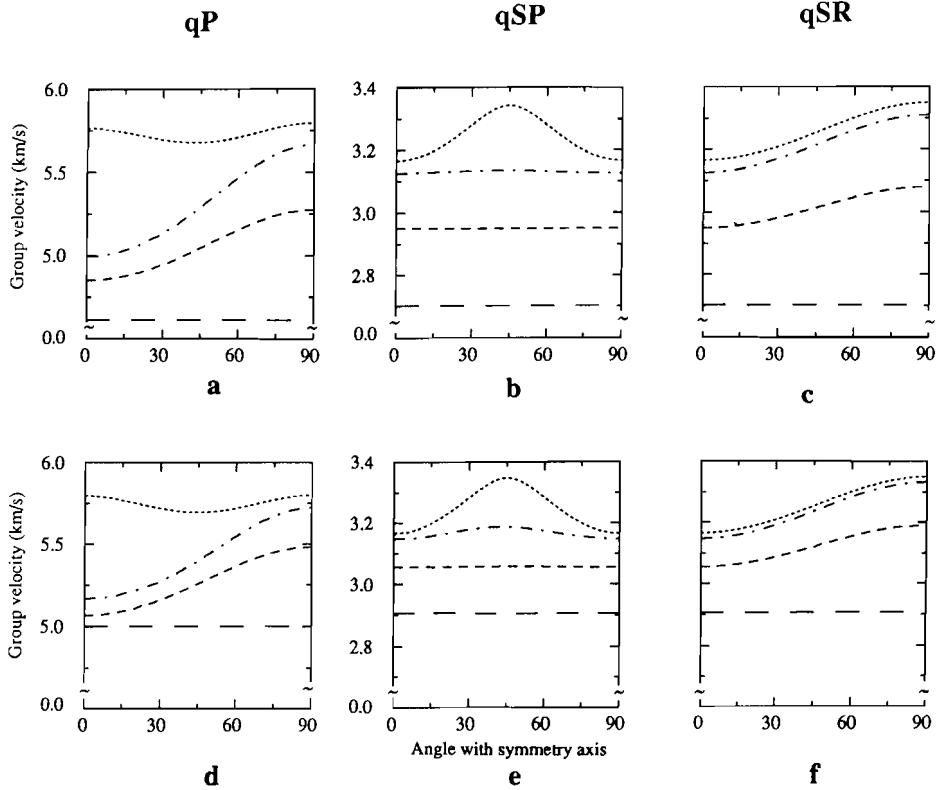


Fig. 2.7. The group velocities of the qP- (a and d), qSP- (b and e), and qSR-waves (c and f) travelling through an isotropic medium containing liquid-filled inclusions as a function of the ray direction. The results are calculated with Nishizawa's model using a constant density of the effective medium (a, b, and c) and using the correct density (d, e, and f). Four aspect ratios are considered: $\alpha = 0.0001$ ($\cdots\cdots$), $\alpha = 0.1$ ($-\cdot-\cdot-$), $\alpha = 0.5$ ($----$), and $\alpha = 1$ ($----$). The crack density of the inclusions is $e = 0.05$.

velocities assuming a constant density ρ_e , whereas Figs 2.7d-f and 2.8d-f show the results for the correct density ρ_e (calculated with equation (8)). The densities ρ_i of the liquid-filled and dry inclusions were $\rho_i = 0.93 \text{ g cm}^{-3}$, and $\rho_i = 0$, respectively. In both sets of figures the velocities were studied for four different aspect ratios $\alpha = 0.0001, 0.1, 0.5$, and 1 (i.e. the inclusions range from flat cracks to spheres). The crack density of the inclusions was $e = 0.05$.

A comparison between the results obtained for the correct density ρ_e with those calculated for a constant density ρ_e shows that the velocities increase when the correct density is taken into account. This effect is negligible for small aspect ratios but becomes strong for large aspect ratios.

Such a phenomenon can be explained by a reduction in the effective density ρ_e . That this reduction is zero for small aspect ratios but becomes significant for larger aspect ratios becomes clear from (8) which shows that ρ_e starts to deviate from ρ_b for increasing

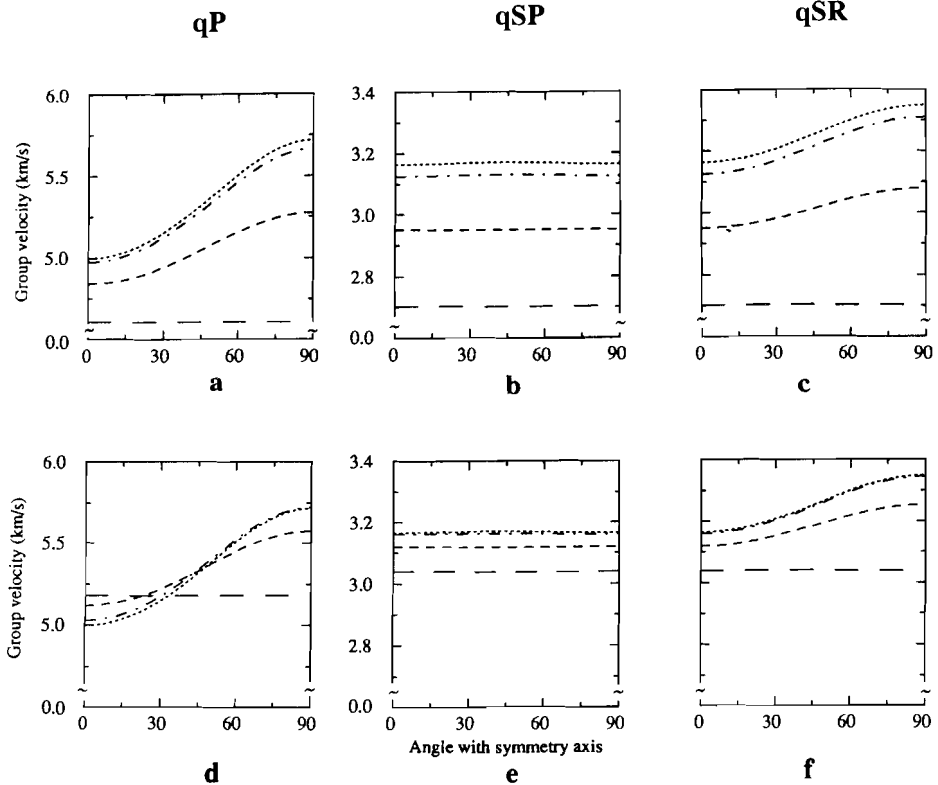


Fig. 2.8. As for Fig. 2.7, but for dry inclusions.

inclusion porosity ϕ . This is only true if $\rho_i \neq \rho_b$ (with significant difference) as in our situation. At a constant crack density an increasing porosity can only be obtained if the aspect ratio increases (see (5)).

From Figs 2.2 and 2.3, calculated at a constant density $\rho_e = \rho_b$, we concluded that the group velocities were reduced by an increasing aspect ratio. From Figs 2.7 and 2.8 we now conclude that a large part of this reduction vanishes due to the decreasing value of the effective density ρ_e for larger aspect ratios. As might be expected, this density ρ_e has the strongest effect on the results of dry cracks (Fig. 2.8), because then the density of the inclusion material ($\rho_i = 0$) differs most from the density of the background medium.

Both Figs 2.7 and 2.8 show that the effective medium is isotropic when the inclusions are spherical ($\alpha = 1$). The velocities no longer depend on the ray direction and there are only two different velocities: the velocity of the qP-waves and the velocity of the qSP-wave that is equal to that of the qSR-wave.

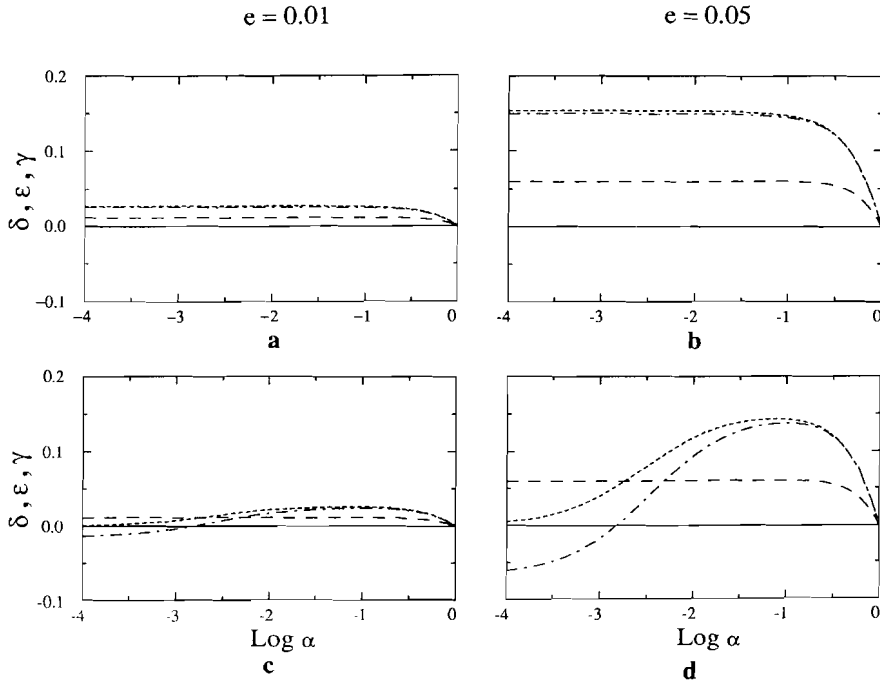


Fig. 2.9. The anisotropy parameters δ (·-·-·), ϵ (----), and γ (——) calculated with Nishizawa's model as a function of the aspect ratio of dry (a and b) and liquid-filled inclusions (c and d). The results are shown for two crack densities $e = 0.01$ (a and c) and $e = 0.05$ (b and d).

2.5.5 Anisotropy analysis using the parameters δ , ϵ , and γ

At the end of this section on numerical results we evaluate the anisotropy due to aligned ellipsoidal inclusions by calculating Thomsen's parameters δ , ϵ , and γ . Nishizawa's model is used to calculate the elastic constants. In Fig. 2.9 the results are shown for dry (Figs 2.9a and 2.9b) and liquid-filled inclusions (Figs 2.9c and 2.9d) at two different crack densities $e = 0.01$ and 0.05 . The aspect ratio of the inclusions varies from $\alpha = 0.0001$ (flat cracks) up to $\alpha = 1$ (spheres). Figure 2.9 shows that the absolute values of δ , ϵ , and γ are within the range 0 - 0.2, indicating that we are dealing with weak-to-moderate anisotropy (Thomsen, 1986). These values increase for increasing crack density as might be expected. They all become zero for an aspect ratio $\alpha = 1$ (spherical inclusions), corresponding to an isotropic situation.

Note that for dry inclusions the values of δ , ϵ , and γ have a non-zero constant value for a large range of aspect ratios and only go to zero for large aspect ratios. Thus for a large group of dry inclusions the resultant anisotropy is hardly affected by a change in aspect ratio. This conclusion corresponds to Fig. 2.3 which shows for dry inclusions a very small variation in group velocities for small aspect ratios.

However, the liquid-filled inclusions show a large variation of the parameters δ and ϵ (Figs 2.9c and 2.9d) with the aspect ratio. Because both parameters are related to the qP- and qSP-wave velocities (see (1a) and (1b)) this variation corresponds to a strong dependence of the qP- and qSP-group velocity on the aspect ratio (as seen in Fig. 2.2). Since the parameter γ (related to the qSR-wave) is constant for a large range of aspect ratios (especially for small aspect ratios), the group velocity of qSR-waves is not strongly affected by (small) aspect ratios (see Fig. 2.2).

For all the situations studied the values of ϵ and γ are positive, indicating that the phase velocities of the qP- and qSR-waves perpendicular to the axis of symmetry are always larger than those along this axis. For liquid-filled inclusions the value of ϵ goes to zero for very small aspect ratios, indicating that the difference between the qP-phase velocities in both directions also goes to zero. Figure 2.2d shows this effect for the qP-group velocity at small aspect ratios. Figures 2.9a and 2.9b show this effect does not occur for dry inclusions where the parameter ϵ is non-zero for small aspect ratios.

Finally, Fig. 2.9 shows an interesting feature of the anisotropy caused by ellipsoidal inclusions, i.e. the parameters δ and ϵ are equal for aspect ratios $\alpha \approx 0.3$ up to $\alpha = 1$ for both liquid-filled and dry inclusions. This implies that the resultant anisotropy is elliptical, i.e. the qP- and qSR-wavefronts are ellipsoidal, while the qSP-wavefronts are spherical. Thus, we may conclude that media containing aligned ellipsoidal inclusions can be elliptically anisotropic.

2.6 CONCLUSIONS

This numerical study has shown that for a large range of aspect ratios of either liquid-filled or dry inclusions Hudson's and Nishizawa's model give similar results. Significant differences between the results exist only for large aspect ratios and crack densities (i.e. $\alpha > 0.3$ and $e = 0.05$).

Although Hudson's flat crack model is strictly valid only for small aspect ratios, it appears to model ellipsoidal inclusions with aspect ratios up to 0.3 reasonably well (considering a crack density $e = 0.05$). This implies that in the modelling of real data one may use Hudson's model even if the aspect ratios of the inclusions are not expected to be very small. For large aspect ratios and crack densities Nishizawa's model is more reliable and should be used. Otherwise Hudson's model is to be preferred because of its simple analytical form and the possibility of studying wave attenuation effects (due to scattering), which can not be done with Nishizawa's model.

For inclusions with large aspect ratios it is necessary to take the density of the effective medium into account. Otherwise the velocities modelled will be too low.

Finally, Thomsen's parameters δ , ϵ , and γ prove to be useful for gaining a good impression of the anisotropy caused by all kind of ellipsoidal inclusions. They show how

inclusions with large aspect ratios result in elliptical anisotropy.

ACKNOWLEDGEMENT

I thank K. Helbig for many discussions on the subject.

2.7 REFERENCES

- Alford, R.M. 1986. Shear data in the presence of azimuthal anisotropy: Dilley, Texas. 56th S.E.G. Meeting, Houston, Expanded Abstracts, 476-479.
- Anderson, D.L., Minster, B. and Cole, D. 1974. The effect of oriented cracks on seismic velocities. *Journal of Geophysical Research* 79, 4011-4015.
- Berryman, J.G. 1979. Long-wave elastic anisotropy produced in transversely isotropic media. *Geophysics* 44, 869-917.
- Crampin, S. 1978. Seismic wave propagation through a cracked solid: polarization as a possible dilatancy diagnostic. *Geophysical Journal of the Royal Astronomical Society* 53, 467-496.
- Crampin, S. 1981. A review of wave motion in anisotropic and cracked elastic-media. *Wave Motion* 3, 343-391.
- Crampin, S. 1984. Effective anisotropic elastic constants for wave propagation through cracked solids. *Geophysical Journal of the Royal Astronomical Society* 76, 135-145.
- Crampin, S. 1985. Evaluation of anisotropy by shear-wave splitting. *Geophysics* 50, 142-152.
- Crampin, S. 1986. Anisotropy and transverse isotropy. *Geophysical Prospecting* 34, 94-99.
- Crampin, S. 1987. Geological and industrial implications of extensive dilatancy anisotropy. *Nature* 328, 491-496.
- Crampin, S., McGonigle, R. and Bamford, D. 1980. Estimating crack parameters from observations of P-wave velocity anisotropy. *Geophysics* 45, 345-360.
- Crampin, S., Chesnokov, E.M. and Hipkin, R.G. 1984. Seismic anisotropy: the state of the art. *Geophysical Journal of the Royal Astronomical Society* 76, 1-16.
- Crampin, S., Evans, R. and Atkinson, B.K. 1984. Earthquake prediction: a new physical basis. *Geophysical Journal of the Royal Astronomical Society* 76, 147-156.
- Crampin, S., McGonigle, R. and Ando, M. 1986. Extensive-dilatancy anisotropy beneath Mount Hood, Oregon and the effect of aspect ratio on seismic velocities through aligned cracks. *Journal of Geophysical Research* 91, 12703-12710.
- Douma, J. and Helbig, K. 1987. What can the polarization of shear waves tell us. *First Break* 5 (3), 95-104.
- Eshelby, J.D. 1957. The determination of the elastic field of an ellipsoidal inclusion, and related problems. *Proceedings of the Royal Society, London, Series A*, 241, 376-396.
- Garbin, H.D. and Knopoff, L. 1973. The compressional modulus of a material permeated by a random distribution of free circular cracks. *Quarterly of Applied Mathematics* 30, 453-464.
- Garbin, H.D. and Knopoff, L. 1975a. The shear modulus of a material permeated by a random distribution of free circular cracks. *Quarterly of Applied Mathematics* 33, 296-300.
- Garbin, H.D. and Knopoff, L. 1975b. Elastic moduli of a medium with liquid-filled cracks. *Quarterly of Applied Mathematics* 33, 301-303.
- Helbig, K. 1956. Die Ausbreitung elastischer Wellen in anisotropen Medien. *Geophysical Prospecting* 4, 71-81.

- Helbig, K. 1958. Elastische Wellen in anisotropen Medien. *Gerlands Beiträge zur Geophysik* 67, 177-211, 256-288.
- Helbig, K. 1979. Discussion on 'The reflection, refraction, and diffraction of waves in media with elliptical velocity dependence' (F. K. Levin). *Geophysics* 44, 987-990.
- Helbig, K. 1983. Elliptical anisotropy-its significance and meaning. *Geophysics* 48, 825-832.
- Helbig, K. 1984. Transverse isotropy in exploration seismics. *Geophysical Journal of the Royal Astronomical Society* 76, 79-88.
- Hoening, A. 1979. Elastic moduli of a non-randomly cracked body. *International Journal of Solids and Structures* 15, 137-154.
- Hudson, J.A. 1980. Overall properties of a cracked solid. *Mathematical Proceedings of the Cambridge Philosophical Society* 88, 371-384.
- Hudson, J.A. 1981. Wave speeds and attenuation of elastic waves in material containing cracks. *Geophysical Journal of the Royal Astronomical Society* 64, 133-150.
- Keith, C.M. and Crampin, S. 1977a. Seismic body waves in anisotropic media: reflection and refraction at a plane interface. *Geophysical Journal of the Royal Astronomical Society* 49, 181-208.
- Keith, C.M. and Crampin, S. 1977b. Seismic body waves in anisotropic media: propagation through a layer. *Geophysical Journal of the Royal Astronomical Society* 49, 209-224.
- Keith, C.M. and Crampin, S. 1977c. Seismic body waves in anisotropic media: synthetic seismograms. *Geophysical Journal of the Royal Astronomical Society* 49, 225-243.
- Krey, Th. and Helbig, K. 1956. A theorem concerning anisotropy of stratified media and its significance for reflection seismics. *Geophysical Prospecting* 4, 294-301.
- Nishizawa, O. 1982. Seismic velocity anisotropy in a medium containing oriented cracks-transversely isotropic case. *Journal of Physics of the Earth* 30, 331-347.
- Postma, G.W. 1955. Wave propagation in a stratified medium. *Geophysics* 20, 780-806.
- Rudzki, M.P. 1911. Parametrische Darstellung der elastischen Welle in anisotropen Medien. *Anzeiger der Akademie der Wissenschaften Krakau*, 503-536.
- Schoenberg, M. and Douma, J. 1988. Elastic wave propagation in media with parallel fractures and aligned cracks. *Geophysical Prospecting* 36, 571-590.
- Thomsen, L. 1986. Weak elastic anisotropy. *Geophysics* 51, 1954-1966.
- Thomsen, L. 1988. Elastic anisotropy due to aligned cracks. *Geophysical Journal of the Royal Astronomical Society* (submitted).
- Uhrig, L.F. and Van Melle, F.A. 1955. Velocity anisotropy in stratified media. *Geophysics* 20, 774-779.
- Yale, D.P. 1985. Recent advances in rock physics. *Geophysics* 50, 2480-2491.

Chapter 3

ELASTIC WAVE PROPAGATION IN MEDIA WITH PARALLEL FRACTURES AND ALIGNED CRACKS

ABSTRACT

A model of parallel slip interfaces simulates the behaviour of a fracture system composed of large, closely spaced, aligned joints. The model admits any fracture system anisotropy: triclinic (the most general), monoclinic, orthorhombic or transversely isotropic, and this is specified by the form of the 3×3 fracture system compliance matrix. The fracture system may be embedded in an anisotropic elastic background with no restrictions on the type of anisotropy. To compute the long wavelength equivalent moduli of the fractured medium requires at most the inversion of two 3×3 matrices. When the fractures are assumed on average to have rotational symmetry (transversely isotropic fracture system behaviour) and the background is assumed isotropic, the resulting equivalent medium is transversely isotropic and the effect of the additional compliance of the fracture system may be specified by two parameters (in addition to the two isotropic parameters of the isotropic background). Dilute systems of flat aligned microcracks in an isotropic background yield an equivalent medium of the same form as that of the isotropic medium with large joints, i.e. there are two additional parameters due to the presence of the microcracks which play roles in the stress-strain relations of the equivalent medium

This chapter has been published as:

Schoenberg, M. and Douma, J. 1988. Elastic wave propagation in media with parallel fractures and aligned cracks. *Geophysical Prospecting* 36, 571-590.

identical to those played by the parameters due to the presence of large joints. Thus, knowledge of the total of four parameters describing the anisotropy of such a fractured medium tells nothing of the size or concentration of the aligned fractures but does contain information as to the overall excess compliance due to the fracture system and its orientation. As the aligned microcracks, which were assumed to be ellipsoidal, with very small aspect ratio are allowed to become non-flat, i.e. have a growing aspect ratio, the moduli of the equivalent medium begin to diverge from the standard form of the moduli for flat cracks. The divergence is faster for higher crack densities but only becomes significant for microcracks of aspect ratios approaching 0.3.

3.1 INTRODUCTION

It is now clear that there are many regions of the subsurface (some say everywhere) showing azimuthal velocity anisotropy and this has been attributed to the presence of aligned vertical microcracks that arise because of tectonic stresses (see e.g. Crampin, 1985; Crampin and Atkinson, 1985; Willis, Rethford and Bielanski, 1986; Crampin and Bush, 1986). That this Crampin model is the actual mechanism causing the azimuthal velocity anisotropy is difficult to say as drilling and coring in such a region distort the stress field locally and perhaps distort and close the cracks that existed in the undeformed rock. A set of robust parameters is needed to give (1) the orientation of the cracks and/or fractures in the subsurface, and (2) a measure of crack density times strength which could be called excess compliance due to the presence of cracks. Such a parameter set could be a valuable indicator of overall stress orientation, and the orientation and strength of the anisotropic part of the permeability tensor. Crack orientation, when cracks are vertical, can be simply determined by the splitting of vertically propagating shear waves. This occurs because of the azimuthal anisotropy induced by microcracks and fractures. The polarization of the faster propagating shear wave according to current theory is parallel to the fractures; the polarization of the slower propagating shear wave is perpendicular to the fractures.

We compare theories that predict elastic anisotropy due to the presence of filled or empty ellipsoidal inclusions with one another and with a theory that predicts elastic anisotropy due to long (compared to wavelength) parallel joints or fractures. For inclusions with small aspect ratios (almost flat cracks), all the models agree with one another and in fact they are indistinguishable from the fracture model. The fracture model is exactly derivable as the limiting case of wave propagation through a region composed of alternating elastic layers. The results for anisotropic layers are reviewed in Section 3.2 and the derivation of the fracture model in its most general form and for special cases is presented in detail in Section 3.3. In Section 3.4, the simplest anisotropy attributable to 'transversely isotropic' fractures in an isotropic background is compared in detail with the anisotropy due to systems of aligned flat microcracks. In both the anisotropy is characterized by two, positive, dimensionless parameters that play the same roles in the

stress-strain relations. The first depends on the tangential compliance of the joints or cracks and the second depends on the normal compliance. From a phenomenological point of view the behaviour of such systems of aligned flat cracks or parallel joints can be reduced to two numbers which, with the isotropic background moduli, determine the five elastic moduli of a transversely isotropic elastic medium. From the elastic moduli themselves nothing more specific concerning crack density, individual crack compliance or crack size can be found.

However, in Section 3.5 it will be shown that for the ellipsoidal inclusions, as the aspect ratio becomes large (up to 1.0), the moduli derivable from the theory of ellipsoidal inclusions (Nishizawa, 1982) deviate from those obtainable from the flat crack or joint theories. This occurs at aspect ratios of about 0.3 for gas- or liquid-filled inclusions at the highest values of crack density of such inclusions for which the theory is thought to be valid.

3.2 ELASTIC MODULI OF STRATIFIED MEDIA

Consider a stratified medium made up of perfectly bonded homogeneous, but not necessarily isotropic, layers. Let the x_3 -axis be perpendicular to the layering and assume that there are n different constituent layers, arranged so that in each sufficiently large interval one finds the same proportion of each medium. The simplest arrangement that satisfies this requirement is a periodic sequence of layers. Each anisotropic constituent i has a relative thickness h_i $i=1, \dots, n$ so that $h_1 + \dots + h_n = 1$, a density ρ_i , and an elastic modulus tensor $c_{pqrs,i}$, relating stress $\sigma_{pq,i}$ with strain $\epsilon_{rs,i}$. In condensed notation, for which subscripts $11 \rightarrow 1, 22 \rightarrow 2, 33 \rightarrow 3, 23 \rightarrow 4, 31 \rightarrow 5$ and $12 \rightarrow 6$, the stress-strain relation may be written

$$\begin{bmatrix} \sigma_1 \\ \sigma_2 \\ \sigma_3 \\ \sigma_4 \\ \sigma_5 \\ \sigma_6 \end{bmatrix} = \begin{bmatrix} c_{11} & c_{12} & c_{13} & c_{14} & c_{15} & c_{16} \\ c_{12} & c_{22} & c_{23} & c_{24} & c_{25} & c_{26} \\ c_{13} & c_{23} & c_{33} & c_{34} & c_{35} & c_{36} \\ c_{14} & c_{24} & c_{34} & c_{44} & c_{45} & c_{46} \\ c_{15} & c_{25} & c_{35} & c_{45} & c_{55} & c_{56} \\ c_{16} & c_{26} & c_{36} & c_{46} & c_{56} & c_{66} \end{bmatrix} \begin{bmatrix} \epsilon_1 \\ \epsilon_2 \\ \epsilon_3 \\ \epsilon_4 \\ \epsilon_5 \\ \epsilon_6 \end{bmatrix}, \quad (1)$$

where

$$\begin{bmatrix} \sigma_1 \\ \sigma_2 \\ \sigma_3 \\ \sigma_4 \\ \sigma_5 \\ \sigma_6 \end{bmatrix} = \begin{bmatrix} \sigma_{11} \\ \sigma_{22} \\ \sigma_{33} \\ \sigma_{23} \\ \sigma_{31} \\ \sigma_{12} \end{bmatrix} \quad \text{and} \quad \begin{bmatrix} \epsilon_1 \\ \epsilon_2 \\ \epsilon_3 \\ \epsilon_4 \\ \epsilon_5 \\ \epsilon_6 \end{bmatrix} = \begin{bmatrix} \epsilon_{11} \\ \epsilon_{22} \\ \epsilon_{33} \\ 2\epsilon_{23} \\ 2\epsilon_{31} \\ 2\epsilon_{12} \end{bmatrix}.$$

The elastic moduli for the homogeneous anisotropic medium, equivalent, in the long wavelength (or quasistatic) limit, to a layered medium composed of anisotropic constituent layers, can be expressed in terms of thickness-weighted averages of functions of the moduli of the constituents. The long wavelength assumption on stress is that all stress components acting on surfaces parallel to the layering are the same in all layers, i.e. $\sigma_{33,i} \equiv \sigma_{3,i} = \sigma_3$, $\sigma_{23,i} \equiv \sigma_{4,i} = \sigma_4$, and $\sigma_{13,i} \equiv \sigma_{5,i} = \sigma_5$. The long wavelength kinematic assumption is that over many layers, the layers move together (so that derivatives of in-plane displacements with respect to in-plane coordinates, x_1 and x_2 , are the same) implying that all strain components lying in the plane of the layering are the same in all layers, i.e. $\epsilon_{11,i} \equiv \epsilon_{1,i} = \epsilon_1$, $\epsilon_{22,i} \equiv \epsilon_{2,i} = \epsilon_2$, and $2\epsilon_{12,i} \equiv \epsilon_{6,i} = \epsilon_6$. The other stress and strain components, $\sigma_{11,i} \equiv \sigma_{1,i}$, $\sigma_{22,i} \equiv \sigma_{2,i}$, $\sigma_{12,i} \equiv \sigma_{6,i}$, $\epsilon_{33,i} \equiv \epsilon_{3,i}$, $2\epsilon_{23,i} \equiv \epsilon_{4,i}$, and $2\epsilon_{13,i} \equiv \epsilon_{5,i}$, may vary from layer to layer. In each layer, such a component may be taken as its average value across the thickness of that layer.

A concise way to pose the problem of finding the effective moduli, even when the constituent layers are anisotropic, is through a matrix formulation which distinguishes components that are constant over many layers from the other components which can vary from layer to layer. Following the procedure first outlined by Helbig and Schoenberg (1987) for general anisotropic layers, define the following vectors

$$\mathbf{S}_{1,i} = \begin{bmatrix} \sigma_{1,i} \\ \sigma_{2,i} \\ \sigma_{6,i} \end{bmatrix}, \quad \mathbf{E}_{2,i} = \begin{bmatrix} \epsilon_{3,i} \\ \epsilon_{4,i} \\ \epsilon_{5,i} \end{bmatrix}, \quad \text{layer dependent}$$

and

$$\mathbf{S}_2 = \begin{bmatrix} \sigma_3 \\ \sigma_4 \\ \sigma_5 \end{bmatrix}, \quad \mathbf{E}_1 = \begin{bmatrix} \epsilon_1 \\ \epsilon_2 \\ \epsilon_6 \end{bmatrix}, \quad \text{layer independent} \quad (2)$$

which allow the stress-strain relations in any layer to be rewritten as

$$\mathbf{S}_{1,i} = \mathbf{M}_i \mathbf{E}_1 + \mathbf{P}_i \mathbf{E}_{2,i}, \quad (3a)$$

$$\mathbf{S}_2 = \mathbf{P}_i^T \mathbf{E}_1 + \mathbf{N}_i \mathbf{E}_{2,i}. \quad (3b)$$

Here

$$\mathbf{M}_i = \begin{bmatrix} c_{11,i} & c_{12,i} & c_{16,i} \\ c_{12,i} & c_{22,i} & c_{26,i} \\ c_{16,i} & c_{26,i} & c_{66,i} \end{bmatrix}, \quad \mathbf{N}_i = \begin{bmatrix} c_{33,i} & c_{34,i} & c_{35,i} \\ c_{34,i} & c_{44,i} & c_{45,i} \\ c_{35,i} & c_{45,i} & c_{55,i} \end{bmatrix}, \quad \mathbf{P}_i = \begin{bmatrix} c_{13,i} & c_{14,i} & c_{15,i} \\ c_{23,i} & c_{24,i} & c_{25,i} \\ c_{36,i} & c_{46,i} & c_{56,i} \end{bmatrix}, \quad (4)$$

with superscript T denoting the matrix transpose. \mathbf{M}_i and \mathbf{N}_i are symmetrical matrices. Then multiplying (3b) by \mathbf{N}_i^{-1} gives

$$\mathbf{N}_i^{-1} \mathbf{S}_2 = \mathbf{N}_i^{-1} \mathbf{P}_i^T \mathbf{E}_1 + \mathbf{E}_{2,i}, \quad (5)$$

and solving this for $\mathbf{E}_{2,i}$ and substituting into (3a) yields

$$\mathbf{S}_{1,i} = \mathbf{M}_i \mathbf{E}_1 + \mathbf{P}_i \left[\mathbf{N}_i^{-1} \mathbf{S}_2 - \mathbf{N}_i^{-1} \mathbf{P}_i^T \mathbf{E}_1 \right]. \quad (6)$$

Now let the thickness-weighted average over all the constituent layers, $\sum_{i=1}^n h_i(\cdot)$, be denoted as $\langle \cdot \rangle$. Then taking first, the thickness-weighted average of (6), and second, the thickness-weighted average of (5) and premultiplying this second result by $\langle \mathbf{N}^{-1} \rangle^{-1}$ gives

$$\langle \mathbf{S}_1 \rangle = \left[\langle \mathbf{M} \rangle - \langle \mathbf{P} \mathbf{N}^{-1} \mathbf{P}^T \rangle \right] \mathbf{E}_1 + \langle \mathbf{P} \mathbf{N}^{-1} \rangle \mathbf{S}_2, \quad (7a)$$

$$\mathbf{S}_2 = \langle \mathbf{N}^{-1} \rangle^{-1} \langle \mathbf{N}^{-1} \mathbf{P}^T \rangle \mathbf{E}_1 + \langle \mathbf{N}^{-1} \rangle^{-1} \langle \mathbf{E}_2 \rangle. \quad (7b)$$

Finally substituting the expression for \mathbf{S}_2 from (7b) into (7a) allows us to write the elastic moduli for the media equivalent to the stratified medium in the long wavelength limit, in matrix form as

$$\langle \mathbf{S}_1 \rangle = \mathbf{M}_e \mathbf{E}_1 + \mathbf{P}_e \langle \mathbf{E}_2 \rangle, \quad (8a)$$

$$\mathbf{S}_2 = \mathbf{P}_e^T \mathbf{E}_1 + \mathbf{N}_e \langle \mathbf{E}_2 \rangle, \quad (8b)$$

with

$$\begin{aligned} \mathbf{N}_e &= \langle \mathbf{N}^{-1} \rangle^{-1}, \quad \mathbf{P}_e = \langle \mathbf{P} \mathbf{N}^{-1} \rangle \mathbf{N}_e, \\ \mathbf{M}_e &= \langle \mathbf{M} \rangle - \langle \mathbf{P} \mathbf{N}^{-1} \mathbf{P}^T \rangle + \langle \mathbf{P} \mathbf{N}^{-1} \rangle \mathbf{N}_e \langle \mathbf{N}^{-1} \mathbf{P}^T \rangle. \end{aligned} \quad (9)$$

If the i th constituent is transversely isotropic with the x_3 -axis, the axis of symmetry, then, from the expressions for \mathbf{M}_i , \mathbf{N}_i , and \mathbf{P}_i in (4), we have

$$\begin{aligned} \mathbf{M}_i &= \begin{bmatrix} c_{11,i} & c_{11,i} - 2c_{66,i} & 0 \\ c_{11,i} - 2c_{66,i} & c_{11,i} & 0 \\ 0 & 0 & c_{66,i} \end{bmatrix}, \\ \mathbf{N}_i &= \begin{bmatrix} c_{33,i} & 0 & 0 \\ 0 & c_{44,i} & 0 \\ 0 & 0 & c_{44,i} \end{bmatrix}, \quad \mathbf{P}_i = \begin{bmatrix} c_{13,i} & 0 & 0 \\ c_{13,i} & 0 & 0 \\ 0 & 0 & 0 \end{bmatrix}. \end{aligned} \quad (10)$$

Note that when the i th constituent layer is isotropic, $c_{44,i} = c_{66,i} = \mu_i$, $c_{11,i} = c_{33,i} = \lambda_i + 2\mu_i$ and $c_{13,i} = \lambda_i$ where λ_i and μ_i are Lamé parameters. If all the constituent layers are transversely isotropic, the equivalent homogeneous medium is transversely isotropic and from (9) the moduli are given by

$$\begin{aligned} \mathbf{N}_e &= \begin{bmatrix} c_{33} & 0 & 0 \\ 0 & c_{44} & 0 \\ 0 & 0 & c_{44} \end{bmatrix} = \begin{bmatrix} 1/\langle 1/c_{33} \rangle & 0 & 0 \\ 0 & 1/\langle 1/c_{44} \rangle & 0 \\ 0 & 0 & 1/\langle 1/c_{44} \rangle \end{bmatrix}, \\ \mathbf{P}_e &= \begin{bmatrix} c_{13} & 0 & 0 \\ c_{13} & 0 & 0 \\ 0 & 0 & 0 \end{bmatrix} = \begin{bmatrix} \langle c_{13}/c_{33} \rangle / \langle 1/c_{33} \rangle & 0 & 0 \\ \langle c_{13}/c_{33} \rangle / \langle 1/c_{33} \rangle & 0 & 0 \\ 0 & 0 & 0 \end{bmatrix}, \\ \mathbf{M}_e &= \begin{bmatrix} c_{11} & c_{11} - 2c_{66} & 0 \\ c_{11} - 2c_{66} & c_{11} & 0 \\ 0 & 0 & c_{66} \end{bmatrix} = \begin{bmatrix} c_{11} & c_{11} - 2\langle c_{66} \rangle & 0 \\ c_{11} - 2\langle c_{66} \rangle & c_{11} & 0 \\ 0 & 0 & \langle c_{66} \rangle \end{bmatrix}, \\ c_{11} &= \langle c_{11} \rangle - \langle c_{13}^2/c_{33} \rangle + \langle c_{13}/c_{33} \rangle^2 / \langle 1/c_{33} \rangle, \end{aligned} \quad (11)$$

identical to the results of Backus (1962).

Note that the combination rules (9) are commutative in layer order. If, instead of

considering the relative thickness h_i of each constituent, the combination operation is thought of as the folding together of a total thickness H_i of each constituent, albeit divided into fine layers, then the combination rules (9) are also associative (Schoenberg and Muir, 1988). Thus, if there are three constituents of total thickness H_1 , H_2 , and H_3 , the properties of the combined medium of thickness $H_1 + H_2 + H_3$ can be determined by first finding the properties of the medium equivalent to constituent 3 mixed with constituent 1, and then stirring in amount H_2 of constituent 2. The resulting equivalent medium is independent of the order of combination.

3.3 GENERAL MODEL FOR LONG THIN PARALLEL FRACTURES

The behaviour of long parallel fractures or joints in an otherwise homogeneous anisotropic background medium may be modelled as a set of thin constituent layers, not necessarily isotropic, embedded in the background. The above derived formalism is used and the fractures are modelled by taking the limit as the thickness and the elastic moduli of the embedded thin layers go to zero together. The formalism enables us to identify the effect of even the most anisotropic fractures on the most anisotropic background, and to see the variation in anisotropic behaviour permitted by sets of large parallel fractures. The fracture behaviour is at its simplest if the material inside the fracture is assumed to be transversely isotropic; the assumption of full isotropy implies no further simplification. This type of fracture behaviour is discussed and compared with the behaviour of dilute concentrations of aligned inclusions that may be assumed to model a medium with internal cracks where the cracks have a preferred orientation.

For now, the material inside the fracture is allowed to have arbitrary anisotropy. The fracture-filling material is assumed to be soft by letting the moduli of the fracture layer, $c_{jk,f}$, be much smaller than a typical non-zero background modulus, say $c_{33,b}$ (the effect of a hard fracture-filling material would tend to vanish as the fracture widths approached zero). In particular, the moduli are assumed to be of the order of the volume ratio of the fractures h_f , i.e. $c_{jk,f}/c_{33,b} = O(h_f)$. Here h_f may be thought of as the total fracture thickness in an interval of width H divided by H . The interval width H must satisfy two criteria. It must be sufficiently large so that the fractured medium has the same total thickness of fractures $h_f H$ in any interval of thickness H . Yet H must be much smaller than the smallest wavelength of interest for the fractured medium to be replaced by a long wavelength equivalent homogeneous medium. The assumption on the $c_{jk,f}$ means that, in the limit, as $h_f \rightarrow 0$ the $c_{jk,f}$ may be replaced by $h_f \tilde{c}_{jk}$ and, from (9) as $h_f \rightarrow 0$,

$$\begin{aligned} \mathbf{N}_e &= \langle \mathbf{N}^{-1} \rangle^{-1} = \left[(1 - h_f) \mathbf{N}_b^{-1} + h_f \mathbf{N}_f^{-1} \right]^{-1} \rightarrow \left[\mathbf{N}_b^{-1} + \tilde{\mathbf{N}}^{-1} \right]^{-1} \\ &= \mathbf{N}_b \left[\mathbf{I} + \tilde{\mathbf{N}}^{-1} \mathbf{N}_b \right]^{-1} \end{aligned} \quad (12)$$

$$\mathbf{P}_e \rightarrow \left[\mathbf{P}_b \mathbf{N}_b^{-1} \right] \mathbf{N}_e, \quad \mathbf{M}_e \rightarrow \mathbf{M}_b - \mathbf{P}_b \mathbf{N}_b^{-1} \mathbf{P}_b^T + \left[\mathbf{P}_b \mathbf{N}_b^{-1} \right] \mathbf{N}_e \left[\mathbf{N}_b^{-1} \mathbf{P}_b^T \right], \quad \langle \rho \rangle \rightarrow \rho_b,$$

where \mathbf{I} is the 3×3 identity matrix. The fracture parameters enter only through $\tilde{\mathbf{N}}$, a symmetrical 3×3 submatrix of the full 6×6 modulus matrix, so that in general there are at most six fracture parameters, the six independent components of $\tilde{\mathbf{N}}$. To see why this must be so, consider (3b) for the fracture medium, which gives the components of the stress traction across the fracture. They are

$$\mathbf{S}_2 = h_f \left[\tilde{\mathbf{P}}^T \begin{bmatrix} \varepsilon_1 \\ \varepsilon_2 \\ \varepsilon_6 \end{bmatrix} + \tilde{\mathbf{N}} \begin{bmatrix} \varepsilon_{3,f} \\ \varepsilon_{4,f} \\ \varepsilon_{5,f} \end{bmatrix} \right]. \quad (13)$$

Since the fractures are soft, strain components in the fracture layers are large and can be approximated by $\varepsilon_{3,f} \approx \Delta u_3 / h_f H$, $\varepsilon_{4,f} \approx \Delta u_2 / h_f H$, and $\varepsilon_{5,f} \approx \Delta u_1 / h_f H$ where $h_f H$ is the total fracture width in an interval of width H and Δu_i are the components of the total slip displacement across all the fractures in that interval of width H . The other strain components in the fracture layers are constrained by the long wavelength assumption to be the same as the corresponding components in the background medium and thus not large. Then, in the limit as $h_f \rightarrow 0$,

$$\mathbf{S}_2 = \begin{bmatrix} \sigma_3 \\ \sigma_4 \\ \sigma_5 \end{bmatrix} = \begin{bmatrix} \sigma_{33} \\ \sigma_{23} \\ \sigma_{13} \end{bmatrix} = h_f \left[\tilde{\mathbf{P}}_f^T \begin{bmatrix} \varepsilon_1 \\ \varepsilon_2 \\ \varepsilon_6 \end{bmatrix} + \tilde{\mathbf{N}} \begin{bmatrix} \Delta u_3 / h_f H \\ \Delta u_2 / h_f H \\ \Delta u_1 / h_f H \end{bmatrix} \right] \rightarrow \tilde{\mathbf{N}} \begin{bmatrix} \Delta u_3 / H \\ \Delta u_2 / H \\ \Delta u_1 / H \end{bmatrix}. \quad (14)$$

In subsequent development the 'fracture system compliance matrix' $\mathbf{Z} \equiv \tilde{\mathbf{N}}^{-1}$ will be used instead of $\tilde{\mathbf{N}}$ as small slip or vanishing of some components of the fracture system slip-strain will cause $\tilde{\mathbf{N}}$ to be very large or undefined, while causing \mathbf{Z} merely to have some small or zero components. Thus (14) becomes

$$\begin{bmatrix} \Delta u_3/H \\ \Delta u_2/H \\ \Delta u_1/H \end{bmatrix} = \mathbf{Z} \begin{bmatrix} \sigma_3 \\ \sigma_4 \\ \sigma_5 \end{bmatrix}. \quad (15)$$

Define the vector on the left, the slip-displacement vector of the fractures in width H divided by H , as the 'fracture system slip-strain'. Then \mathbf{Z} gives the fracture system slip-strain as a linear function of the traction on any $x_3 = \text{constant}$ surface (Schoenberg, 1980). Note that it is perfectly acceptable that some of the components of $\mathbf{N}_f \rightarrow 0$ as $h_f \rightarrow 0$ and for others to remain finite. This is accounted for in the evaluation of the term $h_f \mathbf{N}_f^{-1}$, which approaches \mathbf{Z} , occurring in the first equation of (12) for \mathbf{N}_e .

Rewriting the first equation of (12) as

$$\mathbf{N}_e = \mathbf{N}_b \left[\mathbf{I} + \mathbf{Z} \mathbf{N}_b \right]^{-1}, \quad (16)$$

enables us to write the matrices of the changes from the background moduli due to the fractures, from (12), as

$$\begin{aligned} \Delta \mathbf{N} &= \mathbf{N}_b \left[\left(\mathbf{I} + \mathbf{Z} \mathbf{N}_b \right)^{-1} - \mathbf{I} \right], \\ \Delta \mathbf{P} &= \left[\mathbf{P}_b \mathbf{N}_b^{-1} \right] \Delta \mathbf{N}, \quad \Delta \mathbf{M} = \left[\mathbf{P}_b \mathbf{N}_b^{-1} \right] \Delta \mathbf{N} \left[\mathbf{N}_b^{-1} \mathbf{P}_b^T \right]. \end{aligned} \quad (17)$$

When \mathbf{Z} is so small that all terms of $\mathbf{Z} \mathbf{N}_b \ll 1$, we see that $\mathbf{N}_e \approx \mathbf{N}_b - \mathbf{N}_b \mathbf{Z} \mathbf{N}_b$ and $\Delta \mathbf{N} \approx -\mathbf{N}_b \mathbf{Z} \mathbf{N}_b$.

As an aside, note that had we begun with a compliance formulation, writing strain as an elastic compliance matrix times stress, i.e. $\epsilon_j = s_{jk} \sigma_k$, the strain-stress relations could be written analogously with (3) as

$$\begin{aligned} \mathbf{E}_1 &= \mathbf{A}_i \mathbf{S}_{1,i} + \mathbf{C}_i \mathbf{S}_2, \\ \mathbf{E}_{2,i} &= \mathbf{C}_i^T \mathbf{S}_{1,i} + \mathbf{B}_i \mathbf{S}_2, \end{aligned} \quad (18)$$

then the matrices of the changes from the background compliances due to the presence of the fractures are $\Delta \mathbf{A} = 0$, $\Delta \mathbf{C} = 0$ and $\Delta \mathbf{B} = \mathbf{Z}$.

From the associativity of the process of combining layers, even when there are many types of parallel fractures in the medium, it is the overall compliance of all of them that can be combined to form an 'effective fracture behaviour' which is the average of the different types of fractures weighted by the respective fracture density.

In general, from (15), all three components of the fracture system slip-strain are

coupled to all three components of the traction across the fractures. This is the case of triclinic fracture system anisotropy. For this most general behaviour, six parameters are needed to fully describe fracture behaviour within an otherwise homogeneous medium, the six independent components of the fracture compliance matrix \mathbf{Z} . However, there are three symmetry classes that apply to fracture systems that reduce the number of independent fracture system parameters.

The monoclinic fracture system. Let the fracture system be invariant under reflection about a plane containing the x_3 -axis, say the x_1 - x_3 plane, implying that \mathbf{Z} has the form

$$\mathbf{Z} = \begin{bmatrix} Z_N & 0 & Z_{N1} \\ 0 & Z_2 & 0 \\ Z_{N1} & 0 & Z_1 \end{bmatrix}. \quad (19)$$

This shows that fracture slip in the x_2 -direction is uncoupled from normal slip and tangential slip in the x_1 -direction. The x_1 -tangential slip is not uncoupled from normal slip. Tangential fracture displacement and the tangential component of the stress traction are not colinear. Such fracture system behaviour need not be due to the anisotropy of the infilling material, but could be due to slight micro-corrugation of the fracture surfaces, which then must have its peaks and troughs slightly offset, top to bottom, to couple normal and tangential components. This is shown by the schematic diagram in Fig. 3.1a.

The orthorhombic fracture system. Let the fracture system be invariant under reflection about the x_1 - x_2 plane uncoupling the fracture system displacement normal to the fractures from the tangential fracture system displacement. Then \mathbf{Z} has the form

$$\mathbf{Z} = \begin{bmatrix} Z_N & 0 & 0 \\ 0 & Z_2 & Z_{12} \\ 0 & Z_{12} & Z_1 \end{bmatrix}, \quad (20)$$

but there is always a rotation about the x_3 -axis which diagonalizes \mathbf{Z} giving

$$\mathbf{Z}' = \begin{bmatrix} Z_N & 0 & 0 \\ 0 & Z'_2 & 0 \\ 0 & 0 & Z'_1 \end{bmatrix}. \quad (21)$$

Here, Z'_1 and Z'_2 are the tangential compliances in the x'_1 - and x'_2 -directions respectively. The tangential fracture displacement and the tangential component of the stress traction are not colinear but the normal compliance is uncoupled from the tangential compliance. This

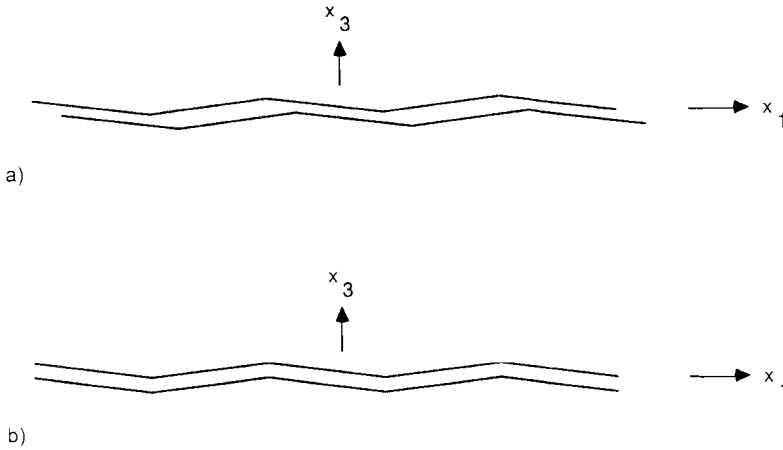


Fig. 3.1. A schematic of a fracture (a) with monoclinic behaviour and (b) with orthorhombic behaviour. In both cases the ridges cause the tangential traction and tangential slip not to be parallel unless they are either parallel or perpendicular to the ridge axis. In (a), additionally, closure or opening of the fracture will cause tangential slip in the x_1 -direction and vice versa but is uncoupled from tangential motion in the x_2 -direction.

can be visualized as a micro-corrugated interface with peaks and troughs aligned, top to bottom (see Fig. 3.1b). Tangential slip compliance along the corrugation is larger than the tangential slip compliance against the corrugation.

The transversely isotropic fracture system. This most symmetrical case occurs when the fracture system behaviour is invariant with respect to rotation about the x_3 -axis. In this case \mathbf{Z} must have the form

$$\mathbf{Z} = \begin{bmatrix} Z_N & 0 & 0 \\ 0 & Z_T & 0 \\ 0 & 0 & Z_T \end{bmatrix}. \quad (22)$$

Z_N and Z_T are normal and tangential compliances respectively of an average fracture of dimension length/stress. The tangential fracture displacement and the tangential component of the stress traction are colinear and the normal and tangential compliances are uncoupled. The form of \mathbf{Z} given here is independent of whether the fracture medium is isotropic or transversely isotropic. However, if the fracture medium were isotropic, stability requires that $Z_T \geq 4Z_N/3 \geq 0$. However, if the fracture medium is merely transversely isotropic the stability requires only that Z_T and Z_N be non-negative.

The long wavelength equivalent medium to the fractured medium is transversely isotropic only if the fracture system is transversely isotropic, i.e. with \mathbf{Z} given by (22), and

it is embedded in a transversely isotropic background medium which has its symmetry axis perpendicular to the fractures. Then, from (16) and (9)

$$\begin{aligned}
 \mathbf{N}_e &= \begin{bmatrix} c_{33} & 0 & 0 \\ 0 & c_{44} & 0 \\ 0 & 0 & c_{44} \end{bmatrix} = \begin{bmatrix} c_{33,b}/(1+E_N) & 0 & 0 \\ 0 & c_{44,b}/(1+E_T) & 0 \\ 0 & 0 & c_{44,b}/(1+E_T) \end{bmatrix}, \\
 \mathbf{P}_e &= \begin{bmatrix} c_{13} & 0 & 0 \\ c_{13} & 0 & 0 \\ 0 & 0 & 0 \end{bmatrix} = \begin{bmatrix} c_{13,b}/(1+E_N) & 0 & 0 \\ c_{13,b}/(1+E_N) & 0 & 0 \\ 0 & 0 & 0 \end{bmatrix}, \\
 \mathbf{M}_e &= \begin{bmatrix} c_{11} & c_{11}-2c_{66} & 0 \\ c_{11}-2c_{66} & c_{11} & 0 \\ 0 & 0 & c_{66} \end{bmatrix} = \begin{bmatrix} c_{11} & c_{11}-2c_{66,b} & 0 \\ c_{11}-2c_{66,b} & c_{11} & 0 \\ 0 & 0 & c_{66,b} \end{bmatrix}, \\
 c_{11} &= c_{11,b} - \frac{c_{13,b}^2}{c_{33,b}} \left[1 - \frac{1}{1+E_N} \right],
 \end{aligned} \tag{23}$$

where

$$E_N \equiv c_{33,b}Z_N, \quad E_T \equiv c_{44,b}Z_T.$$

E_N and E_T are dimensionless compliances that give the fracture system compliances relative to the background medium compliances, normal and tangential to the fracture system, respectively. The modulus matrix depends on seven parameters, the five of the background plus the normal and tangential fracture system compliances. When the background medium is isotropic, the resulting medium is transversely isotropic, but now depends on four parameters, μ_b , λ_b , E_N , and E_T . The moduli are given by (23) with $c_{11,b} = c_{33,b} = \lambda_b + 2\mu_b$, $c_{13,b} = \lambda_b$, and $c_{44,b} = c_{66,b} = \mu_b$. The matrices of the changes from the isotropic moduli due to the presence of the fractures are

$$\Delta \mathbf{N} = - \begin{bmatrix} (\lambda_b + 2\mu_b)E_N/(1 + E_N) & 0 & 0 \\ 0 & \mu_b E_T/(1 + E_T) & 0 \\ 0 & 0 & \mu_b E_T/(1 + E_T) \end{bmatrix},$$

$$\Delta \mathbf{P} = -\lambda_b \frac{E_N}{1 + E_N} \begin{bmatrix} 1 & 0 & 0 \\ 1 & 0 & 0 \\ 0 & 0 & 0 \end{bmatrix}, \quad (24)$$

$$\Delta \mathbf{M} = -\frac{\lambda_b^2}{(\lambda_b + 2\mu_b)} \frac{E_N}{(1 + E_N)} \begin{bmatrix} 1 & 1 & 0 \\ 1 & 1 & 0 \\ 0 & 0 & 0 \end{bmatrix}.$$

This is the very simple model for the behaviour of large joints in an isotropic background. These results agree with those of Morland (1974) and have been used to describe reflectivity from a jointed half-space by Schoenberg (1983).

An isotropic background medium with a transversely isotropic fracture system, as described in (24), is a restricted class of transversely isotropic media. To examine the behaviour of such media, let v_{qp} be the phase speed of the quasi-compressional wave (the fast wave which is purely longitudinal for propagation parallel and perpendicular to the fractures), v_{qs} be the phase speed of the quasi-shear wave (the in-plane wave which is purely transverse for propagation parallel and perpendicular to the fractures), and v_s be the phase speed of the pure shear wave that is always polarized parallel to the fractures. The dimensionless compliances are directly related to the differences between parallel ($//$) and perpendicular (\perp) propagation of the squares of the phase speeds normalized by the isotropic background speeds as, from (24),

$$\frac{[v_{sq}^2 - v_{s\perp}^2]}{\mu_b/\rho_b} = \frac{c_{66} - c_{44}}{\mu_b} = \frac{E_T}{1 + E_T}$$

$$\approx E_T \quad \text{for } E_T \ll 1, \quad (25)$$

$$\frac{[v_{qp\parallel}^2 - v_{qp\perp}^2]}{(\lambda_b + 2\mu_b)/\rho_b} = \frac{c_{11} - c_{33}}{\lambda_b + 2\mu_b} = 4\gamma_b(1 - \gamma_b) \frac{E_N}{1 + E_N}$$

$$\approx 4\gamma_b[1 - \gamma_b]E_N \quad \text{for } E_N \ll 1,$$

where γ_b is the square of the ratio of the background shear speed to compressional speed, i.e. $\gamma_b = \mu_b/(\lambda_b + 2\mu_b)$. Further, substitution of the perturbations to the elastic moduli from (24) for small E_T and E_N (neglecting $O(E^2)$ terms) into the Christoffel equations for the phase velocity (e.g. see Musgrave, 1970) gives

$$\begin{aligned} v_s^2(\theta) &\approx \frac{\mu_b}{\rho_b} \left[1 - E_T \cos^2 \theta \right], \\ v_{qs}^2(\theta) &\approx \frac{\mu_b}{\rho_b} \left[1 - E_T \cos^2 2\theta - \gamma_b E_N \sin^2 2\theta \right], \\ v_{qp}^2(\theta) &\approx \frac{\lambda_b + 2\mu_b}{\rho_b} \left[1 - \gamma_b E_T \sin^2 2\theta - E_N (1 - 2\gamma_b \sin^2 \theta)^2 \right], \end{aligned} \quad (26)$$

where θ is the angle between the wavenumber vector and the x_3 -axis. It is clear from (26) that all the phase speeds at all angles are non-increasing with increasing E_T or E_N . Note that terms depending on $\sin^2 2\theta$ or $\cos^2 2\theta$ are actually $\cos 4\theta$ terms which have period $\pi/2$ and are symmetrical about $\theta = \pi/4$. Thus for small tangential and normal compliances, v_{qs} is 4θ -dependent and is symmetrical about $\theta = \pi/4$ whereas for v_{qp} , the tangential compliance yields a 4θ term symmetrical about $\theta = \pi/4$ while the normal compliance yields a 2θ term necessarily not symmetrical about $\theta = \pi/4$. Note that tangential compliance by itself, even when it is large, yields only 4θ -dependence to both v_{qp} and v_{qs} (Schoenberg, 1983). Tangential compliance contributes a maximum speed decrease for v_{qs} at $\theta = 0$ and $\pi/2$ and no decrease at $\theta = \pi/4$. For v_{qp} , tangential compliance gives maximum decrease at $\theta = \pi/4$ and no decrease at $\theta = 0$ and $\pi/2$. Normal compliance decreases v_{qs} in exactly the same way as tangential compliance decreases v_{qp} while normal compliance decreases v_{qp} with maximum decrease at $\theta = 0$ and minimum decrease at $\theta = \pi/2$. The pure shear wave is uncoupled (in the Christoffel equations) from the other two waves. Its greatest speed decrease is at $\theta = 0$ and there is no decrease at $\theta = \pi/2$.

This is a simplified picture due to the assumptions of (1) small fracture compliance relative to the compliance of the unfractured medium, (2) isotropy for the unfractured medium, and (3) transverse isotropy for the behaviour of the fracture system. None the less, (26) indicates the qualitative effects of the presence of large aligned fractures (and, as will be seen below, also of the presence of aligned microcracks) on wave speeds in much more general circumstances.

Equations (24), and the resulting (26), can be compared with the formulation of Thomsen (1986). His three dimensionless anisotropy parameters for weak transverse isotropy, γ_{Th} , ϵ_{Th} , and δ_{Th} (the subscript Th refers to Thomsen's parameters) along with the shear and compressional wave speed along the symmetry axis of the medium are derivable from the elastic moduli. The three dimensionless parameters express, in general, the

deviation of the weakly transverse isotropy from full isotropy. For a fractured medium, the three parameters can be expressed in terms of E_T and E_N as

$$\gamma_{Th} = E_T/2, \quad \varepsilon_{Th} = 2\gamma_b(1 - \gamma_b)E_N, \quad \delta_{Th} = 2\gamma_b(E_N - E_T). \quad (27)$$

Thus, the three are not independent for a fractured medium and, until the assumption of microcrack flatness is relaxed, the anisotropy depends only on two parameters, E_T and E_N .

3.4 JOINTS AND MICROCRACKS

The anisotropy described by the changes of the moduli from an isotropic background, (24), defines a restricted class of transversely isotropic media. Hudson (1981) pointed out that 'although the geometry of joints is rather different from that of circular cracks ... under certain conditions, the results are very similar.' To see this, we shall examine results from Hudson (1981) and Thomsen (1988) to show that under simple conditions of dilute concentration of very flat microcracks (those where one of the ellipsoidal semi-axes is much smaller than the other two) in an isotropic background, we can always find joint compliances that give identical values for all the anisotropic elastic moduli. This implies that a seismic experiment giving estimates of the moduli for a Crampin model (azimuthal anisotropy due to the presence of a vertical system of aligned microcracks in an isotropic background which cause the medium to be transversely isotropic with a horizontal axis of symmetry) does not distinguish very well between various types of crack systems. Refinements in the theory of scattering due to flat microcracks will not help in inverting for the crack system's characteristic properties, such as crack size, crack density or the contents of the cracks. Only properties that systems of cracks have in common with those of systems of large vertical joints (such as orientation, excess compliance, relative tangential to normal compliance) have a chance of being determined, but in many instances these could be very informative.

Hudson (1981) gives the general form of the 6×6 change of moduli matrix for an isotropic background medium permeated with aligned flat ellipsoidal microcracks to lowest order in wavenumber times mean crack radius a . For ease of comparison we can express Hudson's matrix (denoted by subscript H) using our formulation of three 3×3 matrices, giving

$$\Delta \mathbf{N}_H = -e \begin{bmatrix} (\lambda_b + 2\mu_b)(U_{33}/\gamma_b) & 0 & 0 \\ 0 & \mu_b U_{11} & 0 \\ 0 & 0 & \mu_b U_{11} \end{bmatrix} + O(e^2),$$

$$\Delta \mathbf{P}_H = -e \lambda_b (U_{33}/\gamma_b) \begin{bmatrix} 1 & 0 & 0 \\ 1 & 0 & 0 \\ 0 & 0 & 0 \end{bmatrix} + O(e^2), \quad (28)$$

$$\Delta \mathbf{M}_H = -e \frac{\lambda_b^2}{\lambda_b + 2\mu_b} (U_{33}/\gamma_b) \begin{bmatrix} 1 & 1 & 0 \\ 1 & 1 & 0 \\ 0 & 0 & 0 \end{bmatrix} + O(e^2),$$

where e is the crack density which is equal to the crack number density (number of cracks per unit volume) times a^3 . Note that crack porosity, which is crack number density times the mean crack volume is given by $\phi_c = 4\pi e a^3 / 3$ where α is the (very small) mean aspect ratio of the flat ellipsoidal inclusions. The terms U_{11} and U_{33} appearing in (28) arise in the derivation of the scattered field from a single small crack. Essentially U_{ij} is the integral over the face of the crack of the i th component of the displacement discontinuity due to unit stress σ_{3j} imposed infinitely far from the crack in the $\pm x_3$ -directions.

Comparing (24) and (28) shows that both flat microcracks and large joints in the same isotropic background give exactly the same moduli if, assuming a dilute concentration of inclusions, we let

$$eU_{11} = \frac{E_T}{1 + E_T} \approx E_T \quad \text{for } E_T \ll 1, \quad e \frac{U_{33}}{\gamma_b} = \frac{E_N}{1 + E_N} \approx E_N \quad \text{for } E_N \ll 1. \quad (29)$$

Thomsen (1988) points out that the derivations for dilute concentrations of flat aligned microcracks are valid for e only as large as about 0.05. However, even if second-order terms in e are included (Crampin, 1984), the slip-joint model still conforms to the microcrack model except that there are additional terms proportional to e^2 on the left-hand sides of (29).

Hudson (1981) gives results for U_{11} and U_{33} for three examples which we will write in terms of E_T and E_N . Example 1 is for fluid-filled cracks under the assumptions that (a) the tangential component of the traction on the internal crack surfaces is zero (no shear stress) and (b) the crack is so thin that the normal displacement discontinuity across the crack is zero (only tangential displacement discontinuity across the crack). Then

$$E_T = \frac{16}{3(3 - 2\gamma_b)} e, \quad E_N = 0. \quad (30)$$

Example 2 is for dry cracks under the assumption of zero traction (both normal and tangential) on the internal crack surfaces. These cracks are assumed thick enough to allow non-zero normal displacement discontinuity across the crack. E_T remains the same but E_N is non-zero:

$$E_T = \frac{16}{3(3 - 2\gamma_b)} e, \quad E_N = \frac{4}{3\gamma_b(1 - \gamma_b)} e. \quad (31)$$

Example 3 is for cracks filled with a weak solid with small bulk and shear moduli again allowing non-zero normal displacement discontinuity across the crack. Now

$$E_T = \frac{16}{3[3 - 2\gamma_b + 4\mu' / (\pi\alpha\mu_b)]} e,$$

$$E_N = \frac{4}{3\gamma_b[1 - \gamma_b + (\kappa' + (4/3)\mu') / (\pi\alpha\mu_b)]} e, \quad (32)$$

where μ' and κ' are the shear and bulk moduli of the inclusion medium, respectively. Here terms of order α , $\alpha^2\mu_b/\mu'$ and $\alpha^2\mu_b/\kappa'$ have been neglected relative to $\alpha\mu_b/\mu'$ and $\alpha\mu_b/\kappa'$ (Hudson, 1981). Note that for the moduli of the weak solid to affect the values of E_T and E_N in (32), the values of μ' and κ' must go to zero as the value of the aspect ratio α goes to zero. This is analogous to the requirement for large joints that the moduli of the infilling material in the joints be proportional to h_f as h_f tends to zero. As μ' and κ' actually go to 0, the compliances of (32) go to those of (31) for dry cracks.

For κ'/μ_b and μ'/μ_b not small (of order larger than that of α as $\alpha \rightarrow 0$), E_N and $E_T \rightarrow 0$. For κ'/μ_b not small but $\mu'/\mu_b \rightarrow 0$ as for fluid-filled cracks, (32) go to (30). However, letting κ'/μ_b be small, of order α but with $\mu' = 0$, approximating cracks filled with weak fluid, gives

$$E_T = \frac{16}{3(3 - 2\gamma_b)} e,$$

$$E_N = \frac{4}{3\gamma_b[1 - \gamma_b + \kappa' / (\pi\alpha\mu_b)]} e,$$

$$= \frac{4}{3\gamma_b(1 - \gamma_b)[1 + (3 - 4\gamma_b)\kappa' / 3\gamma_b(1 - \gamma_b)\pi\alpha\kappa_b]} e, \quad (33)$$

where $\kappa_b = (3 - 4\gamma_b)\mu_b/3\gamma_b$ is the background bulk modulus. Substituting (33) into (26) and

(27) gives (3) of Thomsen (1988) for his three anisotropy parameters and resulting phase speeds.

Thomsen (1988) then presented modified results [his (4)] based on the work of Hoenig (1979). These results are similar to (33); E_T is unchanged but κ'/κ_b is replaced by $(\kappa'/\kappa_b)/(1 - (\kappa'/\kappa_b))$ in E_N . When $\kappa'/\kappa_b \alpha$ is $O(1)$, $\kappa'/\kappa_b \ll 1$, there is no difference between the two sets of results. In the stiff fluid limit, when κ'/κ_b (and hence κ'/μ_b also) is $O(1)$, E_N is $O(\alpha)$ and hence tends to zero in both (32) and (33). Thus there is no significant difference between the two sets of results.

Further results are derived by Thomsen (1988) for when the background uncracked medium has equant (non-directional) porosity ϕ_p , i.e. porosity in which the pore space has no dimension significantly larger or smaller than any other and so the pore space can be modelled by spherical pores. His results, again in terms of the dimensionless compliances, E_T and E_N , are that E_T is unchanged due to the presence of equant porosity but E_N , from ε_{Th} [derived by substituting (A34b) into (A16a) Thomsen (1988)] becomes

$$E_N = \frac{4}{3\gamma_b(1 - \gamma_b)} \frac{1 - \frac{\kappa'}{\kappa_b(1 + \phi_p/\phi_c)}}{1 + \frac{\kappa'/\kappa_b}{1 - \kappa'/\kappa_b} \left[\frac{3}{4\gamma_b} + \frac{3 - 4\gamma_b}{3\pi\alpha\gamma_b(1 - \gamma_b)} \frac{1}{1 + \phi_p/\phi_c} \right]} e. \quad (34)$$

As $\phi_p \rightarrow 0$, E_N of (34) goes to Thomsen's (1988) modified result for E_N with no equant porosity, that is, (33) with κ'/κ_b replaced by $(\kappa'/\kappa_b)/(1 - (\kappa'/\kappa_b))$. This may be seen as even when ϕ_p/ϕ_c is $O(1)$ or less, the second term within the brackets of the denominator of (34) dominates the first term due to the presence of the small α , the aspect ratio, in the denominator of that second term. When ϕ_p/ϕ_c is large (which it is in typical sedimentary rocks), so that multiplication by α gives a term of order unity, the two bracketed terms are of the same order of magnitude. Then in the weak fluid limit, $\kappa'/\kappa_b \ll 1$, the right-hand fraction of (34) tends to unity and E_N tends to the value given for it in (31). For a stiff fluid when $\kappa'/\kappa_b \rightarrow 1$, the presence of the $1 - \kappa'/\kappa_b$ term implies that E_N becomes small.

3.5 NON-FLAT ELLIPSOIDAL INCLUSIONS

For all the models discussed so far, an underlying assumption has been that the cracks are flat, i.e. that they can be modelled by ellipsoids with aspect ratio $\alpha \ll 1$. These models have all been shown to be identical in behaviour with the medium with large joints (itself an extreme case of aspect ratio $\rightarrow 0$). Nishizawa (1982) calculated the anisotropy due to small concentrations of aligned rotationally-symmetrical ellipsoidal inclusions of any aspect ratio, even including prolate spheroidal inclusions which have an aspect ratio greater

than unity. As this is an iterative method using only small increments in crack density at each step, Nishizawa claimed that the method is valid even for large concentrations of inclusions.

Following Nishizawa (1982), the effects of a given crack density e of ellipsoids are calculated in an iterative way. First the moduli for an isotropic background medium with a crack density of e/n is calculated, with n the total number of iterations. Then the moduli for this new 'anisotropic background medium' with additional crack density e/n is calculated giving the moduli for the original medium with crack density $2e/n$. This is repeated another $n - 2$ times eventually giving the moduli for the original medium with crack density e , the desired result. Results can be checked by repeating the calculation with larger values of n until no change due to increasing n occurs. The resulting medium is transversely isotropic and we denote the changes in the elastic moduli due to Nishizawa's procedure by $\Delta c_{ij}^N \equiv c_{ij}^N - c_{ij,b}$. To see how well these moduli, and thus the Nishizawa model, can be approximated by the model of large joints in an isotropic background, we construct D^2 , defined to be one-fifth of the sum of the squares of the differences between the dimensionless moduli changes (over the five independent elastic moduli) from the Nishizawa procedure, $\Delta c_{ij}^N/c_{ij,b}$, $ij = 11, 33, 13, 44, 66$ and the dimensionless moduli changes from the joint model, $\Delta c_{ij}^J/c_{ij,b}$, $ij = 11, 33, 13, 44, 66$, from (24). The root mean square of the differences of the five elastic moduli D satisfies

$$5D^2 = \left[\frac{\Delta c_{11}^N}{\lambda_b + 2\mu_b} + \frac{\lambda_b^2}{(\lambda_b + 2\mu_b)^2} \frac{E_N}{(1 + E_N)} \right]^2 + \left[\frac{\Delta c_{33}^N}{\lambda_b + 2\mu_b} + \frac{E_N}{1 + E_N} \right]^2 + \left[\frac{\Delta c_{13}^N}{\lambda_b} + \frac{E_N}{1 + E_N} \right]^2 + \left[\frac{\Delta c_{44}^N}{\mu_b} + \frac{E_T}{1 + E_T} \right]^2 + \left[\frac{\Delta c_{66}^N}{\mu_b} \right]^2. \quad (35)$$

The values of E_T and E_N that minimize D^2 , in terms of the Nishizawa moduli $c_{ij}^N = c_{ij,b} + \Delta c_{ij}^N$, are given by

$$E_T = \frac{\mu_b}{c_{44}^N} - 1, \quad E_N = \frac{\lambda_b^4/(\lambda_b + 2\mu_b)^4 + 2}{\frac{\lambda_b^2}{(\lambda_b + 2\mu_b)^2} \left[\frac{c_{11}^N}{(\lambda_b + 2\mu_b)} - 1 + \frac{\lambda_b^2}{(\lambda_b + 2\mu_b)^2} \right] + \frac{c_{33}^N}{(\lambda_b + 2\mu_b)} + \frac{c_{13}^N}{\lambda_b}} - 1. \quad (36)$$

These values of E_T and E_N give the elastic moduli of the joint model that best fit those of the Nishizawa's ellipsoids model in a least-squares sense. Also note that these values of E_T and E_N are independent of c_{66}^N so that the last term of (35) gives a minimum value to D^2

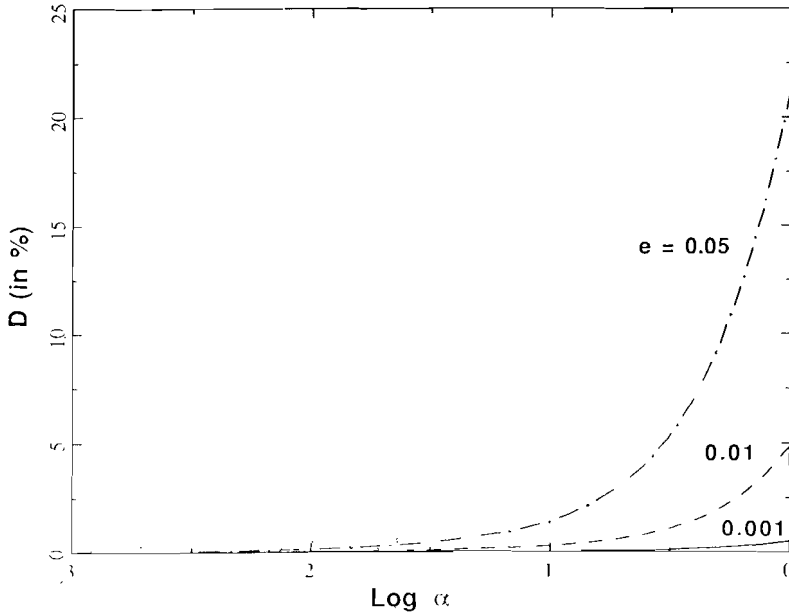


Fig. 3.2. The root mean square normalized difference D (in %) between the five elastic moduli computed according to Nishizawa (1982) and those five moduli computed from values of E_N and E_T which minimize D as functions of aspect ratio α holding e (the crack number density \times the mean crack radius cubed) constant. The curve (—) is for $e = 0.001$, (---) for $e = 0.01$ and (-.-.-) for $e = 0.05$. The background medium has a Poisson's ratio of $1/4$ and the ellipsoids are filled with gas assumed to have vanishing shear modulus and a bulk modulus equal to $0.0128 \times$ the shear modulus of the background medium.

below which no combination of E_T and E_N can cause the value of D^2 to fall. However, as the aspect ratio $\alpha \rightarrow 0$ for any small value of e , Δc_{66}^N and D approach zero. This becomes clear when we calculate the c_{ij}^N over a wide range of aspect ratios (from 10^{-3} to 1) for gas-filled ellipsoidal inclusions. In a homogeneous isotropic background, with $\gamma_b = 1/3$ (Poisson's ratio = $1/4$), the gas is assumed to have a vanishing shear modulus and a bulk modulus equal to $0.0128 \times \mu_b$. For this model, Fig. 3.2 shows D as a function of α while e is held constant at three values, 0.001, 0.01, and 0.05. D is very small for small values of α and only exceeds 0.05 (which we consider the point where meaningful difference between the joint model and the ellipsoidal model begins) for $e = 0.05$ when $\alpha > 0.316$ for which crack porosity $\phi_c > 0.066$. The same calculations have been carried out for empty (dry) inclusions and for liquid-filled inclusions (vanishing shear modulus and bulk modulus equal to $0.0385 \times \mu_b$) giving almost the same results for D . The values of D become smaller with the shrinking of the acoustic contrast between the background medium and the material filling the inclusions. The high contrast between the background and the inclusion medium shown here may be thought of as a worst case for matching with the jointed model.

Figure 3.3 shows D as a function of α for the same gas-filled inclusions while crack

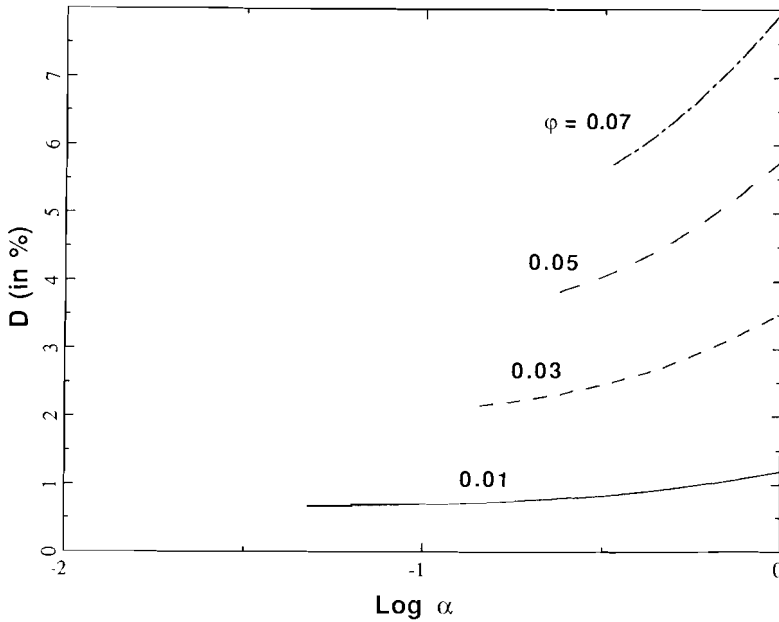


Fig 3.3. As for Fig. 3.2 except here D is shown as a function of aspect ratio α holding crack porosity ϕ_c constant. The curve (—) is for $\phi_c = 0.01$, (·····) for $\phi_c = 0.03$, (---) for $\phi_c = 0.05$, and (-·-·-) for $\phi_c = 0.07$.

porosity ϕ_c is held constant for four values of porosity, $\phi_c = 0.01, 0.03, 0.05$, and 0.07 . To avoid values of e larger than 0.05 , an approximate upper limit for single scattering theory, each curve starts at the aspect ratio corresponding to $e = 0.05$, i.e. at $\alpha_{\text{start}} = 3\phi_c / (4\pi \times 0.05)$. Each curve continues to larger aspect ratios for which the values of e necessary to maintain constant porosity shrink accordingly. D increases with increasing aspect ratio whether crack density is held constant or whether porosity is held constant. For these gas-filled inclusions, a porosity of at least 0.05 is required for D to exceed 5% and that occurs for $\phi_c = 0.05$ at aspect ratio $\alpha = 0.44$ (see Fig. 3.3).

3.6 DISCUSSION AND CONCLUSIONS

The behaviour of parallel linear-slip interfaces has been used to model the long wavelength propagation characteristics of a medium with a set of large parallel joints or fractures much larger than the largest wavelength but spaced much closer than the smallest wavelength. This model gives geometrical insight into the mechanical properties of such a fractured medium by letting us visualize the action of planes of weakness in a solid. In addition, we have shown that the linear-slip interface model exactly describes the behaviour of systems of aligned flat microcracks according to Hudson (1981). However, as

the aspect ratio of the microcracks grows, i.e. the microcracks become less flat, the results of Nishizawa's iterative method to compute moduli for a solid with aligned ellipsoidal inclusions deviate increasingly from the linear-slip interface model. But this linear-slip interface model is a good approximation even for aspect ratios as large as 0.3 when $e = 0.05$ (which is about as large a value of e as one can assume and still hope that single scattering theory is valid).

All possible types of fracture system anisotropy: triclinic, monoclinic, orthorhombic or transversely isotropic, and all anisotropic elastic backgrounds are included in the model. To compute the elastic moduli of the equivalent medium, once the fracture system compliance matrix is given, requires at most the inversion of two 3×3 matrices.

Azimuthal anisotropy has been assumed to be caused by aligned sets of vertical fractures and microcracks. It has been shown that large joints are indistinguishable from dilute systems of flat microcracks. Assuming rotationally isotropic fractures (which is suspect, but perhaps a good first approximation) means that azimuthal anisotropy may be characterized by three scalar quantities, the orientation of the normal to the system and the two compliances, Z_T and Z_N . A good approximation to a vertically cracked earth, for which conventional transverse isotropy is often an order of magnitude larger than the azimuthal anisotropy, might be a transversely isotropic (with a vertical symmetry axis) background with a rotationally isotropic vertical fracture system. Such a model allows for the additional compliance due to the presence of fractures or cracks in a physically meaningful way even when the underlying fracture mechanism is not fully understood. The values of Z_T and Z_N , dimensionless with respect to the appropriate background modulus, quantify in the simplest way the azimuthal anisotropy. In many situations it has been shown that the normal compliance can be very small. Assuming that Z_N vanishes leaves only one parameter quantifying azimuthal anisotropy but this is a key parameter as it still allows for shear-wave splitting for shear waves propagating parallel to the fractures.

ACKNOWLEDGEMENT

We thank Schlumberger-Doll Research for their hospitality to one of the authors (J.D) during the autumn of 1986.

3.7 REFERENCES

- Backus, G.E. 1962. Long-wave anisotropy produced by horizontal layering. *Journal of Geophysical Research* 66, 4427-4440.
- Crampin, S. 1984. Effective anisotropic elastic constants for wave propagation through cracked solids. *Geophysical Journal of the Royal Astronomical Society* 76, 135-145.
- Crampin, S. 1985. Evidence for aligned cracks in the Earth's crust. *First Break* 3, (3), 12-15.

- Crampin, S. and Atkinson, B.K. 1985. Microcracks in the Earth's crust. *First Break* 3, (3), 16-20.
- Crampin, S. and Bush, I. 1986. Shear waves revealed, extensive-dilatancy anisotropy confirmed. 56th S.E.G. meeting, Houston, Expanded Abstracts, 481-484.
- Helbig, K. and Schoenberg, M. 1987. Anomalous polarization of elastic waves in transversely isotropic media. *Journal of the Acoustical Society of America* 81, 1235-1245.
- Hoening, A. 1979. Elastic moduli of a non-randomly cracked body. *International Journal of Solids and Structures* 15, 137-154.
- Hudson, J.A. 1981. Wave speeds and attenuation of elastic waves in material containing cracks. *Geophysical Journal of the Royal Astronomical Society* 64, 133-150.
- Morland, L.W. 1974. Elastic response of regularly jointed media. *Geophysical Journal of the Royal Astronomical Society* 37, 435-446.
- Musgrave, M.J.P. 1970. *Crystal Acoustics*, 84-86. Holden-Day, San Francisco.
- Nishizawa, O. 1982. Seismic velocity anisotropy in a medium containing oriented cracks-transversely isotropic case. *Journal of Physics of the Earth* 30, 331-347.
- Schoenberg, M. 1980. Elastic wave behavior across linear slip interfaces. *Journal of the Acoustical Society of America* 68, 1516-1521.
- Schoenberg, M. 1983. Reflection of elastic waves from periodically stratified media with interfacial slip. *Geophysical Prospecting* 31, 265-292.
- Schoenberg, M. and Muir, F. 1988. Group theoretic methods for finely layered media. *Submitted to Geophysics*.
- Thomsen, L. 1986. Weak elastic anisotropy. *Geophysics* 51, 1954-1966.
- Thomsen, L. 1988. Elastic anisotropy due to aligned cracks. *Submitted to Geophysical Journal of the Royal Astronomical Society*.
- Willis, H.A., Rethford, G.L. and Bielanski, E. 1986. Azimuthal anisotropy, occurrence and effect on shear-wave data quality. 56th S.E.G. meeting, Houston, Expanded Abstracts, 479-481.

*Chapter 4***THE REPRESENTABILITY OF CRACKED MEDIA
BY PERIODICALLY LAYERED MEDIA****ABSTRACT**

Media containing aligned cracks or ellipsoidal inclusions as well as media consisting of sequences of isotropic layers show transverse isotropy with respect to elastic wave propagation. However, the transversely isotropic media which are equivalent to media containing aligned inclusions do not necessarily have to be representable by sequences of stable isotropic layers. These transversely isotropic media can only be modelled by such sequences if several stability conditions are satisfied. Important parameters determining whether these conditions are satisfied are the aspect ratio of the inclusions and the material filling the inclusions, the 'fluid'. An analytical expression describing the range of aspect ratios for which the constraints are satisfied can be derived. This expression (which is a good approximation for several crack models) and numerical calculations show that media containing water-filled inclusions can be represented by sequences of stable isotropic layers if the inclusions have aspect ratios less than 0.1. The limiting aspect ratio decreases for a decreasing ratio of the bulk modulus of the fluid to the shear modulus of the matrix material. Finally, media containing dry inclusions of any aspect ratio can not be modelled by thin isotropic layering. These results depend only weakly on the crack density and on the matrix material. The representation of crack-induced anisotropy by layer-induced

This chapter has been submitted for publication as:

Douma, J. 1988. The representability of cracked media by periodically layered media. Submitted to *Geophysical Prospecting*.

anisotropy might be useful in the separation of the cause of anisotropy and the determination of the nature of the fluid.

4.1 INTRODUCTION

Periodically layered media and media containing aligned cracks are transversely isotropic with respect to elastic wave propagation if the seismic wavelength is large compared to the thickness of the layers or the size of the cracks, respectively. A transversely isotropic medium is a special type of anisotropic medium: whereas the most general type of anisotropic medium is described by 21 independent elastic constants, a transversely isotropic medium (because of its rotational symmetry) is described by at most five independent elastic constants. Seismic waves travelling through a transversely isotropic medium have velocities and polarizations which depend on the angle of incidence against the axis of rotational symmetry. Moreover, just as in any anisotropic medium, shear waves on entering a transversely isotropic medium generally split up into two shear waves with different velocities. Wave propagation in anisotropic media can be modelled if the elastic constants of the media are known.

To calculate the elastic constants of periodically layered media several formulations (all based on the long wavelength approximation, i.e. using a quasi-static elastic approach) have been presented (Bruggeman, 1937; Postma, 1955; Helbig, 1958; and Backus, 1962). With any of these formulations the elastic constants of the equivalent transversely isotropic media are expressed in terms of the elastic constants of the isotropic constituent layers. With the same purpose, but then valid for any anisotropic constituent layer, a matrix formulation was presented, recently (Helbig and Schoenberg, 1987; Schoenberg and Douma, 1988).

To calculate the elastic constants of media containing aligned circular cracks several models, most of them based on different assumptions, have been derived from various points of view. A model based on the scattering of elastic waves by the cracks is Hudson's (1980, 1981) crack model. This model has often been used by Crampin and co-authors (e.g. Crampin, 1984; Crampin, McGonigle and Ando, 1986). Apart from the long wavelength assumption (i.e. the size of the cracks is small compared to the seismic wavelength) it is also assumed that both the density and the aspect ratio α of the cracks is small. Another model (based on a static approach) presented by Nishizawa (1982), however, is valid even for large aspect ratios. Rotationally symmetrical ellipsoidal inclusions with aspect ratios up to $\alpha = 1$ (spherical inclusions) can be studied. The elastic constants are derived by numerical calculations in contrast with Hudson's (1980, 1981) model which gives analytical expressions for the elastic constants. A comparison of the results of Nishizawa's and Hudson's model was carried out (and a review of both models was given) recently by Douma (1988). Douma (1988) showed that Hudson's and Nishizawa's model are almost identical for aspect ratios up to 0.3.

It should be realized that the validity of these models (i.e. whether they describe the real situation of cracked media) only becomes known when the model results can be compared with experimental results. For cracked media with all kind of inclusions such experimental results, however, do not exist yet and therefore the validity of each model is still unknown. What is known are the situations for which the models give identical results and the basic assumptions of each model. This information might only indicate the situations for which the models could be expected to describe real cracked media. Therefore, it is assumed here that Nishizawa's model which does not assume a small aspect ratio is more likely to describe the real situation of aligned inclusions with large aspect ratios than Hudson's model (based on a small aspect ratio).

In this paper crack-induced anisotropy as described by both Hudson's and Nishizawa's model is compared with the anisotropy caused by sequences of thin isotropic layers. Assuming the aligned cracks and the layers have the same axis of rotational symmetry it is investigated whether the resultant crack-induced anisotropy could also be caused by sequences of isotropic layers. As shown by Backus (1962) there are transversely isotropic media that can not be modelled by such sequences. In a paper on a systematic classification of layer-induced anisotropy Helbig (1981) described the conditions a transversely isotropic medium has to satisfy in order to be the equivalent of a sequence of stable isotropic layers. These conditions are used in this paper to study the representability of cracked media by layer sequences. In the following a transversely isotropic medium will be called a RSSIL-medium if it is Representable by Sequences of Stable Isotropic Layers. The range of aspect ratios of the cracks for which the resultant transversely isotropic medium is a RSSIL-medium is studied both analytically (using Hudson's formulations) and numerically (using Nishizawa's formulations). Such a study complements an earlier study carried out by Schoenberg and Douma (1988) that showed the resemblance between crack-induced anisotropy and the anisotropy due to large fractures (constructed from a periodically layered medium). In that particular study the fracture material could be any transversely isotropic medium, whereas in this study only RSSIL-media are studied.

The representability of cracked media by RSSIL-media might have some interesting applications. If there are cracked media which are not RSSIL-media one might be able to distinguish between aligned cracks and sequences of isotropic layers as possible causes of observed anisotropy. Moreover, this representability might be used to classify crack-induced anisotropy.

4.2 STABILITY CONSTRAINTS OF A TRANSVERSELY ISOTROPIC MEDIUM

A transversely isotropic medium with an axis of rotational symmetry in the x_3 -direction is described by an elastic tensor c_{ijkl} which, using the condensed two-suffix notation c_{pq} (see, e.g. Schoenberg and Douma, 1988), is given by

$$c_{pq} = \begin{bmatrix} c_{11} & c_{12} & c_{13} & 0 & 0 & 0 \\ c_{12} & c_{11} & c_{13} & 0 & 0 & 0 \\ c_{13} & c_{13} & c_{33} & 0 & 0 & 0 \\ 0 & 0 & 0 & c_{44} & 0 & 0 \\ 0 & 0 & 0 & 0 & c_{44} & 0 \\ 0 & 0 & 0 & 0 & 0 & c_{66} \end{bmatrix}, \quad (1)$$

where $c_{12} = c_{11} - 2c_{66}$. Eq. (1) shows that a transversely isotropic medium is described by at most five independent elastic constants. For an isotropic medium (a special type of transversely isotropic medium described by only two independent elastic constants) $c_{11} = c_{33} = \lambda + 2\mu$, $c_{12} = c_{13} = \lambda$, and $c_{44} = c_{66} = \mu$, where λ and μ are called the Lamé parameters. The transversely isotropic medium is a stable medium (i.e. no deformation has non-negative internal energy) if the matrix presented in (1) is positive semidefinite. As shown, e.g. by Backus (1962), this is true if

$$c_{44} \geq 0, \quad c_{66} \geq 0, \quad c_{33} \geq 0, \quad c_{11} - c_{66} \geq 0, \quad \text{and} \quad c_{33}(c_{11} - c_{66}) \geq c_{13}^2. \quad (2)$$

There are some further inequalities which, being consequences of (2), can be omitted. For an isotropic medium (2) becomes

$$\mu \geq 0, \quad \text{and} \quad \lambda \geq -\frac{2}{3}\mu, \quad (3a)$$

or equivalently

$$\mu \geq 0, \quad \text{and} \quad 0 \leq \gamma \leq \frac{3}{4}, \quad (3b)$$

where $\gamma = \mu/(\lambda + 2\mu)$ is the ratio of the square of the shear wave velocity to the compressional wave velocity. If only media for which a deformation has positive internal energy are considered, the 'weak stability conditions' of (3b) become

$$\mu > 0, \quad \text{and} \quad 0 < \gamma < \frac{3}{4}. \quad (3c)$$

Throughout this paper an isotropic medium is called stable if the 'strong stability conditions' of (3c) are satisfied. In the next section the stability constraints of a (RSSIL-)

medium that can be represented by sequences of stable isotropic layers are given.

4.3 STABILITY CONSTRAINTS OF PERIODICALLY LAYERED MEDIA

Consider a periodically layered medium. The five independent elastic constants of the (in the long wavelength approximation) equivalent transversely isotropic medium can be expressed as thickness-weighted averages of the elastic constants of the constituent layers. Using the formulae presented by Schoenberg and Douma (1988) (whose results are identical to Backus' (1962) results) we have

$$c_{33} = \frac{1}{\langle 1/c_{33} \rangle}, \quad c_{44} = \frac{1}{\langle 1/c_{44} \rangle}, \quad c_{13} = \frac{\langle c_{13}/c_{33} \rangle}{\langle 1/c_{33} \rangle},$$

$$c_{66} = \langle c_{66} \rangle, \quad c_{11} = \langle c_{11} \rangle - \langle c_{13}^2/c_{33} \rangle + \frac{\langle c_{13}/c_{33} \rangle^2}{\langle 1/c_{33} \rangle}, \quad (4)$$

where the symbol $\langle \rangle$ denotes thickness-weighted averaging. If only stable isotropic constituent layers are assumed Backus (1962) showed that the resultant transversely isotropic media (i.e. RSSIL-media) are a subset of all possible stable transversely isotropic media. Deriving the stability constraints for these RSSIL-media Helbig (1981) introduced two sets of dimensionless parameters, i.e.

a) ρ , σ , τ , and l defined as

$$\rho = \frac{c_{44}}{c_{33}}, \quad \sigma = \frac{1}{4} \left[\frac{c_{13}^2}{c_{33}c_{66}} - \frac{c_{11}}{c_{66}} \right] + 1, \quad \tau = \frac{1}{2} \left[1 - \frac{c_{13}}{c_{33}} \right], \quad l = \frac{c_{44}}{c_{66}}, \quad (5a)$$

and

$$b) \quad h (= \rho - \tau), \quad k (= \sigma - \tau), \quad \tau, \quad \text{and} \quad l. \quad (5b)$$

Note that Helbig (1981) used the symbol λ for l . In this paper, however, the symbol λ denotes already one of the Lamé parameters and therefore the symbol l is introduced. Backus (1962) proved that transversely isotropic media can only be modelled by sequences

of stable isotropic layers with different shear moduli if the following stability constraints (Helbig's (1981) notation is used) are satisfied

$$0 < \tau < \frac{3}{4}, \quad 0 < k + \tau < \frac{3}{4}, \quad 0 < h + \tau < \frac{3}{4}, \quad 0 < l < 1,$$

$$l\tau^2 < (h + \tau)(k + \tau), \quad l \left[\frac{3}{4} - \tau \right]^2 < \left[\frac{3}{4} - (h + \tau) \right] \left[\frac{3}{4} - (k + \tau) \right]. \quad (6)$$

Using Eq. (5b) (6) can easily be transformed into the stability constraints for ρ , σ , τ , and l .

Transversely isotropic media which satisfy the constraints of (6) are called RSSIL-media throughout this paper. Note that with this definition of RSSIL-media, RSSIL-media do not include isotropic media: Backus (1962) proved that a periodically layered medium is an isotropic medium if the following constraints are satisfied

$$l = 1, \quad l\tau^2 = (h + \tau)(k + \tau), \quad \text{and} \quad l \left[\frac{3}{4} - \tau \right]^2 = \left[\frac{3}{4} - (h + \tau) \right] \left[\frac{3}{4} - (k + \tau) \right].$$

These conditions are always satisfied (Backus, 1962) if the constituent layers have identical shear moduli.

It should be noted that the definition of RSSIL-media which requires constituent layers with different shear moduli does not exclude the situation in which some constituent layers have identical shear moduli. As shown by Backus (1962) these particular constituents can be combined to form one equivalent isotropic layer. Having combined these layers the resultant periodically layered medium can be regarded again as a medium consisting of isotropic layers with different shear moduli.

The inequalities of (6) are most easily interpreted by regarding the corresponding equalities as the equations of (hyper) surfaces separating the four-dimensional h, k, τ, l parameter space into a region (the constraint area) where the inequalities of (6) are satisfied and into a region where they are not satisfied. Each transversely isotropic medium can be represented in this four-dimensional parameter space by a point whose coordinates are given by the h, k, τ, l parameters of the medium. If and only if this point lies inside the constraint area the medium is a RSSIL-medium.

The four-dimensional constraint area can be visualized by keeping one of the four h, k, τ, l 'coordinates' constant. With l fixed at $l = 4/9$ Helbig (1981) showed the three-dimensional intersection of the four-dimensional constraint area with the hyperplane $l = 4/9$. This result is shown in Fig. 4.1. The intersection is a finite body limited by the planes $\tau = 0$ and $\tau = 3/4$, and by 'sheared' parabolic hyperboloids.

Media that are represented in the four-dimensional constraint area by points lying on

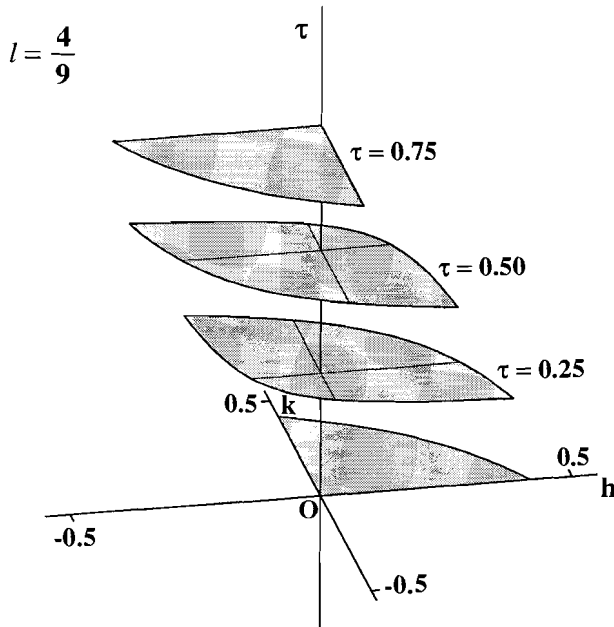


Fig. 4.1. The three-dimensional intersection of the 'stability area' (described by Eq. (6)) with the hyperplane $l = 4/9$. Shown are the two-dimensional intersections of the three-dimensional body with the planes $\tau = 0, 0.25, 0.50,$ and 0.75 , respectively.

the τ -axis ($h = k = 0$) are known as K-media (Krey and Helbig, 1956). A RSSIL-medium is a K-medium if and only if the constituent layers all have the same γ (squared ratio of shear-to compressional wave velocity). The velocity of qP-(quasi-longitudinal) waves travelling through such K-media at moderate angles against the symmetry axis is independent of the direction of wave propagation. Therefore, K-media, assumed to be a very reasonable representation of sedimentary basins, were regarded to be isotropic in standard reflection seismics. Finally, it should be mentioned that for isotropic media (a subset of K-media) $h = k = 0$ and $l = 1$ (Helbig, 1981).

In the next section it is investigated whether cracked media result in transversely isotropic media that can be represented by h, k, τ, l points lying inside the constraint area.

4.4 THE REPRESENTABILITY OF CRACKED MEDIA BY RSSIL-MEDIA

To study the transverse isotropy shown by media containing aligned inclusions several models have been derived. In this section it is investigated whether the resultant transversely isotropic medium as described by some of these models can be represented by sequences of stable isotropic layers.

a) *Hudson's model*

Considering media containing a dilute distribution of aligned cracks Hudson (1980, 1981) presented analytical expressions (based on the scattering of elastic waves by the cracks) to calculate the effective elastic constants of the resultant transversely isotropic medium (these results were discussed in detail by Crampin, 1984). In the derivation of these formulae several assumptions were made: both the crack density $e = Na^3/V$ (where N is the number of cracks of radius a in a volume V) and the aspect ratio α of the cracks (the aspect ratio of rotationally symmetrical ellipsoidal inclusions with semi-axes having lengths a, a, b is defined as $\alpha = b/a$) should be small ($\ll 1$). Moreover, to result in elastic anisotropy the size of the cracks is assumed to be very small compared to the seismic wavelength. The resultant elastic constants c_{ij}^H (the superscript H denotes Hudson's model) of the cracked medium are given as:

$$c_{ij}^H = c_{ij}^{(0)} + c_{ij}^{(1)} + c_{ij}^{(2)}, \quad (7)$$

where $c_{ij}^{(1)}$ and $c_{ij}^{(2)}$ are first- and second-order (in crack density e) perturbations of the elastic constants $c_{ij}^{(0)}$ of the uncracked (isotropic background) medium due to the presence of the cracks (these perturbations are given in terms of the crack parameters by Crampin, 1984). In the calculation of the second-order perturbations crack-crack interactions are accounted for in the scattering of the elastic waves, as opposed to the calculation of the first-order perturbations in which mutual interactions of the cracks are neglected.

To determine whether Hudson's model results in transversely isotropic media that can be represented by sequences of isotropic layers it is investigated whether Hudson's elastic constants c_{ij}^H satisfy the stability constraints described in (6). In this paper this problem is not approached directly by writing out (6) using Hudson's expressions for c_{ij}^H , but by considering the results obtained by Schoenberg and Douma (1988). In a study on the elastic wave propagation in media containing parallel fractures and aligned cracks they showed that Hudson's model (both first- and second-order perturbations) is identical to their model of slip interfaces in an isotropic background medium. This model of parallel slip interfaces simulates the behaviour of a fracture system composed of large closely spaced aligned joints. It has been derived from the model of periodically layered media by letting the thickness and the elastic constants of the constituent thin layers go simultaneously to zero (Schoenberg, 1980, 1983). This means that media containing slip interfaces are a special type of periodically layered media. Therefore, using the identity of Hudson's (1980, 1981) crack model and Schoenberg and Douma's (1988) slip interface model we may conclude that cracked media described by Hudson's model can only be represented by RSSIL-media if the equivalent medium containing slip interfaces is such a medium.

As described by Schoenberg and Douma (1988) the five elastic constants of the transversely isotropic medium which is the long wavelength equivalent of an isotropic medium containing large parallel fractures (filled with a transversely isotropic medium

which has an axis of rotational symmetry perpendicular to the fractures) are given by

$$c_{33}^S = \frac{\lambda_b + 2\mu_b}{1 + E_N}, \quad c_{44}^S = \frac{\mu_b}{1 + E_T}, \quad c_{13}^S = \frac{\lambda_b}{1 + E_N}, \quad c_{66}^S = \mu_b,$$

$$c_{11}^S = \lambda_b + 2\mu_b - \frac{\lambda_b^2}{\lambda_b + 2\mu_b} \left[1 - \frac{1}{1 + E_N} \right], \quad (8)$$

where E_N and E_T are dimensionless compliances (normal and tangential to the fracture system, respectively) that give the fracture system's compliance relative to the background compliances, λ_b and μ_b are the Lamé parameters of the background medium, and the superscript S denotes the slip interface model. Note that only four of the five elastic constants in (8) are independent. E_N and E_T can be expressed in terms of the elastic constants of the isotropic background medium and the transversely isotropic medium inside the fractures (denoted by $c_{ij,f}$), and the fraction f_f of the fracture within one period of layers:

$$E_N = \frac{(\lambda_b + 2\mu_b)f_f}{c_{33,f}} \quad \text{and} \quad E_T = \frac{\mu_b f_f}{c_{44,f}}. \quad (9)$$

Eq. (9) shows that for $f_f = 0$ (i.e. the isotropic situation), $E_N = E_T = 0$. We now assume $f_f \neq 0$. If both the background medium and the medium inside the fractures are stable (3c) requires that both E_N and E_T are positive. If the fracture medium is also a RSSIL-medium, the condition $0 < c_{44,f}/c_{33,f} < 3/4$ (i.e. $0 < h + \tau < 3/4$, Eq. (6)) puts another constraint on E_N and E_T : $0 < \gamma_b E_N/E_T < 3/4$. (In appendix A the same conditions on E_N and E_T are obtained if the values of E_N and E_T are investigated for which the elastic constants c_{ij}^S (see (8)) satisfy all the stability constraints (6) of a RSSIL-medium). Combining these constraints we may conclude that a cracked medium as described by Hudson's model is a RSSIL-medium if the dimensionless compliances E_N and E_T of the equivalent medium containing slip interfaces satisfy

$$E_T > \frac{4}{3} E_N \gamma_b > 0. \quad (10)$$

Using Schoenberg and Douma's (1988) Eq. (24) and Crampin's (1984) Eqs (2) and (3) (but now with the crack normal in the x_3 -direction) E_N and E_T can be expressed in terms of the parameters of Hudson's first- and second-order model.

Hudson's first-order model:

$$\frac{E_N}{1 + E_N} = \frac{eU_{33}}{\gamma_b}, \quad \frac{E_T}{1 + E_T} = eU_{11}, \quad (11a)$$

Hudson's second-order model:

$$\frac{E_N}{1 + E_N} = \frac{eU_{33}}{\gamma_b} - \frac{e^2U_{33}^2q}{15}, \quad \frac{E_T}{1 + E_T} = eU_{11} - \frac{e^2U_{11}^2X}{15\mu_b}, \quad (11b)$$

where $q = 15(\lambda_b/\mu_b)^2 + 28(\lambda_b/\mu_b) + 28$, $X = 2\mu_b(3\lambda_b + 8\mu_b)/(\lambda_b + 2\mu_b)$, and e is the crack density. If the inclusions are filled with a weak isotropic material

$$U_{11} = \frac{16}{3}[(\lambda_b + 2\mu_b)/(3\lambda_b + 4\mu_b)]/(1 + M),$$

$$U_{33} = \frac{4}{3}[(\lambda_b + 2\mu_b)/(\lambda_b + \mu_b)]/(1 + K), \quad (12)$$

where

$$M = [4\mu' / (\pi\alpha\mu_b)] [(\lambda_b + 2\mu_b) / (3\lambda_b + 4\mu_b)],$$

$$K = [\kappa' + (4/3)\mu' / (\pi\alpha\mu_b)] [(\lambda_b + 2\mu_b) / (\lambda_b + \mu_b)],$$

α is the aspect ratio of the cracks and μ' and κ' are the shear and bulk moduli of the medium inside the cracks, respectively. With Eqs (10)-(12) it is possible given the set of elastic constants of the background medium, the medium inside the inclusions, and the crack density e to calculate analytically the range of aspect ratios α of the inclusions for which the resultant transversely isotropic medium is a RSSIL-medium.

In this paper such an analytical calculation is only performed for Hudson's first-order model (11a). For Hudson's second-order model the calculations are carried out numerically. If Hudson's first-order model is considered we get from (11a)

$$E_N = \frac{eU_{33}\gamma_b}{1 - eU_{33}\gamma_b}, \quad E_T = \frac{eU_{11}}{1 - eU_{11}}. \quad (13)$$

In order to satisfy the constraints (10) of a RSSIL-medium E_N and E_T certainly have to be

positive. This implies

$$0 < eU_{33}/\gamma_b < 1 \quad , \quad 0 < eU_{11} < 1 . \quad (14)$$

Rewriting U_{11} and U_{33} (given by (12)) as

$$U_{11} = \frac{16}{3[3 - 2\gamma_b + 4\mu' / (\pi\alpha\mu_b)]} \quad , \quad (15a)$$

$$U_{33} = \frac{4}{3[1 - \gamma_b + (\kappa' + (4/3)\mu') / (\pi\alpha\mu_b)]} \quad , \quad (15b)$$

it is easily seen with $e > 0$, $\alpha > 0$ and the stability constraints (3c) for isotropic media that both eU_{11} and eU_{33}/γ_b are positive. To satisfy the second inequality of each part of (14) both terms also have to be smaller than unity. We assume throughout this paper that $\mu_b \neq 0$ (and therefore $\gamma_b \neq 0$). With crack densities smaller than 0.05 (for larger values Hudson's model, based on dilute concentrations of inclusions, certainly becomes questionable (Thomsen, 1988)) it can easily be concluded from (15) that $eU_{11} < 1$. In order to have $eU_{33}/\gamma_b < 1$ the aspect ratio should satisfy

$$\alpha < \frac{3\gamma_b[\kappa' + (4/3)\mu']}{(4e - 3\gamma_b + 3\gamma_b^2)\pi\mu_b} \quad \text{if } (4e - 3\gamma_b + 3\gamma_b^2) > 0 \quad (16a)$$

or

$$\alpha > \frac{3\gamma_b[\kappa' + (4/3)\mu']}{(4e - 3\gamma_b + 3\gamma_b^2)\pi\mu_b} \quad \text{if } (4e - 3\gamma_b + 3\gamma_b^2) < 0 . \quad (16b)$$

(If $(4e - 3\gamma_b + 3\gamma_b^2) = 0$ the term eU_{33}/γ_b is always smaller than unity for $(\kappa' + (4/3)\mu') > 0$, i.e. for non-dry inclusions). Since α is always non-negative the last constraint (16b) is always satisfied. The other constraint on E_N and E_T in order to satisfy (10) is $E_T > 4\gamma_b E_N/3$. Using (13) and (15) it can be shown that this is satisfied for

$$\frac{4\gamma_b}{3} \left[12e \left[3 - 2\gamma_b + \frac{4\mu'}{\pi\alpha\mu_b} \right] - 64e^2 \right] < \left[48\gamma_b e \left[1 - \gamma_b + \frac{\kappa' + (4/3)\mu'}{\pi\alpha\mu_b} \right] - 64e^2 \right] \quad (17)$$

which becomes (for $e \neq 0$ and $\kappa' \neq 0$)

$$\alpha < \alpha_1 \quad (18)$$

where

$$\alpha_1 = \frac{9\gamma_b \kappa'}{(3\gamma_b^2 - 16e\gamma_b + 12e)\pi\mu_b}.$$

If $\kappa' = 0$, i.e. the inclusions are dry, there is no aspect ratio for which (17) is satisfied. As shown in appendix B the constraint (18) is more restrictive than (16a) and therefore we may conclude that a cracked medium as described by Hudson's first-order model is only a RSSIL-medium if the aspect ratio of the cracks satisfies (18). Eq. (18) shows that the range of aspect ratios for which it is satisfied decreases for decreasing κ'/μ_b and disappears for $\kappa'/\mu_b = 0$, i.e. for dry inclusions. These results show that the representability of cracked media by RSSIL-media might be used to describe the content of the inclusions.

b) Nishizawa's model

Nishizawa (1982) described a numerical model to calculate the elastic constants of a transversely isotropic medium which is the long wavelength equivalent of a medium containing aligned ellipsoidal inclusions. Unlike Hudson's model Nishizawa's model does not assume a small aspect ratio of the inclusions. The aspect ratios α in his model range from $\alpha = 0$ (representing flat cracks) up to $\alpha = 1$ (spherical inclusions). (In principal they can be extended up to $\alpha = \infty$, representing cylindrical inclusions). Nishizawa's (1982) model has been compared with Hudson's crack model by Douma (1988). The comparison showed that these models are almost identical for aspect ratios up to $\alpha = 0.3$. At larger aspect ratios the models deviate. Therefore, in order to determine the aspect ratios for which cracked media as described by Nishizawa's model are RSSIL-media we can not use the constraints as described in (10) (although such a procedure would be valid for α up to 0.3) but have to use the basic constraints as described in (6). It will be calculated numerically whether Nishizawa's results satisfy these constraints.

4.5 CRACKED MEDIA REPRESENTED IN THE h, k, τ, l PARAMETER SPACE

As mentioned before Hudson's (1980, 1981) crack model is identical to Schoenberg and Douma's (1988) slip interface model. Therefore, the dimensionless parameters h, k, τ , and l (and ρ and σ) of Hudson's model are identical to those derived for the slip interface model (see appendix C). So, we have for Hudson's crack model (see (C1)-(C6))

$$l = \frac{1}{1 + E_T}, \quad \tau = \gamma_b, \quad h = \gamma_b \left[\frac{1 + E_N}{1 + E_T} - 1 \right], \quad k = 0, \quad (19)$$

where E_N and E_T are the dimensionless compliances as described in (11a) and (11b), depending on whether Hudson's first- or second-order model is used, respectively. In general, transverse isotropy is described by five independent elastic constants corresponding to four independent dimensionless parameters. Eq. (19), however, shows that cracked media as described by Hudson's model only have 3 independent dimensionless parameters, which define a subspace in the h, k, τ, l parameter space.

Cracked media as described by Hudson's model are characterized by $k = 0$ (see (19)). This means that these media become K-media (described by $h = k = 0$) as soon as the parameter h becomes zero. Eq. (19) shows that this occurs if $E_N = E_T$. Such media are represented in the h, k, τ, l parameter space by points lying on the τ -axis. For Hudson's first-order model the aspect ratio of the inclusions for which this is true can be calculated analytically. With E_N and E_T given by (13) E_N equals E_T if

$$\alpha_k = \frac{\gamma_b[4\kappa' + (16/3)\mu'] - 4\mu'}{(3 - 6\gamma_b + 4\gamma_b^2)\pi\mu_b}. \quad (20)$$

This result is only valid for $\gamma_b(4\kappa' + (16/3)\mu') - 4\mu' \neq 0$, i.e. for fluid-filled inclusions this result is valid for non-dry inclusions. For dry inclusions there is no aspect ratio for which the cracked medium is a K-medium. Eq. (20) shows that α_k is independent on the crack density e . If $E_N = E_T = 0$ (19) shows that the resultant medium is isotropic (i.e. $l = 1, h = k = 0$).

Because Nishizawa's (1982) model is not identical to Hudson's (1980, 1981) crack model for all aspect ratios of the inclusions (this is only true for aspect ratios up to 0.3) Eq. (19) can not be used to represent the cracked medium as described by Nishizawa's model in the h, k, τ, l -space. Therefore, such a representation can only be carried out by calculating the h, k, τ, l parameters numerically from the elastic constants given by Nishizawa's model.

4.6 RESULTS

In this section theoretical cracked media as described by Hudson's (1980, 1981) crack model and Nishizawa's (1982) model are studied. For a large range of aspect ratios (i.e. from $\alpha = 0.0001$ (almost flat cracks) up to $\alpha = 1$ (spherical inclusions)) of the inclusions and for different media inside the inclusions the elastic constants of the resultant transversely isotropic medium are calculated using both models. Then it is investigated

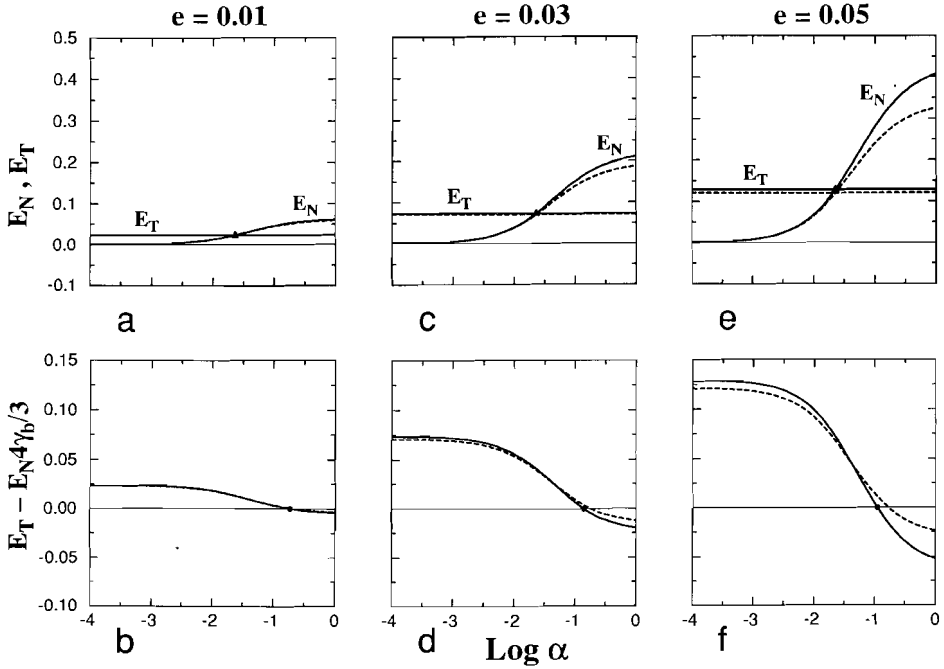


Fig. 4.2. The dimensionless compliances E_N , E_T (a, c, e) and the term $(E_T - E_N 4\gamma_b/3)$ (b, d, f) as a function of the aspect ratio α of water-filled inclusions for three crack densities $e = 0.01$ (a, b), $e = 0.03$ (c, d), and $e = 0.05$ (e, f) using Hudson's first- (solid line) and second-order model (dashed line). The inclusions are embedded in a matrix material with $\gamma_b = 1/3$. The black dot in b, d, and f represents the upper limit of the aspect ratios for which the cracked medium as described by Hudson's first-order model is a RSSIL-medium. The triangle in a, c, and e represents the aspect ratio for which the cracked medium as described by Hudson's first-order model is a K-medium.

whether the resultant medium can be represented by a RSSIL-medium or eventually by a K-medium.

We consider an isotropic background medium described by $\gamma_b = 1/3$. Three types of inclusions are studied: 1) water-filled inclusions with $\kappa' = 0.0771 \times \mu_b$, 2) gas-filled inclusions with $\kappa' = 0.0034 \times \mu_b$, and 3) dry (empty) inclusions with $\kappa' = 0$. All these inclusions have a shear modulus $\mu' = 0$. The dry inclusions are perhaps not a realistic type of inclusions in the Earth, but are considered here as the limiting case of gas-filled inclusions.

a) Hudson's model

First the results obtained with Hudson's model are shown. Cracked media as described by Hudson's model can be represented by RSSIL-media if the constraint (10) (i.e. $E_T > E_N 4\gamma_b/3 > 0$) is satisfied. In Fig. 4.2 the values of E_N , E_T , and $E_T - E_N 4\gamma_b/3$ calculated for water-filled inclusions using Hudson's first- (solid lines) and second-order model (dashed lines) are presented. These values all have to be positive to satisfy (10). The values

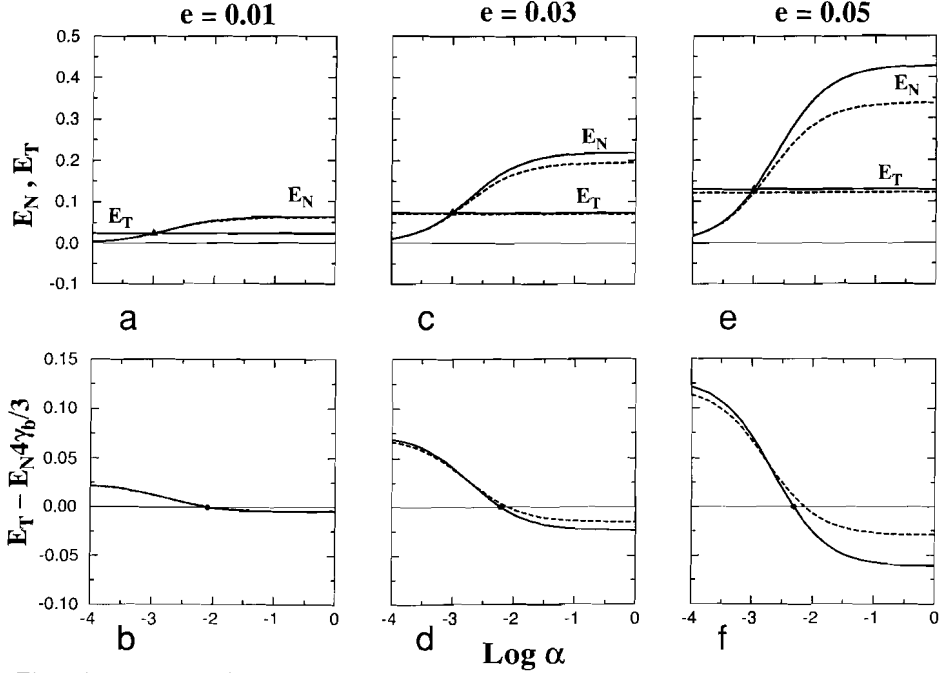


Fig. 4.3. As for Fig. 4.2, but now for gas-filled inclusions.

of E_N and E_T are presented in the upper figures 4.2a, 4.2c, and 4.2e for crack densities $e = 0.01$, 0.03 , and 0.05 , respectively. In the lower figures 4.2b, 4.2d, and 4.2f the values of $E_T - E_N 4\gamma_b/3$ are presented for the same crack densities, respectively. In the lower figures of Fig. 4.2 the point denoted by a black dot corresponds to the analytically calculated upper limit α_l of the range of aspect ratios (18) for which the cracked medium (as described by Hudson's first-order model) can be represented by a RSSIL-medium. In the upper figures the point denoted by a triangle corresponds to the analytically calculated aspect ratio α_k for which the cracked medium (as described by Hudson's first-order model) is a K-medium. From Fig. 4.2 it can be concluded that both E_N and E_T calculated with either Hudson's first- or second-order model are positive. E_T is constant for all aspect ratios and its value increases for increasing crack density e . E_N , however, is not constant: its value decreases for decreasing aspect ratio α and approaches zero for $\alpha \rightarrow 0$. With E_N and E_T being both positive the conditions for the representability of cracked media (as described by Hudson's model) by RSSIL-media can only be violated if $E_T - E_N 4\gamma_b/3$ becomes non-positive. For a crack density $e = 0.05$ and for Hudson's first-order model Fig. 4.2f shows that this occurs at aspect ratios around $\alpha = 0.1$. For smaller aspect ratios the term is positive and the cracked medium is a RSSIL-medium. For larger aspect ratios, however, the term becomes non-positive and the cracked medium is no longer a RSSIL-medium. Figures 4.2b, 4.2d, and 4.2f show that the ultimate aspect ratio for which the cracked medium is a RSSIL-medium depends (although not very strongly) on the model used (Hudson's first-order model results in a smaller ultimate aspect ratio than Hudson's second-order model, especially for large

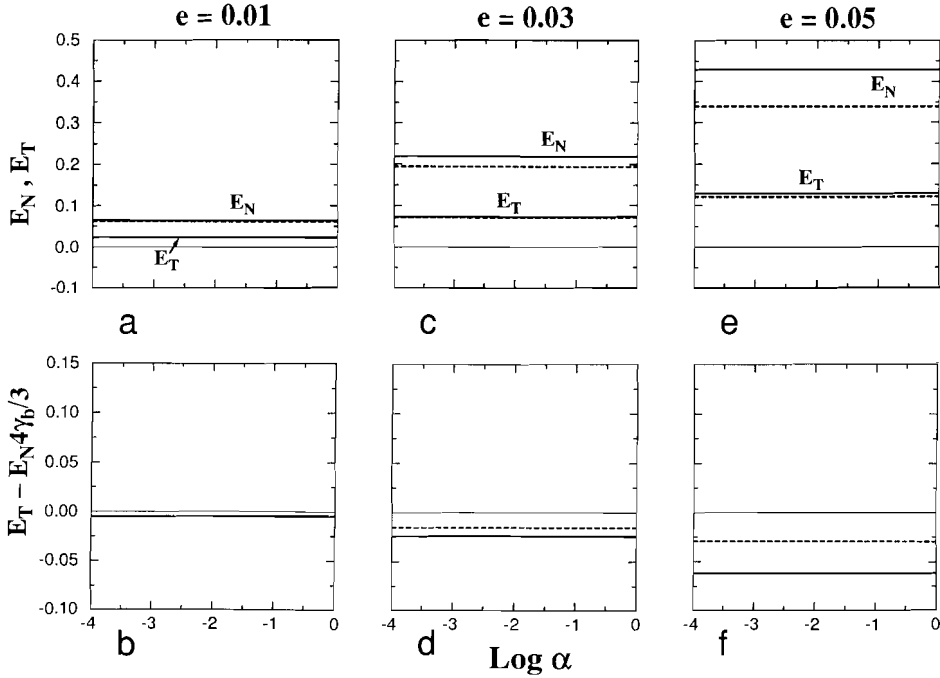


Fig. 4.4. As for Fig. 4.2, but now for dry inclusions.

crack density e) and on the crack density e (for increasing crack density e the ultimate aspect ratio tends to shift towards smaller values). These figures also show that the analytically calculated ultimate aspect ratio (denoted by the black dot) agrees with the ultimate aspect ratio α_1 at which the term $E_T - E_N 4\gamma_b/3$ calculated with Hudson's first-order model is positive (indicating the correctness of (18)). Because the ultimate aspect ratios at which Hudson's first- and second-order model result in a RSSIL-medium are not much different from each other (especially at small crack densities) the aspect ratio α_1 defined in (18) also appears to be a good estimate of the ultimate aspect ratio for which Hudson's second-order model results in a RSSIL-medium.

Finally, it should be pointed out that for the situations studied in Fig. 4.2 there are indeed aspect ratios for which the resultant cracked medium is a K-medium. As discussed in section 4.5 this is true whenever E_N and E_T become equal. Figure 4.2e shows that for a crack density $e = 0.05$ and for Hudson's first-order model this is true for an aspect ratio $\alpha \approx 0.02$. This result corresponds to the analytically calculated aspect ratio α_k (denoted by a triangle) for which the cracked medium is a K-medium. As shown by Figs 4.2a, 4.2c, and 4.2e this result does not seem to depend very much on the crack density e or on whether Hudson's first- or second-order model is used. The former statement is in agreement with (20).

In Fig. 4.3 the results of the same calculations but now for gas-filled inclusions are presented. Most of the conclusions drawn from Fig. 4.2 also hold for Fig. 4.3. The only important difference is that the aspect ratios for which Hudson's model results in a RSSIL-

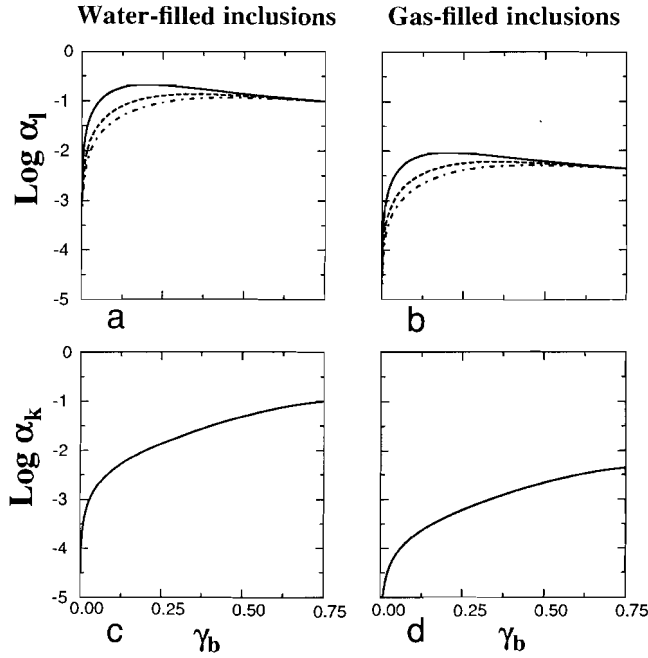


Fig. 4.5. The upper limit α_l (Eq. (18)) of the aspect ratios of water- (a) and gas-filled (b) inclusions for which the resultant cracked medium (as described by Hudson's first-order model) is a RSSIL-medium as a function of γ_b of the background medium for three crack densities $e = 0.01$ (solid line), $e = 0.03$ (dashed line), and $e = 0.05$ (dashed-dotted line). The aspect ratios α_k (Eq. (20)) of water- and gas-filled inclusions for which the resultant cracked medium (as described by Hudson's first-order model) is a K-medium are presented in (c) and (d), respectively. These results are valid for any crack density e .

medium and a K-medium, respectively, become smaller than the corresponding aspect ratios obtained from Fig. 4.2. Figures 4.3b, 4.3d, 4.3f show that the value of the ultimate aspect ratio for which the cracked medium is a RSSIL-medium now lies around $\alpha \approx 0.005$, while the aspect ratio for which the cracked medium is a K-medium is now $\alpha \approx 0.001$. So, we may conclude that for gas-filled inclusions there is a large range of aspect ratios for which the cracked medium is not a RSSIL-medium.

This situation becomes even more distinct when dry inclusions are considered (Fig. 4.4). Figure 4.4 shows that there are no aspect ratios at all for which the cracked medium is a RSSIL-medium or a K-medium because the term $E_T - E_N 4\gamma_b/3$ is negative for all aspect ratios and crack densities being studied (see Figs 4.4b, 4.4d, and 4.4f). This result agrees with the result of (18) for dry inclusions.

The results discussed above were derived for one specific background medium (i.e. $\gamma_b = 1/3$). To find out whether the results depend on the background medium α_l and α_k (i.e. only cracked media as described by Hudson's first-order model are studied) are calculated for all possible stable background media (i.e. $0 < \gamma_b < 3/4$) for both the water- and gas-filled inclusions and presented in Fig. 4.5. Figure 4.5 shows that α_k strongly depends on γ_b : α_k

decreases significantly for decreasing γ_b , whereas α_1 only strongly depends on γ_b if γ_b is small (i.e. $\gamma_b < 0.1$). For values of γ_b around 1/3 (a realistic background medium in the Earth) α_1 only weakly depends on γ_b . Moreover, Fig. 4.5 shows that the effect of the crack density (which only affects α_1) is not very large, especially for γ_b around 1/3.

All these results are similar for both water- and gas-filled inclusions. The only difference between the results for both types of inclusions is that both α_k and α_1 are smaller for gas-filled inclusions than for water-filled inclusions if the same value of γ_b is considered.

The results shown up to here have been calculated with Hudson's model. Next the results calculated with Nishizawa's model are shown.

b) Nishizawa's model

Consider theoretical cracked media that are described by Nishizawa's model. As mentioned in section 4.4 the representability of these media by RSSIL-media is studied by investigating the basic constraints (6) on their dimensionless h , k , τ , l parameters. In Fig. 4.6 these dimensionless parameters together with the parameters

$$S_1 = [3/4 - (h + \tau)][3/4 - (k + \tau)] - l(3/4 - \tau)^2 \quad \text{and}$$

$$S_2 = (h + \tau)(k + \tau) - l\tau^2$$

are presented for water-filled inclusions (a, b, c) and dry inclusions (d, e, f). The crack density used in these calculations is $e = 0.05$. The results have been calculated for Nishizawa's model (dashed line) and Hudson's second-order model (solid line).

If the parameters l and τ , presented in Figs 4.6a and 4.6d for water-filled and dry inclusions, respectively, are considered, Figs 4.6a and 4.6d show that for Hudson's second-order model l and τ are constant and independent on the medium inside the inclusions. With the expressions given for these parameters in (19):

$$l = \frac{1}{1 + E_T} \quad \text{and} \quad \tau = \gamma_b$$

and the results of Figs 4.2 and 4.4 (showing that E_T is constant for both dry and water-filled inclusions) this result can be explained. Important to note is that both l and τ satisfy the stability constraints of a RSSIL-medium, i.e. $l < 1$ and $0 < \tau < 3/4$. This is also true for Nishizawa's l and τ (dashed lines). The value of Nishizawa's τ is almost identical to Hudson's τ , but the value of Nishizawa's l is only identical to Hudson's l at aspect ratios smaller than 0.3. At larger aspect ratios the value of Nishizawa's l goes to unity, corresponding to the isotropic situation (spherical inclusions).

In Figs 4.6b and 4.6e the values of h and k are shown for water-filled and dry inclusions, respectively. From these figures it is concluded that both h and k (calculated with either Hudson's or Nishizawa's model) satisfy the constraints $-\tau < h < (3/4 - \tau)$ and $-\tau < k < (3/4 - \tau)$ (with τ presented in Figs 4.6a and 4.6d) of RSSIL-media. Figures 4.6b

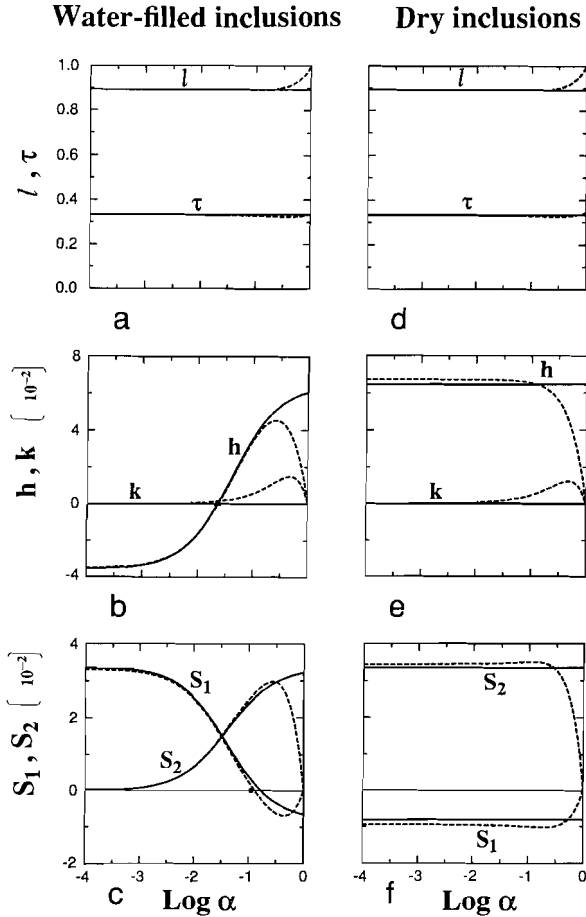


Fig. 4.6. The dimensionless parameters l , τ (a, d), h , k (b, e), and $S_1 = (3/4 - (h + \tau))(3/4 - (k + \tau)) - l(3/4 - \tau)^2$ and $S_2 = (h + \tau)(k + \tau) - l\tau^2$ (c, f) as a function of the aspect ratio α of water-filled (a, b, c) and dry (d, e, f) inclusions embedded in a matrix material with $\gamma_b = 1/3$. The results are calculated for a crack density $e = 0.05$ using Hudson's second-order model (solid line) and Nishizawa's model (dashed line). The dot in (c) and the triangle in (b) have the same meaning as described in Fig. 4.2.

and 4.6e show that Hudson's k is always zero, which agrees with (19). Nishizawa's k , however, is only zero for small aspect ratios ($\alpha < 0.01$) and for $\alpha = 1$. The aspect ratio $\alpha = 1$ is also the only aspect ratio at which Nishizawa's model results in a K-medium (i.e. $h = k = 0$) both for the dry and water-filled inclusions, but this K-medium is an isotropic medium. Unlike Nishizawa's model which does not result in a K-medium at aspect ratios smaller than $\alpha = 1$, Hudson's model does if water-filled inclusions are considered (the triangle again denotes the K-medium according to Hudson's first-order model).

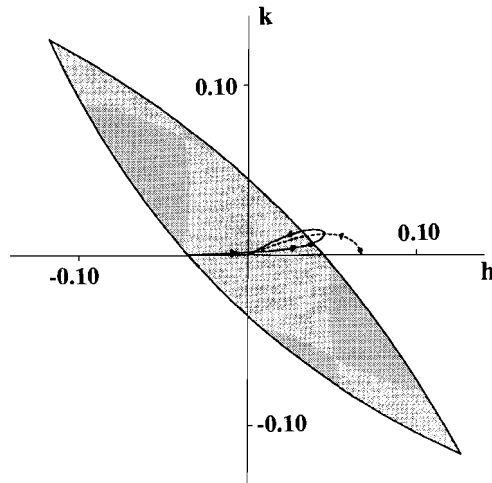


Fig. 4.7. The two-dimensional intersection (shaded area) of the ‘stability area’ (described by Eq. (6)) with the hyperplanes $l = l_c$ and $\tau = \tau_c$ (where l_c and τ_c are constants given by the constant values of l and τ at small aspect ratios in Figs 4.6a and 4.6d). The coordinates of the points lying on the solid and dashed curves represent the h, k parameters (calculated with Nishizawa’s model) of media containing water-filled (solid line) and dry inclusions (dashed line) with aspect ratios α ranging from $\alpha = 0.0001$ (the starting point of each curve) up to $\alpha = 1$ (the endpoint of each curve). The arrow and the thick dot at each curve denote the direction of increasing aspect ratio and the aspect ratio $\alpha = 0.1$, respectively. The crack density $e = 0.05$.

Finally, in Figs 4.6c and 4.6f the parameters S_1 and S_2 are shown. The stability constraints of a RSSIL-medium require that the values of S_1 and S_2 are positive. Both Figs 4.6c and 4.6f show that S_2 is always positive, but that S_1 may be non-positive. This means that the media studied are not RSSIL-media if S_1 becomes non-positive. Figure 4.6c therefore shows that for water-filled inclusions (with $e = 0.05$) Nishizawa’s model only results in RSSIL-media at aspect ratios smaller than $\alpha \approx 0.1$. This result agrees very well with the ultimate aspect ratio α_1 of Hudson’s first-order model (black dot). Figure 4.6f shows that both Nishizawa’s and Hudson’s model do not result in a RSSIL-medium if dry inclusions are considered.

In conclusion we can say that the results of Fig. 4.6 are similar for both Nishizawa’s and Hudson’s (second-order) model at aspect ratios up to 0.3 (which agrees with the similarity between both models as described already by Douma, 1988) but that at larger aspect ratios only Nishizawa’s model converges to an isotropic situation at $\alpha = 1$.

Because for a large range of aspect ratios the dimensionless parameters l and τ of the cracked media are constant these media can be represented in the h, k -subspace of the h, k, τ, l parameter space for a large range of aspect ratios together with the two-dimensional cross-section (at the constant values of l and τ) of the constraint area (representing all RSSIL-media) in this subspace. In Fig. 4.7 this cross-section is plotted as a shaded area in the h, k -space. Together with this constraint area the points representing the cracked media

as described by Nishizawa's model are given for a large range of aspect ratios (from $\alpha = 0.0001$ up to $\alpha = 1$). The h, k coordinates of these points are the h, k parameters calculated for these media (and presented in Figs 4.6b and 4.6e). The points are given in Fig. 4.7 by solid and dashed lines describing the situation of water-filled and dry inclusions (with $e = 0.05$), respectively. The arrows indicate the direction of increasing aspect ratio. Figure 4.7 shows clearly that for water-filled inclusions the resultant cracked medium is a RSSIL-medium at small aspect ratios, but that at a certain aspect ratio, as the point representing the medium in the h, k -space moves out of the constraint area, it is no longer a RSSIL-medium. Only for aspect ratios approaching $\alpha = 1$ (spherical inclusions) the resultant medium lies inside the constraint area again.

For dry inclusions Fig. 4.7 shows that already at small aspect ratios the points representing the cracked media lie outside the constraint area. At these small aspect ratios the resultant medium is not a RSSIL-medium. Only if the aspect ratio approaches $\alpha = 1$ the resultant medium lies inside the constraint area again. Figure 4.7 also shows that for the inclusions and background medium studied here Nishizawa's model only results in a K-medium ($h = k = 0$) at $\alpha = 1$ (both curves end in the origin of the h, k -space).

One should be aware that Fig. 4.7 is misleading for large aspect ratios (i.e. $\alpha \approx 1$). Because the value of l (as calculated with Nishizawa's model) increases at these aspect ratios and approaches $l = 1$ (Figs 4.6a and 4.6d) the constraint area becomes narrower around the origin than shown in Fig. 4.7 (at $\alpha = 1$, the isotropic situation, the constraint area disappears: its boundary is the origin). Consequently, the points representing the cracked medium at large aspect ratios which now seem to lie inside the constraint area actually lie outside the constraint area. To study the situation for large aspect ratios ($\alpha \approx 1$) the results of Fig. 4.6 should be used.

4.7 CONCLUSIONS

Not all media containing rotationally symmetrical aligned inclusions result in transversely isotropic media that can also be modelled by sequences of stable isotropic layers (with a symmetry axis identical to that of the inclusions). Important parameters that determine whether a medium containing aligned inclusions is representable by such sequences of layers are the aspect ratio α of the inclusions and the medium inside the inclusions. The crack density e and the background medium (if γ_b lies around $1/3$) only slightly affect these results. Media (with $\gamma_b = 1/3$) containing water-filled inclusions are only RSSIL-media if the aspect ratio of the inclusions is smaller than $\alpha \approx 0.1$ (for a crack density $e = 0.05$). For larger aspect ratios the resultant medium can not be modelled by sequences of stable isotropic layers. For gas-filled inclusions (i.e. for larger contrast between the medium inside the inclusions and the background medium) the range of aspect ratios for which the resultant cracked medium is a RSSIL-medium becomes smaller, i.e. only media having inclusions with aspect ratios smaller than $\alpha \approx 0.005$ are RSSIL-media.

Finally, for dry inclusions (the limiting case of gas-filled inclusions) there are no aspect ratios at all for which the resultant medium is a RSSIL-medium. The results can be obtained using either Nishizawa's or Hudson's model. Both give almost identical results for α up to 0.3. Using Hudson's first-order model an analytical expression can be obtained for the range of aspect ratios for which the resultant medium is a RSSIL-medium. The value appears to be a good approximation of the range of aspect ratios for which numerical calculations show that Hudson's second-order model and Nishizawa's model result in RSSIL-media.

The representability of cracked media by sequences of isotropic layers might be used in the separation of the cause of observed transverse isotropy: if it is shown that the observed anisotropy can not be modelled by sequences of isotropic layers this would exclude one possible cause of anisotropy, whereas cracked media, which (as shown in this paper) not necessarily have to be representable by such sequences, could still be the cause of the observed anisotropy. Realizing, however, that there are other causes of transverse isotropy the results in this paper should only be considered as a first step towards possible separation methods. Another application of the representability of cracked media by sequences of isotropic layers might be the determination of the medium inside the inclusions. The results of this study show that for a given aspect ratio of the inclusions this representability strongly depends on the medium inside the conclusions. For example if it would be known that a cracked medium containing inclusions with a very small aspect ratio is not a RSSIL-medium this can only be explained by gas-filled inclusions with a very small bulk modulus. Other media (with a larger bulk modulus) inside the inclusions would result in a RSSIL-medium. Therefore, the representability of cracked media by RSSIL-media might be useful to monitor the fluid inside the inclusions changing with time (earthquake prediction) or space (gas exploration) in a uniformly cracked media.

ACKNOWLEDGEMENT

I thank K. Helbig for many discussions on the subject.

4.8 APPENDIX A.

In Eq. (10) the dimensionless compliances E_N and E_T for which a medium containing large fractures (slip interfaces) is the equivalent of a RSSIL-medium were derived by considering the medium inside the fractures (the fracture material itself had to be a RSSIL-medium). In this appendix the same is done, but now by investigating the values of E_N and

E_T for which the elastic constants c_{ij}^S of the medium containing the large fractures satisfy the stability constraints (6) of a RSSIL-medium. Only stable background media (i.e. $\mu_b > 0$ and $0 < \gamma_b < 3/4$) are considered here. The dimensionless h, k, τ, l parameters (or eventually ρ, σ, τ , and l) used in the stability constraints (6) are calculated for the elastic constants c_{ij}^S in appendix C. With these h, k, τ, l parameters (expressed in terms of E_N, E_T , and γ_b) the stability constraints (6) become

1) $0 < l < 1$:

$$0 < \frac{1}{1 + E_T} < 1, \quad (\text{A1})$$

which is satisfied for $E_T > 0$.

2) $0 < \tau < \frac{3}{4}$:

$$0 < \gamma_b < \frac{3}{4}, \quad (\text{A2})$$

which is always satisfied for a stable isotropic background medium (see (3c)).

3) $0 < k + \tau < \frac{3}{4}$ $\left[\text{or } 0 < \sigma < \frac{3}{4} \right]$:

$$0 < \gamma_b < \frac{3}{4}, \quad (\text{A3})$$

which is identical to the previous constraint.

4) $0 < h + \tau < \frac{3}{4}$ $\left[\text{or } 0 < \rho < \frac{3}{4} \right]$:

$$0 < \gamma_b \frac{(1 + E_N)}{(1 + E_T)} < \frac{3}{4},$$

with $E_T > 0$ (see (A1)) this constraint becomes

$$\frac{-4\gamma_b}{3} < \frac{4\gamma_b}{3} E_N < \left[E_T + 1 - \frac{4\gamma_b}{3} \right]. \quad (\text{A4})$$

5) $l\tau^2 < (h + \tau)(k + \tau)$ (or $l\tau^2 < \rho\sigma$) :

$$\frac{1}{1 + E_T} \gamma_b^2 < \gamma_b^2 \frac{(1 + E_N)}{(1 + E_T)}.$$

With $E_T > 0$ (see (A1)) we get

$$E_N > 0. \quad (\text{A5})$$

$$6) l \left[\frac{3}{4} - \tau \right]^2 < \left[\frac{3}{4} - (h + \tau) \right] \left[\frac{3}{4} - (k + \tau) \right] \left[\text{or } l \left[\frac{3}{4} - \tau \right]^2 < \left(\frac{3}{4} - \rho \right) \left(\frac{3}{4} - \sigma \right) \right] :$$

$$\frac{1}{1 + E_T} \left[\frac{3}{4} - \gamma_b \right]^2 < \left[\frac{3}{4} - \gamma_b \right] \left[\frac{3}{4} - \gamma_b \frac{(1 + E_N)}{(1 + E_T)} \right].$$

Using $E_T > 0$ (see (A1)) we get

$$\frac{4\gamma_b}{3} E_N < E_T. \quad (\text{A6})$$

This constraint is (with $0 < \gamma_b < 3/4$) more restrictive than the second inequality of (A4).

In conclusion Eqs (A1)-(A6) show that a transversely isotropic medium which is the long wavelength equivalent of a medium containing slip interfaces is a RSSIL-medium if E_N and E_T satisfy :

$$E_T > \frac{4\gamma_b}{3} E_N > 0. \quad (\text{A7})$$

4.9 APPENDIX B.

In this appendix it is shown that the constraint described in (18) is more restrictive (i.e.

it is satisfied for a smaller range of aspect ratios α) than the constraint described in (16a). This is true if

$$\frac{9\gamma_b\kappa'}{(3\gamma_b^2 - 16e\gamma_b + 12e)\pi\mu_b} < \frac{3\gamma_b(\kappa' + \frac{4}{3}\mu')}{(3\gamma_b^2 - 3\gamma_b + 4e)\pi\mu_b}. \quad (\text{B1})$$

Because the terms in brackets of both denominators in (B1) are positive (in the first term of (B1) because of $0 < \gamma_b < 3/4$ and in the second term because (16a) is only true for $(3\gamma_b^2 - 3\gamma_b + 4e) > 0$) (B1) becomes

$$3\kappa' (3\gamma_b^2 - 3\gamma_b + 4e) < (\kappa' + \frac{4}{3}\mu') (3\gamma_b^2 - 16e\gamma_b + 12e). \quad (\text{B2})$$

(B2) is certainly true if it can be proven that

$$3 (3\gamma_b^2 - 3\gamma_b + 4e) < (3\gamma_b^2 - 16e\gamma_b + 12e), \quad (\text{B3})$$

i.e.

$$\gamma_b(6\gamma_b - 9 + 16e) < 0. \quad (\text{B4})$$

With $\gamma_b \neq 0$ (which was assumed throughout this paper) (B4) is always satisfied for crack densities up to $e \approx 0.28$ (because $0 < \gamma_b < 3/4$). So, we may conclude that the constraint (18) is more restrictive than (16a). This is true for crack densities up to $e \approx 0.28$ and therefore is certainly true for the crack densities (e smaller than 0.05) for which Hudson's model is assumed to be valid (Thomsen, 1988).

4.10 APPENDIX C.

In this appendix the dimensionless parameters ρ , σ , τ , l and h , k corresponding to the elastic constants c_{ij}^S of a transversely isotropic medium which is the long wavelength equivalent of a medium containing large fractures (slip interfaces) are calculated. Using the elastic constants c_{ij}^S as described in (8) we get :

$$l = \frac{c_{44}^S}{c_{66}^S} = \frac{1}{1 + E_T}, \quad (C1)$$

$$\tau = \frac{1}{2} \left[1 - \frac{c_{13}^S}{c_{33}^S} \right] = \frac{1}{2} \left[1 - \frac{\lambda_b}{\lambda_b + 2\mu_b} \right] = \frac{\mu_b}{\lambda_b + 2\mu_b} = \gamma_b, \quad (C2)$$

$$\begin{aligned} \sigma &= \frac{1}{4} \left[\frac{c_{13}^{S2}}{c_{33}^S c_{66}^S} - \frac{c_{11}^S}{c_{66}^S} \right] + 1 = \frac{1}{4} \left[\frac{\lambda_b^2}{(\lambda_b + 2\mu_b)\mu_b} - \frac{\lambda_b + 2\mu_b}{\mu_b} \right] + 1 \\ &= \frac{\mu_b}{\lambda_b + 2\mu_b} = \gamma_b, \end{aligned} \quad (C3)$$

$$\rho = \frac{c_{44}^S}{c_{33}^S} = \frac{\mu_b}{\lambda_b + 2\mu_b} \left[\frac{1 + E_N}{1 + E_T} \right] = \gamma_b \frac{(1 + E_N)}{(1 + E_T)}, \quad (C4)$$

$$h = \rho - \tau = \gamma_b \left[\frac{1 + E_N}{1 + E_T} - 1 \right], \quad (C5)$$

$$k = \sigma - \tau = 0. \quad (C6)$$

Eqs (C1) - (C6) show that both the dimensionless parameter sets ρ, σ, l, τ , and h, k, τ, l only have three independent parameters, which agrees with the four independent elastic constants c_{ij}^S (8).

4.11 REFERENCES

- Backus, G.E. 1962. Long-wave anisotropy produced by horizontal layering. *Journal of Geophysical Research* 66, 4427-4440.
 Bruggeman, D.A.G. 1937. Berechnung der verschiedenen physikalischen Konstanten von

- heterogenen Substanzen. *Annalen der Physik* (5), 29, 160.
- Crampin, S. 1984. Effective anisotropic elastic constants for wave propagation through cracked solids. *Geophysical Journal of the Royal Astronomical Society* 76, 135-145.
- Crampin, S., McGonigle, R. and Ando, M. 1986. Extensive-dilatancy anisotropy beneath Mount Hood, Oregon and the effect of aspect ratio on seismic velocities through aligned cracks. *Journal of Geophysical Research* 91, 12703-12710.
- Douma, J. 1988. The effect of the aspect ratio on crack-induced anisotropy. *Geophysical Prospecting* 36, 614-632.
- Helbig, K. 1958. Elastische Wellen in anisotropen Medien. *Gerlands Beiträge zur Geophysik* 67, 177-211, 256-288.
- Helbig, K. 1981. Systematic classification of layer-induced transverse isotropy. *Geophysical Prospecting* 29, 550-577.
- Helbig, K. and Schoenberg, M. 1987. Anomalous polarization of elastic waves in transversely isotropic media. *Journal of the Acoustical Society of America* 81, 1235-1245.
- Hudson, J.A. 1980. Overall properties of a cracked solid. *Mathematical Proceedings of the Cambridge Philosophical Society* 88, 371-384.
- Hudson, J.A. 1981. Wave speeds and attenuation of elastic waves in material containing cracks. *Geophysical Journal of the Royal Astronomical Society* 64, 133-150.
- Krey, Th. and Helbig, K. 1956. A theorem concerning anisotropy of stratified media and its significance for reflection seismics. *Geophysical Prospecting* 4, 294-301.
- Nishizawa, O. 1982. Seismic velocity anisotropy in a medium containing oriented cracks-transversely isotropic case. *Journal of Physics of the Earth* 30, 331-347.
- Postma, G.W. 1955. Wave propagation in a stratified medium. *Geophysics* 20, 780-806.
- Schoenberg, M. 1980. Elastic wave behavior across linear slip interfaces. *Journal of the Acoustical Society of America* 68, 1516-1521.
- Schoenberg, M. 1983. Reflection of elastic waves from periodically stratified media with interfacial slip. *Geophysical Prospecting* 31, 265-292.
- Schoenberg, M. and Douma, J. 1988. Elastic wave propagation in media with parallel fractures and aligned cracks. *Geophysical Prospecting* 36, 571-590.
- Thomsen, L. 1988. Elastic anisotropy due to aligned cracks. *Submitted to Geophysical Journal of the Royal Astronomical Society.*

Chapter 5

SHEAR-WAVE SPLITTING IN ISOTROPIC MEDIA

ABSTRACT

The direction of polarization of seismic shear waves and the time shift between shear waves of different polarization contain important clues to the internal structure of the medium through which the waves have passed. For instance, the direction of polarization can be used to infer the average orientation of cracks (and thus the direction of tectonic stresses), while the time shift depends not only on the orientation of the ray path with respect to the plane of the cracks, but also on the product of crack density and path length through the cracked medium.

Before the direction of polarization and the time shift can be used for this purpose one must ascertain that these parameters are not contaminated by spurious effects. Disturbances that must be corrected for occur at the free surface, but even in Vertical Seismic Profiling (VSP) disturbances might occur due to transmission through interfaces: unless the shear waves are polarized parallel or perpendicular to the 'plane of propagation' that contains the ray and the normal to the interface (or unless the angle of incidence is zero), the direction of polarization changes at transmission due to the different transmission coefficients of the two component waves. For incidence at and beyond the critical angle, the transmission coefficient of the component parallel to the plane of propagation is complex, resulting in a time shift.

This chapter has been published as:

Douma, J. and Helbig, K. 1987. What can the polarization of shear waves tell us? *First Break* 5, (3), 95-104.

The effects at the free surface and at individual interfaces are relatively small (though not negligible). However, passage through several interfaces can lead to the accumulation of time shifts. In the limit this accumulation results in two shear waves with different velocities, i.e. to anisotropy.

5.1 INTRODUCTION

Of the two different wave types that can propagate in an isotropic elastic medium only the shear waves have a non-predictable polarization: P-waves are, for all practical purposes, polarized in the direction of the ray, but the shear waves can be polarized in any direction in the plane that is perpendicular to the direction of the ray. Since information is contained only in non-predictable parameters, it is the shear-wave polarization from which we can learn something.

What then determines the polarization of a shear wave? We generally describe the polarization implicitly by talking of SH- and SV-waves, i.e. of shear waves with the displacement vector in a horizontal plane and shear waves with the displacement vector in the vertical plane containing the ray. The choice of these two directions is natural as long as we are dealing with, or assume we are dealing with, an isotropic homogeneous medium, a transversely isotropic medium with vertical axis, or any combination of these with horizontal layering. Under these circumstances, the local vertical is an axis of rotational symmetry and thus the pre-ordained reference direction. The tangent of the 'polarization angle' between the direction of shear displacement and the vertical plane containing the ray is then simply the ratio of the SH- and SV-amplitudes.

In isotropic conditions, the propagation velocities of the two shear waves are equal. Since the ray path (as determined by Snell's law) depends only on the velocity distribution, the two wave types travel along the same ray path even if the medium is inhomogeneous. Identical angles of refraction, however, do not imply identical transmission and reflection coefficients, since SH-waves generate only SH-waves, but SV-waves generate both SV- and P-waves at non-normal incidence. Unless the incident wave is purely SH or SV, the polarization angle changes at every interface.

These changes in polarization angle are relatively simply to determine in a horizontally stratified medium. Moreover, they are generally small since for moderate offsets the angle of incidence remains moderate. The polarization observed at a three-component geophone station is determined by the original polarization produced by the source and by the accumulated changes of the two shear components along the ray path. To a degree these concepts have been used in connection with offset-dependent reflection coefficients, though generally only the change in the amplitude of the P-waves is taken into account. Generalization to SV- and SH-waves would make the conclusions drawn from these offset dependences more reliable.

The situation can change drastically when our simplistic model of a stack of isotropic

plane layers breaks down, i.e. for anisotropy or for dipping interfaces. At a dipping interface one has to redefine SV- and SH-waves: the displacement vectors of the 'new' SV-waves lie in the (not necessarily vertical) plane containing the rays and the normal to the interface, the displacement vectors of the 'new' SH-waves are parallel to the interface. For steeply dipping interfaces the angle of incidence can become considerable even for moderate offsets, and significant changes of the polarization angle might occur. In particular, for large angles of incidence the reflection/refraction process can become critical with respect to P- or S-waves in the two media separated by the interface. Beyond the critical angle, reflection coefficients are complex, i.e. in addition to the change in amplitude there is a phase shift.

In anisotropic media the two types of S-waves travel, in general, with different velocities. Combination of the two S-waves, or splitting of one according to a convenient coordinate system, is then no longer possible, except in the special directions where the two velocities happen to be equal. This equality of the two shear-wave velocities occurs for all directions of symmetry, but there are also a few other directions of such 'shear-wave degeneration'. For the immediate vicinity of these directions the differences in the two velocities are small, but even a difference of as little as 1% means that after 50 wavelengths the two signals are shifted by half a wavelength. In other directions the difference can easily reach 10 - 20 %, i.e. a shift by one wavelength is reached after only five to ten wavelengths. If these S-waves, after being affected by the anisotropy, continue in an isotropic medium, this shift remains constant.

If we do not look at the complete signal but at its (sinusoidal) Fourier components, this time (or distance) shift is translated into a phase shift of 360° for every shifted wavelength. Such phase-shifted sinusoidal waves combine to form elliptically polarized S-waves, except for phase shifts that are a multiple of 180° . For these phase shifts the polarization ellipse degenerates into a straight line.

In the last few years the polarization of S-waves and the corresponding time shift have been observed in several investigations in order to obtain information about the anisotropy that has affected it (Crampin, 1985a, b; Gal'perin, 1984). The time shift is often loosely referred to as 'shear-wave splitting'. If the anisotropy is caused by aligned cracks, polarization measurements can help to determine the orientation of the cracks or their spatial density, and thus the polarization of, and the time shift between, shear waves contain information that is potentially valuable for the exploration of hydrocarbons: the polarization is related to the orientation of the cracks, since that determines the axes of symmetry of the medium and thus the 'allowed' direction of polarization, while the time shift is related to the spatial density of the cracks and the orientation of the ray path with respect to the plane of the cracks. Note that different velocities imply different ray paths for the two shear wave signals: for non-vertical incidence they are refracted by different angles according to Snell's law.

Polarization measurements are carried out with three-component geophones at the free surface or below it in boreholes (Vertical Seismic Profiling, VSP). Measurements at the free surface suffer from all kinds of interactions of waves (Evans, 1984) which mask the

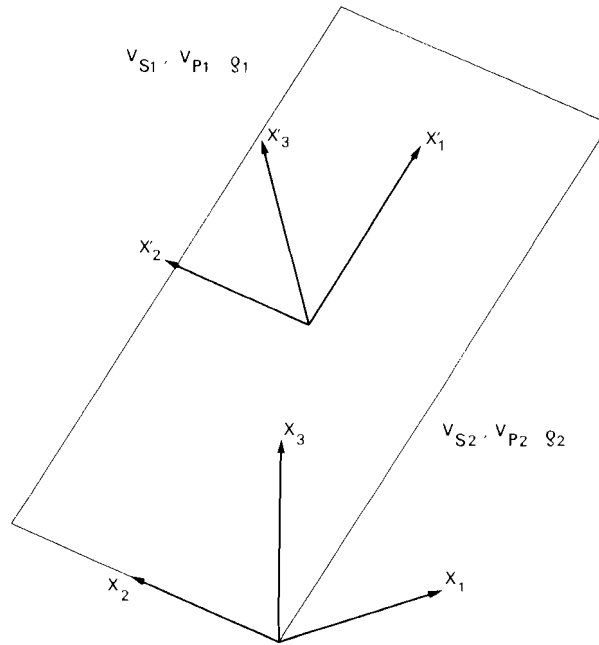


Fig. 5.1. Interface with the local coordinate system x'_1, x'_2, x'_3 .

polarization caused by anisotropy. Measurements within the medium, such as VSPs, are not influenced by these disturbing effects. However, particularly in offset VSPs, where oblique rays are used, one has to take into account the effect of polarization changes at interfaces, since the angle of incidence at a dipping interface can be large. Waves arriving at the receivers in the borehole may have passed through many interfaces, and the accumulated change of the polarization angle may be significant. Thus a part of the polarization changes observed in VSP measurements may have been caused by the passage through interfaces rather than by the passage through an anisotropic medium.

5.2 THEORY

In the theoretical considerations we shall use sinusoidal waves instead of short signals. Accordingly, we talk of phase shifts instead of time shifts. A phase shift that depends linearly on frequency is easily translated into a time shift: for example, a phase shift of 36° per Hz corresponds to a time shift of 0.1 s ($36/360$ s).

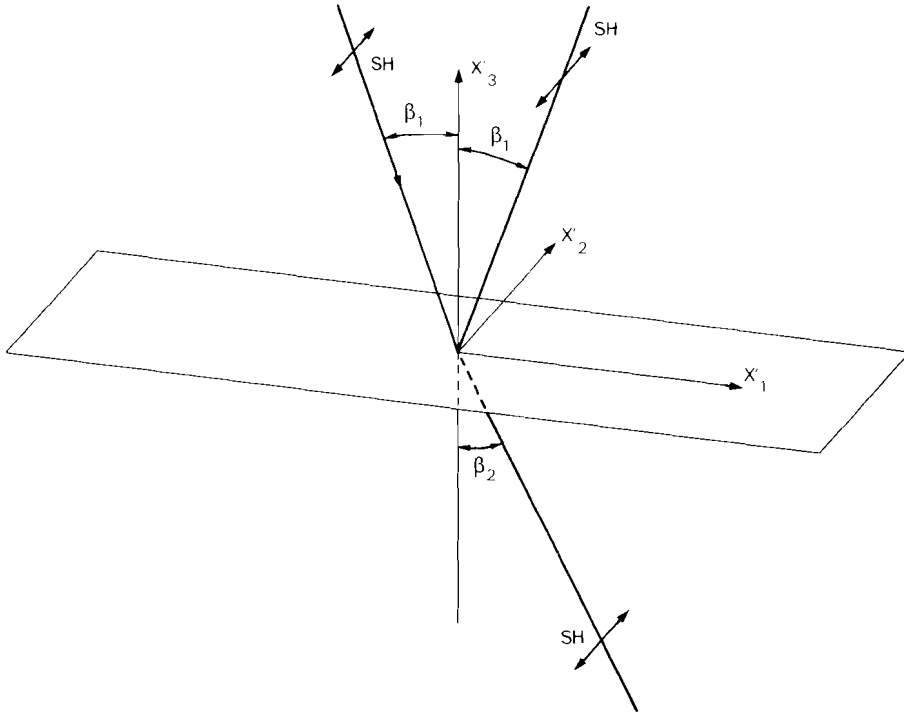


Fig. 5.2. The system of waves generated by an incident SH-wave at an interface between two solids.

5.2.1 Decomposition into SH- and SV-waves

The incident S-wave is decomposed into SH- and SV-waves according to the local coordinate system at the point of incidence. This system consists of a x'_3 -axis normal to the interface and x'_1 - and x'_2 -axes perpendicular to each other in the plane tangent to the interface (see Fig. 5.1). The x'_1 -axis is chosen in such a way that the incident ray lies in the x'_1, x'_3 -plane. The SH- and SV-displacement amplitudes u_{SH} and u_{SV} are the components of the S-wave displacement vector resolved into the direction of the x'_2 -axis and into the x'_1, x'_3 -plane, respectively. The polarization angle ϕ is defined as:

$$\phi = \tan^{-1} \left[\frac{u_{SH}}{u_{SV}} \right]. \quad (1)$$

From the dynamic and kinematic boundary conditions at an interface between two homogeneous solids for both incident SH- and SV-waves, a complete system of generated waves can be determined (Aki and Richards, 1980). As illustrated in Fig. 5.2, an SH-wave

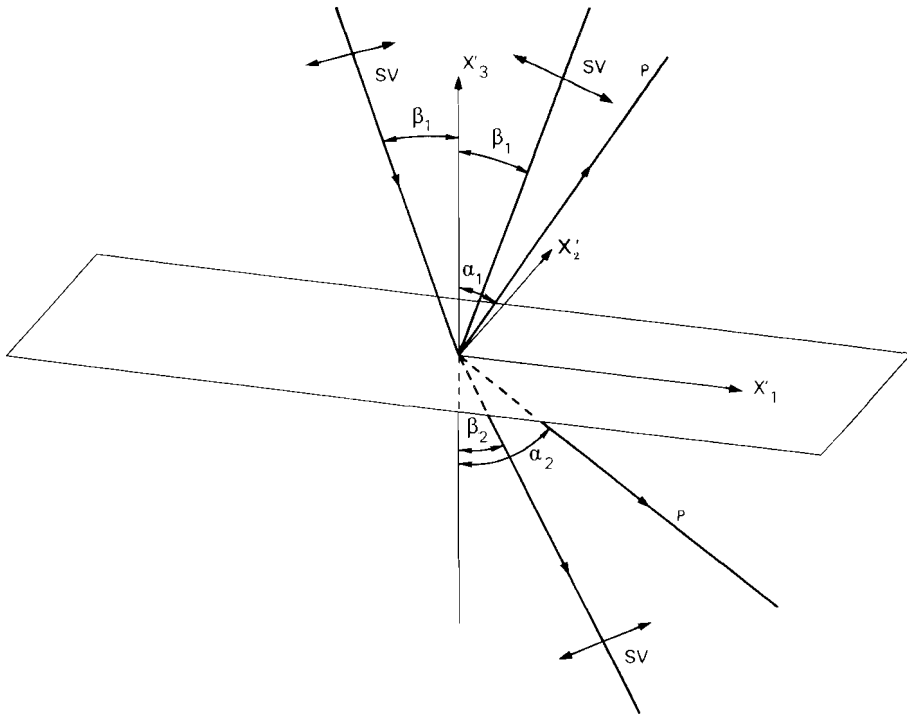


Fig. 5.3. As for Fig. 5.2, but for an incident SV-wave.

incident at an angle β_1 with the normal to the interface generates reflected and transmitted SH-waves. Their angles with the local normal can be derived from Snell's law. Only transverse waves are involved here. An incident SV-wave, however, generates reflected and transmitted P-waves as well as reflected and transmitted SV-waves (Fig. 5.3).

5.2.2 Transmission coefficients

The next step in the determination of the polarization of the transmitted S-wave is to multiply the amplitudes of the incident SH- and SV-waves with the corresponding transmission coefficients. We denote these coefficients by $\tilde{S}_H \tilde{S}_H$ and $\tilde{S}_V \tilde{S}_V$, respectively. In this nomenclature letters indicate the wave type and the superscripted symbols the direction of the ray before and after the interaction with the interface. For instance $\tilde{S}_V \tilde{P}$ indicates the generation of an upgoing (reflected) P-wave by an incident downgoing SV-wave.

The displacement of the incident downgoing SH-wave with amplitude S_1 is described, in a coordinate system with the x'_3 -axis directed upwards, by

| Wave type | Slowness vector \mathbf{s} |
|---------------------|---|
| Incident SV-wave | $\left[\frac{\sin\beta_1}{V_{S1}}, 0, -\frac{\cos\beta_1}{V_{S1}} \right]$ or $\left[p, 0, -\left[\frac{1}{V_{S1}^2} - p^2 \right]^{1/2} \right]$ |
| Reflected SV-wave | $\left[\frac{\sin\beta_1}{V_{S1}}, 0, +\frac{\cos\beta_1}{V_{S1}} \right]$ or $\left[p, 0, +\left[\frac{1}{V_{S1}^2} - p^2 \right]^{1/2} \right]$ |
| Transmitted SV-wave | $\left[\frac{\sin\beta_1}{V_{S1}}, 0, -\frac{\cos\beta_2}{V_{S2}} \right]$ or $\left[p, 0, -\left[\frac{1}{V_{S2}^2} - p^2 \right]^{1/2} \right]$ |
| Reflected P-wave | $\left[\frac{\sin\beta_1}{V_{S1}}, 0, +\frac{\cos\alpha_1}{V_{P1}} \right]$ or $\left[p, 0, +\left[\frac{1}{V_{P1}^2} - p^2 \right]^{1/2} \right]$ |
| Transmitted P-wave | $\left[\frac{\sin\beta_1}{V_{S1}}, 0, -\frac{\cos\alpha_2}{V_{P2}} \right]$ or $\left[p, 0, -\left[\frac{1}{V_{P2}^2} - p^2 \right]^{1/2} \right]$ |

Table 5.1. The slowness vector \mathbf{s} for the five waves described in Fig. 5.3.

$$\mathbf{u}_{SH} = (0, S_1, 0) \exp \left[i\omega \left[\frac{\sin \beta_1}{V_{S1}} x'_1 - \frac{\cos \beta_1}{V_{S1}} x'_3 - t \right] \right], \quad (2)$$

and that of the incident downgoing SV-wave with amplitude S_2 by

$$\mathbf{u}_{\text{SV}} = S_2(\cos \beta_1, 0, \sin \beta_1) \exp \left[i\omega \left[\frac{\sin \beta_1}{V_{S1}} x'_1 - \frac{\cos \beta_1}{V_{S1}} x'_3 - t \right] \right], \quad (3)$$

where β_1 is the angle of incidence, $(\sin \beta_1)/(V_{S1}) = p$ is called the ray parameter in the x'_1, x'_2, x'_3 -coordinate system, ω is the angular frequency, t is time, and V_{S1} is the shear-wave velocity in medium 1. The displacement vector of the incident wave is the sum of these two displacement vectors.

Note that $p = (\sin \beta_1)/(V_{S1})$ is the term occurring in Snell's law and that $\cos \beta_1 = \sqrt{1 - \sin^2 \beta_1} = \sqrt{1 - V_{S1}^2 p^2}$. We thus have the choice of defining a ray by the angle of incidence β or by the ray parameter p (see Table 5.1).

The displacements of the downgoing transmitted SH- and SV-wave are, respectively:

$$\mathbf{u}_{\text{SH}} = (0, S_1, 0) \dot{S}_H \dot{S}_H \exp \left[i\omega \left[p x'_1 - \frac{\cos \beta_2}{V_{S2}} x'_3 - t \right] \right], \quad (4)$$

and

$$\mathbf{u}_{\text{SV}} = S_2(\cos \beta_2, 0, \sin \beta_2) \dot{S}_V \dot{S}_V \exp \left[i\omega \left[p x'_1 - \frac{\cos \beta_2}{V_{S2}} x'_3 - t \right] \right], \quad (5)$$

where V_{S2} is the shear-wave velocity in medium 2 and β_2 is the angle between the transmitted wave and the normal to the interface. The displacement vector of the transmitted S-wave is the sum of the displacement vectors of these two waves. The transmission coefficients of the SH- and SV-waves (e.g. Aki and Richards, 1980) are:

$$\dot{S}_H \dot{S}_H = 2\rho_1 \frac{V_{S1} \cos \beta_1}{\Delta}, \quad (6)$$

with $\Delta = \rho_1 V_{S1} \cos \beta_1 + \rho_2 V_{S2} \cos \beta_2$ and

$$\dot{S}_V \dot{S}_V = 2\rho_1 \frac{\cos \beta_1}{V_{S1}} \frac{E V_{S1}}{D V_{S2}}, \quad (7)$$

with

$$E = b \frac{\cos \alpha_1}{V_{P1}} + c \frac{\cos \alpha_2}{V_{P2}},$$

$$F = b \frac{\cos \beta_1}{V_{S1}} + c \frac{\cos \beta_2}{V_{S2}},$$

$$G = a - d \frac{\cos \alpha_1}{V_{P1}} \frac{\cos \beta_2}{V_{S2}},$$

$$H = a - d \frac{\cos \alpha_2}{V_{P2}} \frac{\cos \beta_1}{V_{S1}},$$

$$D = E F + G H p^2,$$

$$a = \rho_2 (1 - 2V_{S2}^2 p^2) - \rho_1 (1 - 2V_{S1}^2 p^2),$$

$$b = \rho_2 (1 - 2V_{S2}^2 p^2) + 2\rho_1 V_{S1}^2 p^2,$$

$$c = \rho_1 (1 - 2V_{S1}^2 p^2) + 2\rho_2 V_{S2}^2 p^2,$$

$$d = 2 (\rho_2 V_{S2}^2 - \rho_1 V_{S1}^2),$$

where α_1 and α_2 are the angles between the reflected and transmitted P-waves and the normal to the interface, respectively. The subscripts 1 and 2 denote the media 1 and 2, respectively. ρ_1 and ρ_2 are the densities, and V_{P1} and V_{P2} are the P-wave velocities. The parameters E , F , G , H , D , a , b , c , and d are abbreviations. Without them the expression for $\hat{S}_V \hat{S}_V$ would be even more complex. Fortunately, the polarization angle can be discussed without dissecting this complicated expression.

With the transmission coefficients $\hat{S}_H \hat{S}_H$ and $\hat{S}_V \hat{S}_V$, the displacements of the transmitted SH- and SV-waves can be calculated using (4) and (5), after which the displacements due to each wave can be summed vectorially to result in the total displacement for the transmitted S-wave.

5.2.3 Complex transmission coefficients

The expressions (6) and (7) for the transmission coefficients contain functions of the angles β_1 , β_2 , α_1 , and α_2 . The first of these four angles can be freely chosen between 0° and 90° , but the other three angles are determined from their sines by Snell's law. Beyond the critical angle, the sines of these angles become larger than 1. This means that, because of the relation $\cos \beta = \sqrt{1 - \sin^2 \beta}$, the cosine then becomes imaginary, resulting in complex transmission coefficients. Of special interest are the situations where $\hat{S}_V \hat{S}_V$ happens to be complex. A complex transmission coefficient means that waves with an imaginary x'_3 -component of the normal to the wavefront are generated in medium 2. Such waves are called 'inhomogeneous'.

The real part of the normal to the wavefront specifies the direction of wave propagation; the imaginary part specifies a direction of exponential decay. This can be seen from the 'phase term' in (2) and (3) - i.e. $(\sin \beta/V) x'_1 - (\cos \beta/V) x'_3$ which can be regarded as the dot product of the slowness vector $\mathbf{s} = [(\sin \beta/V), 0, (-\cos \beta/V)]$ with the position vector $\mathbf{x}' = (x'_1, 0, x'_3)$. The slowness vector has the direction of the normal to the wavefront and magnitude $1/V$. The phase term appears in (2) and (3) as part of the argument of the exponential function. Thus for a real phase term we have a cosine or sine, but any imaginary part of the phase term, on multiplication by $i\omega$, becomes real, and results in an 'ordinary exponential'. The algebraic sign of the real part of the exponential is always such that the amplitude falls off with distance from the interface, so exponential growth never occurs.

Inhomogeneous waves decay away from the interface (they are 'bound' to the interface) and could be observed only in its immediate vicinity. What can be observed is the effect the generation of inhomogeneous waves has on the coexisting homogeneous waves. In our context we thus should look for changes in the non-critically transmitted SV-wave caused by the generation of inhomogeneous P-waves. To see under what conditions inhomogeneous P-waves are generated, we study the slowness vector of all waves generated by the incident SV-wave. In Table 5.1 these vectors are given in two different ways, once in terms of the angles between the normal to the wavefront and the x'_3 -axis and once in terms of the ray parameter p (the horizontal component of the slowness vector). The ray parameter is, of course, equal for all waves (this statement is tantamount to Snell's law). For an incident S-wave $p = (\sin \beta_1)/V_{S1}$. From Table 5.1 we conclude that an inhomogeneous transmitted or reflected P-wave is generated for $|p| > 1/V_{P2}$ or $|p| > 1/V_{P1}$, respectively.

Suppose we have

$$V_{S1} < V_{S2} < V_{P1} < V_{P2}, \text{ i.e. } \frac{1}{V_{P2}} < \frac{1}{V_{P1}} < \frac{1}{V_{S2}} < \frac{1}{V_{S1}}.$$

We consider an incident SV-wave with ray parameter p between $|p| = 0$ (normal incidence) and $|p| = 1/V_{S1}$ (grazing incidence). If

$$\frac{1}{V_{P1}} > |p| = \left[\frac{\sin \beta_1}{V_{S1}} \right] > \frac{1}{V_{P2}},$$

the transmitted P-wave is inhomogeneous, whereas all other waves remain homogeneous. The imaginary component s_3 of the slowness vector \mathbf{s} of the transmitted P-wave is

$$s_3 = -i \left[p^2 - \frac{1}{V_{P2}^2} \right]^{1/2}. \quad (8)$$

This expression takes the place of $-(\cos \alpha_2)/V_{P2}$ in the formulation of $\hat{S}_V \hat{S}_V$ in (7). Thus

E and H in (7) become complex, resulting in a complex value of $\dot{S}_V \dot{S}_V$. $\dot{S}_H \dot{S}_H$ is independent of the P-wave and its slowness vector, and thus remains real.

For

$$\frac{1}{V_{S2}} > |p| > \frac{1}{V_{P1}} > \frac{1}{V_{P2}}$$

the reflected P-wave also becomes inhomogeneous, with

$$s_3 = + i \left[p^2 - \frac{1}{V_{P1}^2} \right]^{1/2}$$

taking the place of $((\cos \alpha_1)/V_{P1})$. G in (7) is now also complex. The value of $\dot{S}_V \dot{S}_V$ is complex, whereas that of $\dot{S}_H \dot{S}_H$ remains real.

To be meaningful $|p|$ can assume values up to $|p| = 1/V_{S2}$ only. At larger values the transmitted S-waves would also become inhomogeneous and there would be no transmission in the ordinary sense. So the highest angle of incidence for which there is 'ordinary' transmission is given by $\sin \beta_1 = V_{S1}/V_{S2}$. This angle β_1 is the critical angle for SH-waves.

It can be seen from (7) that as soon as *any* of the cosines is imaginary the transmission coefficient $\dot{S}_V \dot{S}_V$ is complex since E , F , G , and H occur in the expression.

What does a complex transmission coefficient mean? A complex number $z = x + iy$ can be written as $r \exp^{i\theta}$ (where $r = \sqrt{x^2 + y^2}$) and $\theta = \tan^{-1}(y/x)$. $r = |z|$ is called the 'amplitude' of z and θ is called the 'phase' of z . A complex transmission coefficient for SV-waves means that the amplitude of the incident wave is multiplied by $|\dot{S}_V \dot{S}_V|$ and the phase is shifted by θ . For the situation we study (i.e. $0 \leq |p| < 1/V_{S2}$), $\dot{S}_H \dot{S}_H$ is always real, whereas $\dot{S}_V \dot{S}_V$ is real for $|p| \leq 1/V_{P2}$ and complex for $|p| > 1/V_{P2}$. A complex $\dot{S}_V \dot{S}_V$ may be written as

$$\dot{S}_V \dot{S}_V = |\dot{S}_V \dot{S}_V| \exp^{i\theta}. \quad (9)$$

Using (9) we rewrite (5) as:

$$\mathbf{u}_{SV} = S_2(\cos \beta_2, 0, \sin \beta_2) |\dot{S}_V \dot{S}_V| \exp \left[i\omega \left(px'_1 - \frac{\cos \beta_2}{V_{S2}} x'_3 - t \right) + i\theta \right]. \quad (10)$$

In other words, a phase shift θ occurs for $|p| = |(\sin \beta_1)/V_{S1}| > 1/V_{P2}$. It should be noted that the intervals of $|p|$ described here apply if $V_{S1} < V_{S2} < V_{P1} < V_{P2}$. A change in the order of these velocities changes the intervals of $|p|$.

5.2.4 The polarization of the transmitted S-wave

To find the polarization of the transmitted S-wave, we combine the displacements of the transmitted SH- and SV-waves. For $|p| \leq 1/V_{P2}$ the two are in phase, and the resultant wave is linearly polarized with an amplitude

$$A = \left[S_1^2 | \dot{S}_H \dot{S}_H |^2 + S_2^2 | \dot{S}_V \dot{S}_V |^2 \right]^{1/2}, \quad (11)$$

and an angle of polarization

$$\phi = \tan^{-1} \left[\frac{S_1 | \dot{S}_H \dot{S}_H |}{S_2 | \dot{S}_V \dot{S}_V |} \right]. \quad (12)$$

For $|p| > 1/V_{P2}$ the resultant wave is elliptically polarized. The polarization ellipse is described by Smith and Ward (1974):

$$\frac{U_{SH}^2}{S_1^2 | \dot{S}_H \dot{S}_H |^2} + \frac{U_{SV}^2}{S_2^2 | \dot{S}_V \dot{S}_V |^2} - 2 \frac{U_{SH} U_{SV} \cos \theta}{S_1 | \dot{S}_H \dot{S}_H | S_2 | \dot{S}_V \dot{S}_V |} = \sin^2 \theta \quad (13)$$

(see Fig. 5.4). The parameters U_{SH} and U_{SV} are the displacement amplitudes of the SH- and SV-waves, respectively, and θ is the phase difference between the SV- and SH-waves. The displacement \mathbf{u}_{SH} is parallel to the x'_2 -axis, marked X in Fig. 5.4, and the displacement \mathbf{u}_{SV} is in the x'_1, x'_3 -plane along the Z-axis in Fig. 5.4. If $\theta = 0^\circ$, the polarization ellipse in (13) degenerates into a line, i.e. the wave is linearly polarized. If $\theta = 90^\circ$ the resulting ellipse has its axes lying along the X- and Z-axes. The sign of the phase difference θ determines the orientation of the rotating displacement vector. For positive and negative phase differences, the direction of rotation is clockwise and anti-clockwise, respectively. The polarization angle ϕ for elliptically polarized waves is defined as:

$$\phi = \pm \tan^{-1} \left[\frac{S_1 | \dot{S}_H \dot{S}_H |}{S_2 | \dot{S}_V \dot{S}_V |} \right]. \quad (14)$$

The polarization angle ϕ is positive for ellipses with a major axis lying in the first and third quadrants of the X, Z coordinate system, and is negative when the major axis lies in the second and fourth quadrant.

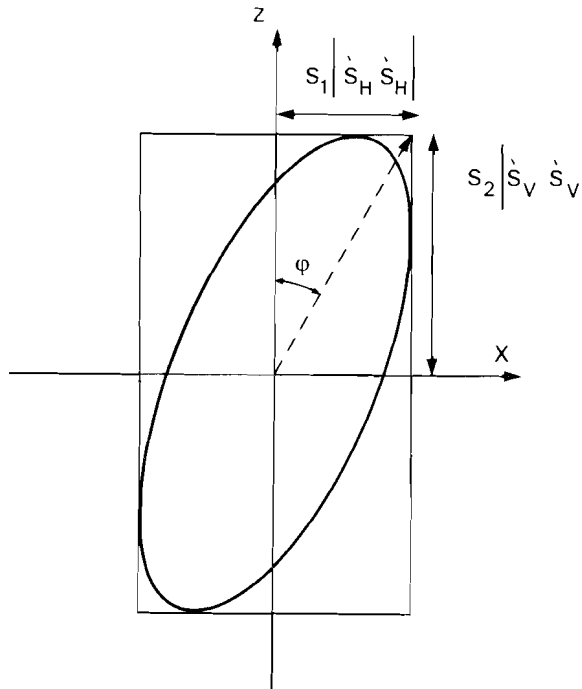


Fig. 5.4. The displacement of an elliptically polarized wave. The SH- and SV-displacements are along the X- and Z-axes, respectively. ϕ is the angle of polarization.

5.3 EXAMPLE: INTERFACE BETWEEN SANDSTONE AND HALITE

Consider an interface between sandstone (medium 1) and halite (medium 2) representing, for example, the edge of a salt dome. The velocities and densities are: $V_{S1} = 1904 \text{ m s}^{-1}$, $V_{P1} = 3047 \text{ m s}^{-1}$, $V_{S2} = 2697 \text{ m s}^{-1}$, $V_{P2} = 4618 \text{ m s}^{-1}$, $\rho_1 = 2.65 \text{ g cm}^{-3}$, and $\rho_2 = 2.16 \text{ g cm}^{-3}$. The dip δ of the interface is 45° and its strike is along the x_2 -direction (Fig. 5.5). The incident S-wave, travelling in medium 1 with its propagation direction in the x_1, x_3 -plane, has a polarization angle $\phi = 45^\circ$.

The determination of the polarization of the transmitted S-wave can be summarized as follows:

1. Choose a new local coordinate system at the interface of interest.
2. Decompose the displacement of the incident S-wave into SH- and SV-waves according to this system.
3. Calculate the displacements of the transmitted SH- and SV-waves.
4. Recombine them to the resultant transmitted S-wave.
5. Determine the polarization of the transmitted S-wave.

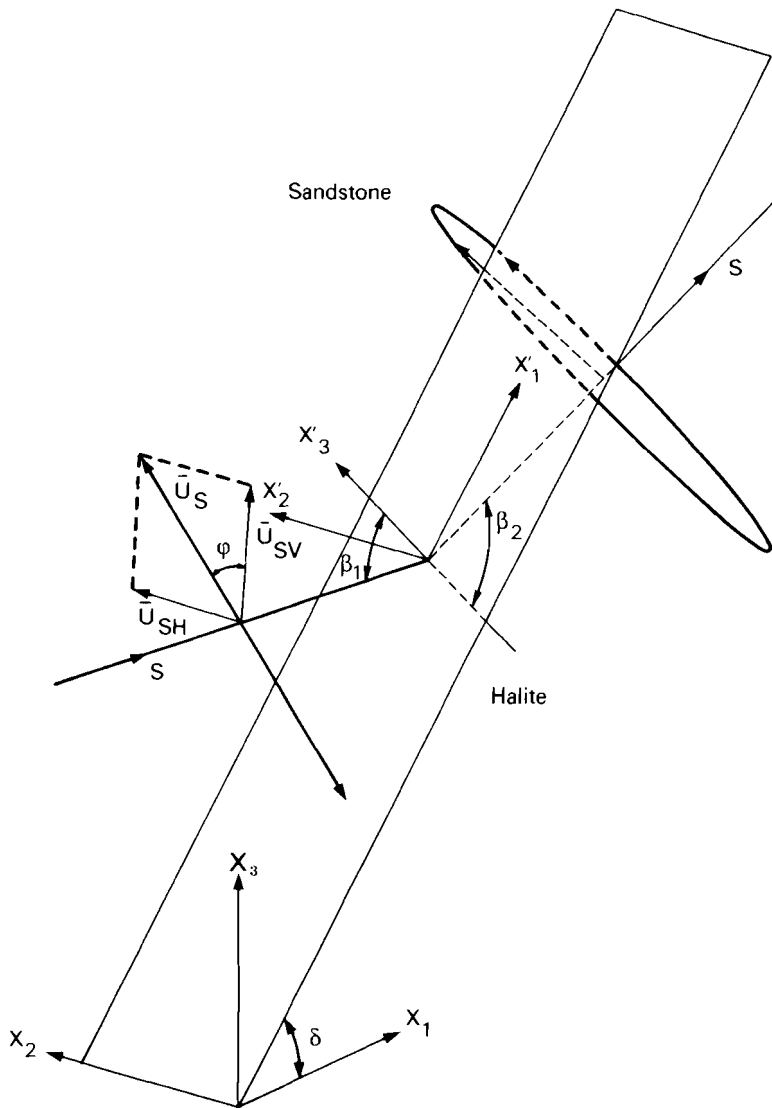


Fig. 5.5. Interface between sandstone (medium 1) and halite (medium 2). The interface has a dip $\delta = 45^\circ$, and a strike along the x_2 -axis. An incident S-wave ($\beta_1 = 40^\circ$) having a polarization angle $\phi = 45^\circ$ is shown, together with the transmitted elliptically polarized S-wave.

Due to our choice of the strike, the x_1, x_3 - plane and the x'_1, x'_3 -plane are parallel, and x_2 and x'_2 identical. For a polarization angle $\phi = 45^\circ$ the SV- and SH-displacements in both systems are identical.

The next step is to calculate the displacements of the transmitted SV- and SH-waves. The transmission coefficients for the incident SV- and SH-waves are presented in Figs 5.6 and 5.7, respectively. They are given as a function of the angle $\psi = \beta_1 + \delta$ between the incident ray and the horizontal. For $\psi = 45^\circ$ we have normal incidence at the interface, thus both figures are symmetric with respect to 45° . For $\psi < 45^\circ$, $p > 0$, and for $\psi > 45^\circ$, $p < 0$. The calculations have been done for the interval $0 \leq |p| < 1/V_{S2}$, i.e. for the entire range of 'ordinary' transmission.

Figure 5.6 shows that the SV-transmission coefficient generally increases (for $|p| > 1/V_{P2}$) with increasing $|p|$. Furthermore, one sees how the amplitude is affected by the generation of inhomogeneous P-waves. At the angles corresponding to the values of $|p| = 1/V_{P2}$ and $|p| = 1/V_{P1}$ the slope of the amplitude curve changes discontinuously as the transmitted and reflected P-wave, respectively, become inhomogeneous. The SH-transmission coefficient is not affected by these inhomogeneous waves (see Fig. 5.7). Its amplitude also increases with increasing $|p|$, but smoothly.

In Fig. 5.8 the phase difference between the SV- and SH-waves is plotted. For angles corresponding to $|p| \leq 1/V_{P2}$ there is no phase difference since both SH- and SV-transmission coefficients are real. At values of $|p| = 1/V_{P2}$ and $|p| = 1/V_{P1}$, discontinuities are observed in this figure also. For $|p| > 1/V_{P2}$ the phase difference is non-zero. This is due to the fact that the SV-transmission coefficient becomes complex, whereas the SH-coefficient remains real. The phase difference is positive for our example and increases with $|p|$.

From these data the polarization of the transmitted S-wave can be calculated as described earlier. The results are presented in Fig. 5.9. At normal incidence, i.e. at an angle of 45° to the horizontal, the polarization of the transmitted wave is the same as for the incident wave, i.e. $\phi = 45^\circ$. For increasing angles of incidence (i.e. for increasing $|p|$) the polarization angle increases until inhomogeneous waves are generated at $|p| = 1/V_{P2}$. For $|p| > 1/V_{P2}$ the angle decreases over a short interval. From Fig. 5.9 we conclude that the largest polarization change in our sandstone-halite model is about 3° . Despite this relative small change, the total polarization change of these waves may increase considerably when more interfaces are involved: if more interfaces are traversed by the S-wave before it reaches the receiver, the polarization changes accumulate.

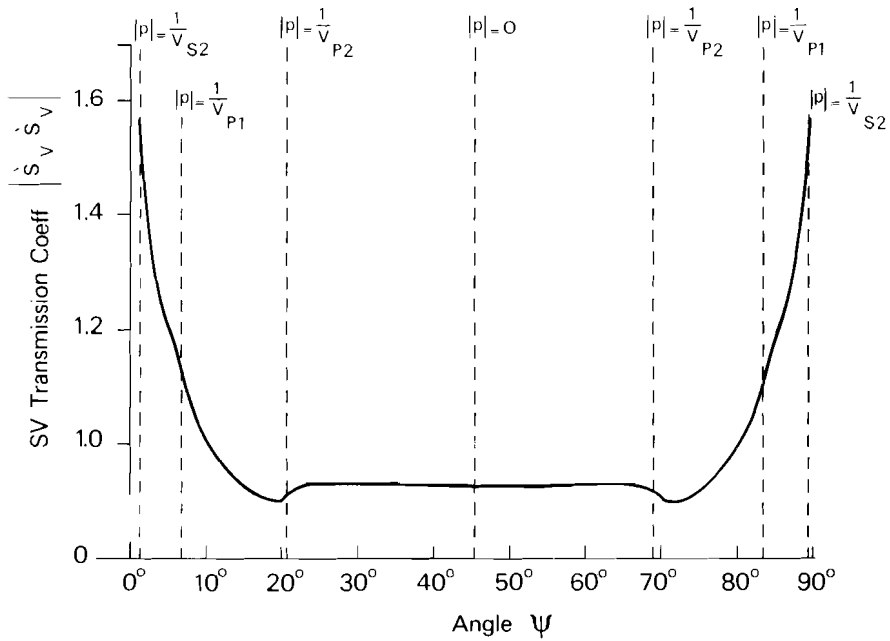


Fig. 5.6. The amplitude $|\hat{s}_V \hat{s}_V|$ of the SV-transmission coefficient as a function of the angle ψ between the incident ray and the horizontal. Some values of $|p|$ are given to illustrate the effect of inhomogeneous waves on the amplitude.

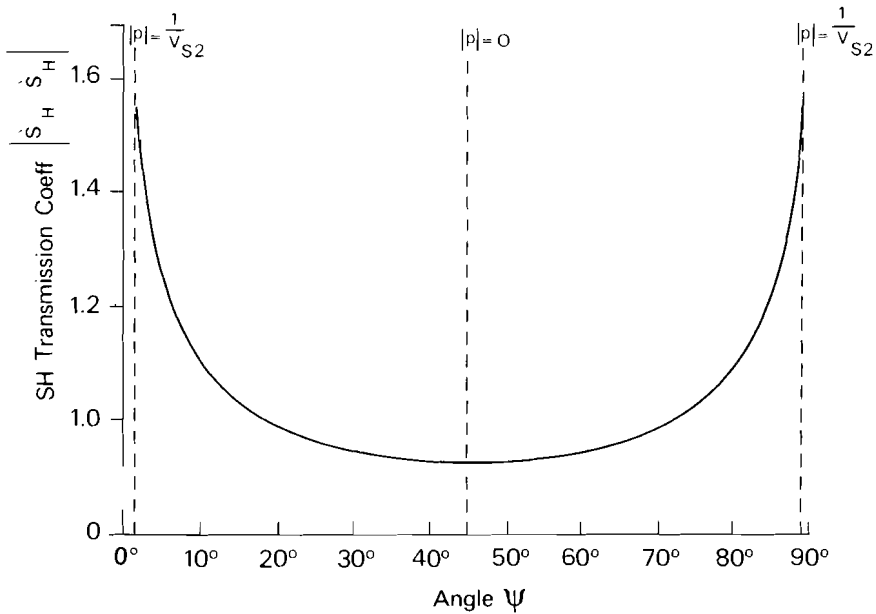


Fig. 5.7. As for Fig. 5.6, but for the amplitude $|\hat{s}_H \hat{s}_H|$ of the SH-transmission coefficient.

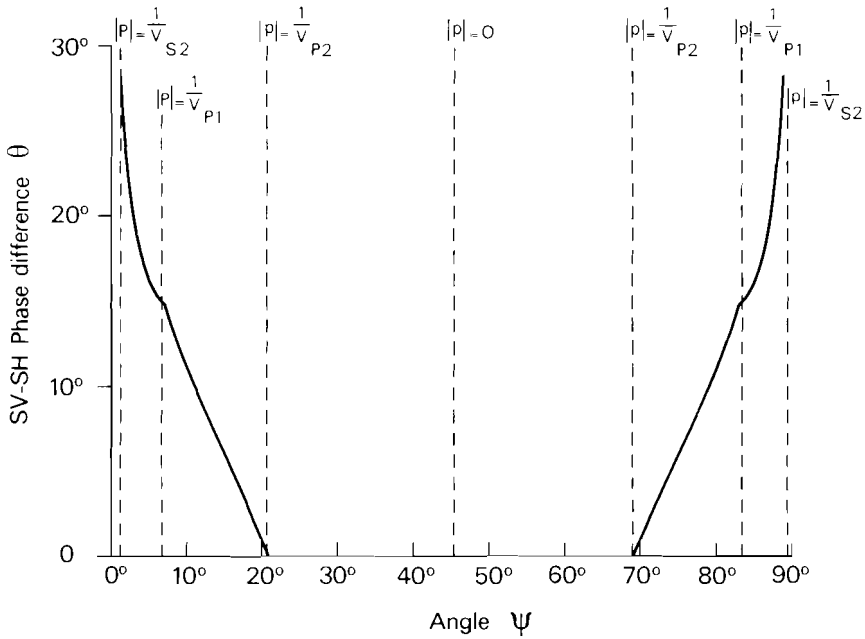


Fig. 5.8. The phase difference θ between the SV- and SH-components of the transmitted S-wave as a function of the angle ψ between the incident ray and the horizontal.

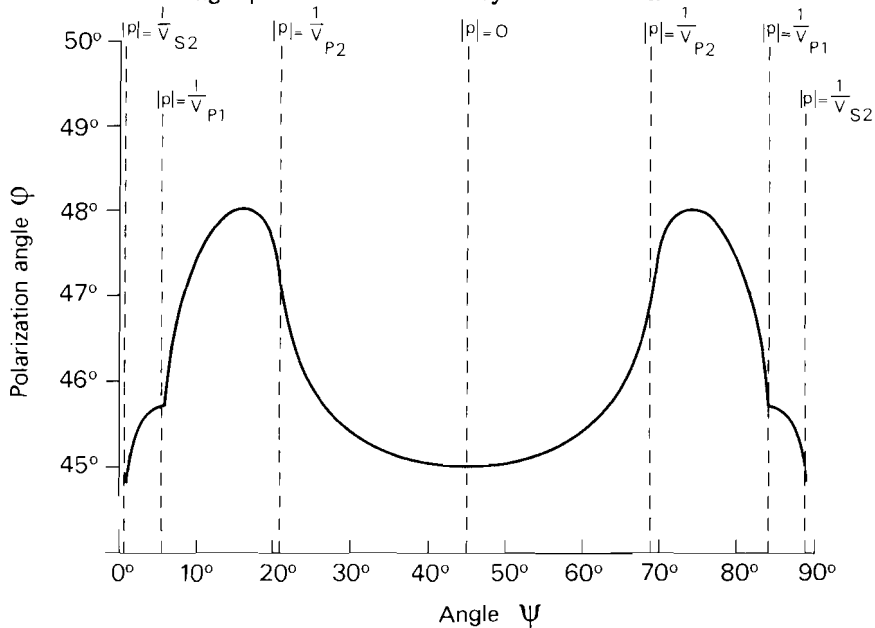


Fig. 5.9. The polarization angle ϕ of the transmitted S-wave as a function of the angle ψ between the incident ray and the horizontal.

5.4 CONCLUSIONS

The direction of polarization of an S-wave incident at an interface between two solids generally changes due to the SV- and SH-components having different transmission coefficients. The polarization change is small for small angles of incidence (at normal incidence it vanishes), and increases with increasing angle of incidence until inhomogeneous waves are generated. Because the total polarization change may be considerable, it has to be taken into account in all methods that are based on shear-wave polarization.

If any of the secondary waves becomes inhomogeneous, transmission in addition causes a time shift between the two S-arrivals. The time shift at an individual interface is generally small, but since it can accumulate it has to be taken into account in all methods that are based on the difference in arrival time of the two shear waves.

It is worth noting that anisotropy and shear-wave splitting observed in finely layered media are caused by precisely this mechanism: the many layers arranged in a periodic spatial pattern produce systematically accumulating time shifts between the two shear waves, i.e. changes in the velocities.

5.5 REFERENCES

- Aki, K. and Richards, P.G.. 1980. *Quantitative Seismology, volume 1*, W.H. Freeman and Company, San Francisco.
- Crampin, S. 1985a. Evaluation of anisotropy by shear wave splitting. *Geophysics* 50, 142-152.
- Crampin, S. 1985b. Evidence for aligned cracks in the Earth's crust. *First Break* 3, (3), 12-15.
- Evans, R. 1984. Effects of the free surface on shear wavetrains. *Geophysical Journal of the Royal Astronomical Society* 76, 165-172.
- Gal'perin, E.I. 1984. *The polarization method of seismic exploration*. Reidel Publishing Co.
- Smith, B.D. and Ward, S.H. 1974. Short note: On the computation of polarization ellipse parameters. *Geophysics* 39, 867-869.

Chapter 6

THE EFFECT OF A CHANGING ASPECT RATIO OF ALIGNED CRACKS ON SHEAR-WAVE VSPs

ABSTRACT

Media containing parallel cracks or preferentially oriented pores show elastic anisotropy. A change in the aspect ratio of these inclusions affects the resultant anisotropy. Curves, showing the velocity dependence of the two shear waves on the direction of wave propagation in such media, intersect in a singularity in a direction of propagation which depends on the size of the aspect ratio. The angle, this direction makes with the symmetry axis of the anisotropic medium, decreases for increasing aspect ratio. Characteristic of wave propagation around this angle is a change in the polarization of the leading shear wave. To demonstrate how this affects VSP measurements synthetic multi-offset VSPs at different azimuths are modelled with synthetic seismograms for media containing inclusions with small and large aspect ratios. For inclusions with small aspect ratios the polarization of the initial shear wave may change abruptly as the direction of propagation changes, whereas for large aspect ratios there is no change or the change may be more gradual. Such observations of changes of polarization and variation of delays between the split shear waves can be used to monitor the stress field as the stress changes.

This chapter has been submitted for publication as:

Douma, J. and Crampin, S. 1988. The effect of a changing aspect ratio of aligned cracks on shear-wave VSPs: a theoretical study. Submitted to *Journal of Geophysical Research*.

6.1 INTRODUCTION

Media containing aligned cracks or pores show elastic anisotropy (Crampin, 1978). Once wave propagation through such media could be modelled (Garbin and Knopoff, 1973, 1975a, 1975b; Hudson, 1980, 1981; Crampin, 1984), the resultant azimuthal anisotropy was recognized in seismic data by the comparison of observed and synthetic data. Observations of this anisotropy (summarized in Table 1 of Crampin, 1987a) are made above small earthquakes, in geothermal reservoirs, in vertical seismic profiles (VSPs), in reflection surveys and with refracted P-waves. Shear-wave splitting (indicative of the anisotropy) is observed in many different types of rocks (sedimentary, igneous, and metamorphic), and it is concluded that distributions of stress-aligned cracks exist throughout most rocks in the Earth's crust. These distributions of aligned cracks are known as extensive-dilatancy anisotropy or EDA (Crampin, 1987a; Crampin, Evans and Atkinson, 1984).

Analysing the anisotropy caused by stress-aligned cracks or pores opens wide perspectives for different geophysical disciplines. Information about the direction and density of the inclusions is important for exploration and production purposes (Crampin, 1987a). Investigating the build-up of stress before an earthquake by studying the change in the anisotropy (caused by a changing geometry of the cracks) could be of great help in earthquake prediction (Crampin, 1987b). Important characteristics of wave propagation in anisotropic media that are used to obtain this information are the shear-wave splitting and the polarizations of the split shear waves. The time delay between the split shear waves is a measure of the anisotropy along the raypath (and therefore is an indication of the density of the cracks), while the polarization of the first arriving shear wave provides information about the orientation of the cracks.

VSP probably offers the best possibilities to detect and analyse changes in anisotropy related to changes in crack geometry, especially when multi-offset shear-wave sources are used (Crampin, 1985; Crampin, 1987b; Chen, Booth and Crampin, 1987). Other methods like surface recordings of small earthquakes or reflection seismics may also show shear-wave splitting but the interpretation of the delays in the shear-wave arrivals in terms of changing crack geometry and changing stress-field is difficult because the shear waves interact at the free surface resulting in disturbed waveforms and polarizations (Evans, 1984). VSP measurements, characterized by subsurface recording of the seismic signal, are not influenced by this disturbing free-surface effect. Another advantage of VSPs above small earthquakes is the control of the source that can be fired at any time at any place. This is one of the main reasons that multi-offset shear-wave VSPs are recommended in earthquake prediction research (Crampin, 1987b), where observations may be hindered by the absence of suitable earthquakes at crucial times.

In exploration seismics some shear-wave VSPs demonstrating shear-wave splitting have already been carried out (Becker and Perelberg, 1986; Johnston, 1986; Crampin, Bush, Naville and Taylor, 1986a; Leary, Li and Aki, 1987; Li, Leary and Aki, 1987). They could all be interpreted in terms of aligned cracks. In one of them (Crampin et al., 1986a)

the observed three-dimensional waveforms were very well-matched with synthetic seismograms for waves travelling through cracked media. This demonstrates how repeated VSPs could be used to monitor changes in crack geometry and hence in the stress-field.

In this paper we will demonstrate the influence of a changing aspect ratio of the cracks on multi-offset shear-wave VSPs by calculating synthetic seismograms and their corresponding polarization diagrams (PDs). Such a study can be used in earthquake prediction research where it has been concluded that temporal changes in the anisotropy preceding an earthquake are most likely due to changing aspect ratios of the cracks (Peacock, Crampin, Fletcher and Booth, 1988; Crampin, 1987b). In exploration seismics or production engineering such a theoretical study could be of help to find out whether the cause of observed anisotropy are either cracks (having a small aspect ratio) or flattened pores (having large aspect ratios). The aspect ratio, AR , of inclusions is defined as the ratio of the thickness and the diameter of the inclusions.

6.2 THE INFLUENCE OF THE ASPECT RATIO ON CRACK-INDUCED ANISOTROPY

The models often used to describe wave propagation through cracked media are those derived by Hudson (1980 and 1981). The basic assumptions of these models are that the cracks are in dilute concentrations with a small aspect ratio. Assuming that the upper limit of the aspect ratio for which Hudson's equations are valid is probably about $AR = 0.1$, Crampin, McGonigle and Ando (1986b) showed variations of group- and phase-velocity for body waves propagating through parallel cracks with a range of aspect ratios up to 0.1. Douma (1988) investigated the range of aspect ratios for which Hudson's model gives the same results as a model, i.e. Nishizawa's (1982) ellipsoidal inclusion model, which does not assume a small aspect ratio (a review of both models is given by Douma (1988)). He showed that Nishizawa's (1982) and Hudson's (1980, 1981) formulations give almost the same results for aspect ratios up to $AR = 0.3$. In this paper Nishizawa's model is used to calculate the elastic constants of the cracked media.

Varying small aspect ratios AR ($AR = 0.001$ and $AR = 0.05$) Crampin (1987b) showed how the average time delay between shear waves, travelling at angles between 50° and 75° to the crack normal, approximately doubles, whereas it remains the same between 75° and 90° . This modelled time delay was very similar to the behaviour observed in the shear-wave splitting above small earthquakes in California (Peacock et al., 1988). Although there are several parameters describing the crack geometry (crack orientation, crack density, aspect ratio, pore-fluid, and pore-fluid pressure, Crampin, 1987a) it can be argued (Crampin, 1987b) that if the stress changes value without changing orientation this is likely to have largest effect on the crack aspect ratio.

In Fig. 6.1 the phase velocities of shear waves travelling through media containing distributions of inclusions having aspect ratios ranging from $AR = 0.0001$ to $AR = 0.3$ are shown. The results have been calculated using Nishizawa's model. The density ρ of the

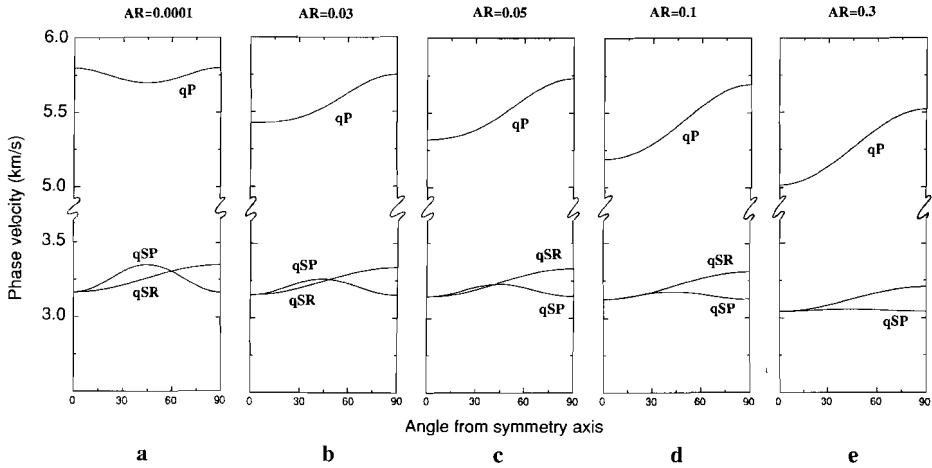


Fig. 6.1. Variation of body-wave phase-velocities in distributions of parallel liquid-filled cracks over a quadrant of directions from normal (0°) to parallel (90°) to the crack faces (after Nishizawa, 1982). The uncracked matrix velocities are $V_p = 5.8$ and $V_s = 3.349$ km s $^{-1}$. The three body waves are a quasi P-wave, qP, with nearly radial polarization and two quasi shear waves, qSP polarized parallel, and qSR polarized at right angles to the plane of incidence through the crack normal. The cracks have a crack density $CD = Na^3/V = 0.05$ (where N is the number of cracks of radius a and half-thickness d in a volume V) and aspect ratios: (a) $AR = d/a = 0.0001$ (Medium I); (b) 0.03; (c) 0.05; (d) 0.1; and (e) 0.3 (Medium II).

effective medium is assumed to be the density of the matrix material. Figure 6.1 shows that over a quadrant of directions, ranging from normal (0°) to parallel (90°) to the plane of the inclusions, the velocity variations have some characteristic features: increasing the aspect ratio moves the point where both shear-wave velocity curves intersect to smaller angles. This singular point (actually a line singularity in hexagonal anisotropic symmetries, Crampin and Yedlin, 1981) is the direction of wave propagation where the phase-velocity surfaces of the two split shear waves intersect and the first arriving shear wave changes polarization (in case of wave propagation in a symmetry plane from qSP to qSR or qSR to qSP). Moreover, Fig. 6.1 shows that as the aspect ratio increases the singularity continues to shift towards the crack-normal until it coalesces with the kiss singularity (Crampin and Yedlin, 1981) along the normal, where the two shear-wave surfaces touch tangentially.

These polarization changes may be detected in PDs, especially when wave propagation at a large range of angles is studied, as in multi-offset VSP. Identification of the singular points with their corresponding angle of wave propagation in such VSPs could be used in the analysis of temporal changes before an earthquake.

Knowledge of these points could also be used in exploration or production applications. If it is not known whether the cause of anisotropy are aligned cracks (with small aspect ratios) or aligned flattened pores (with large aspect ratios) the exact location of the singular points could help answering these questions. In this paper, the effects of

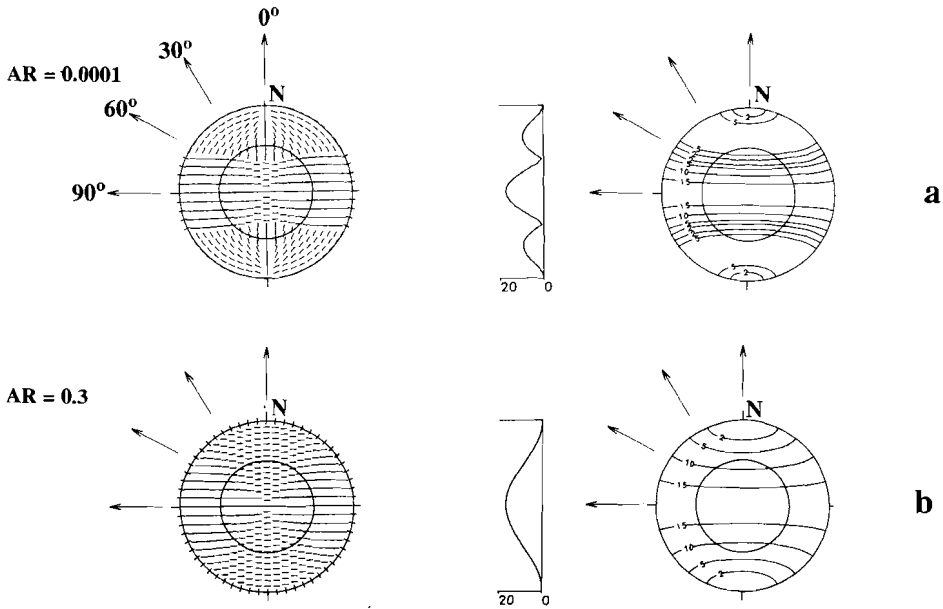


Fig. 6.2. Equal-area projections of the horizontal polarizations of the first arriving shear wave (lefthand side) and the delays between the split shear waves (righthand side) through the Media I (a) and II (b) with the vertical cracks aligned in the East-West direction. The delays are contoured in ms for path lengths of 1 km. On the left of each projection of delays is a North-South section. The inner circle represents the boundary of the effective shear-wave window at the free surface at an angle of incidence of 45° (see Evans, 1984). The calculations are based on plane-wave propagation. The corresponding phase-velocities are shown in Figs 6.1a and 6.1e, respectively. The arrows indicate the azimuths of the VSP sources used in this paper.

singular points will be identified in synthetic VSP datasets to demonstrate how their positions are influenced by a changing aspect ratio.

6.3 THE MODEL

6.3.1 The anisotropic medium

Two homogeneous anisotropic media are studied. Both contain vertically aligned liquid-filled inclusions (EDA-cracks) with a crack-normal directed to the North. In the first medium (Medium I) the inclusions have an aspect ratio $AR = 0.0001$ (almost flat cracks), whereas in the second medium (Medium II) $AR = 0.3$ (flattened pores). The matrix material is the same as used by Crampin (1984), density $\rho = 2.6 \text{ g cm}^{-3}$, Lamé constants λ and μ are respectively, 291.4 and 291.6 kbar (corresponding to P- and S-wave velocities of 5.8 and

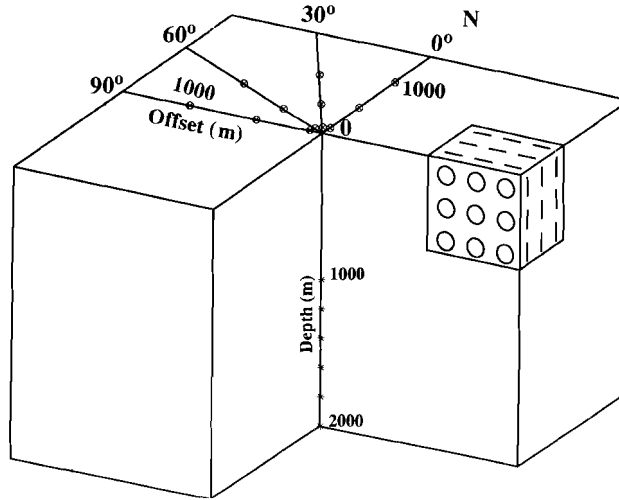


Fig. 6.3. The geometry of the multi-offset shear-wave VSP. The depths of the receivers range from 1000 to 2000 m. The sources are located at offsets of 100, 500, and 1000 m at azimuths of 0°, N30°W, N60°W, and N90°W. The distributions of vertical parallel cracks strike East-West.

3.349 km/s, respectively), and the inclusions contain water. The crack density, $CD (= Na^3/V$, where N is the number of cracks of radius a in a volume V), for both media is 0.05. The elastic constants of the compound Media I and II are calculated using Nishizawa's model and the velocity variations of the body waves travelling through these resultant anisotropic media are shown in Figs 6.1a and 6.1e, respectively. Figure 6.1a ($AR = 0.0001$) shows a shear-wave singularity at approximately 60°. At angles larger than this value the leading shear wave is a qSR-wave and at smaller angles it is a qSP-wave. In Fig. 6.1e the singularity is very close to the normal direction.

Further detail about wave propagation through these two media is shown in Figs 6.2a-b, where equal-area projections of the theoretical variations of the horizontal polarizations of the leading shear wave and the time delays between both split shear waves are presented. Figure 6.2a shows that, for the cracks with $AR = 0.0001$, the horizontal polarizations of the leading shear wave are parallel to the strike of the vertical cracks (East-West) in a wide band across the centre of the projection. Outside this band the horizontal polarizations change by nearly 90°. Along the line with an azimuth of 0° or 180° the change is the largest: from parallel to perpendicular to the strike of the cracks. At other azimuths the change is smaller. The angles that correspond to the change-over of the horizontal polarizations denote the shear-wave singularities. In contrast to Fig. 6.2a, Fig. 6.2b does not show any singularities: at all the angles of wave propagation the polarization of the leading shear wave is polarized parallel to the strike of the inclusions.

6.3.2 The VSP geometry

The VSP acquisition geometry (shown in Fig. 6.3) used in this theoretical study consists of 6 receivers located at depths of 1000, 1200, 1400, 1600, 1800, and 2000 m in the borehole. Sources are located at 3 different offsets: 100, 500, and 1000 m and at 4 different azimuths between 0° and $N90^\circ W$ (these directions are also indicated in Figs 6.2a and 6.2b). Horizontal point forces simulating shear-wave sources are used. The direction of the forces makes an angle of 45° with the azimuthal direction. If a homogeneous medium is assumed, this VSP geometry offers the possibility to study wave propagation at ray directions between approximately 3° and 45° with the vertical.

6.4 THE MODELLING

We used the ANISEIS program to calculate synthetic VSP seismograms and their corresponding polarization diagrams for the model and geometry described above. Figures 6.4-6.7 show the results for different azimuths of the sources. In Figs 6.4a-h where the sources have an azimuth of 0° it can be seen that at source offsets 100 and 500 m both Media I and II result in a first shear-wave arrival on the horizontal transverse geophone at all geophone depths. This can be seen in the synthetic seismograms and in the horizontal PDs. The polarization of this leading shear wave is in the direction of the strike of the inclusions. Given the locations of the 6 receivers and the 2 sources (resulting in ray directions between approximately 63° and 87° with the horizontal) this result corresponds to the theoretical horizontal polarizations of Fig. 6.2 at an azimuth of 0° .

At the same azimuth, different polarizations are found if larger offsets are used. In Figs 6.4i-l, at an offset of 1000 m, the ray direction varies between approximately 45° and 63° with the horizontal. For Medium I the polarization of the first arriving shear wave is perpendicular to the strike of the inclusions at receiver depths 1000, 1200, and 1400 m. At a depth of 1600 m (ray direction 58°) the ray is very close to the direction of the shear-wave singularity. There is almost no delay between the split shear waves and the linear motion of the source is preserved. At 1800 m, however, there is shear-wave splitting again, but now with the polarization of the leading shear wave parallel to the strike of the inclusions, as in Figs 6.4a-h. Medium II does not have a point singularity, and Figs 6.4k-l show consistent initial polarization at all depths (in the direction of the strike of the inclusions).

In Fig. 6.5 the same calculations have been carried out as for Fig. 6.4, but now for sources at an azimuth of $N30^\circ W$. The results are in general similar to those of Fig. 6.4, but the singular point of the shear-wave velocities for Medium I is now located closer to the horizontal direction: a sudden change in the horizontal polarization now takes place at a receiver depth of 1400 m instead of 1600 m at a source offset of 1000 m. This result agrees with Fig. 6.2. In Figs 6.6 and 6.7 the results are shown for

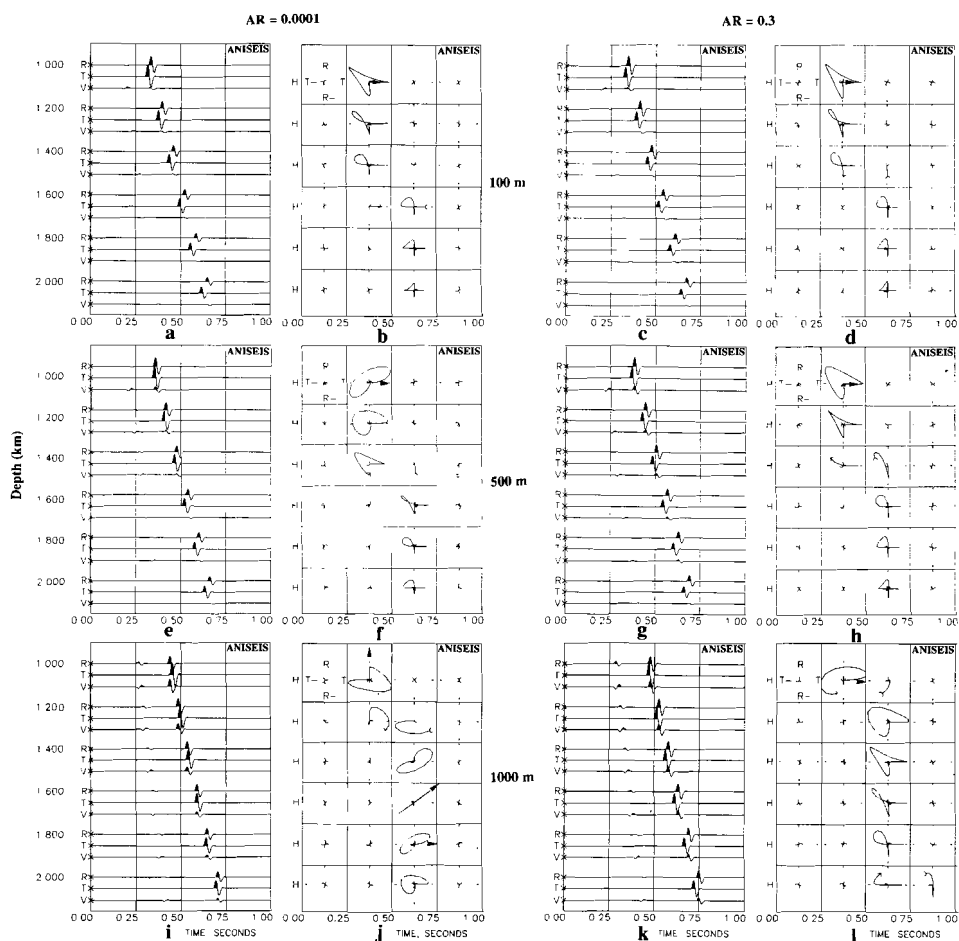


Fig. 6.4. VSP synthetic seismograms (a, e, i) and (c, g, k) and their corresponding horizontal polarization diagrams (b, f, j) and (d, h, l) for the Media I and II, respectively. The source offsets used are 100 m (a-d), 500 m (e-h), and 1000 m (i-l). All have an azimuth of 0° . The seismograms are shown for three-component geophones. The directions V, R and T are fixed in the sagittal plane: V = vertical, R = horizontal radial and T = horizontal transverse. The direction of the leading shear wave is indicated by an arrow in the top window of each polarization diagram. The arrow is repeated only if the initial polarization changes.

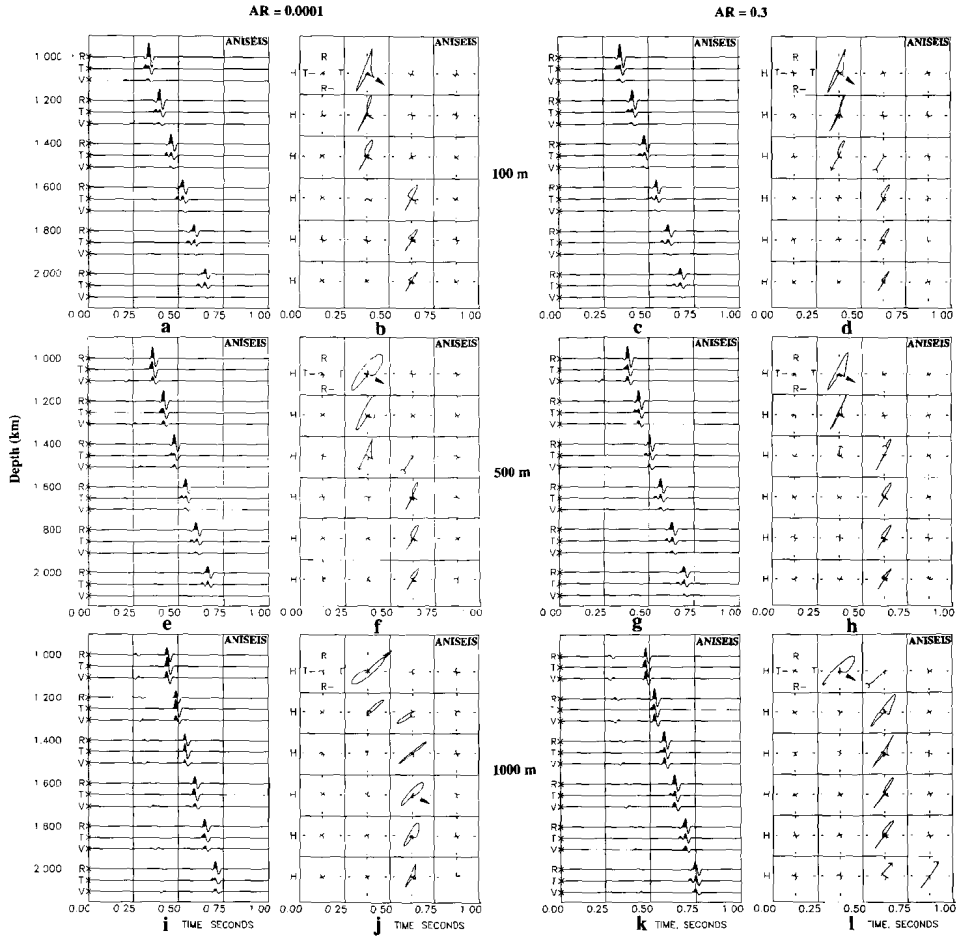


Fig. 6.5. As for Fig. 6.4, but for sources at an azimuth of N30°W.

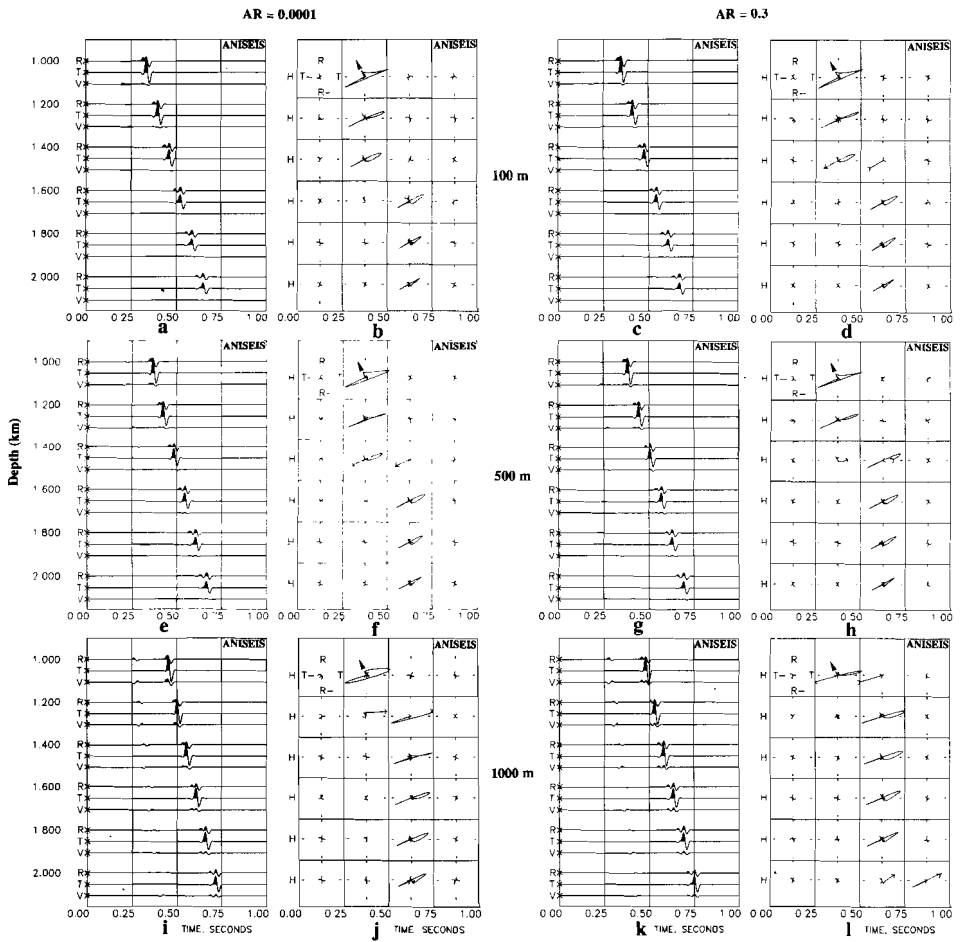


Fig. 6.6. As for Fig. 6.4, but for sources at an azimuth of $N60^\circ W$.

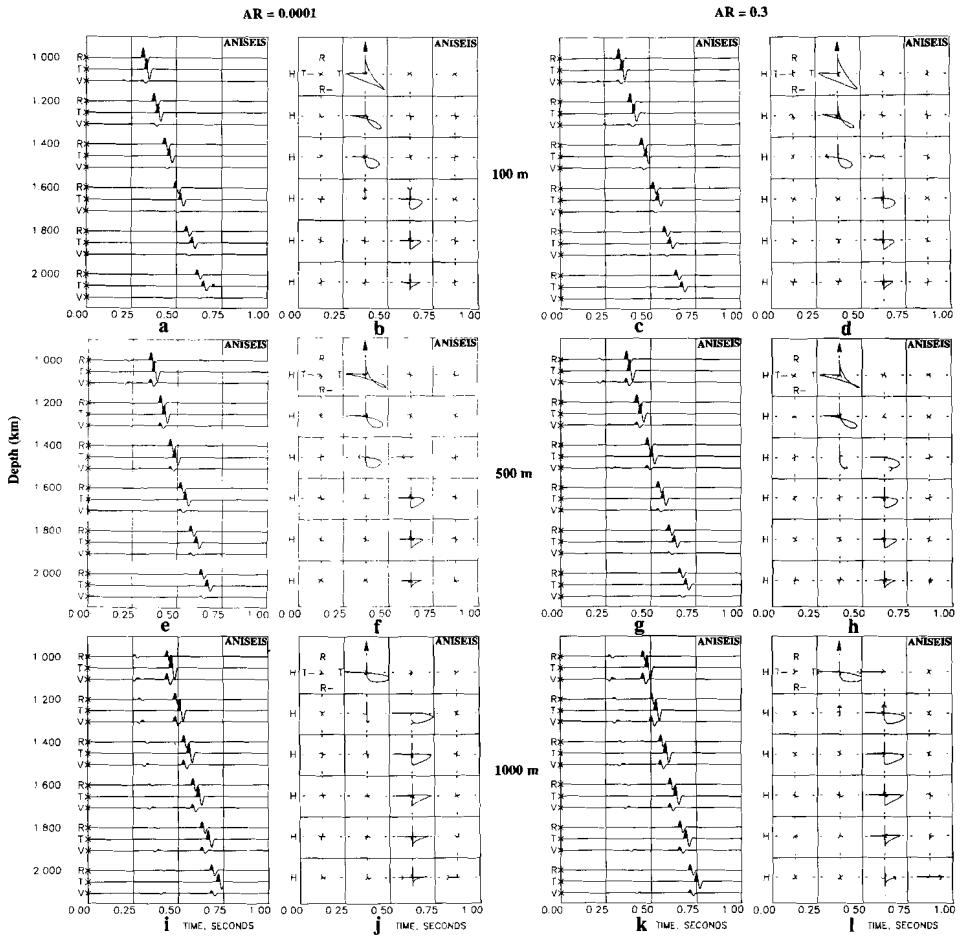


Fig. 6.7. As for Fig. 6.4, but for sources at an azimuth of $N90^\circ W$.

sources at an azimuth of N60°W and N90°W, respectively. Both figures do not show any sudden change in the polarization of the leading shear wave: it is parallel to the strike of the inclusions throughout the figures. Considering the angles of wave propagation in our VSP geometry this result agrees again with Fig. 6.2.

6.5 CONCLUSIONS

Changes of the aspect ratio of cracks influence crack-induced anisotropy. An important diagnostic for changing aspect ratios is the identification of the shear-wave singularity where the two shear-wave velocity surfaces intersect and where no shear-wave splitting exists. At the corresponding angle of wave propagation the polarization of the first arriving shear wave suddenly changes. Variations of the aspect ratio correspond to changes in these angles.

It has been demonstrated how multi-offset VSP-data, providing us with data for wave propagation at a large range of angles, is an excellent data-acquisition technique to observe such changes. If the VSPs are carried out at different moments with exactly the same geometry temporal variations of the stress-field can be monitored. It is shown that if the aspect ratio increases due to such stress-changes the directions of the singularities move closer to the horizontal. This means that the singularities in multi-offset VSPs will be observed at shallower depths if the same source offset and azimuth are used. Our synthetic results also show that the polarization changes are accompanied by a change in the rotation of the particle motion: it changes from clock-wise to anti-clockwise or vice versa. These observations are promising diagnostics to analyse stress changes in VSPs. It should be noted that shear-wave splitting has very little effect on seismograms conventionally displayed as time series, but has very distinctive effects when the seismograms are displayed in polarization diagrams.

ACKNOWLEDGEMENTS

We thank Macro Ltd. and Applied Geophysical Software Inc. for permission to use the ANISEIS package for calculating the seismograms and plotting all the figures except Figs 6.1 and 6.3. One of the authors (JD) thanks the British Geological Survey for the opportunity given to carry out part of this research during a short visit to Edinburgh. The work of SC and the computing was supported by the Natural Environment Research Council and this paper is published with the approval of the Director of the British Geological Survey (NERC).

6.6 REFERENCES

- Becker, D.F., and Perelberg, A.I. 1986. Seismic detection of subsurface fractures. 56th S.E.G. Meeting, Houston, Expanded Abstracts, 466-468.
- Chen, T.-C., Booth, D.C. and Crampin, S. 1987. Shear-wave polarizations near the North Anatolian Fault - III. Observations of temporal changes. *Geophysical Journal of the Royal Astronomical Society* 91, 287-311.
- Crampin, S. 1978. Seismic wave propagation through a cracked solid: polarization as a possible dilatancy diagnostic. *Geophysical Journal of the Royal Astronomical Society* 53, 467-496.
- Crampin, S. 1984. Effective anisotropic elastic constants for wave propagation through cracked solids. *Geophysical Journal of the Royal Astronomical Society* 76, 135-145.
- Crampin, S. 1985. Evidence for aligned cracks in the Earth's crust. *First Break* 3, (3), 12-15.
- Crampin, S. 1987a. Geological and industrial implications of extensive dilatancy anisotropy. *Nature* 328, 491-496.
- Crampin, S. 1987b. The basis for earthquake prediction. *Geophysical Journal of the Royal Astronomical Society* 91, 331-347.
- Crampin, S., Bush, I., Naville, C. and Taylor, D.B. 1986a. Estimating the internal structure of reservoirs with shear-wave VSPs. *The Leading Edge* 5, No. 11, 35-39.
- Crampin, S., Evans, R. and Atkinson, B.K. 1984. Earthquake prediction: a new physical basis. *Geophysical Journal of the Royal Astronomical Society* 76, 147-156.
- Crampin, S., McGonigle, R. and Ando, M. 1986b. Extensive-dilatancy anisotropy beneath Mount Hood, Oregon and the effect of aspect ratio on seismic velocities through aligned cracks. *Journal of Geophysical Research* 91, 12703-12710.
- Crampin, S. and Yedlin, M. 1981. Shear-wave singularities of wave propagation in anisotropic media. *Journal of Geophysics* 49, 43-46.
- Douma, J. 1988. The effect of the aspect ratio on crack-induced anisotropy. *Geophysical Prospecting* 36, 614-632.
- Evans, R. 1984. Effects of the free surface on shear wavetrains. *Geophysical Journal of the Royal Astronomical Society* 76, 165-172.
- Garbin, H.D. and Knopoff, L. 1973. The compressional modulus of a material permeated by a random distribution of free circular cracks. *Quarterly of Applied Mathematics* 30, 453-464.
- Garbin, H.D. and Knopoff, L. 1975a. The shear modulus of a material permeated by a random distribution of free circular cracks. *Quarterly of Applied Mathematics* 33, 296-300.
- Garbin, H.D. and Knopoff, L. 1975b. Elastic moduli of a medium with liquid-filled cracks. *Quarterly of Applied Mathematics* 33, 301-303.
- Hudson, J.A. 1980. Overall properties of a cracked solid. *Mathematical Proceedings of the Cambridge Philosophical Society* 88, 371-384.
- Hudson, J.A. 1981. Wave speeds and attenuation of elastic waves in material containing cracks. *Geophysical Journal of the Royal Astronomical Society* 64, 133-150.
- Johnston, D.H. 1986. VSP detection of fracture-induced velocity anisotropy. 56th S.E.G. Meeting, Houston, Expanded Abstracts, 464-466.
- Leary, P.C., Li, Y.-G and Aki, K. 1987. Observation and modelling of fault-zone fracture seismic anisotropy-I. P, SV and SH travel times. *Geophysical Journal of the Royal Astronomical Society* 91, 461-484.
- Li, Y.-G, Leary, P.C. and Aki, K. 1987. Observation and modelling of fault-zone fracture seismic anisotropy-II. P-wave polarization anomalies. *Geophysical Journal of the Royal Astronomical Society* 91, 485-492.
- Nishizawa, O. 1982. Seismic velocity anisotropy in a medium containing oriented cracks - transversely isotropic case. *Journal of Physics of the Earth* 30, 331-347.

Peacock, S., Crampin, S., Fletcher, J.B. and Booth, D.C. 1988. Shear-wave splitting in the Anza seismic gap, Southern California: temporal variations as possible precursors. *Journal of Geophysical Research* 93, 3339-3356.

*Chapter 7***VSP TRAVELTIME INVERSION FOR
TRANSVERSELY ISOTROPIC MEDIA****ABSTRACT**

Traveltime inversion of multi-offset VSP data is used more and more in exploration seismics. **Isotropic traveltime inversion** applied to multi-offset VSP arrival times of quasi P- and S-waves propagating through layered transversely isotropic media, may introduce errors in the depths of the interfaces between the layers. With the vertical velocities obtained at the borehole as the isotropic velocities of the layers, this inversion establishes interfaces which result in traveltimes that fit the traveltimes for the anisotropic media the best. For a medium consisting of a horizontal isotropic low-velocity layer on top of a transversely isotropic layer 2D isotropic inversion results in an anticline (with a form depending on the azimuth) if the axis of symmetry of the transversely isotropic layer is horizontal, whereas the result is a syncline (independent on the azimuth) for a vertical axis of symmetry. **Transversely isotropic traveltime inversion** (based on the azimuthal dependence of critically refracted qP- and qS-waves recorded just below the interface) results in the original transversely isotropic model if the axis of symmetry is horizontal. Moreover, this inversion scheme can successfully be used to determine the strike and dip of slightly dipping interfaces.

This chapter has been submitted for publication as:

Douma, J. 1988. Traveltime inversion applied to VSP arrival times in transversely isotropic media. Submitted to *Journal of Geophysical Research*.

7.1 INTRODUCTION

Vertical Seismic Profiling (VSP) is a rapidly evolving technique in exploration seismics. It offers the possibility to analyse reflected and transmitted seismic waves generated by a source located at the surface and recorded by geophones positioned in a borehole (or vice versa). From such an analysis the properties of the medium around the borehole through which the waves have travelled can be studied. Processing and interpretation techniques for VSP data have been described in detail by Gal'perin (1974), Hardage (1985), and Balch and Lee (1984). Most of the applications of VSP have been summarized by Oristaglio (1985).

One of the methods to study the medium in the vicinity of the well is traveltime inversion. In this paper the traveltime inversion of multi-offset VSP data (the sources have different offsets from the borehole) is investigated. Such an inversion has already been carried out by many authors in order to obtain seismic velocities of layered media (Stewart, 1984; Pujol, Burridge and Smithson, 1985), the structure of the interfaces separating the layers (Miller, 1983; Lines, Bourgeois and Covey, 1984) or even both (Deplante and Oristaglio, 1986). With the same objective rather similar tomographic methods have also been developed and applied to VSP data (Chiu and Stewart, 1987).

All these inversion schemes (except for the method of Chiu and Stewart (1987)) assume an isotropic medium. This implies that if one or more layers are anisotropic the result of these schemes may become questionable. Seismic waves travelling in different directions through an anisotropic layer generally have different velocities, whereas in isotropic layers the velocities are equal for all directions. Whenever such a dependence of velocity on direction is neglected in processing, errors in the final results may be introduced. It is investigated what the effect of anisotropy is on the final results of a traveltime inversion scheme (based on isotropy) when this scheme is applied to synthetic multi-offset VSP data calculated for a transversely isotropic subsurface.

The effects of disregarding anisotropy in standard processing techniques have already been noted in reflection seismics: reflector-depths calculated from P- and S-wave stacking velocities and event times show large differences against each other and against actual depths obtained from well logs (Banik, 1984; Winterstein, 1986). These results are not always troublesome; on the contrary, they can be of great help to identify anisotropic subsurface layers (Winterstein, 1986). In seismology it has also been reported how the failure to take account of anisotropy may give erroneous results: the hypocentral locations of local earthquakes can seriously be mislocated (Doyle, McGonigle and Crampin, 1982).

All these misleading results can be corrected as soon as the anisotropy of the medium is known. To invert for all the 21 independent elastic constants of a general anisotropic medium seems to be hopeless at present (Červený and Firbas, 1984a). Therefore, assumptions about the type and degree of anisotropy and about its direction of symmetry (e.g. assuming weak transverse isotropy with a horizontal axis of rotational symmetry) are often made to make the inversion simpler. Such assumptions seem to be justified by the large amount of anisotropy observations that can be modelled by 'simple' anisotropic

models (e.g. Crampin, Bush, Naville and Taylor, 1986a; Alford, 1986). Most of the inversion results published so far are based on Backus' (1965) approximate equations for the angular variation of the quasi P-wave (qP-wave) phase velocity over a plane in a weakly anisotropic medium. Several authors used these equations to explain observed angular variations of qP-wave velocities in refraction studies over oceanic and continental regions (Backus, 1965; Bamford, 1977; Crampin and Bamford, 1977; Bamford and Nunn, 1979; Crampin, McGonigle and Bamford, 1980; White and Whitmarsh, 1984; Shearer and Orcutt, 1985; Crampin, McGonigle and Ando, 1986b), but the equations have also been used in large 3D P-wave travelt ime inversion of earthquake data (Hirahara and Ishikawa, 1984). Approximate equations have also been derived for the quasi-shear waves (Crampin, 1977). However, only a few authors (Shearer and Orcutt, 1986) used both Backus' and Crampin's approximate equations to analyse observed velocity variations of qP- and qS-waves in refraction data. From the coefficients of these equations the elastic parameters of the anisotropic medium can be derived. Other inversion methods which are not based on these equations have also been used or suggested (Doyle, Crampin, McGonigle and Evans, 1985; White, Martineau-Nicoletis and Monash, 1983; Chiu and Stewart, 1987; Ivansson, 1987) to invert for the anisotropy parameters.

In this paper Backus' (1965) and Crampin's (1977) approximate formulae for qP- and qS-waves are used to study synthetic multi-offset VSP data generated in transversely isotropic media (with a horizontal axis of rotational symmetry). The elastic parameters of these media are inverted for by applying these formulae to critically refracted qP- and qS-waves. It is investigated whether a transversely isotropic model, (geologically) simpler than the isotropic model obtained with the isotropic travelt ime inversion, exists which results in travelt imes that fit the synthetic travelt ime data just as good as the travelt imes for the isotropic model.

7.2 THEORY

Anisotropy with respect to elastic wave propagation is recognized more and more in the Earth's crust and upper mantle. Not only in seismology studies but also in exploration seismics anisotropy has been observed (Crampin, 1987). Necessary to recognize and understand anisotropy are forward and inverse modelling schemes. Before such schemes will be discussed wave propagation in anisotropic media is reviewed.

7.2.1 Review of elastic wave propagation in anisotropic media

In anisotropic media there are three body waves in each direction of phase propagation. For weakly anisotropic media the three waves are a quasi-compressional qP-wave, and two quasi-shear qS-waves. These waves have velocities (which are generally

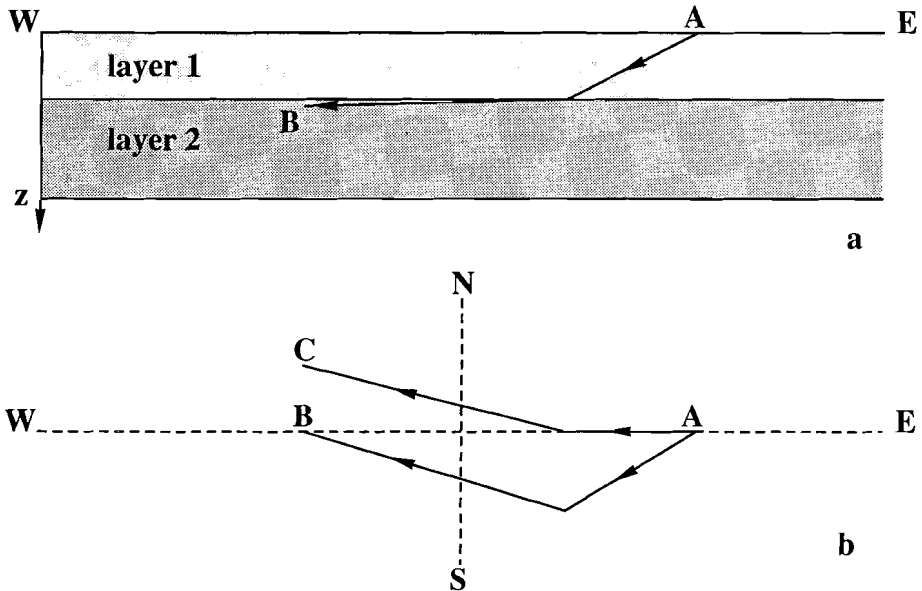


Fig. 7.1. Rays travelling through a medium consisting of an isotropic layer 1 on top of an anisotropic layer 2. At their interface the rays are critically refracted. If the construction plane (the cross-section (a)) perpendicular to the interface containing both source *A* and receiver *B* is not a symmetry plane the ray starting at *A* in this plane has to deviate from the plane in order to arrive at *B*, as shown in the plan view (b). If the ray would not deviate it would after refraction arrive at *C* (outside the construction plane).

different from each other) that are a function of the direction of phase propagation and their polarizations (being mutually orthogonal) are usually not parallel to the propagation vector or wavefront. Only in isotropic media (a special case of anisotropic media) the velocities are independent on the direction of phase propagation and the polarization directions are parallel to the propagation vector or the wavefront.

The dependence of the body wave velocity on the phase direction in anisotropic media implies that the velocity of energy transport (group velocity) is generally not directed perpendicular to planes of equal phase (propagating with the phase velocity). Therefore, in an anisotropic medium body waves emanating from a point source travel along rays (at the group velocity) with directions that are usually different from the phase propagation directions along which plane waves travel (at the phase velocity). Whereas the magnitude and direction of the phase- and group velocity are generally different in anisotropic media these quantities are equal in non-dispersive isotropic media. It is the group velocity and the direction of energy transport (the ray direction) that are measured in most of the observations, whereas it is the phase velocity that is described in most analytical formulae.

The phase velocity and polarization of plane waves travelling through anisotropic media can be obtained by solving an eigenvalue problem (see e.g. Helbig, 1958; Musgrave,

1970; Crampin, 1981). The three eigenvalues and eigenvectors obtained for each direction of the wave normal correspond to the phase velocities (or its inverse value: the slowness) and the mutual orthogonal polarizations of the plane waves, respectively. The result for all phase directions is a phase velocity surface spanned by all the endpoints of the phase velocity vectors or a slowness surface spanned by all the slowness vectors. For detailed information how these surfaces are related to the wave surface (describing the angular dependence of the group velocity) and the ray slowness surface (describing the angular dependence of the inverse of the group velocity: the ray slowness) the reader is referred to other papers, e.g. Helbig (1958, 1984) and Musgrave (1970).

The difference between phase- and group velocity affects the ray path in layered anisotropic media (Booth and Crampin, 1983; Shearer and Orcutt, 1985). Consider a horizontal isotropic layer 1 on top of an anisotropic layer 2 (Fig. 7.1a). In order to calculate the traveltimes of wave energy travelling from a source *A* at the surface to a receiver *B* in the anisotropic layer the ray path has to be known. If the medium would be isotropic the ray would lie in the plane perpendicular to the interface containing both source and receiver (the construction plane). In our anisotropic model, however, energy radiating from the source *A* and propagating in the construction plane deviates from this plane (unless the plane is a symmetry plane) as soon as it is refracted at the interface between both layers and arrives at a point *C* (outside the construction plane) instead of at the receiver *B* (Fig. 7.1b). This phenomenon can be explained by the fact that refraction at the interface is controlled by the phase velocity direction, whereas energy transport is controlled by the group velocity. Because both velocity vectors may differ significantly in an anisotropic medium the deviation shown in Fig. 7.1b may be large. Thus in order to have the ray started at the source *A* and ended at the receiver *B* it immediately has to deviate away from the construction plane as it leaves the source. Once its path is known the corresponding traveltimes can be calculated.

The time-distance curve of critically refracted waves travelling from *A* to *B* is a straight line with a slope equal to the inverse value of the magnitude of the group velocity along the refractor in the direction of the source-receiver azimuth (see Appendix) if the construction plane is a symmetry plane (then there are no ray-path deviations). If the construction plane is not a plane of symmetry the time-distance curve is no longer a straight line, but becomes curved (Shearer and Orcutt, 1985). Only at large distances (large source offsets) the slope of this curve is related again to the group velocity in the direction of the source-receiver azimuth. At intermediate distances it is related to the group velocity in other directions. Shearer and Orcutt (1985) showed, however, that even for large anisotropy the time-distance curves can be approximated very well by straight lines with slopes corresponding to the group velocity in the direction of the source-receiver azimuth. This indicates that the traveltimes perturbations due to ray perturbations are only a second-order effect.

7.2.2 Forward modelling schemes in anisotropic media

In recent years various methods have been developed to calculate traveltimes and amplitudes of body waves travelling through layered anisotropic media. Methods based on the anisotropic reflectivity method for calculating synthetic seismograms from point sources in horizontally layered anisotropic media have been developed by Booth and Crampin (1983) and Fryer and Frazer (1984, 1987). A numerical scheme valid for these kind of media and based on the Cagniard-de Hoop method has been developed quite recently by van der Hijden (1987).

A method that can deal with laterally inhomogeneous anisotropic media is the ray method. Although the ray method is an approximate method and less accurate than the schemes just mentioned its ability to describe wave propagation in complex geological situations is an important advantage above the more exact methods. According to Červený (1972) early work (published in Russian) on the application of the ray method to inhomogeneous anisotropic media was carried out by Babich (e.g. Babich (1961)). Differential equations describing the wave propagation in these media and allowing the computation of the rays, traveltimes, and amplitudes were derived. In western literature such work was done by Vlaar (1968, 1969) and later on by Červený and co-authors (e.g. Červený (1972)). (A graphical approach of the ray method in spherically layered anisotropic media was given by Helbig (1966)). Although most of the differential equations derived are valid for 3D geometries, most of the applications were restricted to 2D anisotropic situations (Červený, Molotkov and Pšenčík, 1977; Červený and Firbas, 1984a). Only quite recently Gajewski and Pšenčík (1987, 1988) developed the numerical algorithm ANRAY86 (a description of the program is given by Gajewski and Pšenčík (1986)) for ray tracing in 3D laterally varying anisotropic media. The anisotropic layers in their algorithm may have 21 independent elastic constants which even may vary in one and the same layer. However, just as in all other ray techniques it is assumed that the variation of the medium parameters within a seismic wavelength is small.

In the study described in this paper the ANRAY86 program is used as the forward modelling program to calculate traveltimes in a multi-offset VSP geometry. Although the program has originally been designed for seismology purposes (i.e. the source is located in the subsurface, whereas the receivers are at the free surface) it can be used to calculate the rays and traveltimes in a VSP geometry by using the principle of reciprocity (i.e. in the program the sources and receivers are located at the positions of the receivers and sources in our actual VSP, respectively). At this stage normally two-point ray tracing is carried out to calculate the ray connecting the source and receivers and the corresponding traveltime. However, two-point ray tracing in three dimensions is quite complicated and time-consuming. Therefore, boundary value ray tracing is performed in the program: all the rays are sought that connect the source (positioned at a VSP receiver position) with an arbitrary point on a specified line at the surface. If a large number of rays are found that end at this line, the ray connecting the source and a specified receiver position on the line and the corresponding traveltime are obtained by applying the paraxial ray method (Červený,

Klimeš and Pšenčík, 1984b). This paraxial ray method interpolates the ray information obtained at all the rays ending at the line to a ray ending at the specified endpoint position. In the VSP situation studied in this paper this endpoint is our source position, whereas the starting points of the rays are the receiver positions in our borehole.

The ray method has already been used to study VSP data in anisotropic media (Leary, Li and Aki, 1987; Li, Leary and Aki, 1987), but the models used were restricted to 2D anisotropic models. In the current study also 3D anisotropic models will be studied.

7.2.3 *Isotropic traveltimes inversion of VSP data*

There are several inversion schemes which result in the parameters of a final subsurface model from a given set of observed traveltimes for multi-offset VSP and from some initial subsurface model. The final model gives traveltimes that fit the observed traveltimes best according to some error criterion. Most of these schemes are based on the assumption of an isotropic subsurface and therefore will be called 'isotropic traveltimes inversion schemes'. The 2D isotropic inversion method used in this paper (the Schlumberger program FERMAT) is almost similar to the one described by Deplante and Oristaglio (1986). The model parameters that can be inverted for in this 2D method are the isotropic P- and S-wave velocities within the subsurface layers and the depths of the points sampling the interfaces (represented by cubic splines) separating these layers (in this paper, however, FERMAT is only used to invert for the interfaces). Starting with an initial model of the subsurface (often based on well log information or zero-offset VSP) standard isotropic 2D ray tracing is performed through this model. The calculated traveltimes are compared with the observed traveltimes and the mismatch between both is used to update the initial model. The model parameters are updated in such a way that the difference between both sets of traveltimes is minimized in a least squares sense. The process is repeated until some convergence criterion is satisfied, e.g. the difference in traveltimes lies within some small error.

7.2.4 *Transversely isotropic traveltimes inversion of VSP data*

Applying isotropic traveltimes inversion to data obtained in anisotropic media may give erroneous results (Doyle et al., 1982). In this paper a traveltimes inversion scheme for multi-offset VSP data in transversely isotropic media with a horizontal axis of rotational symmetry is presented. This transversely isotropic traveltimes inversion is based on the azimuthal phase-velocity variations of critically refracted qP- and qS-waves. The velocities of these waves are estimated from the arrival times of the waves at a receiver close to the interface of refraction: if ΔT is the difference in traveltimes of the critically refracted wave if the source is moved (at a constant azimuth) over a horizontal distance $\Delta x = S_2 - S_1$ (Fig. 7.2) then the magnitude V_a of the apparent velocity is given by: $V_a = \Delta T / \Delta x$. The dependence of

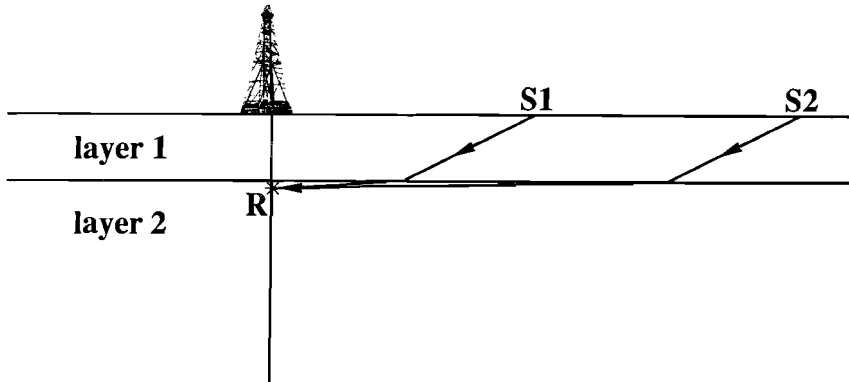


Fig. 7.2. The apparent velocity of critically refracted waves in layer 2 can be determined in a VSP from their difference in arrival time at the borehole receiver R if the source is moved from $S1$ to $S2$.

this velocity on the azimuth ϕ can be obtained by repeating the measurement with sources at different azimuths with respect to the borehole.

a) Horizontal layers

The apparent velocity measured in such refraction experiments for horizontally layered media is the group velocity along the refractor in the direction of the source-receiver azimuth (see Appendix, equation (A3)). The assumption made here is that the direction of the ray path is identical to the direction of the source-receiver azimuth. As described before this is only strictly true for construction planes being symmetry planes, but is also a very good approximation if only traveltimes are being studied (as in this paper). Further we will assume that the magnitude and the direction of the group velocity can be approximated by the magnitude and direction of the phase velocity, which is the case for weak anisotropy (Backus, 1965).

The azimuthal phase-velocity variations of the critically refracted qP- and qS-waves thus obtained can be interpreted with Backus' (1965) and Crampin's (1977) approximate equations for the azimuthal velocity variations of qP- and qS-waves. These equations are strictly applicable only in planes of mirror symmetry and are only valid for first order differences in the elastic constants of the anisotropic and the isotropic medium, i.e. for weakly anisotropic media (Crampin and Kirkwood, 1981; Crampin, 1982). Only for some special symmetry systems Backus' equations can also be applied to off-symmetry planes (Crampin and Kirkwood, 1981). Backus' equation for the qP-wave and Crampin's equations for the qS-waves have coefficients that are linear combinations of the elastic

constants of the anisotropic medium. Therefore, the equations can be applied to observed angular velocity variations in order to invert for the elastic constants of the medium. In refraction studies such an inversion has often been carried out, but only in a few of these studies receivers in a borehole have been used (Stephen, 1985).

Consider an anisotropic medium with three orthogonal symmetry planes $x_1 = 0$, $x_2 = 0$, $x_3 = 0$, where x_3 is the vertical. Crampin and Radovich (1982) showed (using Backus' (1965) and Crampin's (1977) equations) that for such an anisotropic medium the phase velocity variations in one of the vertical symmetry planes ($x_2 = 0$) are approximately:

$$\rho V_{qP}^2(\phi) = A + B\cos 2\phi + C\cos 4\phi, \quad (1a)$$

$$\rho V_{qSP}^2(\phi) = D + E\cos 4\phi, \quad \text{and} \quad (1b)$$

$$\rho V_{qSR}^2(\phi) = F + G\cos 2\phi, \quad (1c)$$

where

$$A = \left[3(c_{3333} + c_{1111}) + 2(c_{1133} + 2c_{1313}) \right] / 8;$$

$$B = (c_{3333} - c_{1111}) / 2;$$

$$C = \left[c_{3333} + c_{1111} - 2(c_{1133} + 2c_{1313}) \right] / 8;$$

$$D = \left[c_{3333} + c_{1111} - 2(c_{1133} - 2c_{1313}) \right] / 8;$$

$$E = -C;$$

$$F = (c_{2323} + c_{1212}) / 2;$$

$$G = (c_{2323} - c_{1212}) / 2;$$

ρ is the density, V_{qP} , V_{qSP} , and V_{qSR} are the phase velocities, respectively, of the qP-wave and of the two qS-waves, qSP polarized parallel, and qSR polarized perpendicular, to the plane of incidence, c_{ijkl} are the elastic constants referred to the x_1 , x_2 , and x_3 -axes and ϕ is the direction of the phase velocity measured from the vertical x_3 -direction. There is no problem using these equations for phase velocity variations in a horizontal symmetry plane: the x_3 -axis is then defined to be horizontal and ϕ becomes the azimuth measured from this horizontal axis (from now on ϕ will be measured positively clockwise from its origin). The elastic constants are then referred to the new coordinate system.

If the anisotropic medium is transversely isotropic with an axis of rotational symmetry

in an arbitrary horizontal x_3 -direction the coefficients A - G in equations (1a-c) become (using the condensed two-suffix notation c_{pq} for the elastic constants c_{ijkl} , see e.g. Thomsen (1986)):

$$A = \left[3(c_{33} + c_{11}) + 2(c_{13} + 2c_{44}) \right] / 8;$$

$$B = (c_{33} - c_{11}) / 2;$$

$$C = \left[c_{33} + c_{11} - 2(c_{13} + 2c_{44}) \right] / 8;$$

$$D = \left[c_{33} + c_{11} - 2(c_{13} - 2c_{44}) \right] / 8;$$

$$E = -C;$$

$$F = (c_{44} + c_{66}) / 2;$$

$$G = (c_{44} - c_{66}) / 2;$$

When equations (1a-c) are used to fit observed velocity data the x_3 -direction is usually unknown. Therefore, the direction ϕ in these equations has to be replaced by $\phi - \alpha$, where α is the angular separation of the x_3 -axis from the origin of ϕ , in order to keep using the equations (1a-c) for fitting observed velocity variations. Substituting $\phi - \alpha$ in (1a-c) gives:

$$\rho V_{qP}^2(\phi) = A + B_1 \cos 2\phi + B_2 \sin 2\phi + C_1 \cos 4\phi + C_2 \sin 4\phi, \quad (2a)$$

$$\rho V_{qSP}^2(\phi) = D + E_1 \cos 4\phi + E_2 \sin 4\phi, \quad \text{and} \quad (2b)$$

$$\rho V_{qSR}^2(\phi) = F + G_1 \cos 2\phi + G_2 \sin 2\phi, \quad (2c)$$

where

$$B_1 = B \cos 2\alpha, \quad B_2 = B \sin 2\alpha$$

$$C_1 = C \cos 4\alpha, \quad C_2 = C \sin 4\alpha$$

$$E_1 = E \cos 4\alpha, \quad E_2 = E \sin 4\alpha$$

$$G_1 = G \cos 2\alpha, \quad G_2 = G \sin 2\alpha,$$

and ϕ is measured now from an arbitrarily chosen reference direction making an angle α with the (yet unknown) x_3 -direction. With equation (2a) to fit observed qP-wave velocity variations the best fitting coefficients B_1 , B_2 , C_1 , and C_2 can be determined. Two directions of symmetry (α_1 and α_2) for the 2ϕ variation can be derived from the coefficients B_1 and

B_2 :

$$\alpha_1 = \frac{1}{2} \tan^{-1} \left[\frac{B_2}{B_1} \right] \text{ and } \alpha_2 = \alpha_1 + 90^\circ . \quad (3)$$

One of these directions corresponds to the direction of maximum velocity, the other to the direction of minimum velocity for the 2ϕ velocity variation. To indicate which of the two is the direction of rotational symmetry additional information is needed. The vertical qP-velocity in transversely isotropic media with a horizontal symmetry axis is directed perpendicular to the symmetry axis and is therefore equal to the horizontal qP-velocity perpendicular to this axis. Thus by comparing the vertical qP-velocity with the horizontal qP-velocities in the α_1 - and α_2 -direction, the axis of rotational symmetry can be indicated (provided the two horizontal velocities are not equal).

The same can of course be done with the coefficients E_1 and E_2 or G_1 and G_2 when equations (2b) and (2c) are used to fit the velocity variations of qSR- and qSP-waves. Once all the coefficients $A - G$ are determined using either equations (1a-c) or (2a-c) the five elastic constants of the transversely isotropic medium can be calculated:

$$\begin{aligned} c_{11} &= A - B + C \\ c_{33} &= A + B + C \\ c_{66} &= F - G \\ c_{44} &= F + G \\ c_{13} &= -1.5 (c_{33} + c_{11}) - 2c_{44} + 4A . \end{aligned} \quad (4)$$

b) Dipping layers

The equations of the previous section can be applied to describe the azimuthal velocity variations of critically refracted waves recorded just below a horizontal refractor. For dipping refractors, however, additional terms are required to account for the azimuthal velocity variation caused by the dip of the refractor. In the Appendix an approximate equation (A16) for the apparent velocity variation of critically refracted qP-waves has been derived for a slightly dipping refractor separating an isotropic and a weakly anisotropic layer. Just as for the horizontal refractor it has been assumed that the ray path lies in the construction plane. Equation (A16) shows (when compared with (2a)) that the additional terms caused by the refractor dip describe a ϕ velocity variation (in contrast with the 2ϕ and 4ϕ variations caused by anisotropy). From the coefficients of these additional terms the dip

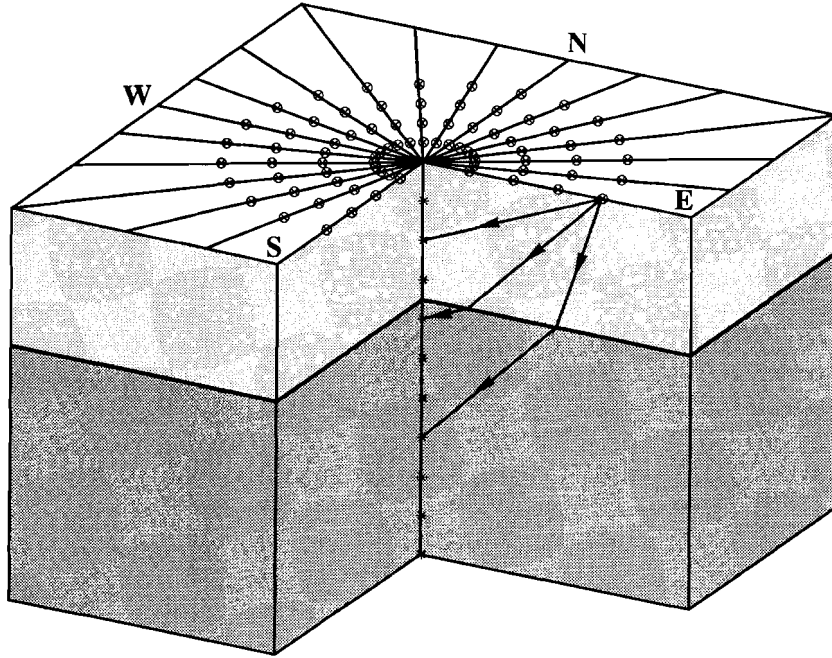


Fig. 7.3. The VSP geometry: the sources (circles) located at different azimuths and offsets from the borehole generate waves that are recorded at receivers (stars) in the borehole.

and strike of the refractor can be determined, whereas the remaining 2ϕ and 4ϕ coefficients describe some of the elastic constants of the anisotropic layer. The remaining elastic constants can be derived using the critically refracted qS-waves for which similar equations as for the qP-waves can be derived.

7.3 THE VSP GEOMETRY

In this theoretical study arrival times of body waves travelling through anisotropic media are studied for a large range of source-receiver combinations. In the borehole there are 30 receivers at equidistant depths between 20 m and 600 m and at the free surface there are 10 sources with offsets between 10 m and 900 m. Large offsets are used in order to have a wide lateral coverage of the subsurface and to be able to study critically refracted waves. The sources not only have different offsets from the borehole, but also have different azimuths. In this way azimuthal variations of the velocities or the subsurface can be studied. The geometry of such a multi-offset 'walk around' VSP is given in Fig. 7.3.

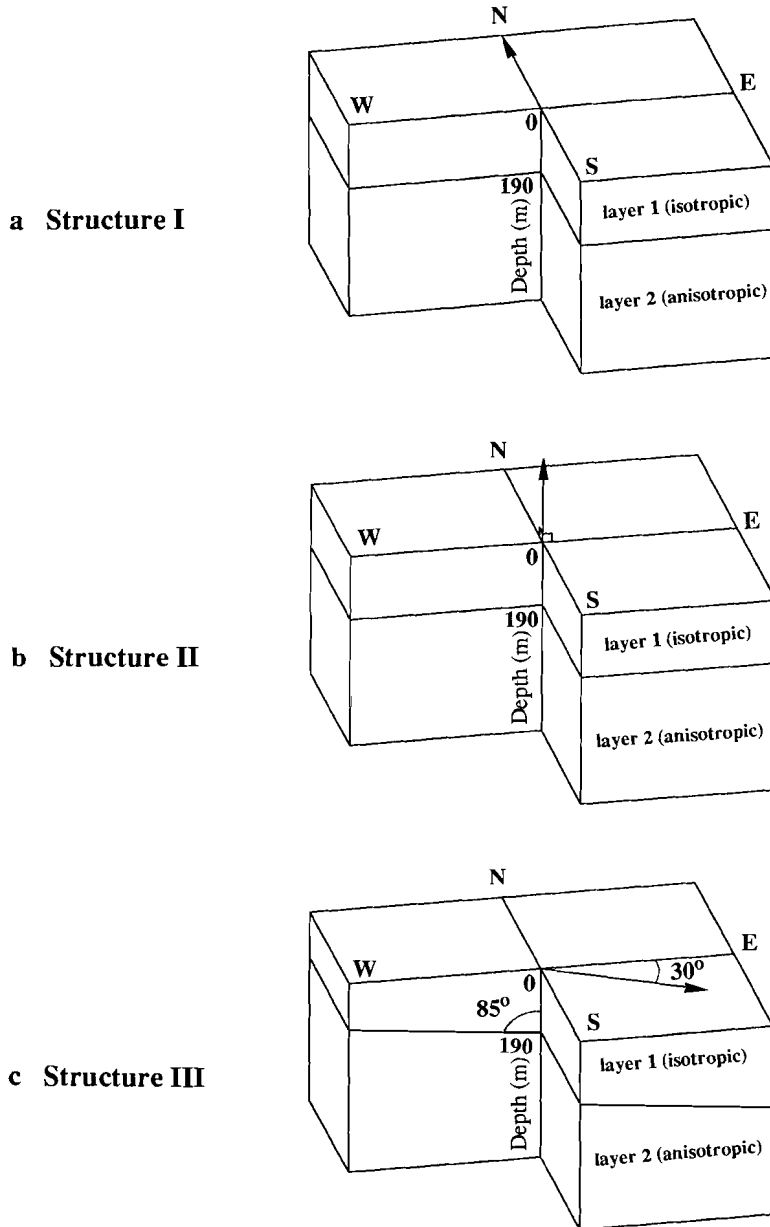


Fig. 7.4. Three transversely isotropic structures (a) structure I, (b) structure II, and (c) structure III consisting of an isotropic low-velocity layer 1 on top of a transversely isotropic layer 2. The arrows indicate the direction of rotational symmetry in the transversely isotropic layer.

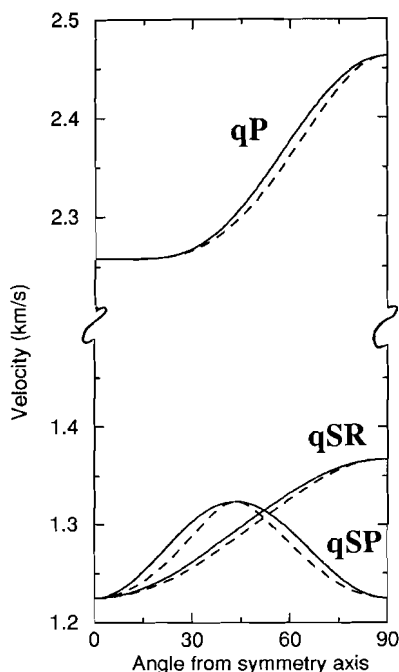


Fig. 7.5. The phase- (solid line) and group velocity (dashed line) variation from parallel (0°) to perpendicular (90°) to the axis of rotational symmetry in the transversely isotropic layer 2 of the structures shown in Fig. 7.4. The variation is shown for the quasi longitudinal qP-wave, with nearly radial polarization and for the two quasi shear waves, qSP polarized parallel, and qSR polarized at right angles to the plane of incidence through the axis of rotational symmetry.

7.4 THE TRANSVERSELY ISOTROPIC STRUCTURES

Three transversely isotropic structures are studied in this paper. All structures consist of an isotropic low-velocity layer on top of a transversely isotropic layer (Fig. 7.4). The interface separating both layers is horizontal in structure I and II, but slightly dipping eastwards in structure III (the dip is 5° and the strike is $N0^\circ E$). This interface intersects the borehole at a depth of 190 m. The isotropic layer 1 has P- and S-wave velocities of $V_p = 1800$ m/s and $V_s = 986$ m/s, respectively. The transversely isotropic layer 2 is the equivalent of an isotropic medium (with $V_p = 2500$ m/s and $V_s = 1367$ m/s) containing aligned water-filled inclusions. The crack density $CD = Na^3/\nu = 0.1$ and the aspect ratio $AR = d/a = 0.1$ (where N is the number of inclusions with radius a and half-thickness d in a volume ν). In all layers the density $\rho = 2.6$ g/cm³. The five independent elastic constants of the resultant transversely isotropic layer 2 (based on Nishizawa (1982)) are presented in Table 7.1a and 7.1b.

In structure I the axis of rotational symmetry in layer 2 is horizontal and directed to

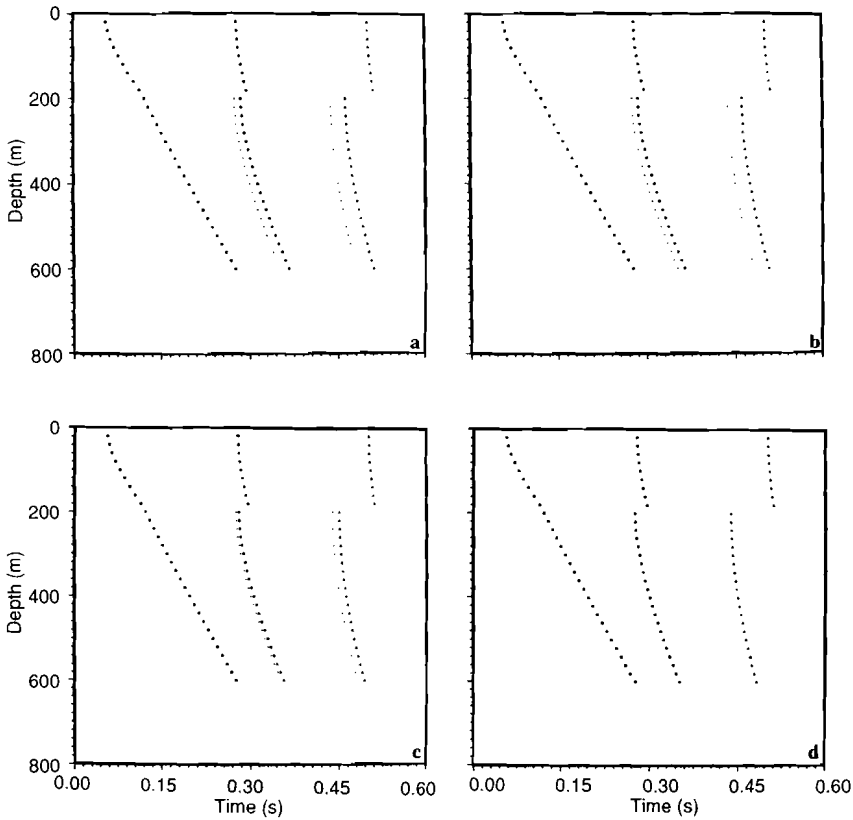


Fig. 7.6. Synthetic arrival times of the direct qP-waves as a function of the receiver depth calculated for the initial isotropic model of structure I (small dots) and for the original anisotropic structure I (large dots) at source azimuths (a) N0°E, (b) N30°E, (c) N60°E, (d) N90°E. At each azimuth the results have been calculated for three source offsets: 100 m (left series of arrival times), 500 m (middle series), and 900 m (right series).

the North; in structure II this axis is vertical and in structure III it is horizontal with an azimuth N120°E (Figs 7.4a-c). The velocities in layer 2 along and perpendicular to this symmetry axis are for the qP-wave $V_{qP//} = 2258$ m/s and $V_{qP\perp} = 2463$ m/s, respectively (they have a relative difference of about 9 %) and for the leading qS-wave $V_{qS//} = 1225$ m/s and $V_{qS\perp} = 1367$ m/s, respectively (with a relative difference of about 11 %). This implies that the vertical velocities of the qP- and the leading qS-wave in the transversely isotropic layer of structure I and III (that are perpendicular to the symmetry axis) are larger than those in structure II. The variation of the phase- and group velocity in this layer is shown in Fig. 7.5.

7.5 RESULTS

7.5.1 *Isotropic traveltimes inversion*

To demonstrate the errors traveltimes inversion based on isotropy may introduce when applied to multi-offset VSP data in transversely isotropic media, the isotropic inversion scheme FERMAT is applied to synthetic multi-offset VSP traveltimes calculated for structures I, II, and III with the ANRAY86 program.

To carry out this inversion an initial isotropic subsurface model is required. Such a model is usually constructed with a priori information about the subsurface obtained from e.g. well logging or zero-offset VSP data. In this paper we assume that once identified in these data the different subsurface layers intersected by the borehole are laterally extended away from the borehole in a horizontal direction, resulting in a horizontally layered initial model. The velocities assigned to the different layers (assumed to be isotropic) in this model are the vertical velocities obtained at the borehole.

For structure I the initial isotropic model consists of a layer 1 with $V_{P,1} = 1800$ m/s and $V_{S,1} = 986$ m/s (where $V_{P,i}$ and $V_{S,i}$ denote the isotropic P- and S-wave velocities in layer i , respectively) on top of a layer 2 with $V_{P,2} = 2463$ m/s and $V_{S,2} = 1367$ m/s (note these are the vertical velocities in the transversely isotropic layer 2 of structure I). The interface between both layers is horizontal at a depth of 190 m. The arrival times at the borehole receivers of the direct P- and S-waves travelling through this initial isotropic model are calculated using standard isotropic ray tracing and presented in Figs 7.6 and 7.7, respectively, for three source offsets (100, 500, and 900 m) and four source azimuths (N0°E, N30°E, N60°E, and N90°E). These traveltimes are expected to be observed in a multi-offset VSP experiment if the subsurface is identical to the initial isotropic model. Since structure I is transversely isotropic the traveltimes in it may be different from those calculated for the initial model. To demonstrate how large this difference may be the arrival times (calculated with ANRAY86) of the direct qP- and leading qS-waves travelling through structure I are also presented in Figs 7.6 and 7.7. A comparison of both sets of traveltimes shows that at receivers positioned above the interface (i.e. for depths smaller than 190 m) there is no difference in traveltimes, because the top layer 1 is the same in both the initial model and in structure I. At receivers below the interface, however, traveltimes differences can be observed for some azimuth and offset combinations. In general, the traveltimes for structure I are larger than those for the initial model. This difference is most pronounced for the azimuth $\phi = \text{N}0^\circ\text{E}$ and increases for increasing source offsets: at 100 m offset the difference is negligible, whereas at 900 m offset the difference can be around 30 and 60 ms for P- and S-waves, respectively. For $\phi = \text{N}90^\circ\text{E}$ (Figs 7.6d and 7.7d), however, no difference is observed, because waves generated by sources at N90°E travel through layer 2 of structure I with the same velocities as the velocities of the initial isotropic model (because just as in the initial model the waves at $\phi = \text{N}90^\circ\text{E}$ travel perpendicular to the axis of rotational symmetry). At other azimuths the waves in layer 2 of structure I in general

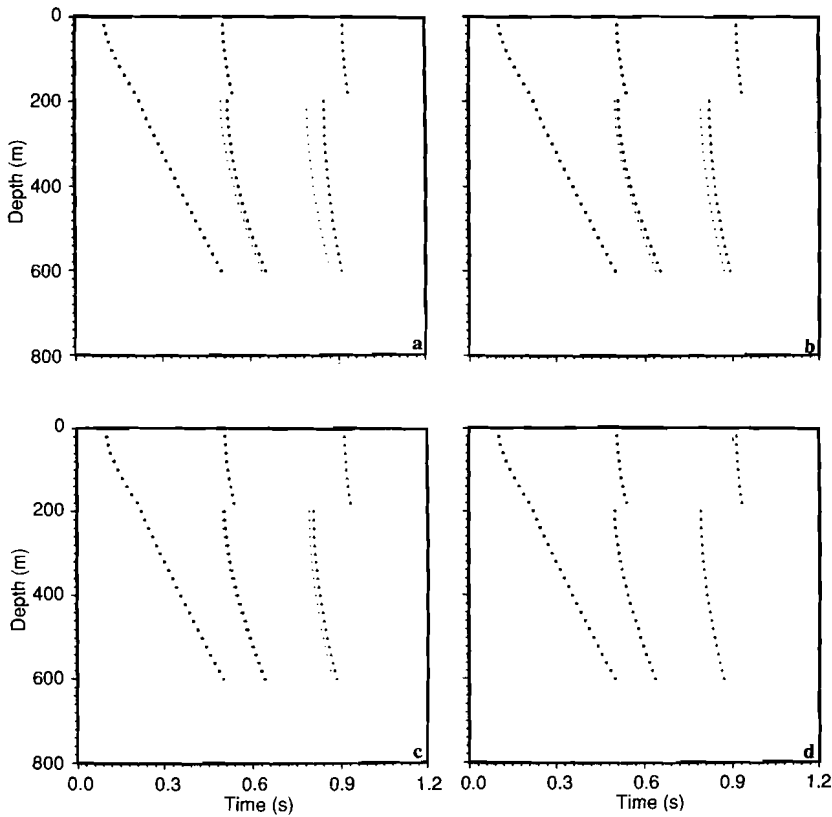


Fig. 7.7. The same as for Fig. 7.6, but now for the leading qS-waves.

travel with smaller velocities, which explains the difference in arrival times in layer 2 at azimuths different from N90°E.

Isotropic traveltimes inversion is applied to the traveltimes calculated for structure I. The traveltimes used are the qP- and leading qS-wave arrival times at the receivers below the interface calculated for source offsets (varying from 10 - 900 m) at two sides of the borehole (i.e. at ϕ and $\phi + 180^\circ$). With this traveltimes data set and the isotropic initial model derived for structure I the FERMAT inversion scheme looks for a final isotropic subsurface model best-fitting the traveltimes data set. In the inversion the velocities of the different layers are kept constant so that the fit can only be established by adjustments of the interfaces. The inversion stops as soon as the final model results in traveltimes that fit the traveltimes for structure I within 2%.

In Figs 7.8a-d the final inversion results for several source azimuths are shown together with the original position of the interface. From Fig. 7.8 it can be concluded that isotropic inversion when applied to the traveltimes data set of structure I results in an anticline structure with a form depending on the azimuth of the sources and with a top at

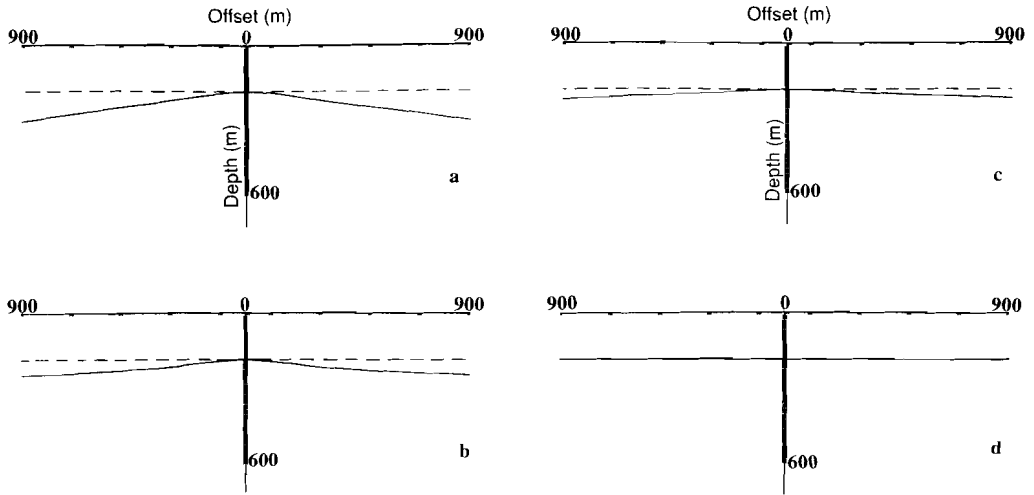


Fig. 7.8. The original interface (dashed line) of structure I and the interface (solid line) obtained by isotropic travelt ime inversion when applied to the qP- and leading qS-traveltime data calculated for structure I at different source azimuths: (a) $N0^{\circ}E/N180^{\circ}E$, (b) $N30^{\circ}E/N150^{\circ}W$, (c) $N60^{\circ}E/N120^{\circ}W$, (d) $N90^{\circ}E/N90^{\circ}W$. The first direction in this notation is along the right-hand side of the borehole in (a)-(d).

the borehole at 190 m depth. For the source azimuths $N0^{\circ}E/N180^{\circ}E$ the largest difference between the original and the resultant interface can be observed (Fig. 7.8a). For increasing azimuth this difference decreases and disappears at $N90^{\circ}E/N90^{\circ}W$. To indicate how large this difference may be we need to know which part of the resultant interface has actually been crossed by the rays, because the inversion result is only reliable for that part of the interface. In Fig. 7.9a the rays travelling through the final model obtained at $N0^{\circ}E/N180^{\circ}E$ have been plotted and they show that the resultant interface is illuminated by rays up to around 650 m offset at both sides of the borehole. Thus it can be concluded from Figs 7.9a and 7.8a that the largest difference between the original and the resultant interface is around 85 m at 650 m offset. This difference is zero at the borehole.

The anticline form of the resultant interface can be explained by considering the travelt ime differences shown in Figs 7.6 and 7.7. The travelt imes for structure I are generally larger than those for the initial model. In the inversion used here the travelt ime data for structure I can only be fitted by varying the depth of the interface in the initial model; this depth is generally increased in order to have a larger part of a ray travelling through the low-velocity layer 1 (and a smaller part through layer 2), so that the larger travelt imes fit the travelt imes for structure I.

The arrival times of the direct elastic waves travelling through the final model at $N0^{\circ}E$ (see Fig. 7.9a) and through the original structure I are presented in Figs 7.9b and 7.9c for qP- and leading qS-waves, respectively. These figures show how the travelt imes for the final model fit the travelt imes for structure I better than the travelt imes for the initial model

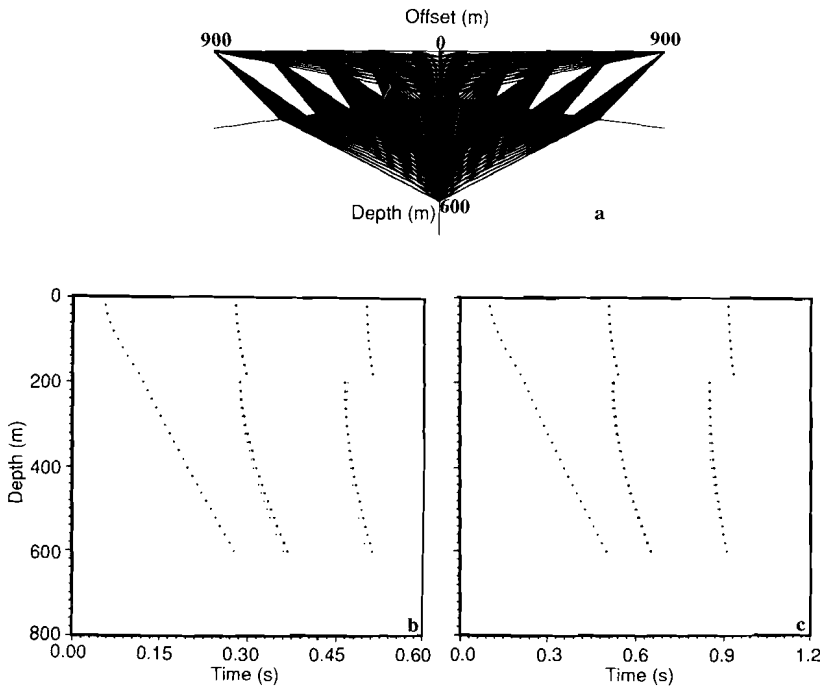


Fig. 7.9. (a) The ray paths of the direct qP- and leading qS-waves travelling through the isotropic inversion result of Fig. 7.8a and their corresponding traveltimes (small dots) presented in (b) and (c), respectively, together with the traveltimes calculated for the original anisotropic structure I (large dots) for three source offsets (the same as for Fig. 7.6) as a function of the receiver depth.

(Figs 7.6a and 7.7a).

Isotropic inversion is also applied to traveltimes data calculated for structure II, which is transversely isotropic with a vertical axis of symmetry. We follow the same procedure as for structure I. The initial model for structure II contains the same isotropic top layer and horizontal interface as the initial model for structure I, but it has a different isotropic layer 2: $V_{P,2}$ and $V_{S,2}$ are now 2258 m/s and 1225 m/s, respectively (these are the vertical velocities in the transversely isotropic layer 2 of structure II). Figs 7.10a and 7.10b show that the traveltimes calculated for the qP- and leading qS-wave at receivers below the interface are smaller in structure II than in the corresponding initial model. This is because in all directions different from the vertical (the direction of rotational symmetry) the velocities in layer 2 of structure II are larger than the vertical velocities (see Fig. 7.5), which are assigned to the isotropic layer 2 in the initial model. This also explains why the result of isotropic inversion applied to the traveltimes calculated for structure II is a synclinal structure (independent of the azimuth of the sources) with its lowest point at the borehole at 190 m depth (Fig. 7.11a): in order to decrease the difference in traveltimes

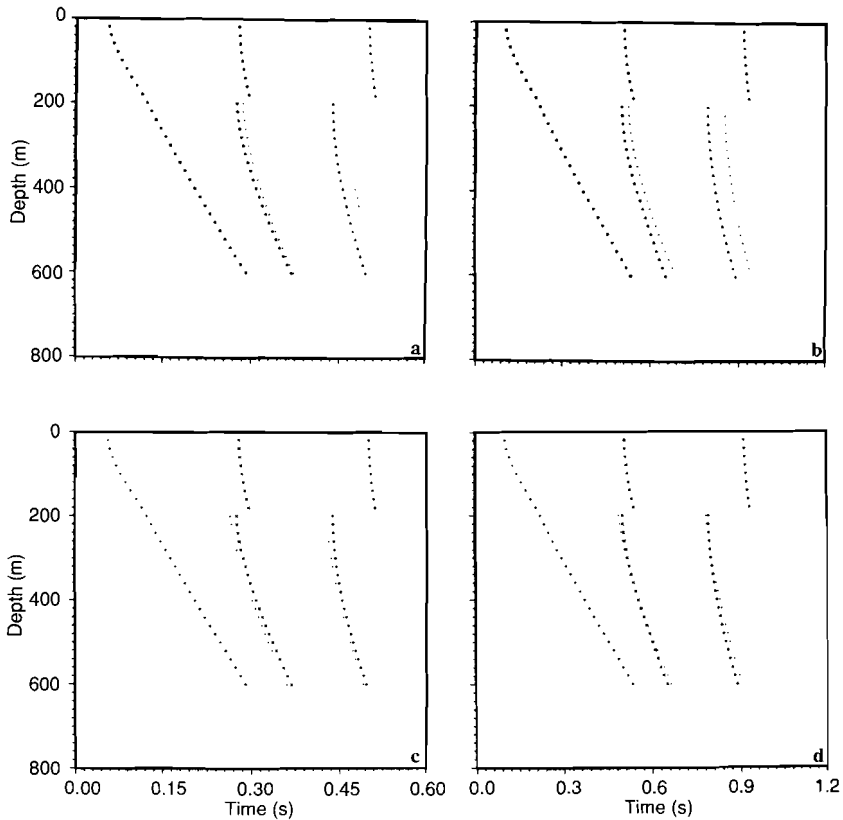


Fig. 7.10. Synthetic arrival times (small dots) of the direct qP- (a) and leading qS-waves (b) for three source offsets (the same as for Fig. 7.6) as a function of the receiver depth in the initial isotropic model of structure II together with the arrival times (large dots) of these waves in the original structure II. The same, but then for the qP- and qS-traveltimes (small dots) calculated for the isotropic inversion result of Fig. 7.11a is shown in (c) and (d), respectively, together again with the traveltimes in structure II (large dots).

between the initial model and structure II the depth of the interface away from the borehole is decreased so that the ray paths through the low-velocity layer 1 become shorter (and through layer 2 larger) resulting in smaller arrival times. The rays of the direct qP- and qS-waves travelling through the final isotropic model obtained by inversion are plotted in Fig. 7.11b and the corresponding traveltimes are presented in Figs 7.10c and 7.10d, respectively. Figs 7.10c and 7.10d show that these traveltimes fit the traveltimes for structure II very well. The raypaths in Fig. 7.11b indicate that the resultant interface is illuminated by the rays up to an offset of 850 m from the borehole. We may conclude from Fig. 7.11a that the maximum difference in depth between this interface and the original one is around 125 m at 850 m offset. This difference is zero at the borehole.

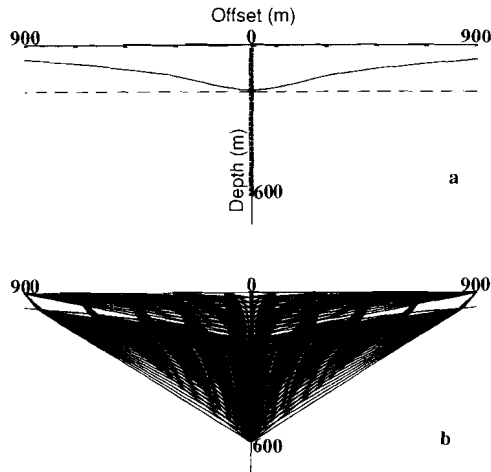


Fig. 7.11. (a) The original interface (dashed line) of structure II and the interface (solid line) obtained by isotropic traveltimes inversion when applied to the qP- and leading qS-traveltime data for structure II. (b) The raypaths of the direct qP- and qS-waves travelling through the isotropic inversion result of (a).

Finally, isotropic inversion is applied to traveltimes data calculated for structure III, which has a dipping interface and whose horizontal symmetry axis has a direction N120°E. The initial model for structure III is exactly the same as the one for structure I. The result of the isotropic inversion applied to the traveltimes data for structure III is shown in Figs 7.12a-f for several source azimuths. From these figures it can be concluded that the inversion only gives the correct interface for the source azimuths N150°W/N30°E (Fig. 7.12d), which are directed perpendicular to the symmetry axis of layer 2 in structure III. Such a result was also obtained for structure I for an azimuth perpendicular to the symmetry axis in its layer 2 and therefore the explanation of the phenomenon is exactly the same as given for structure I. For other azimuths Figs 7.12a-f show that the resultant interface is a tilted anticline intersecting the borehole at a depth of 190 m. Just as for structure I the difference between this interface and the original one in structure III is the largest for azimuths along the symmetry axis of layer 2 (here N60°W/N120°E). It can be shown that this difference may be around 115m.

7.5.2 Transversely isotropic traveltimes inversion

In the transversely isotropic traveltimes inversion described in this paper for multi-offset VSP data the azimuthal velocity dependence of critically refracted qP- and qS-waves is used. Because it is assumed that the axis of rotational symmetry of the transversely isotropic medium is horizontal only structures I and III will be studied. The apparent

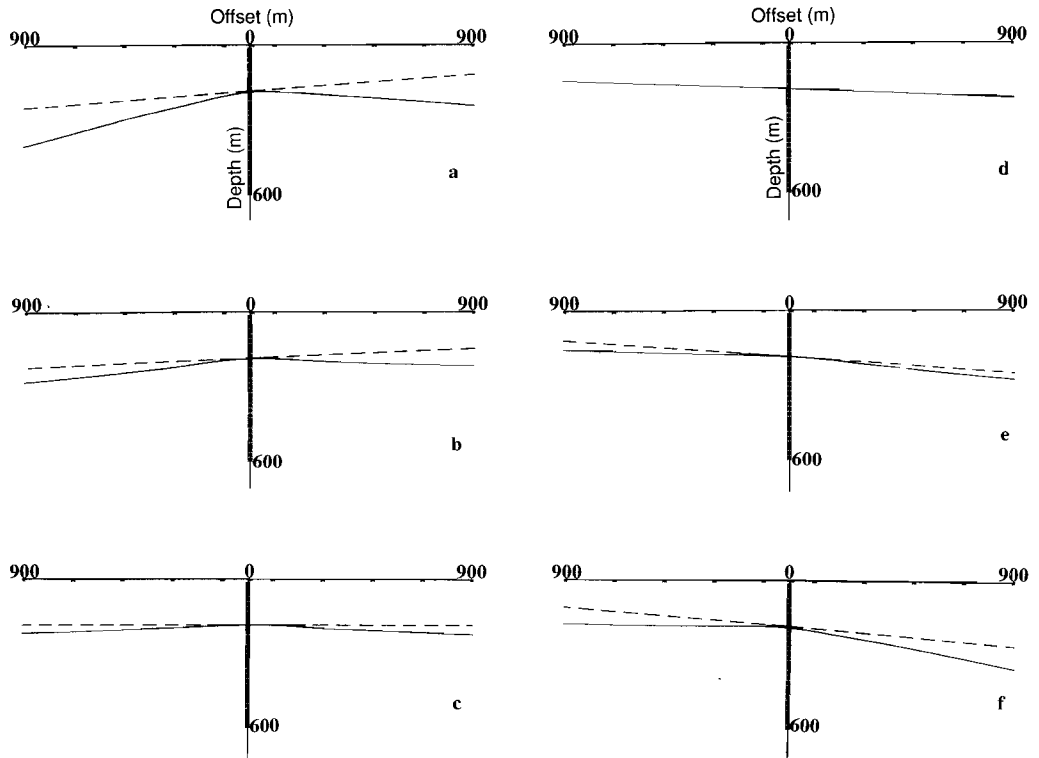


Fig. 7.12. The same as for Fig. 7.8, but now for structure III at source azimuths: (a) N60°W/N120°E, (b) N30°W/N150°E, (c) N0°E/N180°E, (d) N30°E/N150°W, (e) N60°E/N120°W, (f) N90°E/N90°W.

velocities of the critically refracted waves are derived from their arrival times at a receiver (at 200 m depth) just below the interface in both structures. Having calculated the arrival times for source offsets up to 900 m the apparent velocities are determined from the best fitting straight line through the time-distance curves. Repeating this for a large range of source azimuths velocity variations in layer 2 of both structures can be studied.

a) STRUCTURE I

In Figs 7.13a-b the velocities of the critically refracted qP- and leading qS-waves calculated for layer 2 of structure I are shown for several azimuths. Because these waves travel in the symmetry plane of the weakly anisotropic layer 2 the qP-velocities (Fig. 7.13a) can be fitted in a least squares sense by curves of the form presented in equation (2a). The best fitting curve is given by:

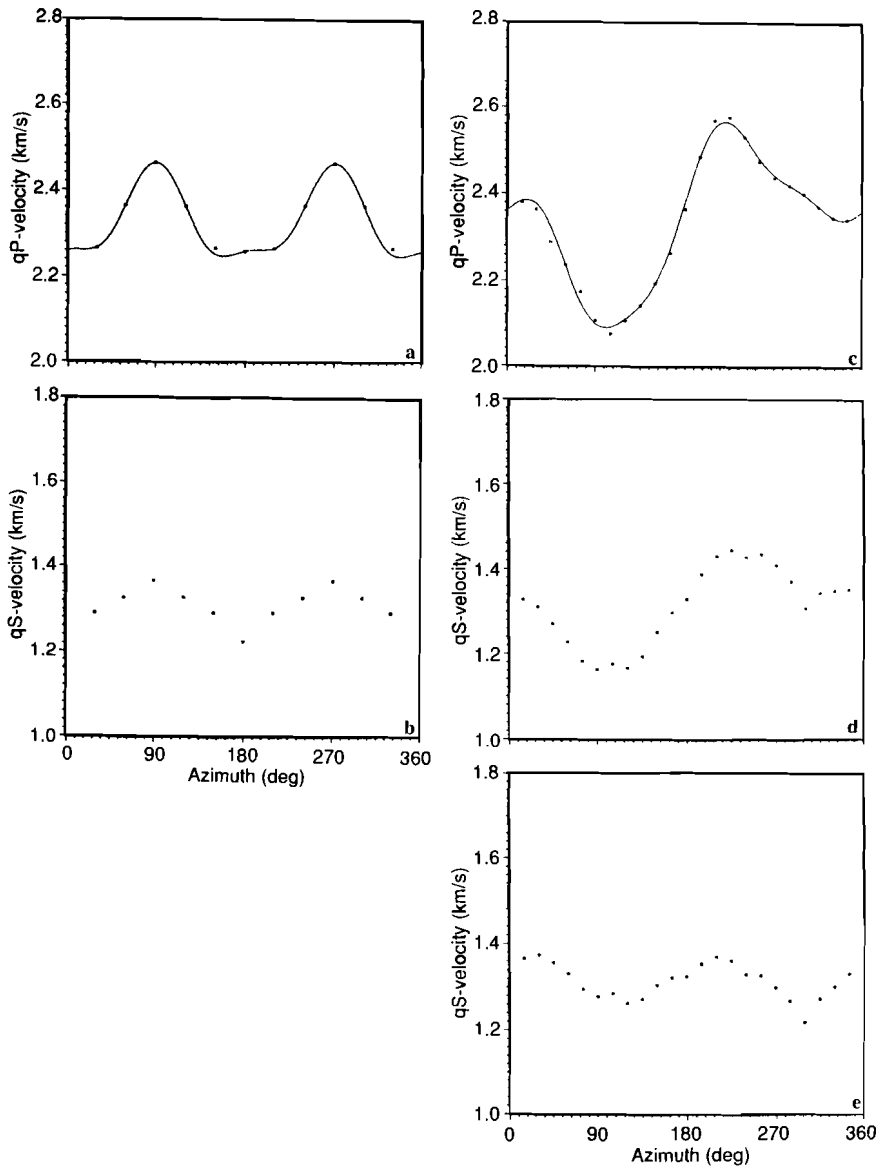


Fig. 7.13. The apparent velocity variation of the critically refracted qP- and leading qS-waves as a function of the azimuth. In (a) and (c) the qP-velocities, together with the least squares fit (solid line) are shown for layer 2 of structure I and III, respectively, whereas in (b) and (d) the leading qS-velocities are shown for layer 2 of structure I and III, respectively. The qS-velocities (d) are corrected for the dip of the interface in structure III and are shown in (e).

$$V_{qP}^2(\phi) = V_{qP_N}^2(1.0632 - 0.0942\cos 2\phi + 0.0038\sin 2\phi + 0.0310\cos 4\phi + 0.0038\sin 4\phi), \quad (5)$$

where $V_{qP_N} = 2259$ m/s is the qP-velocity at $\phi = 0^\circ$ (North). This curve is also presented in Fig. 7.13a. Using equations (5) and (3) the symmetry directions α_1 and α_2 of the 2ϕ velocity variation can be determined from the 2ϕ coefficients: there is a minimum velocity direction $\alpha_1 = N1.2^\circ W$, with $V_{qP}(\alpha_1) = 2258$ m/s (calculated from (5)) and a maximum velocity direction $\alpha_2 = N88.8^\circ E$ with $V_{qP}(\alpha_2) = 2462$ m/s. Comparing the vertical qP-velocity $V_{qP_V} = 2463$ m/s in layer 2 of structure I (assumed to be known from other information) with these velocities it is concluded that the direction of rotational symmetry $\alpha = \alpha_1 = N1.2^\circ W$ in this layer. This value corresponds very well to the actual direction ($N0^\circ E$) of the symmetry axis (see Fig. 7.4a). It also corresponds to the symmetry direction $N1.7^\circ E$ that can be derived from the 4ϕ terms in equation (5) and therefore using $\alpha = N1.2^\circ W$ equation (5) can be approximated by a reduced form :

$$V_{qP}^2(\phi) = V_{qP_N}^2 \left[1.0632 - 0.0943\cos 2\phi + 0.0311\cos 4\phi \right], \quad (6)$$

where ϕ is measured from $\alpha = N1.2^\circ W$. With $\rho = 2.6$ g/cm³ the coefficients A , B , and C (see equation (1a)) can be derived from (6) and from these values the elastic constants c_{11} and c_{33} can be calculated with equation (4) (see Table 7.1a).

In Fig. 7.13b the velocity variation of the leading shear wave in layer 2 of structure I is presented. In this study it has been assumed that in an actual measurement due to partial overlapping of the qSP- and qSR-waves only the arrival times of the leading shear wave can be measured accurately enough. Therefore, only the velocities of the leading shear wave are presented here. Because the type of this wave changes (from qSP- to qSR-wave or vice versa) as a function of the direction of wave propagation (Fig. 7.5) it is not possible to use equations like (1b-c) or (2b-c) to fit the qS-velocities in the same way as was done for the qP-waves. To derive additional elastic constants from the velocity variation of the leading shear wave the following method is proposed. As shown by equation (1b-c) the qSR- and qSP-wave have identical velocities in the direction of the axis of rotational symmetry:

$$V_{qSR}(0^\circ) = V_{qSP}(0^\circ) = \sqrt{\frac{c_{44}}{\rho}}.$$

| Model parameters | | | | | | |
|----------------------------|----------|----------|----------|----------|----------|----------|
| Model | c_{11} | c_{33} | c_{13} | c_{44} | c_{66} | α |
| Structure I | 15.77 | 13.26 | 5.32 | 3.90 | 4.86 | N0.0°E |
| Structure I ^{inv} | 15.77 | 13.27 | 5.07 | 3.90 | 4.86 | N1.2°W |

a

| Model parameters | | | | | | | | |
|------------------------------|----------|----------|----------|----------|----------|----------|--------|------|
| Model | c_{11} | c_{33} | c_{13} | c_{44} | c_{66} | α | strike | dip |
| Structure III | 15.77 | 13.26 | 5.32 | 3.90 | 4.86 | N120.0°E | N0.0°E | 5.0° |
| Structure III ^{inv} | 15.91 | 13.35 | 5.03 | 3.98 | 4.86 | N121.0°E | N3.6°W | 5.1° |

b

Table 7.1. The elastic constants (in 10^9 N/m²) of layer 2 of structure I (a) and III (b) together with the constants of the corresponding structures obtained by transversely isotropic inversion. Moreover, the direction of rotational symmetry α and the strike and dip of the interface in structure III (b) are compared.

Perpendicular to this axis the velocities are different:

$$V_{qSR}(90^\circ) = \sqrt{\frac{c_{66}}{\rho}}, \text{ and}$$

$$V_{qSP}(90^\circ) = \sqrt{\frac{c_{44}}{\rho}}.$$

This means that c_{44} in layer 2 of structure I can be derived from the qS-velocity (1225 m/s) estimated from Fig. 7.13b at the symmetry direction N1.2°W. If the vertical velocity V_{qSv} (perpendicular to the symmetry axis in structure I) of the leading shear wave is larger than the velocity in this horizontal symmetry direction (which is true for structure I because $V_{qSv} = 1367$ m/s) it means that $c_{66} > c_{44}$ and c_{66} can be determined from V_{qSv} . However, if V_{qSv} would be equal to this horizontal velocity (implying $c_{66} \leq c_{44}$) additional information is needed in order to estimate c_{66} . Once c_{44} and c_{66} have been determined the elastic constant c_{13} can be derived from c_{44} and the other constants c_{11} , c_{33} , and A can be calculated from the qP-velocity variation (using equation (4)). All the resultant elastic constants of structure

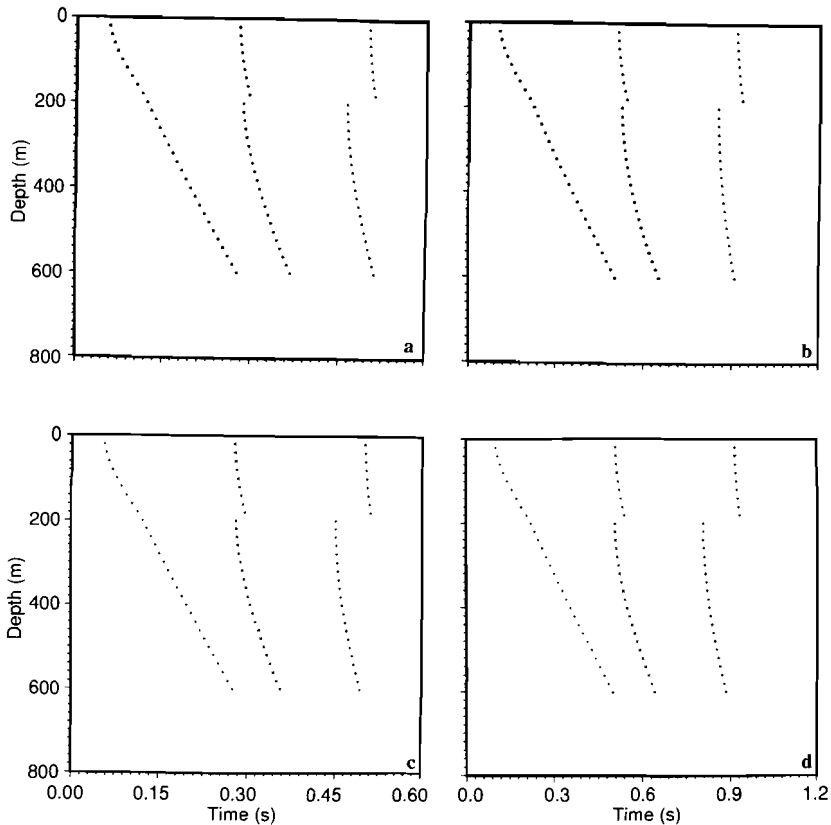


Fig. 7.14. The traveltimes (small dots) of the direct qP-(a) and leading qS-waves (b) calculated for the inverted structure I (obtained by transversely isotropic inversion) and for the original structure I (large dots) for three source offsets (the same as for Fig. 7.6) as a function of the receiver depth at a source azimuth $N0^\circ E$. The same but then for the qP- and qS-waves in structure III is shown in (c) and (d), respectively.

I determined in this way are presented in Table 7.1a. Table 7.1a shows that the inversion results fit the original constants very well.

With the inversion results an 'inverted structure I' can be composed: it consists of the original isotropic layer 1 (assumed to be determined from other information) on top of the transversely isotropic layer 2 described by the elastic constants determined in the inversion and presented in Table 7.1a. The interface between both layers is horizontal.

In Figs 7.14a and 7.14b the traveltimes of the direct qP- and the leading qS-waves are calculated for the inverted structure I and compared with the traveltimes for the original structure I. This is done for a source azimuth $N0^\circ E$. No difference between both sets of traveltimes can be observed. This is also true for other azimuths not shown here.

From these results and the results of isotropic inversion the non-uniqueness of

traveltimes inversion is noted: both an isotropic and an anisotropic model result in traveltimes that fit the traveltimes calculated for the original structure I very well. To judge whether the geologically simple transversely isotropic model (horizontally layered) or the geologically more complicated isotropic model (that may contain anticlines) is the correct model additional information is needed (e.g. surface seismics or other VSPs).

In the transversely isotropic inversion applied to the data for structure I the interface between layer 1 and 2 was assumed to be horizontal at a depth (190m) observed at the borehole. However, as will be shown an eventual dip of this interface can also be determined with transversely isotropic inversion.

b) STRUCTURE III

The transversely isotropic inversion has also been applied to the velocities of the critically refracted qP- and qS-waves calculated for structure III. These velocities (shown in Figs 7.13c-d) clearly show a ϕ variation due to the dipping interface in structure III. The qP-velocity variation (Fig. 7.13c) is fitted with curves of the form given by equation (A16). The best fitting curve (also presented in Fig. 7.13c) is given by:

$$V_{qP}^2(\phi) = V_{qP_n}^2(0.9834 - 0.0091\cos\phi - 0.1438\sin\phi + 0.0416\cos 2\phi + 0.0781\sin 2\phi - 0.0159\cos 4\phi + 0.0171\sin 4\phi), \quad (7)$$

where $V_{qP_n} = 2358$ m/s and ϕ measured from North. As shown in the Appendix the dip direction γ of the refractor can be determined from the quotient of the $\sin\phi$ - and $\cos\phi$ terms. For the velocity variation given in (7) this results in $\gamma = N86.4^\circ E$ (equivalent to a strike $N3.6^\circ W$) which corresponds very well to the true dip direction ($N90.0^\circ E$) of the refractor in structure III. The dip of the refractor (as shown by equation (A16)) can be determined from either the $\cos\phi$ - or $\sin\phi$ term if ρ , V_1 (the P-wave velocity in layer 1), and A are known. ρ and V_1 are assumed to be known from other information (being 2.6 g/cm^3 and 1800 m/s, respectively), whereas A can be derived from (7). The resultant dip δ is 5.1° , which agrees very well with the true dip (5.0°) of the refractor.

To determine the elastic constants of layer 2 in structure III the same procedure as used for structure I is applied to the velocity variations shown in Figs 7.13c-d. Using (7) the symmetry directions of the transversely isotropic layer 2 can be derived from the quotient of the 2ϕ coefficients: there are two directions $\alpha_1 = N31.0^\circ E$ and $\alpha_2 = N121.0^\circ E$, corresponding to the maximum and minimum velocity direction of the 2ϕ variation, respectively. Although the 2ϕ and 4ϕ velocity variations in equation (7) (according to (A12)) describe the velocity variation in the plane of the refractor, it has been assumed that this variation is a good approximation of the velocity variation in the horizontal plane of

layer 2 if the refractor is slightly dipping and layer 2 is weakly anisotropic. The horizontal qP-velocities V_{qP_h} in the two symmetry directions α_1 and α_2 are then approximated from (7) by omitting the $\cos\phi$ and $\sin\phi$ terms: $V_{qP_h}(\alpha_1) \approx 2467$ m/s and $V_{qP_h}(\alpha_2) \approx 2259$ m/s. With the vertical qP-velocity $V_{qP_v} = 2463$ m/s in layer 2 (being almost identical to $V_{qP_h}(\alpha_1)$) it is concluded that α_2 (= N121.0°E) is the direction of rotational symmetry in layer 2 of structure III. This direction agrees very well with the actual direction N120°E (Fig. 7.4c) of the symmetry axis. Using α_2 (= N121.0°E) the elastic constants c_{11} and c_{33} can be derived from the 2ϕ and 4ϕ coefficients of (7) just as was done for structure I. The results are shown in Table 7.1b.

In order to derive the remaining elastic constants of layer 2 in structure III from the leading shear wave velocities (shown in Fig. 7.13d) these velocities are corrected for the ϕ variation caused by the dipping interface. This is done by fitting the qS-velocities with curves of the form: $V_{qS}(\phi) = [a + b \cos\phi]$, where ϕ is measured from the dip direction (N86.4°E) determined from the qP-velocity variation. The best fitting curve is :

$$V_{qS}(\phi) = V_{qS}(0) \left[1.0930 - 0.0930 \cos\phi \right], \quad (8)$$

where $V_{qS}(0)$ (= 1201 m/s) is the qS-velocity in the N86.4°E direction. Then the $\cos\phi$ contribution of (8) is subtracted from the qS-velocities shown in Fig. 7.13d and the resultant velocities (assumed to be only due to anisotropy) are shown in Fig. 7.13e. Because the velocities V_{S1} (= 1259 m/s) and V_{S2} (= 1215 m/s) estimated from Fig. 7.13e in the directions of rotational symmetry (N121.0°E and N59.0°W, respectively) are not equal, their average (1237 m/s) is taken as an estimate of the leading qS-velocity in those directions. From this average velocity the elastic constant c_{44} is calculated (see Table 7.1b). The constant c_{66} is calculated from the vertical qS-velocity in layer 2 of structure III (the same as for structure I) and c_{13} is calculated from the constants c_{11} , c_{33} , c_{44} , and A . All the resultant elastic constants (summarized in Table 7.1b) that are obtained for layer 2 in structure III agree (within 5 %) with the actual elastic constants of this layer.

In Figs 7.14c-d the traveltimes of the direct qP- and leading qS-waves are calculated for the inverted structure III (consisting of the isotropic layer 1 on top of a layer 2 that is described by the parameters shown in Table 7.1b) and compared with the traveltimes for the original structure III. This is done for a source azimuth N0°E. Both traveltime data sets correspond very well to each other: no difference in traveltime can be noticed. This is also true for other source azimuths not shown here, so that again can be concluded that both an isotropic and a transversely isotropic model can explain the traveltimes calculated for structure III.

7.6 CONCLUSIONS

Isotropic traveltimes inversion used to locate the interfaces in layered media may give erroneous results when some of the layers are anisotropic. This has been demonstrated for synthetic multi-offset VSP traveltimes data calculated for structures consisting of an isotropic low-velocity layer on top of a transversely isotropic layer. If both the interface separating the layers and the axis of rotational symmetry are horizontal 2D isotropic inversion only results in the original interface for VSP sources with azimuths perpendicular to the symmetry axis. For all other azimuths the resultant interface is an anticline with its top at the borehole and with a form depending on the azimuth. This is also true for a slightly dipping interface, but the anticline is tilted then. However, if the axis of rotational symmetry is vertical while the interface is horizontal the resultant interface is a syncline bottoming at the borehole and with a form that is independent on the source azimuth.

For these three types of structures it has been shown that the difference in depth between the interface obtained by isotropic inversion and the correct interface in these structures may be very large; therefore it is concluded that this inversion may introduce serious errors in the interpretation of multi-offset VSP data when anisotropy is not taken into account. A key identifier of anisotropy is shear-wave splitting. As soon as this phenomenon is observed in multi-offset VSP measurements the results of isotropic traveltimes inversion should be judged very critically. The same should be done of course if the inversion results do not fit with additional information (obtained from e.g. surface seismics, well logging, or other VSPs).

Transversely isotropic traveltimes inversion has also been applied to the synthetic VSP data calculated in this paper. The inversion method, based on the assumption of transverse isotropy with a horizontal axis of symmetry, has been applied to the arrival times of critically refracted qP- and qS-waves calculated for structures I and III. Using the azimuthal dependence of the velocities derived from these traveltimes the elastic constants of the transversely isotropic layer and the strike and dip of the interface could successfully be determined. It is expected that the method is also successful for other transversely isotropic structures with a horizontal symmetry axis, if the anisotropy is weak and the dip of the interface small.

Because of all its assumptions the transversely isotropic inversion method is a robust method. However, it has not been the intention of this paper to develop an elegant multi-purpose anisotropy inversion scheme. The transversely isotropic inversion has been suggested here in order to show that not only geologically complicated isotropic structures (with anticlines or synclines) can be derived that explain a given VSP traveltimes data set, but geologically simpler transversely isotropic structures (with plane interfaces) as well.

ACKNOWLEDGEMENTS

The author thanks Schlumberger-Doll Research (Ridgefield, CT) for the possibility offered to carry out this research at their laboratory during the autumn of 1987. All the people at their Geoacoustics department and K. Helbig are thanked for the many fruitful discussions on the subject. The author also wants to thank D. Gajewski, who was so kind to give the author a free copy of the ANRAY86 ray tracing program.

7.7 APPENDIX

In this Appendix the velocity variation of critically refracted waves, travelling through media that consist of a homogeneous isotropic layer 1 on top of a homogeneous anisotropic layer 2 and for which the separating interface is slightly dipping, is studied for a VSP geometry. This is done by deriving time-distance curves for these waves. Although the VSP geometry is different from the usual geometry used in refraction studies (i.e. both sources and receivers at the surface) the methods to derive the time-distance curves are the same. Throughout the Appendix it has been assumed that the ray path does not deviate from the construction plane (perpendicular to the interface and containing both source and receiver). As shown earlier in this paper this is a valid approximation if traveltimes are studied.

Consider a cross-section at right angles to the strike of the interface as shown in Fig. 7.A1. Two lines are drawn perpendicular to the interface I from the borehole receiver R and from the source S . These lines intersect the surface and the interface at the points A and B , respectively and have lengths h_A and h_B . The distance between A and S is X' . From B a line is drawn in the direction of the plane wavefront that is critically refracted at the interface. From S a perpendicular is dropped on this wavefront, intersecting at the point S' .

Following Helbig (1964), who studied the refraction for a layer 1 and layer 2 being both anisotropic, the total traveltime $t_s(X')$ of a critically refracted wave from S to R is equal to the distance $B-R$ divided by the group velocity g_2 along the interface in layer 2 plus the time the wavefront (which is critically refracted) needs to travel from S to S' , which in our situation of an isotropic layer 1 is equal to the distance $S-S'$ divided by the velocity V_1 in layer 1. So, it may be concluded that the total traveltime of a seismic pulse from the shotpoint S via the refractor I to the receiver R as a function of the distance X' is:

$$t_s(X') = \frac{X' \cos \delta}{g_2(\delta)} + \frac{h_B \cos i_c}{V_1}, \quad (\text{A1})$$

where i_c is the critical angle of incidence and δ is the dip of the refractor. More useful

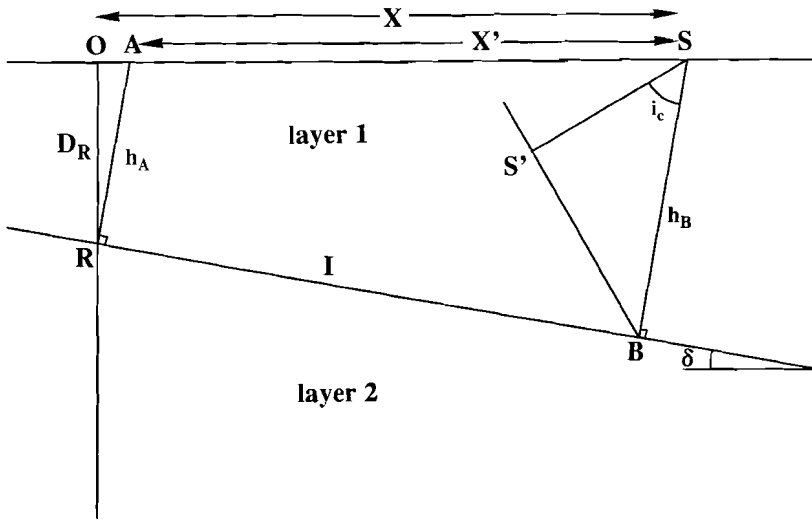


Fig. 7.A1. Cross-section at right angles to the strike of the dipping refractor *I*.

would be to express this equation in terms of the depth D_R of the borehole receiver and the offset X of the source from the borehole. With

$$X' = X - h_A \sin\delta, \quad h_B = h_A + X' \sin\delta, \quad \text{and} \quad h_A = \frac{D_R}{\cos\delta},$$

(A1) becomes:

$$t_S(X) = D_R \left[\frac{\cos i_c}{V_1 \cos\delta} - \frac{\tan\delta \sin\delta \cos i_c}{V_1} - \frac{\sin\delta}{g_2(\delta)} \right] + X \left[\frac{\cos\delta}{g_2(\delta)} + \frac{\sin\delta \cos i_c}{V_1} \right]. \tag{A2}$$

The first term on the right hand side is the intercept time of the time-distance curve and the factor of X is the reciprocal of the apparent velocity V_a :

$$\frac{1}{V_a} = \frac{\cos\delta}{g_2(\delta)} + \frac{\sin\delta \cos i_c}{V_1}. \tag{A3}$$

This resultant velocity is identical to the apparent velocity which can be derived for

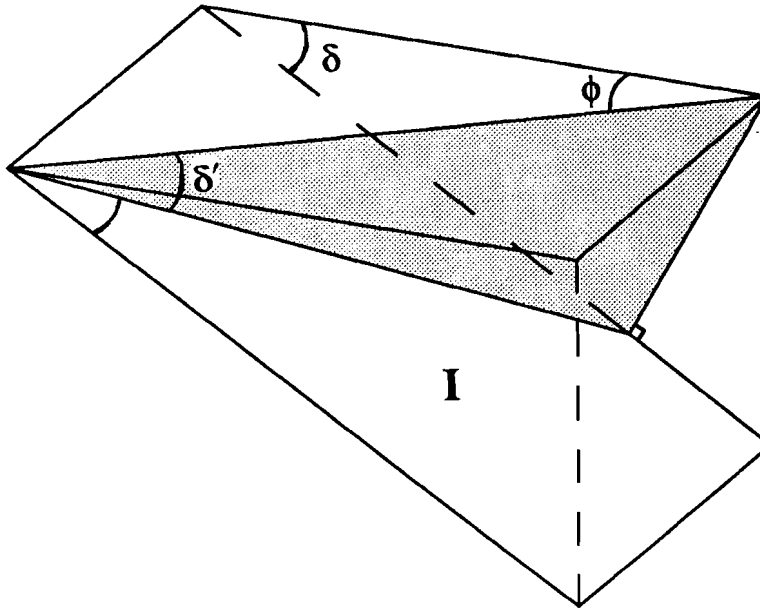


Fig. 7.A2. The construction plane (shaded area) containing source and receiver perpendicular to the dipping refractor *I*. The dip of the refractor (denoted by δ) becomes δ' when measured in the tilted construction plane. The projection of the azimuth ϕ of the construction plane on the plane of the refractor is given by ϕ' .

refraction studies carried out in the same medium with sources and receivers at the surface (see Helbig, 1964). Moreover, equation (A3) shows that for a horizontal refractor ($\delta = 0^\circ$) $V_a = g_2(0^\circ)$ (which is the group velocity in layer 2 along the refractor in the direction of the profile). Using Snell's law, which gives the relation between the critical angle i_c , V_1 and $g_2(\delta)$:

$$\frac{\sin i_c(\delta)}{V_1} = \frac{1}{g_2(\delta)}, \quad (\text{A4})$$

V_a can be written as:

$$V_a = \frac{V_1}{\sin i_c(\delta)\cos\delta + \sin\delta \cos i_c(\delta)} \quad \text{or} \quad (\text{A5})$$

$$V_a = \frac{g_2(\delta)}{\cos\delta + \sin\delta \cot i_c(\delta)} .$$

(Note in these equations that the critical angle depends on the direction of the group velocity g_2 .) Equations (A5) give the apparent velocity V_a that would be determined in a refraction study carried out along a profile at right angles to the strike of the interface. The method used to derive these equations, however, can also be used to determine the apparent velocities at other azimuths of the profiles. The construction as shown in Fig. 7.A1 and the formulae derived from it are valid for all construction planes being perpendicular to the refractor and containing sources and receiver. However, the dip of the refractor is measured in this tilted plane and therefore it is not the true dip. The relationship between the dip δ' measured in the construction plane and the true dip δ is shown in Fig. 7.A2 and is given by:

$$\sin\delta' = \sin\delta \cos\phi \quad \text{and} \quad \cos\delta' = \left[1 - \sin^2\delta \cos^2\phi\right]^{1/2} , \quad (\text{A6})$$

where ϕ is the azimuth of the profile along the surface measured from the normal to the strike. Using δ' instead of δ equations (A5) become:

$$V_a(\phi) = \frac{V_1}{\sin[i_c(\phi') + \delta']} = \frac{V_1}{\sin[i_c(\phi') + \sin^{-1}(\sin\delta \cos\phi)]} \quad (\text{A7})$$

or

$$V_a(\phi) = \frac{g_2(\phi')}{\left[1 - \sin^2\delta \cos^2\phi\right]^{1/2} + \sin\delta \cos\phi \cot i_c(\phi')} ,$$

where g_2 and i_c are now functions of ϕ' , which is the projection of the azimuth ϕ on the refractor and which is given by the relation (see Fig. 7.A2):

$$\tan\phi' = \frac{\sin\phi}{\cos\phi \cos\delta} . \quad (\text{A8})$$

The formulae presented in (A7) are exact formulae. However, in order to describe the azimuthal apparent velocity variations in terms of linear combinations of the elastic constants of the anisotropic layer 2 some approximations are made. Assuming weak anisotropy the group velocity $g_2(\phi')$ along the refractor can be approximated by the phase velocity $V_2(\phi')$ along the refractor in layer 2 (Backus, 1965). If further the dip δ of the refractor is assumed to be small and the value of $\cot i_c(\phi')$ is not too large (e.g.

$\cot i_c(\phi) < 1$) the approximate relation between the apparent velocity and the phase velocity in layer 2 can be derived from the second equation given in (A7):

$$V_a(\phi) \approx V_2(\phi) \left[1 - \sin\delta \cot i_c(\phi) \cos\phi \right]. \quad (\text{A9})$$

To illustrate for what dips this approximation is valid let's consider the isotropic case for which $V_2(\phi)$ and $\cot i_c(\phi)$ become constants (denoted by V_2 and $\cot i_c$, respectively). Equation (A9) then becomes:

$$V_a(\phi) \approx V_2 \left[1 - \sin\delta \cot i_c \cos\phi \right]. \quad (\text{A10})$$

For the same situation a similar equation was derived by Backus (1965):

$$V_a(\phi) \approx V_2 \left[1 - \tan\delta \cot i_c \cos\phi \right]. \quad (\text{A11})$$

Although Backus considered wave propagation in a vertical plane through the refractor to derive (A11) instead of wave propagation in the construction plane perpendicular to the refractor for which (A10) has been derived, both (A10) and (A11) are almost identical for small dips of the refractor (since then $\sin\delta \approx \tan\delta$). In Fig. 7.A3 the approximate velocity variations described by (A10) and (A11) are compared with the correct velocity variation as described by (A7) with $g_2(\phi') = V_2 = 2000$ m/s and $i_c(\phi') = i_c = 50^\circ$ for three different dips of the refractor. Fig. 7.A3 shows that for small dips equations (A10) and (A11) are indeed almost identical and that both are very good approximations of the exact equation (A7), but that the difference increases for increasing dips (the difference is approximately 5% for $\delta = 10^\circ$). These conclusions also hold for the approximate equation (A9) describing the anisotropic situation.

To develop equation (A9) in terms of the elastic constants of the anisotropic layer 2 we further assume the plane of the refractor is a symmetry plane of layer 2 so that when we take the square of (A9) equation (2a) for the qP-phase velocity can be used in order to obtain the resultant apparent qP-velocity variation:

$$\rho V_a^2(\phi) \approx \left[A + B \cos 2(\phi - \alpha) + C \cos 4(\phi - \alpha) \right] \left[1 - 2 \sin\delta \cos(\phi - \gamma) \cot i_c(\phi - \alpha) \right], \quad (\text{A12})$$

where ρ is the density in layer 2 and ϕ is measured from an arbitrarily chosen reference direction making an angle α with the axis of rotational symmetry in layer 2 and an angle γ with the dip direction (normal to the strike) of the refractor. A , B , and C are combinations

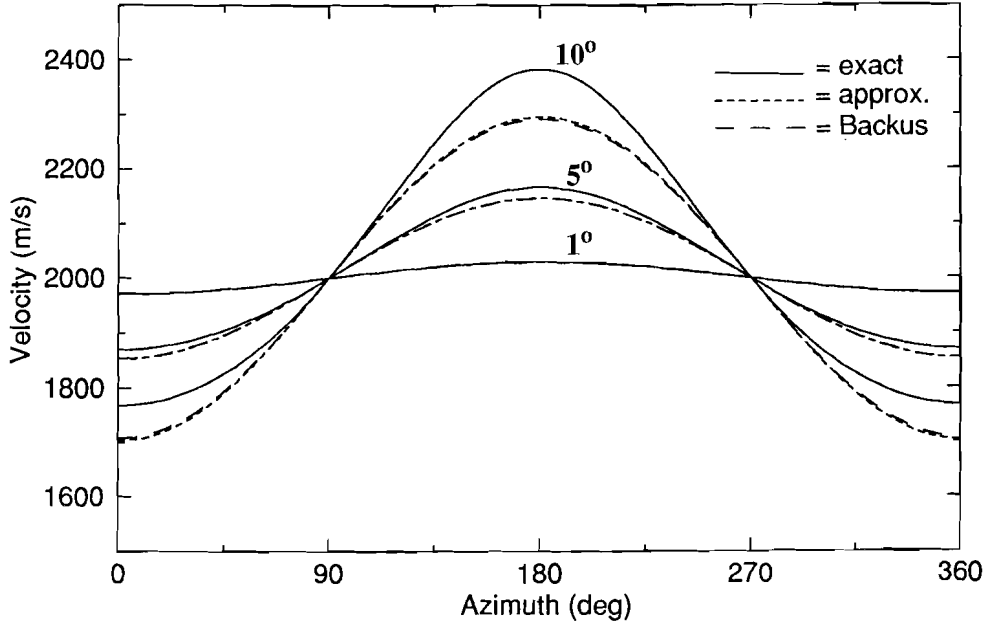


Fig. 7.A3. The apparent velocity variations of critically refracted waves for three dipping refractors (with dip $\delta = 1^\circ$, $\delta = 5^\circ$, and $\delta = 10^\circ$). The velocity variations are calculated with exact equation (A7) (solid line), the approximate equation (A10) (short dashed line), and Backus' approximate equation (A11) (long dashed line).

of elastic constants as given at equation (1a-c).

To further simplify (A12) consider the term $\cot i_c(\phi-\alpha)$. With the assumptions made the critical angle $i_c(\phi-\alpha)$ is given by:

$$\sin i_c(\phi-\alpha) = \frac{V_1}{V_2(\phi-\alpha)} \quad (\text{A13})$$

or

$$\sin^2 i_c(\phi-\alpha) = \frac{\rho V_1^2}{A + B\cos 2(\phi-\alpha) + C\cos 4(\phi-\alpha)}$$

With (A13) we find

$$\cot^2 i_c(\phi-\alpha) = \frac{A + B\cos 2(\phi-\alpha) + C\cos 4(\phi-\alpha) - \rho V_1^2}{\rho V_1^2} \quad (\text{A14})$$

$$= \cot^2 i_c^I \left[1 + \frac{B \cos 2(\phi - \alpha)}{A - \rho V_1^2} + \frac{C \cos 4(\phi - \alpha)}{A - \rho V_1^2} \right],$$

where i_c^I is given by $\cot^2 i_c^I = \frac{A - \rho V_1^2}{\rho V_1^2}$. If the terms $\frac{B}{A - \rho V_1^2}$ and $\frac{C}{A - \rho V_1^2}$ are much smaller than 1 (which is true for weak anisotropy) we find:

$$\cot i_c(\phi - \alpha) \approx \cot i_c^I \left[1 + \frac{1}{2} \frac{B \cos 2(\phi - \alpha)}{A - \rho V_1^2} + \frac{1}{2} \frac{C \cos 4(\phi - \alpha)}{A - \rho V_1^2} \right]. \quad (\text{A15})$$

With (A15) equation (A12) becomes (neglecting products of the cosine terms):

$$\rho V_a^2(\phi) \approx A + D_1 \cos \phi + D_2 \sin \phi + B_1 \cos 2\phi + B_2 \sin 2\phi + C_1 \cos 4\phi + C_2 \sin 4\phi, \quad (\text{A16})$$

where

$$D_1 = -2A \sin \delta \cot i_c^I \cos \gamma$$

$$D_2 = -2A \sin \delta \cot i_c^I \sin \gamma,$$

and $A, B_1, B_2, C_1,$ and C_2 are constants described at equation (2a-c).

So, we may conclude that if the apparent velocity of qP-waves is fitted with curves of the form described in (A16) the dip direction γ of the refractor can be determined from the quotient of the best fitting coefficients D_1 and D_2 . Once $V_1, A,$ and ρ are known $\cot i_c^I$ is known and the dip δ of the refractor can be determined from either D_1 or D_2 .

In (A16) the apparent velocity variation is given for qP-waves. If, however, instead of equation (2a) equations (2b-c) are used in (A9) similar equations like (A16) but then for the quasi-shear waves can also be derived.

It should be noted that rather similar equations as derived here (especially (A7)) were used by Vetter and Minster (1981) (but a derivation was not given) who fitted observed apparent qP-velocity variations presented in polar diagrams by ellipses.

7.8 REFERENCES

- Alford, R.M. 1986. Shear data in the presence of azimuthal anisotropy: Dilley, Texas. 56th S.E.G. Meeting, Houston, Expanded Abstracts, 476-479.
- Babich, V.M. 1961. Ray method for the computation of the intensity of wave fronts in elastic inhomogeneous anisotropic medium. *Problems of the Dynamic Theory of Propagation of Seismic Waves* Vol. 5, 36-46, Leningrad University Press, Leningrad (in Russian).
- Backus, G.E. 1965. Possible forms of seismic anisotropy of the uppermost mantle under oceans. *Journal of Geophysical Research* 70, 3429-3439.
- Balch, A.H. and Lee, M.W. (Editors). 1984. *Vertical Seismic Profiling: Techniques, applications, and case histories*. International Human Resources Dev. Corp.
- Bamford, D. 1977. P_n velocity anisotropy in a continental upper mantle. *Geophysical Journal of the Royal Astronomical Society* 49, 29-48.
- Bamford, D. and Nunn, K.R. 1979. In situ seismic measurements of crack anisotropy in the carboniferous limestone of northwest England. *Geophysical Prospecting* 27, 322-338.
- Banik, N.C. 1984. Velocity anisotropy of shales and depth estimation in the North Sea basin. *Geophysics* 49, 1411-1419.
- Booth, D.C. and Crampin, S. 1983. The anisotropic reflectivity technique: theory. *Geophysical Journal of the Royal Astronomical Society* 72, 755-766.
- Červený, V. 1972. Seismic rays and ray intensities in inhomogeneous anisotropic media. *Geophysical Journal of the Royal Astronomical Society* 29, 1-13.
- Červený, V. and Firbas, P. 1984a. Numerical modelling and inversion of travel times of seismic body waves in inhomogeneous anisotropic media. *Geophysical Journal of the Royal Astronomical Society* 76, 41-51.
- Červený, V., Klimeš, L. and Pšenčík, I. 1984b. Paraxial ray approximations in the computation of seismic wavefields in inhomogeneous media, *Geophysical Journal of the Royal Astronomical Society* 79, 89-104.
- Červený, V., Molotkov, I.A. and Pšenčík, I., 1977. *Ray method in seismology*. Charles University Press, Prague.
- Chiu, S.K.L. and Stewart, R.R. 1987. Tomographic determination of three-dimensional seismic velocity structure using well logs, vertical seismic profiles, and surface seismic data. *Geophysics* 52, 1085-1098.
- Crampin, S. 1977. A review of the effects of anisotropic layering on the propagation of seismic waves. *Geophysical Journal of the Royal Astronomical Society* 49, 9-27.
- Crampin, S. 1981. A review of wave motion in anisotropic and cracked elastic-media. *Wave Motion* 3, 343-391.
- Crampin, S. 1982. Comments on 'Possible forms of anisotropy of the uppermost mantle under oceans' by George E. Backus. *Journal of Geophysical Research* 87, 4636-4640.
- Crampin, S. 1987. Geological and industrial implications of extensive dilatancy anisotropy. *Nature* 328, 491-496.
- Crampin, S. and Bamford, D. 1977. Inversion of P-wave velocity anisotropy. *Geophysical Journal of the Royal Astronomical Society* 49, 123-132.
- Crampin, S., McGonigle, R. and Bamford, D. 1980. Estimating crack parameters from observations of P-wave velocity anisotropy. *Geophysics* 45, 345-360.
- Crampin, S. and Kirkwood, S.C. 1981. Velocity variations in systems of anisotropic symmetry. *Journal of Geophysics* 49, 35-42.
- Crampin, S. and Radovich, B.J. 1982. Interpretation of synthetic common-depth-point gathers for a single anisotropic layer. *Geophysics* 47, 323-335.
- Crampin, S., Bush, I., Naville, C. and Taylor, D.B. 1986a. Estimating the internal structure of reservoirs with shear-wave VSPs. *The Leading Edge* 5, No. 11, 35-39.

- Crampin, S., McGonigle, R. and Ando, M. 1986b. Extensive-dilatancy anisotropy beneath Mount Hood, Oregon and the effect of aspect ratio on seismic velocities through aligned cracks. *Journal of Geophysical Research* 91, 12703-12710.
- Deplante, C. and Oristaglio, M. 1986. Traveltime inversion of offset vertical seismic profiles using an application of Fermat's principle. 56th S.E.G. Meeting, Houston, Expanded Abstracts, 577-579.
- Doyle, M., McGonigle, R. and Crampin, S. 1982. The effects of crack anisotropy on the hypocentral locations of local earthquakes. *Geophysical Journal of the Royal Astronomical Society* 69, 137-157.
- Doyle, M., Crampin, S., McGonigle, R. and Evans, R. 1985. Inversion of arrival-times in a region of dilatancy anisotropy. *Pure and Applied Geophysics* 123, 375-387.
- Fryer, G.J. and Frazer, L.N. 1984. Seismic waves in stratified anisotropic media. *Geophysical Journal of the Royal Astronomical Society* 78, 691-710.
- Fryer, G.J. and Frazer, L.N. 1987. Seismic waves in stratified anisotropic media-II. Elastodynamic eigensolutions for some anisotropic systems. *Geophysical Journal of the Royal Astronomical Society* 91, 73-101.
- Gajewski, D. and Pšenčík, I. 1986. *Numerical modelling of seismic wavefields in 3-D laterally varying layered anisotropic structures- Program ANRAY86*. Internal Report, Inst. of Earth and Planet. Phys., University of Alberta, Edmonton.
- Gajewski, D. and Pšenčík, I. 1987. Computation of high-frequency seismic wavefields in 3-D laterally inhomogeneous anisotropic media. *Geophysical Journal of the Royal Astronomical Society* 91, 383-411.
- Gajewski, D. and Pšenčík, I. 1988. Ray synthetic seismograms for a 3-D anisotropic lithospheric structure. *Physics of the Earth and Planetary Interiors* (in press).
- Gal'perin, E.I. 1974. *Vertical Seismic Profiling*. Society of Exploration Geophysicists, Tulsa.
- Hardage, B.A. 1985. *Vertical Seismic Profiling, Part A: Principles, second enlarged edition*. Geophysical Press, London-Amsterdam.
- Helbig, K. 1958. Elastische Wellen in anisotropen Medien. *Gerlands Beiträge zur Geophysik* 67, 177-211, 256-288.
- Helbig, K. 1964. Refraction seismics with an anisotropic overburden-a graphical method of interpretation. *Geophysical Prospecting* 12, 383-396.
- Helbig, K. 1966. A graphical method for the construction of rays and travel times in spherically layered media, Part 2: Anisotropic case, theoretical considerations. *Bulletin of the Seismological Society of America* 56, 527-559.
- Helbig, K. 1984. Transverse isotropy in exploration seismics. *Geophysical Journal of the Royal Astronomical Society* 76, 79-88.
- Hirahara, K. and Ishikawa, Y. 1984. Travel time inversion for three-dimensional P-wave velocity anisotropy. *Journal of Physics of the Earth* 32, 197-218.
- Ivansson, S. 1987. Crosshole transmission tomography. In *Seismic Tomography* (editor G. Nolet), 159-188, Reidel Publishing Company, Dordrecht, The Netherlands.
- Leary, P.C., Li, Y.-G and Aki, K., 1987. Observation and modelling of fault-zone fracture seismic anisotropy-I. P,SV and SH travel times. *Geophysical Journal of the Royal Astronomical Society* 91, 461-484.
- Li, Y.-G, Leary, P.C. and Aki, K. 1987. Observation and modelling of fault-zone fracture seismic anisotropy-II. P-wave polarization anomalies. *Geophysical Journal of the Royal Astronomical Society* 91, 485-492.
- Lines, L.R., Bourgeois, A. and Covey, J.D. 1984. Traveltime inversion of offset vertical seismic profiles: A feasibility study. *Geophysics* 49, 250-264.
- Miller, D.E. 1983. Arrival times and envelopes: inverse modeling for subsurface seismics. 53rd S.E.G. Meeting, Las Vegas, Expanded Abstracts, 449-450.
- Musgrave, M.J.P. 1970. *Crystal Acoustics*. Holden-Day, San Francisco, California.
- Nishizawa, O. 1982. Seismic velocity anisotropy in a medium containing oriented cracks -

- transversely isotropic case. *Journal of Physics of the Earth* 30, 331-347.
- Oristaglio, M.L. 1985. A guide to current uses of vertical seismic profiles. *Geophysics* 50, 2473-2479.
- Pujol, J., Burridge, R. and Smithson, S.B. 1985. Velocity determination from offset Vertical Seismic Profiling data. *Journal of Geophysical Research* 90, 1871-1880.
- Shearer, P.M. and Orcutt, J.A. 1985. Anisotropy in the oceanic lithosphere - theory and observations from the Ngendei seismic refraction experiment in the south-west Pacific. *Geophysical Journal of the Royal Astronomical Society* 80, 493-526.
- Shearer, P.M. and Orcutt, J.A. 1986. Compressional and shear wave anisotropy in the oceanic lithosphere - the Ngendei seismic refraction experiment. *Geophysical Journal of the Royal Astronomical Society* 87, 967-1003.
- Stephen, R.A. 1985. Seismic anisotropy in the Upper Oceanic Crust. *Journal of Geophysical Research* 90, 11383-11396.
- Stewart, R.R. 1984. VSP interval velocities from traveltine inversion. *Geophysical Prospecting* 32, 608-628.
- Thomsen, L. 1986. Weak elastic anisotropy. *Geophysics* 51, 1954-1966.
- van der Hijden, J.H.M.T. 1987. *Propagation of Transient Elastic Waves in Stratified Anisotropic Media*. North-Holland, Amsterdam.
- Vetter, U. and Minster, J.B. 1981. P_n velocity anisotropy in southern California. *Bulletin of the Seismological Society of America* 71, 1511-1530.
- Vlaar, N.J. 1968. Ray theory for an anisotropic inhomogeneous elastic medium. *Bulletin of the Seismological Society of America* 58, 2053-2072.
- Vlaar, N.J. 1969. Rays and travel times in a spherical anisotropic Earth. *Bulletin of the Seismological Society of America* 59, 1051-1060.
- White, R.S. and Whitmarsh, R.B. 1984. An investigation of seismic anisotropy due to cracks in the upper oceanic crust at 45°N, Mid-Atlantic Ridge. *Geophysical Journal of the Royal Astronomical Society* 79, 439-467.
- White, J.E., Martineau-Nicoletis, L. and Monash, C. 1983. Measured anisotropy in Pierre Shale. *Geophysical Prospecting* 31, 709-725.
- Winterstein, D.F. 1986. Anisotropy effects in P-wave and SH-wave stacking velocities contain information on lithology. *Geophysics* 51, 661-672.

Chapter 8

SUMMARY AND CONCLUSIONS

Media containing aligned rotationally symmetrical inclusions show transverse isotropy with respect to elastic wave propagation. The characteristics of this type of anisotropy have been investigated in the first part of this thesis (chapters 2, 3, and 4) while its implications on Vertical Seismic Profiling have been investigated in the second part of this thesis (chapters 5, 6, and 7).

Transverse isotropy due to aligned inclusions has been studied for inclusions ranging from flat cracks (very small aspect ratio α) up to spheres ($\alpha = 1$) using Nishizawa's model (chapter 2). The resultant anisotropy as described by this model (which is based on a static approach) is identical to the anisotropy described by Hudson's crack model (based on the scattering of elastic waves) for inclusions with aspect ratios up to 0.3. This result, which is surprising because Hudson's model has been derived for small aspect ratios ($\alpha \ll 1$), implies (assuming the validity of Nishizawa's model) that Hudson's model which is often used to interpret anisotropy observations can be applied to much larger aspect ratios than the aspect ratios for which it has been derived.

Another characteristic of the anisotropy as described by Nishizawa's model is that almost spherical inclusions ($\alpha \approx 1$) result in elliptical anisotropy, which is a type of anisotropy that can never be due to sequences of thin isotropic layers.

Sequences of isotropic layers and systems of large aligned fractures are just like aligned inclusions possible causes of transverse isotropy. Although these fractures and sequences of isotropic layers have a geometry that is different from the geometry of aligned inclusions they may result in the same anisotropy as aligned inclusions (chapters 3 and 4). The model describing the anisotropy due to large aligned fractures turns out to be identical to Hudson's crack model, whereas the model describing the anisotropy due to fine layering is identical to Hudson's model for ranges of aspect ratios that strongly depend on the fluid inside the inclusions. For the situations that these models are similar observed anisotropy can only be interpreted in terms of crack distributions if additional information shows the existence of cracks. However, for the situations where the similarity does not hold it is possible to distinguish between the causes of transverse isotropy (chapter 4). It should be

realized, however, that other causes of transverse isotropy exist. Therefore, the 'separation' method described in this thesis should only be considered as a first step towards distinguishing between the causes of transverse isotropy.

Because the 'representability' of cracked media by finely layered media strongly depends on the fluid inside the cracks, this 'representability' might not only be an interesting way to distinguish between the causes of transverse isotropy, but might also be an useful tool to investigate the nature of the fluid. Considering an uniformly cracked medium monitoring the nature of the fluid as a function of time or space could be very important for earthquake prediction or gas exploration, respectively.

Studying anisotropy observations is a powerful way to obtain information about the internal structures of the rocks (such as aligned inclusions, thin layering) which have dimensions much smaller than the seismic wavelength used. Studying crack-induced anisotropy offers the possibility to monitor the stress-field that aligns the cracks. There is evidence that a changing stress strongly affects the aspect ratio of the cracks. The results of the first part of this thesis on the effect of a changing aspect ratio on crack-induced anisotropy have been used to develop methods to interpret anisotropy observations in multi-offset shear-wave VSPs in terms of a changing aspect ratio. Changes in the aspect ratio can be monitored in such VSPs (chapter 6) by studying the changes in the direction of wave propagation at which there is no shear-wave splitting. This technique which has been applied to synthetic shear-wave VSPs could become important if repeated VSPs are carried out to analyze temporal changes in anisotropy in terms of a changing stress-field.

Although shear-wave splitting is often used as a key identifier of anisotropy one should be aware that shear-wave splitting can also be caused by transmission effects at interfaces in isotropic media (chapter 5). This effect should be taken into account first before shear-wave splitting is interpreted in terms of anisotropy.

Anisotropy may give valuable information about the internal structures of rocks, but it may also lead to erroneous interpretations, when it is not properly taken into account. In chapter 7 this has been shown for an isotropic travelttime inversion scheme which, when applied to multi-offset VSP travelttime data in layered transversely isotropic media, may introduce errors in the depths of the interfaces separating the layers. Therefore, anisotropy should be included in inversion schemes. In a first attempt to develop inversion schemes that do take anisotropy into account a transversely isotropic travelttime inversion scheme has been developed and successfully applied to synthetic multi-offset VSP-data. The method developed is a robust method and further research is necessary to develop more elegant methods. Despite the robustness of the method the results of the transversely isotropic travelttime inversion scheme show, when compared with the results of the isotropic inversion scheme, that both an isotropic and a transversely isotropic model can explain the same travelttime data set (consisting of the arrival times of P- and first arriving S-waves). To attack this problem of non-uniqueness additional information (such as polarization, shear-wave splitting) should be incorporated in the inversion.

SAMENVATTING (SUMMARY IN DUTCH)

Media, welke georiënteerde rotatie-invariante insluitsels bevatten, vertonen transversale isotropie m.b.t. elastische golfvoortplanting. In het eerste gedeelte van dit proefschrift (hoofdstukken 2, 3 en 4) zijn de karakteristieke kenmerken van dit type anisotropie onderzocht, terwijl in het tweede gedeelte (hoofdstukken 5, 6 en 7) de gevolgen van deze anisotropie voor Vertical Seismic Profiling (VSP) zijn onderzocht.

Transversale isotropie t.g.v. georiënteerde insluitsels is onderzocht voor insluitsels variërend van cracks (welke een erg kleine aspect ratio α hebben) tot aan bolvormige insluitsels ($\alpha = 1$) door gebruik te maken van Nishizawa's model (hoofdstuk 2). De resulterende anisotropie, zoals die door dit model (dat gebaseerd is op een statische benadering) wordt beschreven, is identiek aan de anisotropie, zoals die beschreven wordt door Hudson's crack model (dat gebaseerd is op de verstrooiing van elastische golven) voor insluitsels met een aspect ratio tot aan 0.3. Dit resultaat, dat verrassend genoemd mag worden omdat Hudson's model afgeleid is voor kleine aspect ratios ($\alpha \ll 1$), betekent (als we de juistheid van Nishizawa's model aannemen) dat Hudson's model, dat vaak toegepast wordt om anisotropie waarnemingen te kunnen verklaren, gebruikt kan worden voor veel grotere aspect ratios dan de aspect ratios, waarvoor het oorspronkelijk afgeleid is.

Een andere eigenschap van de anisotropie, zoals deze beschreven wordt door Nishizawa's model, is dat bijna bolvormige insluitsels ($\alpha \approx 1$) in elliptische anisotropie resulteren. Dit type anisotropie kan nooit veroorzaakt worden door opeenvolgingen van dunne isotrope laagjes.

Opeenvolgingen van isotrope laagjes en grote breuksystemen zijn net als georiënteerde insluitsels mogelijke oorzaken van transversale isotropie. Hoewel deze breuken en opeenvolgingen van isotrope laagjes een geometrie hebben, welke verschillend is van de geometrie van de georiënteerde insluitsels, kunnen ze allebei resulteren in dezelfde anisotropie als die t.g.v. de insluitsels (hoofdstukken 3 en 4). Het model, dat de anisotropie t.g.v. grote georiënteerde breuken beschrijft, blijkt identiek te zijn aan Hudson's crack model, terwijl het model dat de anisotropie t.g.v. fijne gelaagdheid beschrijft alleen identiek is aan Hudson's model voor waarden van de aspect ratio, die sterk afhankelijk zijn van het medium in de insluitsels. Voor de situaties, waarin deze modellen identiek zijn, kan men waargenomen anisotropie alleen maar interpreteren in termen van crack verdelingen indien aanvullende informatie duidt op de aanwezigheid van cracks. Voor de situaties echter, waarin de modellen niet meer gelijk zijn, is het mogelijk om de oorzaken van de transversale isotropie te onderscheiden (hoofdstuk 4). Men moet zich echter wel realiseren, dat er meer oorzaken van transversale isotropie bestaan dan diegene welke hier genoemd zijn. Daarom moet men de 'scheidingsmethode', zoals die in dit proefschrift beschreven wordt, slechts zien als een eerste stap op weg naar het onderscheiden van de verschillende

oorzaken van transversale isotropie.

Omdat het 'representeren' van media met cracks d.m.v. fijn gelaagde media sterk afhankelijk is van het materiaal in de cracks, zou zo'n 'representatie' niet alleen een interessante manier zijn om de oorzaken van transversale isotropie te onderscheiden, maar zou het ook goed gebruikt kunnen worden bij het bestuderen van de aard van het materiaal in de cracks. Het bestuderen hiervan in een uniform medium met cracks als een functie van de tijd of de plaats zou erg belangrijk kunnen zijn voor respectievelijk aardbevingsvoorspellingen en gas exploratie.

Het bestuderen van anisotropie waarnemingen is een machtig middel om informatie te verkrijgen omtrent de interne structuur (zoals georiënteerde insluitels, fijne gelaagdheid) van gesteenten, welke vaak afmetingen heeft, die veel kleiner zijn dan de gebruikte seismische golflengte. Het bestuderen van anisotropie, die veroorzaakt wordt door spanningsgeoriënteerde cracks, biedt de mogelijkheid om het spanningsveld, dat de cracks oriënteert, te onderzoeken. Er is bewijs, dat een veranderende spanning in sterke mate de aspect ratio van de cracks beïnvloedt. De resultaten uit het eerste gedeelte van dit proefschrift, welke het effect van een veranderende aspect ratio op de resulterende anisotropie laten zien, zijn gebruikt om methoden te ontwikkelen om anisotropie waarnemingen in multi-offset shear-wave VSPs te interpreteren in termen van een veranderende aspect ratio. Variaties in de aspect ratio kunnen geanalyseerd worden in zulke VSPs (hoofdstuk 6) door de variaties in de richting van golfvoortplanting, waar geen shear-wave splitting plaatsvindt, te bestuderen. Deze techniek, die toegepast is op synthetische shear-wave VSPs, zou belangrijke toepassingen kunnen krijgen indien VSPs herhaaldelijk uitgevoerd worden om tijdelijke variaties in anisotropie te kunnen analyseren in termen van een veranderend spanningsveld.

Hoewel shear-wave splitting vaak gebruikt wordt als een identificatie van anisotropie moet men zich wel realiseren dat shear-wave splitting ook veroorzaakt kan worden door transmissie effecten aan grenslagen in isotrope media (hoofdstuk 5). Met dit effect dient rekening gehouden te worden voordat shear-wave splitting geïnterpreteerd kan worden in termen van anisotropie.

Anisotropie kan waardevolle informatie geven over de interne structuur van gesteenten maar kan ook leiden tot foutieve interpretaties indien met haar bestaan geen rekening wordt gehouden. In hoofdstuk 7 wordt dit gedemonstreerd aan de hand van een isotroop inversie programma dat, wanneer het toegepast wordt op VSP-aankomsttijden in gelaagde transversaal isotrope media, fouten kan introduceren in de bepaling van de diepten van de grenslagen. Dit is de reden, dat anisotropie opgenomen dient te worden in inversie methoden. In een eerste poging hiertoe is een transversaal isotroop inversie programma ontwikkeld, dat met succes toegepast is op synthetische multi-offset VSP-data. De ontwikkelde methode is robuust en verder onderzoek is nodig om elegantere methoden te ontwikkelen. Ondanks de robuuste vorm van de methode, laten de resultaten van de transversaal isotrope inversie zien, wanneer ze vergeleken worden met de resultaten van de isotrope inversie, dat zowel een isotroop als een transversaal isotroop model dezelfde dataset van aankomsttijden (van zowel P- als eerst binnenkomende S-golven) kan

verklaren. Om dit probleem van een niet-uniek antwoord op te lossen zal in de inversie gebruik gemaakt moeten worden van aanvullende informatie (zoals polarizatie en shear-wave splitting)

ACKNOWLEDGEMENTS

The research described in this thesis could only be carried out with the help and support of others.

I am very grateful that I had the chance to cooperate with some fascinating scientists working in the field of anisotropy. First of all there is Prof. K. Helbig, who inspired me during the complete term of my research. The many discussions we had together often formed the basis of the results described in this thesis, but also put me on the right track when necessary. His guidance throughout my research, not only professionally but also personally, are highly appreciated. Exciting was the time that I worked together with Mike Schoenberg (Schlumberger-Doll Research). He not only taught me many things about fractures and slipping interfaces, but also how research and wandering around in nature should be combined. Finally, there is Stuart Crampin (British Geological Survey), who I want to thank for the hospitality shown to me during a working visit in September 1987. The modelling studies we did and the discussions we had were very stimulating for me.

I want to thank Schlumberger-Doll Research, who twice (autumns 1986, 1987) gave me the opportunity to work as a summer-student at their beautiful laboratory in Ridgefield (CT, U.S.A.). Both periods gave many new impulses to my research. Especially, the people at their geoaoustics department are thanked for the many fruitful discussions.

I am very grateful to Dirk Gajewski and Ivan Pšenčik, who gave me a free copy of their anisotropic ray-tracing program ANRAY86. Programming became also much easier with the tricks I learned from Jan Brouwer. Sharing room O318 with him was a great pleasure. It was also a pleasure to work together with the other colleagues at Utrecht University. I want to thank all who helped completing this thesis. In particular, I want to thank Dé Pattynama, who supported me throughout my study.

Amoco, the American Geophysical Union (AGU), Conoco, Shell, and the Netherlands Organization for the Advancement of Pure Research (ZWO) are thanked for the financial support given to me to visit geophysical meetings.

I am also grateful to the Editorial Office of the European Association of Exploration Geophysicists for giving permission to publish some of my articles in this thesis.

Last but certainly not least I thank all my relatives and friends for the mental support given to me to finish my study and this thesis, especially: my parents, whose support I shall never forget; Ivonne, who had patience with me and encouraged me whenever she could; my former landlady Mrs. Bleeker, who gave me a 'home' near Utrecht; and Carla, Arnout, Evert, Hans, Ronald, Yin, Peter, and Ernst, who showed what friends are for.

CURRICULUM VITAE

- December 17th 1961 Born in Harkema, The Netherlands
- 1974 - 1980 Gymnasium/Atheneum, Alkmaar, The Netherlands
(preparation school for universities)
- 1980 - 1985 Basic academic training; major Geophysics;
minors Signal Analysis and Computer Sciences;
(drs. degree)
University of Utrecht, The Netherlands
- 1985 - 1988 Research assistant at the Department of
Exploration Geophysics,
University of Utrecht, The Netherlands

Other professional activities:

- 1985 - 1988 Assistant Editor of Geophysical Prospecting
- Oct - Nov 1986/1987 Summer student at Schlumberger-Doll Research,
Ridgefield, U.S.A.